Study of the B → X(3872)K → D*0D̄0K Decay at Belle

THÈSE N^O 4321 (2009)

PAR

Nicolas ZWAHLEN

EPFL

ÉCOLE POLYTECHNIQUE
FÉDÉRALE DE LAUSANNE

Suisse
2009

Résumé

Récemment, plusieurs nouvelles particules inattendues ont été découvertes à des masses voisines de 4 GeV/c^2. Elles sont connues collectivement sous le nom de mésons XYZ et bien que certaines d'entre elles aient été identifiées en tant que charmonium, la plupart ont des propriétés qui ne correspondent pas à la classification en quark-antiquark, et restent inclassables. Le méson $X(3872)$ a été découvert en premier et est la plus étudiée de ces particules, et il y a de nombreuses hypothèses quant à sa nature. On mentionnera également les mésons $X(3940)$ et $Y(3940)$, qui ont la même masse et des largeurs proches ; on ne sait pas s'il s'agit d'un seul état ou pas. La compréhension de ces particules exige davantage de données expérimentales.

Nous présentons l'étude de la désintégration $B \to X(3872)K$ suivie de $X(3872) \to D^{*0}\bar{D}^0$. Cette étude est basée sur un échantillon de 657 millions de paires $B\bar{B}$ enregistrées à la résonance $\Upsilon(4S)$ avec le détecteur Belle du collisionneur à e^+e^- KEKB. Nous étudions les deux canaux $D^{*0} \to D^0\gamma$ et $D^{*0} \to D^0\pi^0$.

Nous obtenons un signal total de $50.1\,^{+14.8}_{-11.1}$ événements, une masse de $3872.9\,^{+0.6}_{-0.4}\,^{+0.4}_{-0.5}$ MeV/c^2, une largeur de $3.9\,^{+2.8}_{-1.4}\,^{+0.4}_{-1.1}$ MeV/c^2 et un produit de rapports d'embranchement

$$\mathcal{B}(B \to X(3872)K) \times \mathcal{B}(X(3872) \to D^{*0}\bar{D}^0) = (0.80 \pm 0.20 \pm 0.11) \times 10^{-4}.$$

Ce signal a une significance statistique de 7.9σ.

Par ailleurs, nous obtenons une limite supérieure avec un niveau de confiance de 90% sur le produit de rapports d'embranchement

$$\mathcal{B}(B \to Y(3940)K) \times \mathcal{B}(Y(3940) \to D^{*0}\bar{D}^0) < 0.67 \times 10^{-4},$$

ce qui suggère que les mésons $X(3940)$ et $Y(3940)$ sont des états différents.

Mots-clé : physique des hautes énergies, Belle, physique des B, charmonium, nouvelles particules.

Abstract

Recently, many unexpected new particles were discovered with masses around 4 GeV/c^2. They are collectively called XYZ mesons and while some of them have been identified as charmonium states, many others have properties that don't fit into the quark-antiquark classification, and so far remain unclassified. The $X(3872)$ meson was the first to be discovered and is the most studied of these states, and there is a variety of hypotheses on its nature. Other new states include the $X(3940)$ and $Y(3940)$ mesons, which have the same mass and similar widths; it is not clear if they are the same state or not. More experimental evidence is required to understand these particles.

We report a search for $B \to X(3872)K$ with $X(3872)$ decaying to $D^{*0}\bar{D}^0$ using a sample of 657 million $B\bar{B}$ pairs recorded at the $\Upsilon(4S)$ resonance with the Belle detector at the KEKB asymmetric-energy e^+e^- collider. The study is performed for both $D^{*0} \to D^0\gamma$ and $D^{*0} \to D^0\pi^0$ decay modes.

We find a total signal of $50.1\,^{+14.8}_{-11.1}$ events with a mass of $3872.9\,^{+0.6}_{-0.4}\,^{+0.4}_{-0.5}$ MeV/c^2, a width of $3.9\,^{+2.8}_{-1.4}\,^{+0.4}_{-1.1}$ MeV/c^2 and a product branching fraction

$$\mathcal{B}(B \to X(3872)K) \times \mathcal{B}(X(3872) \to D^{*0}\bar{D}^0) = (0.80 \pm 0.20 \pm 0.11) \times 10^{-4}.$$

The statistical significance of the signal is 7.9σ.

Furthermore, from the same study we also set an upper limit at 90% confidence level on the product branching fraction

$$\mathcal{B}(B \to Y(3940)K) \times \mathcal{B}(Y(3940) \to D^{*0}\bar{D}^0) < 0.67 \times 10^{-4},$$

which suggests that the $X(3940)$ and $Y(3940)$ mesons are different states.

Keywords: high energy physics, Belle, B physics, charmonium, new particles.

Acknowledgements

Contents

Introduction

My Ph.D. work started in March 2005 at EPFL's *Laboratoire de Physique des Hautes Energies* (LPHE). The main scientific activity of this laboratory is experimental research in hadronic flavor physics, conducted within two large international collaborations, called LHCb and Belle, running big detectors at particle accelerators.

The two experiments are at different stages of their lives: the Belle experiment is running and taking data in steady state, while the next-generation experiment LHCb is currently in the final stages of preparation. Since the timescale of such experiments is of the order of 10–20 years (i.e. much longer than that of a Ph.D. thesis), I have taken the opportunity to work on both projects, gaining experience not only in detector design, construction and simulation with LHCb, but also in detector operations and physics data analysis with Belle.

In practice, I spent the first 18 months of my thesis work on contributions to the development of the High-Level Trigger software of the LHCb experiment, described in Appendix B; while the second part of my work, described in Chapters 4–6, consisted of an analysis of the Belle data in relation with the $X(3872)$ particle. I started working on this second topic in August 2006; I made two visits to the KEK laboratory in Tsukuba, Japan, the first one from September to December 2006, and the second one from early June to early July 2007. These periods at KEK, where the experiment is operated, allowed me to interact with my colleagues, participate in collaboration meetings as well as take an active part in the ongoing data-taking shifts.

The analysis is based on a 605 fb^{-1} data sample (experiments 7–55), corresponding to $N_{B\bar{B}} = (656.7 \pm 8.9)$ million $B\bar{B}$ pairs collected at the $\Upsilon(4S)$ resonance. Preliminary results were presented at the 34th International Conference on High-Energy Physics (ICHEP 2008) held in August 2008 in Philadelphia, USA [1]. This study is also described in an internal Belle document, the Belle note 1006 [2].

In the first chapter of this document an introduction to the Standard Model of particle physics is given. The second chapter describes some of the newly discovered XYZ states, with particular emphasis on the $X(3872)$ which is the main subject of this thesis. Experimental observations and theoretical models are discussed. In the third chapter the experimental apparatus is described, including the KEKB e^+e^- collider and the Belle detector installed around the interaction point, which delivered the data used in this thesis.

Chapter 4 describes the decay chain, the reconstruction procedure and the optimization of the selection criteria. Chapter 5 describes the obtained $X(3872)$ mass signal, the background studies and the construction of the fitting function. Chapter 6 concerns the extraction of the signal from the reconstructed Belle data, various checks of the obtained

results, and the estimation of systematic uncertainties. Appendix A contains several additional Monte Carlo studies, such as the choice of a strategy for kinematical fits, additional Monte Carlo samples for $X(3872) \to D^{*0}\bar{D}^0$, the comparison of the $D^{(*)0}$ mass resolutions with those in data, and $X(3872)$ mass resolution checks.

Chapter 1

The Standard Model
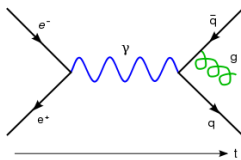
This chapter gives a short introduction to the Standard Model of particle physics. For a more detailed description, see Ref. [3].

The Standard Model of particle physics is a quantum field theory describing the fundamental interactions between elementary particles. These interactions are the electromagnetic interaction and the weak and strong forces. Gravity is not included in the model; gravitational forces are insignificant at the level of particle physics, at least at energies currently accessible in the lab. The Standard Model includes both the electroweak theory and quantum chromodynamics and it is compatible with special relativity and quantum mechanics. So far all experimental results agree with its predictions.

The particles of the model are divided into particles of matter and force-mediating particles (see Table 1.1).

1.1   Particles of matter

Elementary particles of matter are fermions (spin 1/2) and are divided into leptons (electron, muon, tau and their neutrinos) and quarks (up, down, charm, strange, top, bottom or beauty). Each particle has its corresponding antiparticle, which has the same mass but opposite charges.

Leptons and quarks are grouped in three generations or flavours:

$$l = \begin{pmatrix} \nu_e \\ e \end{pmatrix}, \quad \begin{pmatrix} \nu_\mu \\ \mu \end{pmatrix}, \quad \begin{pmatrix} \nu_\tau \\ \tau \end{pmatrix}$$

$$q = \begin{pmatrix} u \\ d \end{pmatrix}, \quad \begin{pmatrix} c \\ s \end{pmatrix}, \quad \begin{pmatrix} t \\ b \end{pmatrix}$$

1.2 Force-mediating particles

The force-mediating particles are bosons (spin 1). They are exchanged between particles of matter when they interact through one of the three fundamental interactions described by the Standard Model:

- The electromagnetic interaction is mediated between electrically charged particles by the photon, which is massless and neutral.

- The weak force has three mediators: the Z^0 and the $W^\pm$. The Z^0 is electrically neutral and has a mass of about 91 GeV/c^2; the $W^\pm$ are electrically charged and have masses of about 80 GeV/c^2.

- The strong force is mediated between coloured particles (quarks) by eight gluons. They are massless and electrically neutral; however they carry a colour-anticolour charge, thus they can also interact among themselves. Leptons don't interact through the strong force, as they don't carry a colour charge.

type	charge	spin	particles			
leptons	-1	1/2	e^-	μ	τ	
	0	1/2	ν_e	ν_μ	ν_τ	
quarks	$+2/3$	1/2	u	c	t	
	$-1/3$	1/2	d	s	b	
mediators	0	1	γ			electromagnetic
	$-1, 0, +1$	1	W^-	Z^0	W^+	weak force
	0	1	gluons			strong force

Table 1.1: Elementary particles.

The Standard Model also contains the yet unobserved Higgs boson, a hypothetical massive scalar elementary particle. The role of this boson is to explain why particles have mass; more specifically, it explains the difference between the massless photon and the massive $W^\pm$ and Z^0 through spontaneous breaking of the electroweak gauge symmetry.

The Standard Model doesn't predict the mass of the Higgs boson, which is not yet observed experimentally. The current experimental limits indicate the Higgs mass to be greater than 114.4 GeV/c^2 at 95% confidence level [4]. The search for the Higgs boson is one of the main goals of CERN's Large Hadron Collider (LHC), which is expected to start taking data in 2009.

1.3 The quark model

Quarks are confined within composite particles called hadrons, bound by the strong interaction field. The quark model is a classification scheme for hadrons in terms of their valence quarks. Table 1.2 shows the properties of the known quarks. Quark masses are taken from Ref. [4].

Quark	electric charge (e)	Mass	Isospin I_z	B
up u	2/3	1.5–3.3 MeV/c^2	1/2	1/3
down d	−1/3	3.5–6.0 MeV/c^2	−1/2	1/3
charm c	2/3	$1.27\,^{+0.07}_{-0.11}$ GeV/c^2	0	1/3
strange s	−1/3	70–130 MeV/c^2	0	1/3
top t	2/3	171.2 ± 2.1 GeV/c^2	0	1/3
bottom (beauty) b	−1/3	$4.2\,^{+0.17}_{-0.07}$ GeV/c^2	0	1/3

Table 1.2: Properties of quarks: electric charge, mass, isospin and baryon number.

Quarks and gluons have an additional quantum number called *colour charge*, which characterizes three states: red, green and blue (r, g, b). A quark can take one of the three colours, while an antiquark takes an anticolour. Gluons carry both a colour and an anticolour. The colour confinement principle requires hadrons to be colourless. There are two common types of hadrons: mesons and baryons.

1.3.1 Mesons

Mesons are bosons composed of a quark-antiquark pair and thus have zero baryon number. Each meson has a corresponding antimeson, where quarks are replaced by their corresponding antiquarks and oppositely. For example, the B^0 particle is a bottom meson, composed of a down quark d and a bottom antiquark $\bar{b}$. Similarly, the B^+ meson is composed of an up quark u and a bottom antiquark $\bar{b}$. The D^{*0} and the D^0 are charmed mesons both composed of a charm quark c and an up antiquark $\bar{u}$. Other particles which appear in this thesis, such as the kaons and pions, are also mesons, composed of the lighter u, d and s quarks.

A flavorless meson composed of a heavy quark and its own antiquark is called a quarkonium. It is called a bottomium if it is a $b\bar{b}$ meson, such as the $\Upsilon(4S)$ produced at Belle; or a charmonium if it is a $c\bar{c}$ meson like the J/ψ. Charmonium states have masses around 3 GeV/c^2, and bottomium states around 10 GeV/c^2. The toponium doesn't exist, because the top quark is so heavy that it decays before a bound state can form.

1.3.2 Baryons

Baryons are fermions composed of three quarks and have unit baryon number. The proton (composed of uud quarks) and the neutron (udd) are well-known examples of baryons. The proton is the only stable baryon. Each baryon has its corresponding antibaryon with −1 baryon number, where each quark is replaced by its antiquark.

1.4 Symmetries and quantum numbers

Symmetries play an important role in the model. For each continuous symmetry, there is a corresponding conserved quantity. The Standard Model also has three discrete symmetries:

- Charge symmetry (C) : replace every particle by its antiparticle.

- Parity symmetry (P) : reflect the three spatial coordinates as in a mirror.

- Time symmetry (T) : reverse the direction of time.

Particles are characterized by their quantum numbers, which describe values of conserved quantities. The isospin I_z is a quantum number related to the strong interaction and depending on the up and down quark content of the hadron, so that $I_z = \frac{1}{2}(N_u - N_d)$, where N_u and N_d are the numbers of up and down quarks, respectively.

The total angular momentum J of a hadron is the combination of the orbital angular momentum L between the quarks and the total spin S, which is the combination of the spins of the quarks. S is equal to 0 or 1 for mesons, and to $\frac{1}{2}$ or $\frac{3}{2}$ for baryons.

Since the charge and parity symmetries are unitary operators ($C^2 = P^2 = 1$), their eigenvalues can only take the values ± 1. For mesonic states, the parity eigenvalue is related to the orbital angular momentum through $P = (-1)^{L+1}$. In addition, for quarkonia, which are eigenstates of the charge conjugation, one has $C = (-1)^{L+S}$.

q	electric charge	
B	baryon number	$\frac{1}{3}$ for quarks, 0 for leptons
S	spin	
I_z	isospin	$I_z = \frac{1}{2}(N_u - N_d)$
L	orbital angular momentum	
J	angular momentum	$|L - S| \leq J \leq L + S$
P	intrinsic parity	$P = (-1)^{L+1}$ for mesons
C	charge conjugation	$C = (-1)^{L+S}$ for quarkonia

Table 1.3: Quantum numbers and some relations between them.

The quantum numbers of a quarkonium state are often labelled using the J^{PC} notation. These states are also described using the spectroscopic notation $n^{2S+1}L_J$, where n is the radial quantum number and symbols for $L = 0, 1, 2, 3, 4, 5$ are S, P, D, F, G, H respectively. For example, a 2^3P_1 meson has $J^{PC} = 1^{++}$.

1.5 Beyond the quark model

With the discovery of quantum chromodynamics, it was understood that the quark model is a simplified vision of the structure of hadrons. Hadrons are composed not only of their valence quarks, but must include virtual quark-antiquark pairs as well as virtual gluons.

In addition, there may be hadrons which lie outside the quark model, although they are still always colourless:

- **Glueballs** contain only valence gluons and no quarks. Theoretical calculations show that glueballs could exist at energy ranges accessible to current colliders; however they are extremely difficult to identify, because they mix with ordinary meson states. So far they have not been observed and identified with certainty; one possible candidate is the $f_J(1710)$ [5].

- **Hybrids** contain valence quarks as well as one or more gluons. The mass spectrum of hybrids was predicted in Ref. [6] and the ground state hybrid masses are expected around 1.7 to 1.9 GeV/c^2. Candidates include the $\pi_1(1400)$, a $J^{PC} = 1^{-+}$ exotic meson reported in the $\pi^- p \to \eta\pi^- p$ reaction [7], and the $\pi_1(1600)$, another 1^{-+} state reported in the $\pi^- p \to \pi^- \rho^0 p$ reaction [8].

- **Tetraquark** mesons contain two quark-antiquark pairs. There have been no confirmed reports of a tetraquark state to date, although the $f_0(980)$ is considered by some authors to be a $J^{PC} = 0^{++}$ light tetraquark state [9]. The B factories recently observed two very narrow states, the $D_{sJ}(2317)^{*\pm}$ and the $D_{sJ}(2460)^{*\pm}$ [10, 11], which have also been interpreted as tetraquark states.

- **Pentaquark** baryons contain four quarks and one antiquark. In 2003, the LEPS collaboration reported evidence for the Θ^+, a $udud\bar{s}$ pentaquark candidate with a mass of 1540 ± 10 MeV/c^2, with a 4–5σ statistical significance. The Θ^+ was then confirmed by ten experimental papers with significances ranging from 3 to 7σ. However, it was not seen by the B factories and other high-energy experiments. Because of these non-confirmations, it is doubted that the Θ^+ really exists [12].

Recently there has been a revival of interest in the possible existence of mesons with a more complex structure than the simple $q\bar{q}$ states of the quark model. These types of particles are often looked for in systems that include a $c\bar{c}$ charmed-anticharmed quark pair, because in some of these cases the states are expected to have clean experimental signatures and relatively narrow widths. The XYZ mesons described in the next chapter are often interpreted as such exotic states.

1.6 CP violation

Both experiments I contributed to during my thesis were designed to study the effects of CP violation. CP violation is the violation of the CP symmetry, the product of charge conjugation (C) and parity (P). The strong and electromagnetic interactions appear to be invariant under CP, however it is violated in certain types of weak decays. The first CP violation was discovered in 1964 in neutral kaon decays.

In 2001 two new experiments, Belle and BaBar, started to study CP violation in B decays and found several CP-violating processes. CP violation is one of the crucial mechanisms generating the observed matter-antimatter asymmetry of the Universe. CP violation is incorporated in the Standard Model through a complex phase in the CKM matrix of quark mixing. For a detailed description of CP violation, see Ref. [13].

1.7 Limitations of the Standard Model

The Standard Model has several limitations and problems, which lead many to think that it is not the ultimate theory of particle physics.

- The model does not attempt to describe gravity.

- It doesn't explain why there are three generations of quarks and leptons with very different masses. Why are there 14 orders of magnitude between the neutrino masses $(10^{-3} \text{ eV}/c^2)$ and the top quark mass $(1.71 \times 10^{11} \text{ eV}/c^2)$?

- It has a large number of free parameters (18, not including the neutrino masses), the values of which are only accessible through experiment. Is there a more complete theory that could predict some of these values?

- The hierarchy problem: the weak scale and the Planck scale are very disparate. In other words: why is the weak force 10^{32} times stronger than gravity ?

- It is not clear how to reconcile the emerging understanding of cosmology with the Standard Model.

- The model does not explain the large matter-antimatter asymmetry of the universe. The observed CP violation alone is insufficient.

Chapter 2

The XYZ mesons
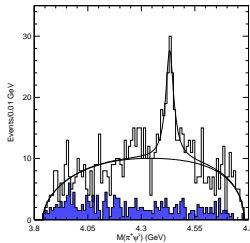
We introduce the recently discovered XYZ mesons, with particular emphasis on the $X(3872)$. The experimental observations and theoretical models are summarized.

Recently the B factories have discovered a number of new and unexpected states with masses around 4 GeV/c^2, collectively known as XYZ mesons [14]. Among these are the $X(3872)$, $Z(3930)$, $X(3940)$, $Y(3940)$, $Y(4260)$ and $Z^\pm(4430)$. The main properties of these XYZ states are summarised in Table 2.1.

Some of them were assigned to $c\bar{c}$ charmonium states, but most of them don't fit into the quark-antiquark spectrum and remain unclassified; in these cases a multiquark or two-meson composition seems more likely. Several theoretical models have been proposed to explain the observed states, for example bound molecular states of $D^*\bar{D}$ mesons, diquark-antidiquark tetraquark states, or $c\bar{c}g$ charmonium-gluon hybrids. However, these models are usually confined to subsets of the observed states, and their predictions have had limited success. No single model seems to be able to successfully describe the whole set of XYZ states.

For a detailed description of the XYZ mesons, see References [14, 15, 16].

2.1 $X(3872)$

2.1.1 Discovery and experimental observations

The $X(3872)$ was discovered by the Belle collaboration in 2003 in the charged B-meson decay $B^+ \to X(3872)K^+ \to J/\psi\,\pi^+\pi^-K^+$ [17] with a mass of $3872.0 \pm 0.6 \pm 0.5$ MeV/c^2 and a width smaller than 2.3 MeV/c^2 at 90% confidence level (Figure 2.1). It was later confirmed by the CDF [19] and DØ [20] collaborations through inclusive production in proton-antiproton collisions, and by the BaBar collaboration [18], in the same decay

state	M (MeV)	Γ (MeV)	production mode	decay mode	seen by
$X(3872)$	3871.5 ± 0.4	< 2.3	$B \to X(3872)K$	$J/\psi\,\pi^+\pi^-$	Belle [17], BaBar [18], CDF [19], DØ [20]
$X(3875)$	3875.2 ± 0.7	$3.0\,^{+2.1}_{-1.7}$	$B \to X(3875)K$	$D^0\bar{D}^0\pi^0, D\bar{D}^*$	Belle [21], BaBar [22]
$Z(3930)$	3929 ± 5	29 ± 10	$\gamma\gamma \to Z(3930)$	$D\bar{D}$	Belle [23]
$X(3940)$	3943 ± 6	39 ± 26	$e^+e^- \to X(3940)J/\psi$	$D\bar{D}^*$	Belle [24]
$Y(3940)$	3943 ± 17	87 ± 34	$B \to Y(3940)K$	$J/\psi\,\omega$	Belle [25], BaBar [26]
$X(4160)$	4156 ± 29	$139\,^{+113}_{-65}$	$e^+e^- \to X(4160)J/\psi$	$D^*\bar{D}^*$	Belle [27]
$Y(4008)$	$4008\,^{+82}_{-49}$	$226\,^{+97}_{-80}$	e^+e^- (ISR)	$J/\psi\,\pi^+\pi^-$	Belle [28]
$Y(4260)$	4264 ± 12	83 ± 22	e^+e^- (ISR)	$J/\psi\,\pi^+\pi^-$	BaBar [29], Belle [28], CLEO [30]
$Y(4350)$	4361 ± 13	74 ± 18	e^+e^- (ISR)	$\psi(2S)\pi^+\pi^-$	BaBar [31], Belle [32]
$Y(4660)$	4664 ± 12	48 ± 15	e^+e^- (ISR)	$\psi(2S)\pi^+\pi^-$	Belle [32]
$Z_1^+(4050)$	4051 ± 14	$82\,^{+21}_{-17}$	$B^0 \to Z_1^+(4050)K^-$	$\chi_{c1}\pi^+$	Belle [33]
$Z_2^+(4250)$	$4248\,^{+44}_{-29}$	$177\,^{+54}_{-39}$	$B^0 \to Z_2^+(4250)K^-$	$\chi_{c1}\pi^+$	Belle [33]
$Z^\pm(4430)$	4433 ± 5	$45\,^{+35}_{-18}$	$B \to Z^\pm(4430)K$	$\psi(2S)\pi^\pm$	Belle [34]

Table 2.1: Summary of the main properties of some of the XYZ mesons.
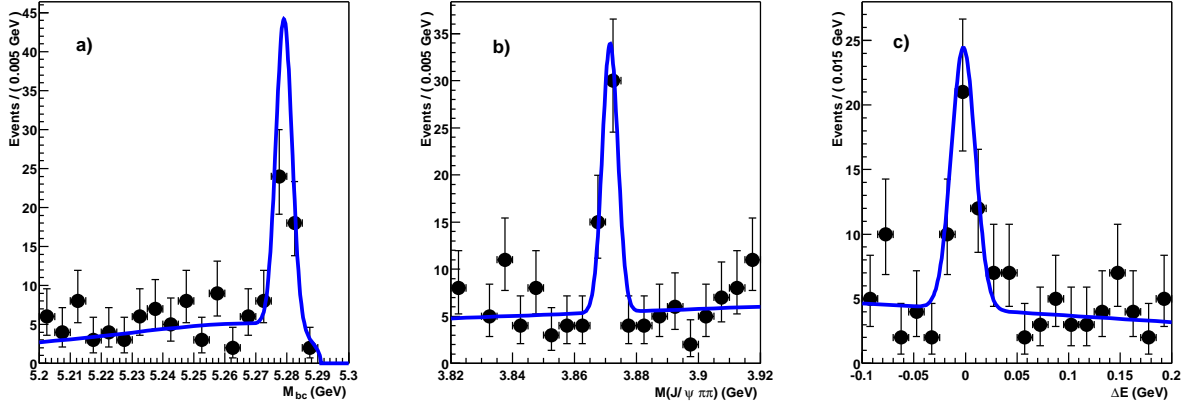
Figure 2.1: Discovery of $X(3872)$ in the $B \to J/\psi\,\pi^+\pi^- K$ channel by Belle [17]. Signal-band projections of (a) $M_{\rm bc}$, (b) $M_{J/\psi\pi^+\pi^-}$ and (c) ΔE for the $X(3872) \to J/\psi\pi^+\pi^-$ signal region. The curves are the results of unbinned fits.

channel as Belle.

An important feature of the $X(3872)$ is that its mass is very close to the $D^{*0}\bar{D}^0$ threshold $(3871.8 \pm 0.3$ MeV/c^2 [4]). A recent preliminary measurement by the CDF collaboration gives a mass of $3871.61 \pm 0.16 \pm 0.19$ MeV/c^2 [35]. This is the most precise measurement of the $X(3872)$ mass to date. The current average mass in the $J/\psi\pi^+\pi^-$ channel is 3871.56 ± 0.20 MeV/c^2 (averaging the most recent measurements from Belle, BaBar, CDF and DØ [36, 37, 35, 20], Figure 2.2) and the full width is less than 2.3 MeV/c^2 at 90% confidence level.

Concerning the quantum numbers, the observation by Belle and BaBar of the decay $X(3872) \to J/\psi\,\gamma$ fixes the charge conjugation number $C = 1$ [38, 39]. Recent studies from Belle and CDF combining angular information and the kinematic properties of the dipion pair rule out the $J^{PC} = 0^{++}$ or 0^{-+} values and strongly favor a 1^{++} or 2^{-+} assignment [40, 41, 42].

The $X(3872)$ was also observed by Belle as a near-threshold enhancement in the $D^0\bar{D}^0\pi^0$ invariant mass spectrum of the $B \to D^0\bar{D}^0\pi^0 K$ channel [21], with a peak at 3875.18 ± 0.68 MeV/c^2, a Gaussian width of 2.42 ± 0.55 MeV/c^2 and a product branching fraction $\mathcal{B}(B \to X(3872)K) \times \mathcal{B}(X(3872) \to D^0\bar{D}^0\pi^0) = (1.22 \pm 0.31\,^{+0.23}_{-0.30}) \times 10^{-4}$. This study was based on a 414 fb^{-1} data sample and the signal has a statistical significance of 6.4σ. However, it could not determine whether the $X(3872)$ decays through a D^{*0} or not.

The BaBar collaboration recently published an observation of 33 ± 7 $B \to X(D^{*0}\bar{D}^0)K$ events with a 4.9σ significance (Ref. [22], Figure 2.3). Their study is based on a 347 fb^{-1} data sample. The observed mass is $3875.1\,^{+0.7}_{-0.5} \pm 0.5$ MeV/c^2 and the width is $3.0\,^{+1.9}_{-1.4} \pm 0.9$ MeV/c^2, with a product branching fraction $\mathcal{B}(B^+ \to X(3872)K^+) \times \mathcal{B}(X(3872) \to D^{*0}D^0) = (1.67 \pm 0.36 \pm 0.47) \times 10^{-4}$. The recent precision determination of the D^0 mass by the CLEO collaboration is used, giving a $D^{*0}\bar{D}^0$ threshold mass value of 3871.81 ± 0.36 MeV/c^2 [43].

The state observed by Belle and BaBar in double-charmed decays is suspected to be another state, sometimes called $X(3875)$, since the observed mass $(3875.1 \pm 0.6$ MeV/$c^2)$
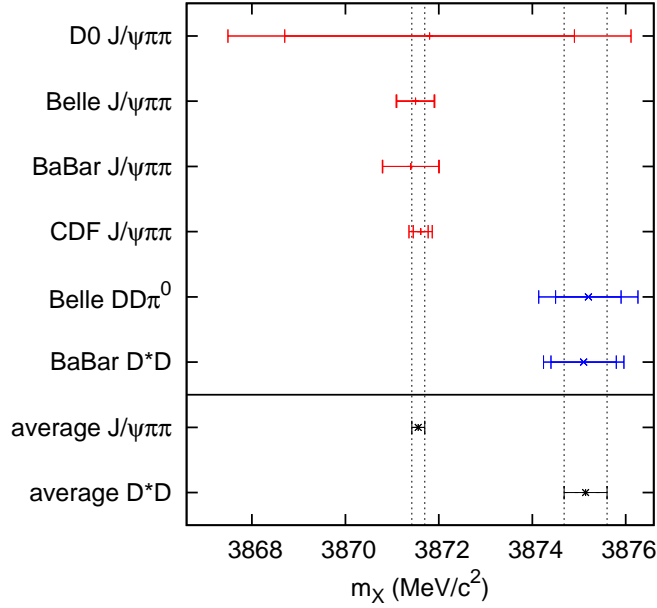
Figure 2.2: Experimental $X(3872)$ mass measurements and averages in the $J/\psi\pi^+\pi^-$ [20, 36, 37, 35] and $D^{*0}\bar{D}^0$ [21, 22] channels.

is 5.4σ higher than the current average value for $X(3872)$ (see Figure 2.2). It should be noted that measurements of the $X(3872)$ mass from $X(3872) \to D^{*0}\bar{D}^0$ decays have a strong dependance on the value of the $D^{*0}\bar{D}^0$ threshold mass; this is important since the nominal D^0 and D^{*0} masses are not yet known with a very good precision.

Table 2.2 gives a summary of observed $X(3872)$ decay modes.

2.1.2 Theoretical models

There is a variety of theoretical interpretations for the $X(3872)$, most of which go beyond the simple $q\bar{q}$ state. It may be:

- A $c\bar{c}$ charmonium state: however, in the discovery mode $J/\psi\,\pi^+\pi^-$, the $\pi^+\pi^-$ invariant masses concentrate near the upper kinematic boundary, corresponding to the ρ^0 meson mass. Charmonium decays to $J/\psi\,\rho^0$ are isospin violating and are expected to be strongly suppressed. In addition, the mass is not near any expected charmonium state (see Table 2.3). The candidates matching the 1^{++} or 2^{-+} quantum numbers are χ'_{c1} and η_{c2}. The χ'_{c1} is the name given to the 2^3P_1 state; it has $J^{PC} = 1^{++}$ and its predicted mass is 3953 MeV/c^2 [45, 44]. The η_{c2} is the 1^1D_2 state; it has $J^{PC} = 2^{-+}$ and its predicted mass is 3837 MeV/c^2. However its branching fraction to $J/\psi\,\pi^+\pi^-$ is expected to be very small. Thus it is difficult to accomodate the $X(3872)$ with a charmonium state. As charmonium, the ratio of $B^0 \to X(3872)K^0$ to $B^+ \to X(3872)K^+$ decays is expected to be unity.

- A mesonic molecule: a set of two mesons bound together by the strong force; the mesonic equivalent of the deuteron (a proton-neutron system bound by pion ex-
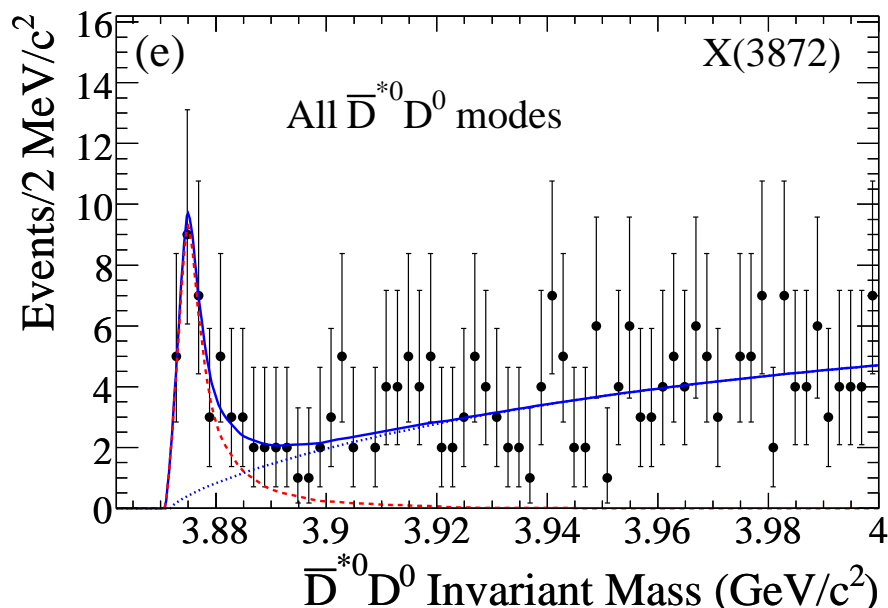
Figure 2.3: Invariant $\bar{D}^{*0}D^0$ mass distribution in the data for events in the B signal region from the BaBar experiment [22]. Points with errors are data events, the solid line represents the fit to the data, the dashed line shows the contribution of the $X(3872)$ signal, and the dotted line shows the background contribution.

channel	collab.	mass (MeV/c^2)	width (MeV/c^2)	signif.	Ref.
$B \to J/\psi\,\pi\pi K$	Belle	$3872.0 \pm 0.6 \pm 0.5$	< 2.3	10σ	[17]
$p\bar{p} \to J/\psi\,\pi\pi$	CDF	$3871.3 \pm 0.7 \pm 0.4$	resolution	11.6σ	[19]
$p\bar{p} \to J/\psi\,\pi\pi$	DØ	$3871.8 \pm 3.1 \pm 3.0$	resolution	5.2σ	[20]
$B \to J/\psi\,\pi\pi K$	BaBar	3873.4 ± 1.4	-	3.5σ	[18]
$B \to J/\psi\,\pi\pi K$	Belle	$3871.5 \pm 0.4 \pm 0.1$	-	$> 10\sigma$	[36]
$B \to J/\psi\,\pi\pi K$	BaBar	$3871.4 \pm 0.6 \pm 0.1$	< 3.3	8.6σ	[37]
$p\bar{p} \to J/\psi\,\pi\pi$	CDF	$3871.61 \pm 0.16 \pm 0.19$	-	-	[35]
$B \to D^0\bar{D}^0\pi^0 K$	Belle	$3875.2 \pm 0.7 \pm 0.8$	5.7 ± 1.3	6.4σ	[21]
$B \to D^{*0}\bar{D}^0 K$	BaBar	$3875.1\,^{+0.7}_{-0.5} \pm 0.5$	$3.0\,^{+1.9}_{-1.4} \pm 0.9$	4.9σ	[22]
$B \to J/\psi\gamma K$	Belle	-	-	4.0σ	[38]
$B \to J/\psi\gamma K$	BaBar	-	-	3.6σ	[39]
$B \to \psi(2S)\gamma K$	BaBar	-	-	3.5σ	[39]

Table 2.2: Observed $X(3872)$ decay channels, with corresponding mass and width if available.

change). The molecule hypothesis is motivated by the proximity of the $X(3872)$ to the $D^{*0}\bar{D}^0$ threshold. In Ref. [46] Törnqvist discusses the possibility that the $X(3872)$ is a two-meson system bound by an attractive pion exchange mechanism. Such $D^*\bar{D}$ deuteron-like states were predicted long ago with masses close to 3870 MeV/c^2 [47]. In this model, the ratio of $B^0 \to X(3872)K^0$ to $B^+ \to X(3872)K^+$ decays can be different from unity [48].

- A tetraquark state: a hypothetical meson composed of four valence quarks. Maiani *et al* [49] study diquark-antidiquark spectra and identify the $X(3872)$ with the $J^{PC} = 1^{++}$ state of $[cq][\bar{c}\bar{q}]$. They find a 2^{++} state at 3952 MeV/c^2 which could be identified with the $X(3940)$, and several other states which remain unseen. Their model also predicts two charged partners $X^\pm$, and two neutral X states, $[cu][\bar{c}\bar{u}]$ and $[cd][\bar{c}\bar{d}]$, with a mass difference of 8 ± 3 MeV/c^2. They argue that the $X(3872)$ state decaying into $J/\psi\,\pi^+\pi^-$ is the $[cd][\bar{c}\bar{d}]$ neutral state, while the $X(3876)$ decaying into $D^0\bar{D}^0\pi^0$ is the $[cu][\bar{c}\bar{u}]$ state [50].

- A $c\bar{c}g$ hybrid meson: a $c\bar{c}$ system possessing a valence gluon [51], which would decay predominantly through $X(3872) \to J/\psi gg \to J/\psi\pi\pi$. However, current model expectations for the masses of $c\bar{c}g$ hybrids are in the range $4200 - 4400$ MeV/c^2, which is difficult to accomodate with the $X(3872)$ mass. In this model, the ratio of $B^0 \to X(3872)K^0$ to $B^+ \to X(3872)K^+$ decays is expected to be unity.

- The authors of Ref. [52] attempt to reconcile the $X(3872)$ with the near-threshold enhancement seen by Belle in the $D^0\bar{D}^0\pi^0$ final state [21]. They perform a Flatté analysis of the Belle data and conclude that the structure seen at 3875 MeV/c^2 is a manifestation of the $X(3872)$, where the mean mass is below the $D^{*0}\bar{D}^0$ threshold and only the high-mass tail of the mass distribution contributes to the $X(3872) \to D^{*0}\bar{D}^0$ decay. See Section 6.2.3 for more details on the Flatté distribution.

2.1.3   Recent experimental observations

Recently, the Belle collaboration released updated preliminary results on the $X(3872)$ produced in $B^+ \to X(3872)K^+$ and $B^0 \to X(3872)K_S^0$ decays, where $X(3872)$ decays to $J/\psi\,\pi^+\pi^-$ [36]. The analysis is based on a 605 fb^{-1} data sample. The first statistically significant observation of $B^0 \to X(3872)K_S^0$ is reported, with a 5.9σ significance. The average mass is $3871.46 \pm 0.37 \pm 0.07$ MeV/c^2 and the ratio of branching fractions

$$\frac{\mathcal{B}(B^0 \to X(3872)K^0)}{\mathcal{B}(B^+ \to X(3872)K^+)} = 0.82 \pm 0.22 \pm 0.05$$

is consistent with unity. The mass difference between the $X(3872)$ states produced in B^+ and B^0 decays is

$$\delta M = M_{XK^+} - M_{XK^0} = (0.18 \pm 0.89 \pm 0.26) \text{ MeV}/c^2,$$

consistent with zero.

For the ratio of branching fractions, BaBar finds [37]

$$\frac{\mathcal{B}(B^0 \to X(3872)K^0)}{\mathcal{B}(B^+ \to X(3872)K^+)} = 0.41 \pm 0.24 \pm 0.05.$$
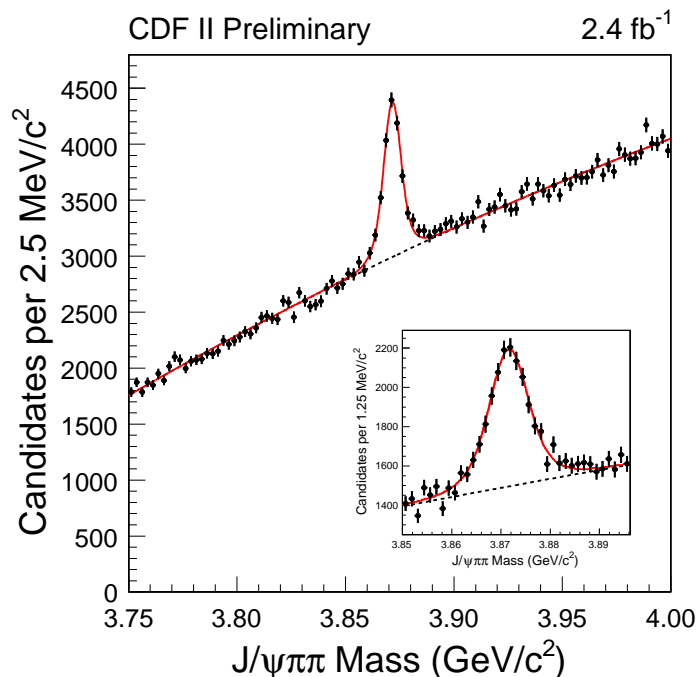
Figure 2.4: Distribution of the $J/\psi\pi^+\pi^-$ mass at CDF [35]. The points represent data, the full line the total fit and the dashed line the combinatorial background. The inset shows a zoom to the region of the $X(3872)$.

In summer 2008, the CDF collaboration published the most precise measurement of the $X(3872)$ mass to date, with a mass of $3871.61 \pm 0.16 \pm 0.19$ MeV/c^2 obtained from the decay mode to $J/\psi\pi^+\pi^-$ [35] (Figure 2.4). In addition, they probe the possibility of existence of two nearby states by comparing the expected width of one- and two-state hypotheses to the measured width in data. No indication for two states is found, and they set an upper limit on the mass difference between two possible states of $\Delta m < 3.2$ MeV/c^2 at 90% CL.

The BaBar collaboration also published an evidence for $B \rightarrow X(3872)K$ radiative decays with $X(3872) \rightarrow J/\psi\,\gamma$ and $X(3872) \rightarrow \psi(2S)\gamma$[1] with 3.6σ and 3.5σ significance, respectively [39]. They find a relatively large branching fraction for $X(3872) \rightarrow \psi(2S)\gamma$, which is inconsistent with a purely $D^{*0}\bar{D}^0$ molecular interpretation of the $X(3872)$ and indicates a possible mixing of molecular and charmonium components.

2.2 Other XYZ mesons

2.2.1 $X(3940)$ and $Y(3940)$

The $X(3940)$ was discovered by Belle in $e^+e^- \rightarrow X(3940)J/\psi$ with $X(3940) \rightarrow D^{*0}\bar{D}^0$ [24]. Its mass is $3943 \pm 6 \pm 6$ MeV/c^2 and its width is 39 ± 26 MeV/c^2, consistent with

---

[1]the $\psi(2S)$ is sometimes called ψ'.

zero within the large statistical error (Figure 2.5). The authors also set the 90% CL limits $\mathcal{B}(X(3940) \to \omega J/\psi) < 0.26$ and $\mathcal{B}(X(3940) \to D^{*0}\bar{D}^0) > 0.45$.

Another state, the $Y(3940)$, was also discovered by Belle in $B \to Y(3940)K$ with $Y(3940) \to \omega J/\psi$ [25]. It has the same mass as the $X(3940)$: 3943 ± 17 MeV/c^2, but it is somewhat wider, with 87 ± 34 MeV/c^2 (Figure 2.5). The obtained product branching fraction is

$$\mathcal{B}(B \to Y(3940)K) \times \mathcal{B}(Y(3940) \to \omega J/\psi) = (0.71 \pm 0.13 \pm 0.31) \times 10^{-4}.$$

This state was later confirmed by BaBar [26], although with a smaller mass ($3914.6\,^{+3.8}_{-3.4} \pm 1.9$ MeV/c^2) and width ($34\,^{+12}_{-8} \pm 5$ MeV/c^2). BaBar finds a product branching fraction of

$$\mathcal{B}(B^+ \to Y(3940)K^+) \times \mathcal{B}(Y(3940) \to \omega J/\psi) = (0.49 \pm 0.10 \pm 0.05) \times 10^{-4},$$

in agreement with Belle. It is possible that the $X(3940)$ and the $Y(3940)$ are the same states.

In addition, a third state with a similar mass, the $Z(3930)$, was discovered by Belle in two-photon collisions $\gamma\gamma \to D\bar{D}$ with a mass of 3929 ± 5 MeV/c^2 [23]. This particle is interpreted as the $\chi_{c2}(2P)$ charmonium state.

2.2.2 $Y(4260)$

The $Y(4260)^2$ was discovered by BaBar as a broad $J^{PC} = 1^{--}$ resonance in the invariant-mass spectrum of $J/\psi\,\pi^+\pi^-$ in $e^+e^- \to \gamma_{\mathrm{ISR}}J/\psi\,\pi^+\pi^-$ initial-state radiation events [29]. Their data can be characterized by a single resonance with a mass of about 4260 MeV/c^2 and a width of about 90 MeV/c^2, or by multiple narrow resonances; the number of new states can't be distinguished.

Since this state wasn't observed in open charm decays, while it is far from the $D\bar{D}$ threshold, it was proposed that it may be a $c\bar{c}g$ hybrid meson [53]. The $Y(4260)$ was confirmed by CLEO in initial-state radiation events [30], and by Belle, who also found a second cluster of events around 4.0 GeV/c^2, called $Y(4008)$ [28].

Additional states from the initial-state radiation family include the $Y(4350)$ observed by BaBar [31] and confirmed by Belle [32], and the $Y(4660)$ observed by Belle [32].

2.2.3 $Z^+(4430)$

The $Z^+(4430)$ (Figure 2.7) was discovered by Belle in $B \to Z^+(4430)K \to \pi^+\psi(2S)K$ [34] and is the first of the XYZ states to be electrically charged. Thus it cannot be a $c\bar{c}$ charmonium or a $c\bar{c}g$ hybrid since these are electrically neutral. The remaining possibilities are a tetraquark state or a molecule [54].

The BaBar collaboration also presented a search for $Z^+(4430) \to J/\psi\,\pi^+$ and $Z^+(4430) \to \psi(2S)\pi^+$ in $B \to J/\psi\,(\psi(2S))K\pi^+$ decays [55], but no significant evidence for the existence of the $Z^+(4430)$ was obtained.

Two other charged states, the $Z_1^+(4050)$ and $Z_2^+(4250)$, were observed by Belle in $B^0 \to Z_{1,2}^+ K^- \to \chi_{c1}\pi^+ K^-$ decays [33].

---

[2] the $Y(4260)$ is called $X(4260)$ in the PDG 2008 [4].

State	mass (MeV/c^2)	State	mass (MeV/c^2)
1^3D_3	3849	2^3P_2	3979
1^3D_2	3838	2^3P_1	3953
1^3D_1	3819	2^3P_0	3916
1^1D_2	3837	2^1P_1	3956

Table 2.3: Predicted masses of $1D$ and $2P$ charmonium states, from Ref. [44].
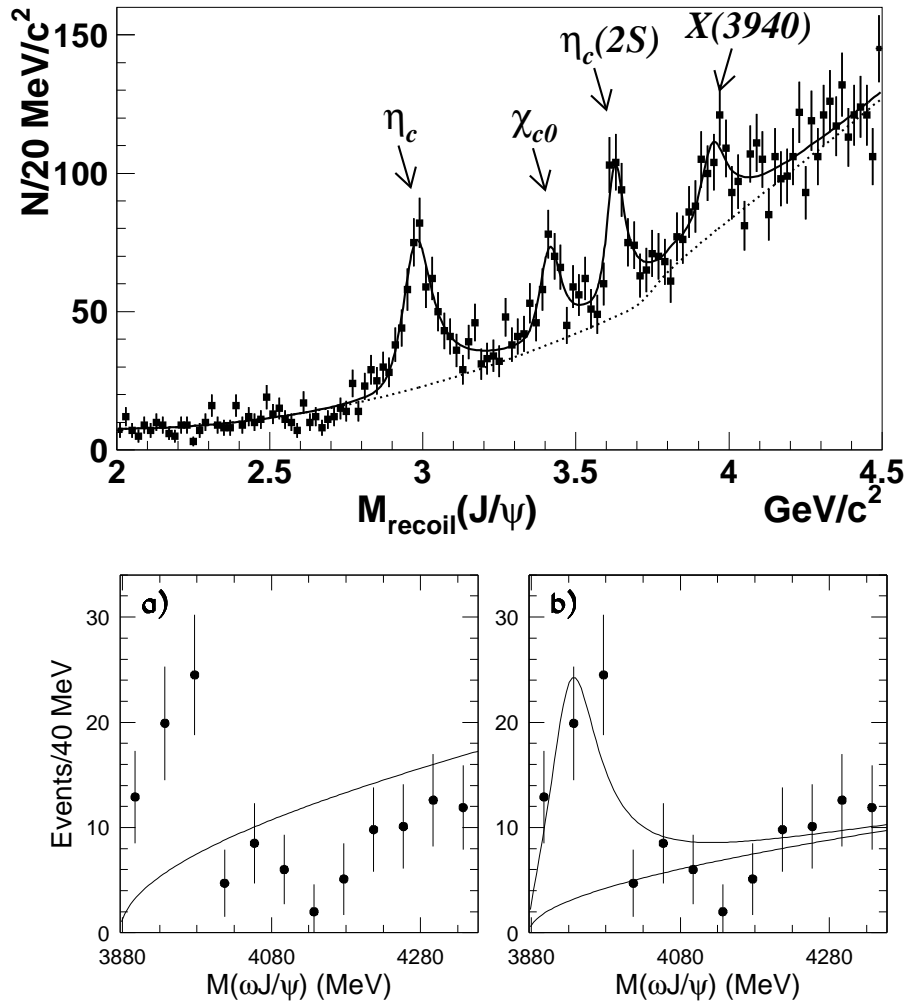
Figure 2.5: Discovery of $X(3940)$ and $Y(3940)$ at Belle. Top: distribution of the mass of the system recoiling against J/ψ in inclusive $e^+e^- \rightarrow J/\psi X$ events [24]. The $X(3940)$ is visible as a fourth enhancement in addition to previously reported η_c, χ_{c0} and $\eta_c(2S)$ peaks. Bottom: $Y(3940)$ signal in the $\omega J/\psi$ mass distribution in $B \rightarrow \omega J/\psi K$ decays [25]. The curve in (a) is the result of a fit that includes only a phase-space-like threshold function, while the curve in (b) also includes a Breit-Wigner resonance term.
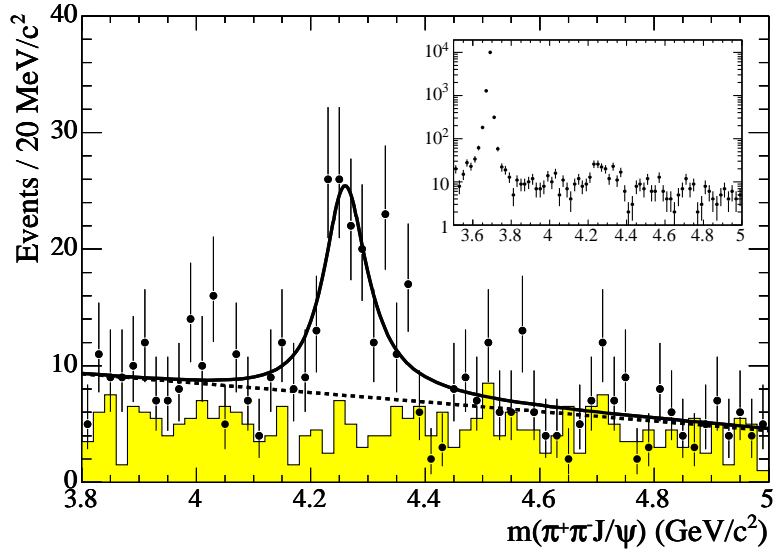
Figure 2.6: Discovery of $Y(4260)$ in the $\pi^+\pi^- J/\psi$ mass distribution in $e^+e^- \rightarrow \gamma_{\mathrm{ISR}} J/\psi \,\pi^+\pi^-$ initial-state radiation events at BaBar [29]. The solid curve is the result of a single-resonance fit; the dashed curve represents the background component, and the shaded histogram represents the scaled data from neighboring e^+e^- and $\mu^+\mu^-$ mass regions. The inset shows a wider mass range including the $\psi(2S)$.
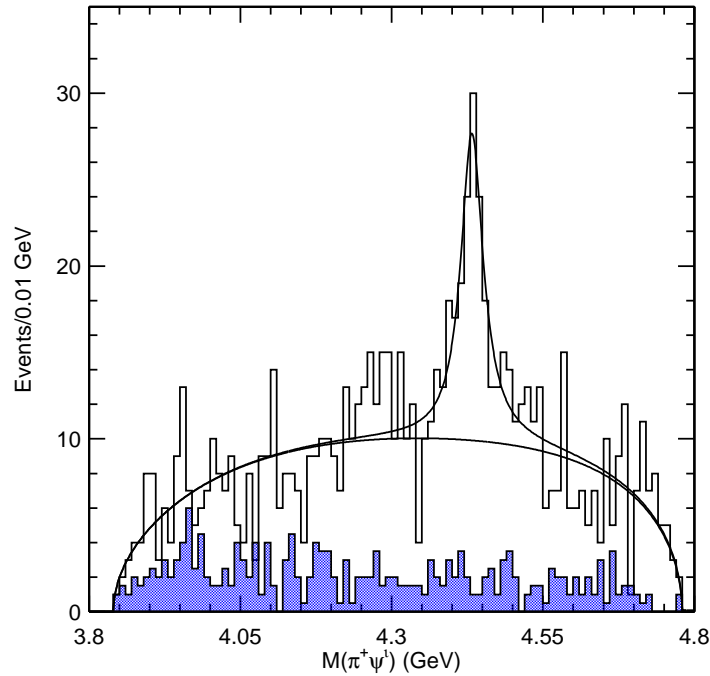
Figure 2.7: Discovery of $Z^+(4430)$ in the $M(\pi^+\psi(2S))$ distribution from $B \rightarrow \pi^+\psi(2S)K$ decays at Belle [34]. The curve is the sum of a relativistic Breit-Wigner function and a smooth phase-space-like function. The filled histogram shows scaled results from the ΔE sideband.

Chapter 3

The Belle experiment

In this chapter a general description of the Belle experiment is given. First the KEKB accelerator is presented, then the Belle detector and its subdetectors are described.

3.1 The KEKB accelerator

The KEKB accelerator is located at the KEK (Kō Enerugi Kasokuki Kenkyū Kikō) laboratory in Tsukuba, Japan. It is a high luminosity asymmetric e^+e^- collider operating at the $\Upsilon(4S)$ resonance. The construction of the accelerator was completed in November 1998. A detailed description of the accelerator can be found in Ref. [56].

The accelerator (Figure 3.1) is composed of two side-by-side rings fed by a linear accelerator (linac). The rings are installed in a 3 km long tunnel buried 10 m below the surface. In a first stage of the linac, electrons are accelerated to an energy of 4 GeV. Positrons are then produced by hitting a thin tungsten monocrystal target with some of these electrons, which will radiate photons. These photons create electron-positron pairs and the positrons are collected and accelerated to 3.5 GeV. The electron beam is then accelerated further, and both beams are directly injected into the rings at full energies: the high-energy ring (HER) contains electrons at 8.0 GeV energy and the low-energy ring (LER) contains positrons at 3.5 GeV.

There is only one interaction point, called Tsukuba, where the beams cross each other in the center of the Belle detector. The crossing angle is ± 11 mrad (22 mrad in total). Colliding the beams gives a 10.58 GeV center-of-mass energy, equal to the nominal mass of the $\Upsilon(4S)$. This resonance decays to $B\bar{B}$ almost 100% of the time; thus KEKB is called a B factory. Due to the beam energy asymmetry, the B meson pairs are created with a Lorentz boost factor of $\beta\gamma = 0.425$.

The design luminosity is 1×10^{34} cm^{-2} s^{-1}, and the record peak luminosity was reached in 2006 at 1.71×10^{34} cm^{-2} s^{-1}. Since it started taking data in 2000, the Belle experiment has accumulated over 850 fb^{-1} of data. This high performance is made possible by the
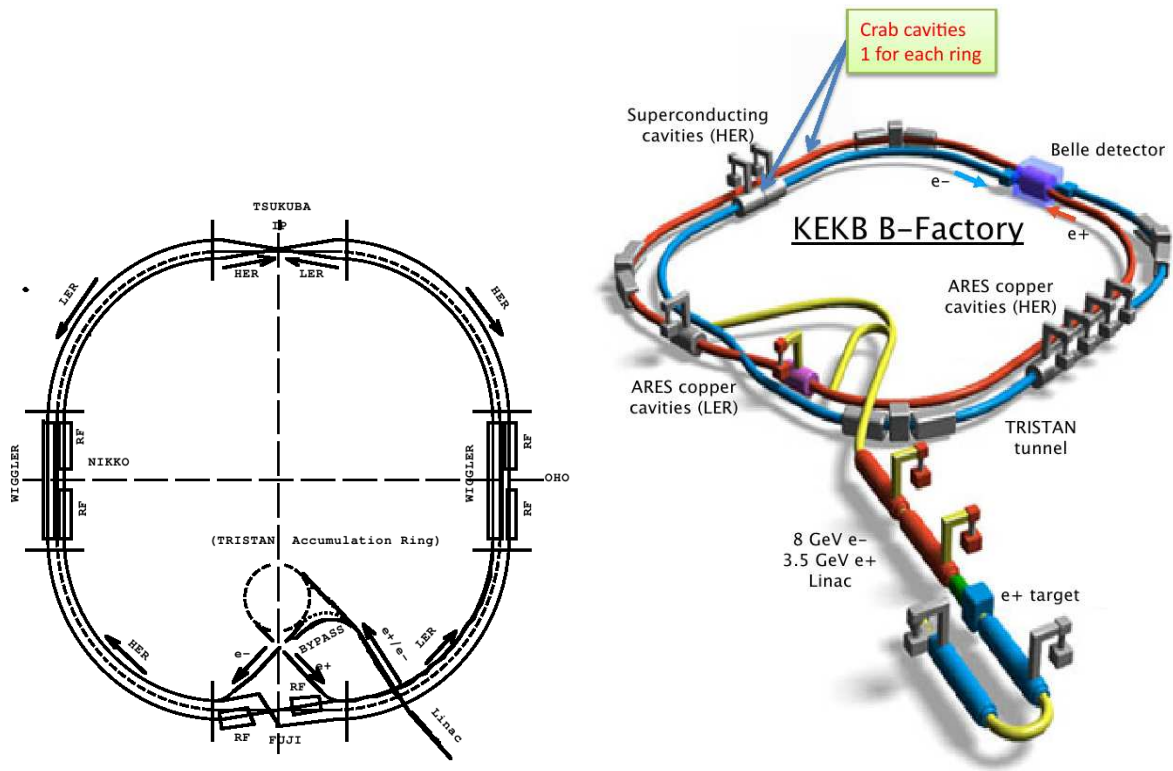
Figure 3.1: Layout of the KEKB accelerator.

continuous beam injection technique used at KEKB, where the detector keeps taking data while the electron and positron beams are being injected into the accelerator.

In 2007, new devices called *crab cavities* were installed at KEKB. Their goal is to achieve effective head-on collisions of the beams while retaining the 22 mrad crossing angle. The crab cavities are superconducting radio-frequency cavities that tilt bunches sideways (like the way a crab walks). One cavity was installed in each ring in January 2007 and commissioned until the end of June of the same year. This new technology was expected to increase the Belle luminosity by a factor 2. Figure 3.2 shows that the crab cavities indeed allowed for an increase in the specific luminosity; however the peak luminosity has not yet reached its 2006 level.

3.2 The Belle detector

The Belle detector [57] is a multi-layer 4π spectrometer, designed to study CP violation in the b-quark sector and rare B-meson decay modes with very small branching fractions. A high luminosity and a very good vertex position resolution are required to achieve the scientific goals of the Belle collaboration.

The detector is composed of the following subdetectors (see Figures 3.3 and 3.4):

- Silicon vertex detector (SVD), for vertexing and tracking;

- Central drift chamber (CDC) in a solenoid magnet, for tracking;
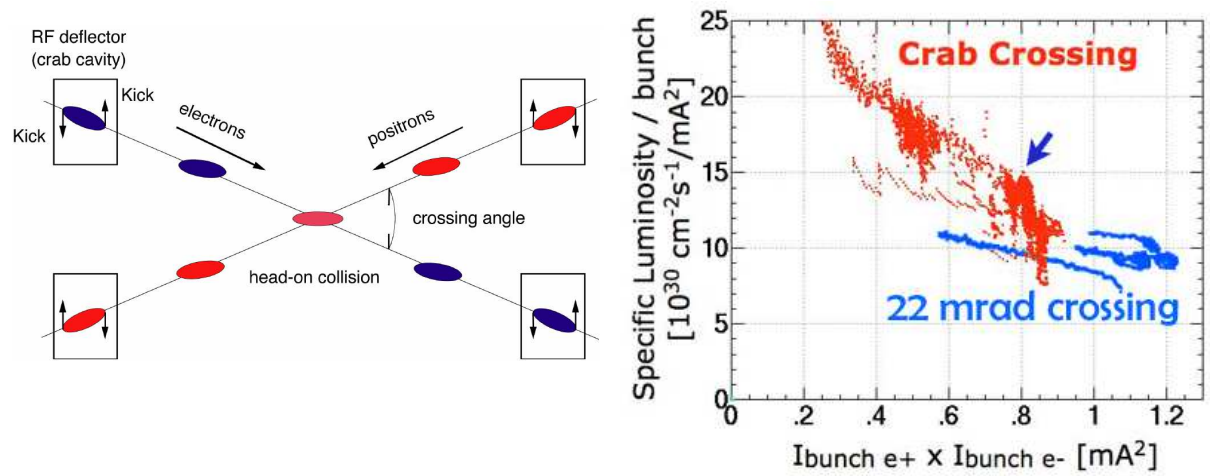
Figure 3.2: Bunch crossing scheme with crab cavities (left) and specific luminosity as a function of the product of bunch currents (right).
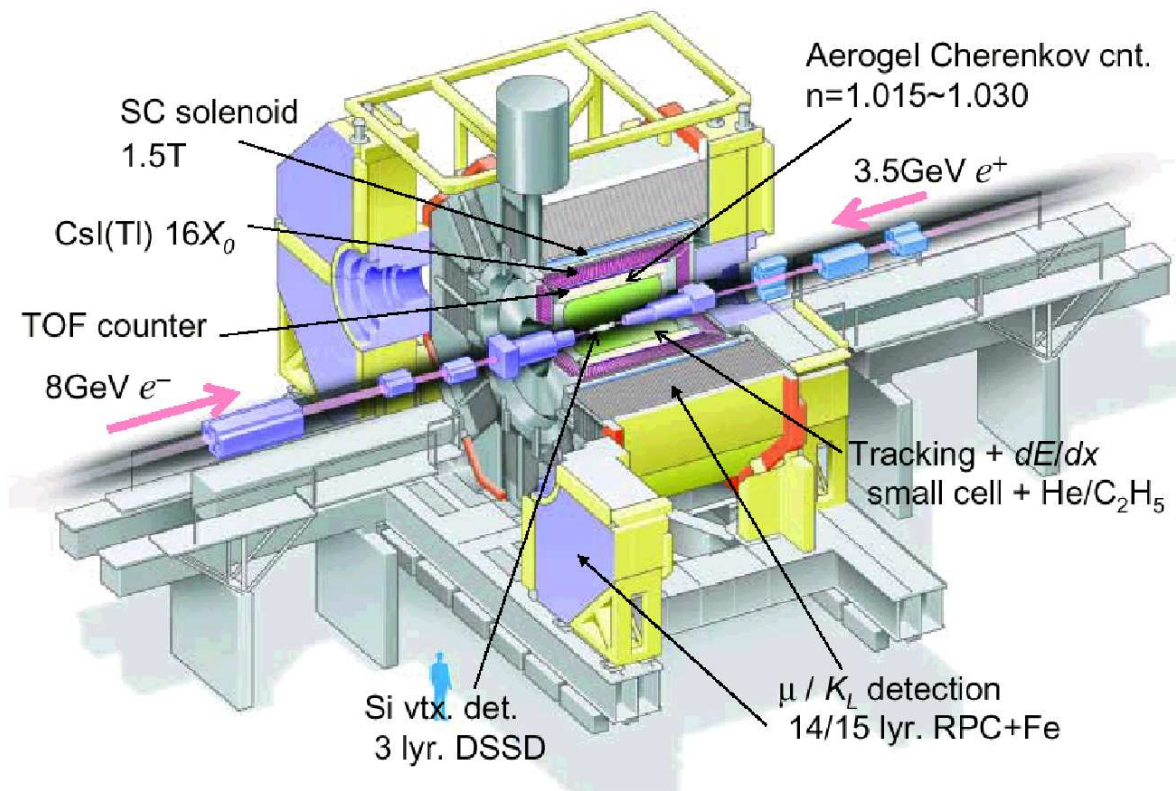
Figure 3.3: The Belle detector.
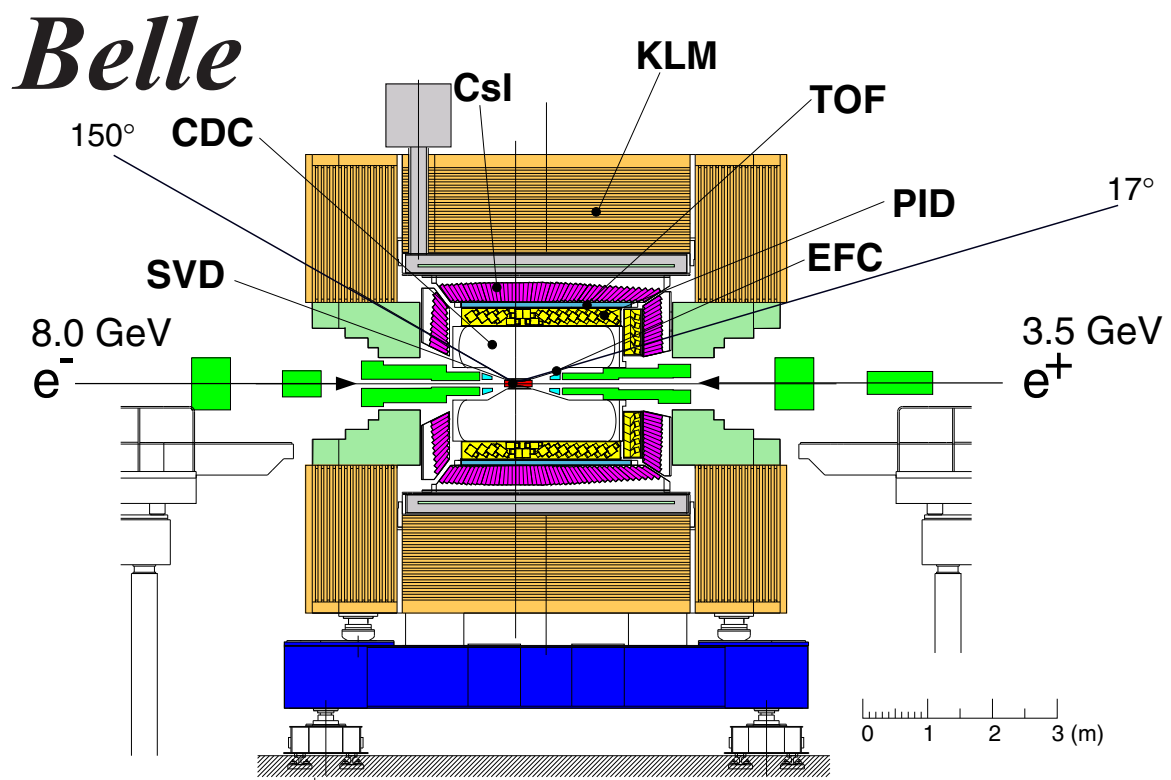
Figure 3.4: Side view of the Belle detector.

- Aerogel Cherenkov counters (ACC), for distinguishing kaons from pions;

- Time-of-flight counters (TOF), for particle identification;

- Electromagnetic calorimeter (ECL, EFC), for measuring photons and electrons;

- K_L and muon detection system (KLM), for detecting muons.

3.2.1 Interaction region

The interaction region (Figure 3.5) lies at the center of the Belle detector. The central part of the beam pipe is a double-walled Beryllium cylinder with an inner radius of 20 mm. Both walls are 0.5 mm thick. The beam pipe is cooled with liquid Helium flowing between the inner and outer walls.
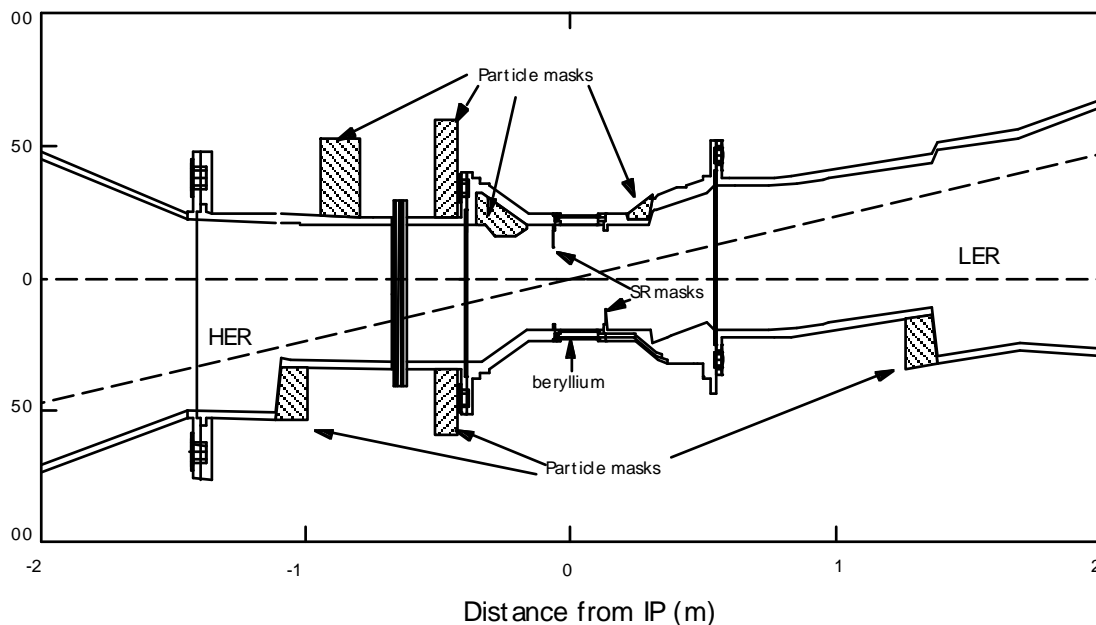
Figure 3.5: Arrangement of the beam pipe around the interaction region.

3.2.2 Silicon vertex detector

The Silicon vertex detector (SVD) was designed to measure the difference in z vertex positions for B meson pairs with a precision of about 100 μm. It is also useful for the tracking. Two versions of the SVD have been used.

The SVD1 (Figure 3.6) consisted of three layers of double-sided Silicon strip detectors (DSSD) covering 86% of the total solid angle. It was placed around the interaction point, surrounding the beam pipe at distances between 30 and 60.5 mm of the beam axis.

The SVD was upgraded to SVD2 in October 2003. It has a fourth layer of DSSD and is placed closer to the interaction point, at a distance of 15 mm. It covers 92% of the

total solid angle, and with this upgrade, the resolution of the vertex position is improved by 25%.

3.2.3 Central drift chamber

The goal of the central drift chamber (CDC, Figure 3.7) is the reconstruction of charged particle tracks and the precise determination of their momenta. It is also useful for triggering and charged particle identification through the measurement of dE/dx.

The CDC is composed of 8400 drift cells filled with a gas mixture of 50% helium and 50% ethane. The field wires and sense wires are parallel to the beam axis. The overall tracking resolution in r and ϕ is 130 μm.

Track parameters are improved by combining the SVD and CDC information. The combined performance is

$$
\begin{aligned}
\sigma_{xy} &= 19 \oplus \frac{50}{p\beta \sin^{3/2}\theta} \, \mu\text{m}, \\
\sigma_z &= 36 \oplus \frac{42}{p\beta \sin^{5/2}\theta} \, \mu\text{m}, \\
\frac{\sigma_{p_t}}{p_t} &= (0.34 \oplus 0.19 p_t) \, \%,
\end{aligned}
$$

where the momentum p and the tranverse momentum p_t are in GeV/c, β is the particle's speed and θ its polar angle, and $\oplus$ represents a quadratic sum.

3.2.4 Aerogel Cherenkov counters

The goal of the Aerogel Cherenkov counters (ACC, Figure 3.8) is particle identification, especially the ability to distinguish $\pi^{\pm}$ from $K^{\pm}$. A Cherenkov counter is based on the fact that an energetic particle travelling in a transparent medium with a speed greater than the speed of light in that medium will emit a cone of Cherenkov radiation. In a threshold Cherenkov counter, the detection or non-detection of this Cherenkov light allows one to set a limit on the speed of the particle, and knowing its momentum, on its mass, thus identifying the particle.

Belle uses 960 aerogel threshold Cherenkov counter modules in the barrel region and 228 in the end-cap region. A counter module is composed of silica aerogel in a thin aluminum container and a photomultiplier tube to detect the Cherenkov light. The aerogel have refractive indices between 1.01 and 1.03 depending on the polar angle. Pions will emit a signal in the modules, kaons not.

3.2.5 Time-of-flight counters

The principle of a time-of-flight (TOF) counter is to measure the speed of a particle with known momentum, thus identifying it through its mass. Belle uses plastic scintillators 1.2 m away from the interaction point, with a time resolution of 100 ps. This is effective for particles with momenta below 1.2 GeV; for kaons and pions the separation is at least 2σ.
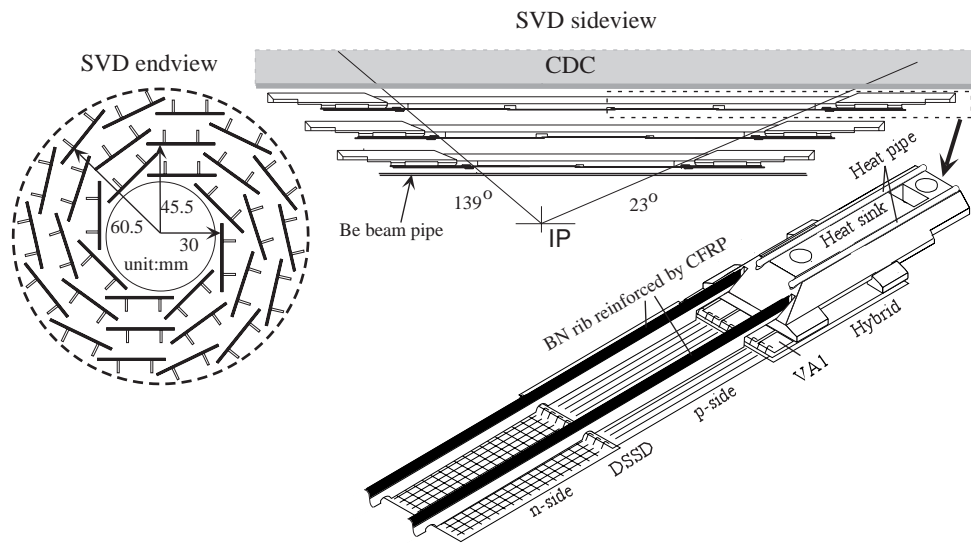
Figure 3.6: Configuration of the SVD1 subdetector.
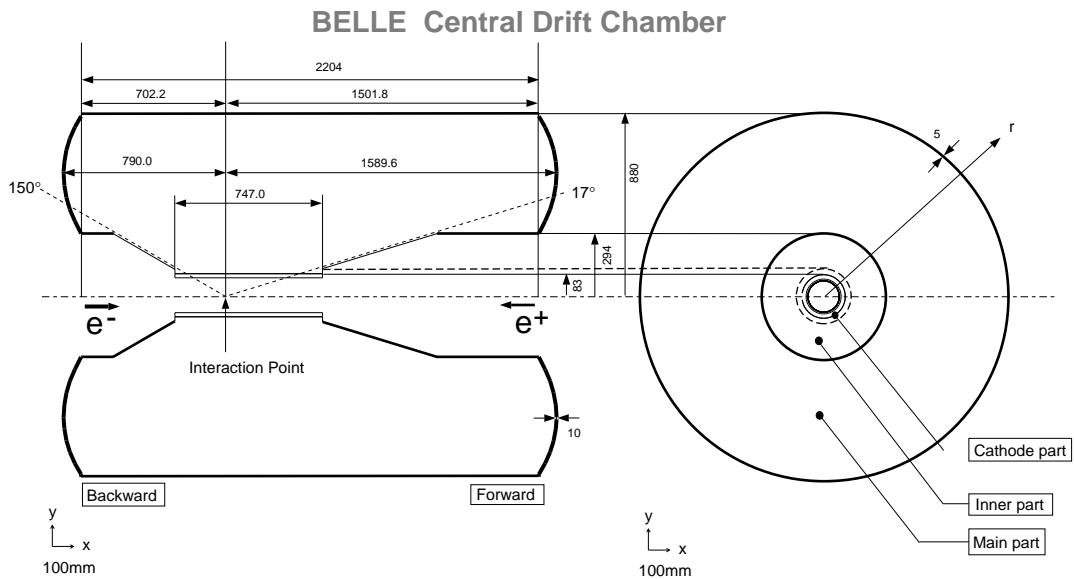
Figure 3.7: Overview of the CDC subdetector.
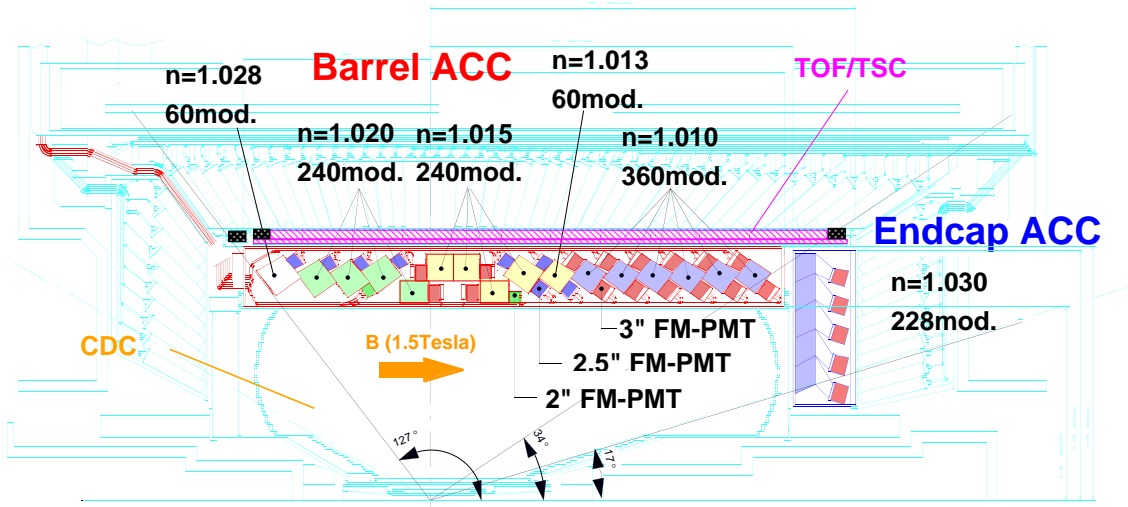
Figure 3.8: Arrangement of the ACC subdetector.

In addition to particle identification, the TOF also gives fast timing signals for the trigger.

3.2.6   Electromagnetic calorimeters

The main purpose of the electromagnetic calorimeter (ECL, Figure 3.9) is the detection of photons with a good energy and position resolution. It is also useful to distinguish electrons from pions, using the energy deposition. The ECL is an array of 8736 CsI(Tl) crystals pointing to the interaction point and covering 91% of the total solid angle.

Photons or electrons hitting the calorimeter will produce an electromagnetic shower by Brehmsstrahlung and pair creation. Photon energies are reconstructed using the energy depositions in 3×3 and 5×5 crystal matrices around the crystal with the maximum energy (E_9 and E_{25}, respectively). The photon quality ratio E_9/E_{25} is used to reject fake photons. The photon energy resolution is shown in Figure 3.10 and can be described as a function of the photon energy by

$$\frac{\sigma_E}{E} = \frac{0.066\,\%}{E} \oplus \frac{0.81\,\%}{E^{1/4}} \oplus 1.34\,\%,$$

where E is in GeV. For the photons with energy $E > 100$ MeV used in this analysis, the energy resolution is about 2%. The position resolution is

$$\sigma_x = 0.27 + \frac{3.4}{E^{1/2}} + \frac{1.8}{E^{1/4}}$$

where E is in GeV and σ_x in mm.

The extreme forward calorimeter (EFC) extends the angular coverage around the beam pipe. It is composed of 2×160 Bismuth Germanate (BGO) cells. The EFC is also used as a luminosity monitor for the Belle experiment.

BELLE CsI ELECTROMAGNETIC CALORIMETER
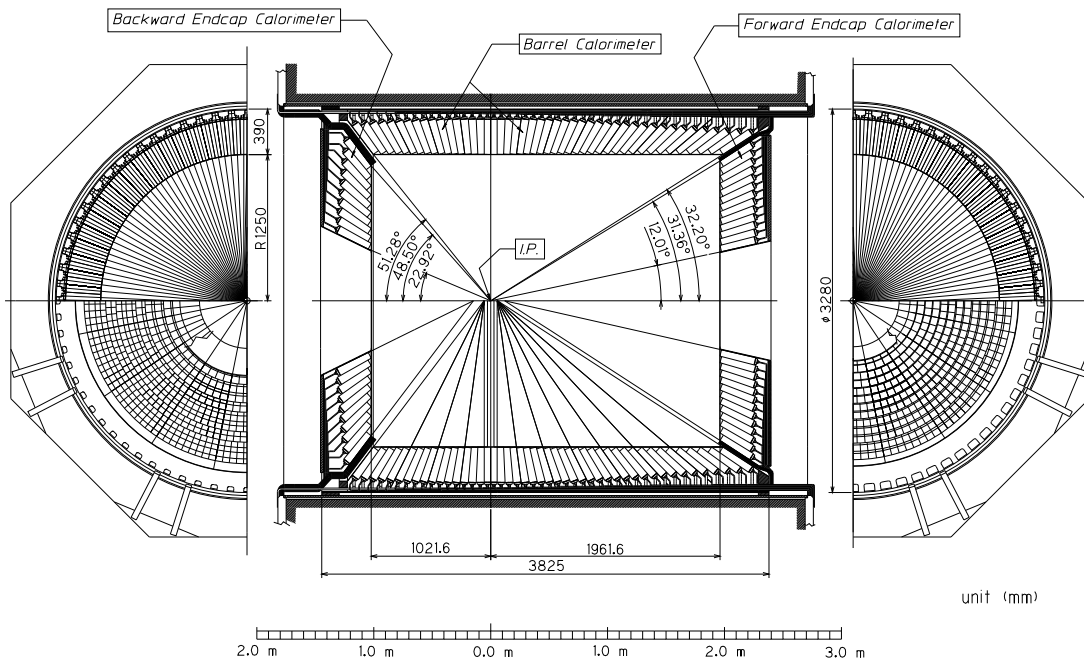
Figure 3.9: Configuration of the ECL subdetector.
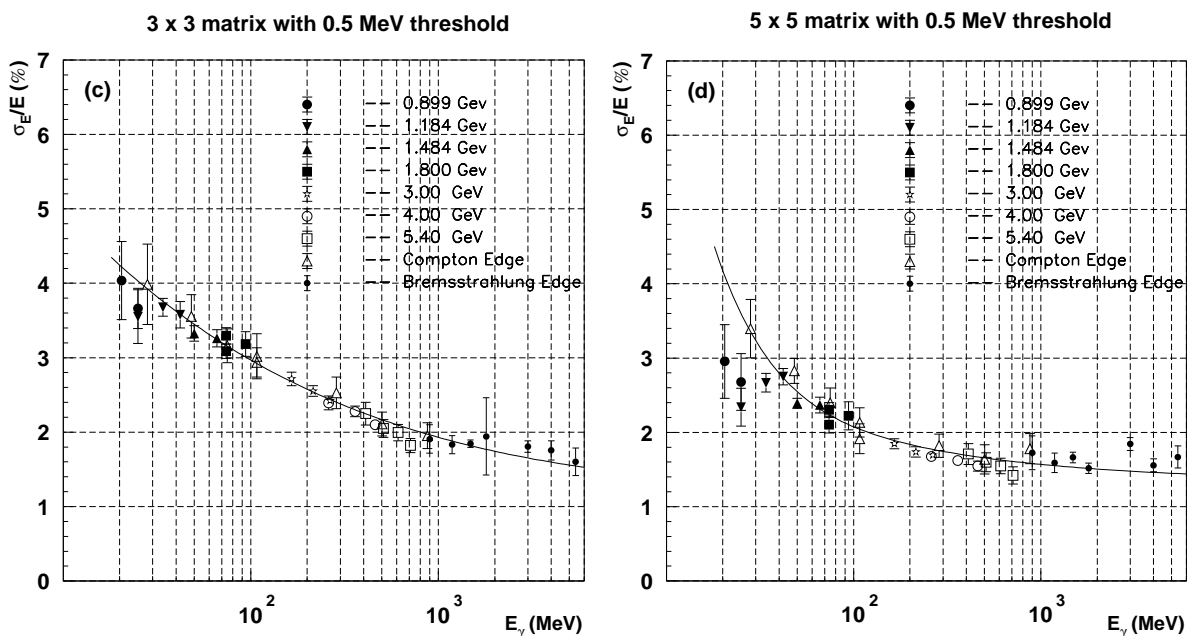
Figure 3.10: Energy resolution of the ECL as a function of the incident photon energy for the 3×3 (left) and 5×5 matrices (right).

3.2.7 K-long and muon detection system

The K_L and muon system (KLM) is designed to identify K_L and muons over a wide momentum range. It consists of alternating layers of charged particle detectors (glass-electrode resistive plate counters) and iron plates, providing a total of 3.9 interaction lengths of material. Since muons travel much farther and with smaller deflections than hadrons, these multiple layers allow to discriminate between them based on their range and transverse scattering.

3.2.8 Solenoid magnet

The Belle magnet is a superconducting solenoid with an inner radius of 170 cm, providing a magnetic field of 1.5 T. This field bends the trajectories of charged particles, allowing for the measurement of their momenta and the determination of their charge.

3.3 The trigger

At the high luminosity at which the Belle experiment is operating, the event rate is too high to allow the storage of each event. The trigger system is responsible of recognising physically interesting events as they happen and storing only these.

Belle has two trigger levels: Level-1 is a hardware trigger and Level-3 is implemented in software.

3.3.1 The Level-1 trigger

The Level-1 trigger decision is based on information from most subdetectors (CDC, TOF, ECL, KLM, EFC) in the form of track triggers and energy triggers (Figure 3.11).

- The CDC trigger is the key element of the trigger system and is divided into an r-ϕ trigger and a z trigger. The r-ϕ trigger identifies tracks originating from the IP and discriminates on the track transverse momentum p_t and on the direction and number of tracks. The z trigger estimates the z position of the tracks to suppress tracks from beam-gas events, from interactions with material around the beam pipe or from cosmic rays.

- The TOF trigger provides timing signals with a time jitter less than 10 ns and information on event multiplicity and topology.

- The ECL triggers on neutral and charged tracks using a total energy trigger and a cluster count trigger.

- The KLM trigger saves as many events containing muon tracks as possible.

- The EFC trigger provides Bhabha scattering and $\gamma\gamma$ event samples used to monitor the luminosity.
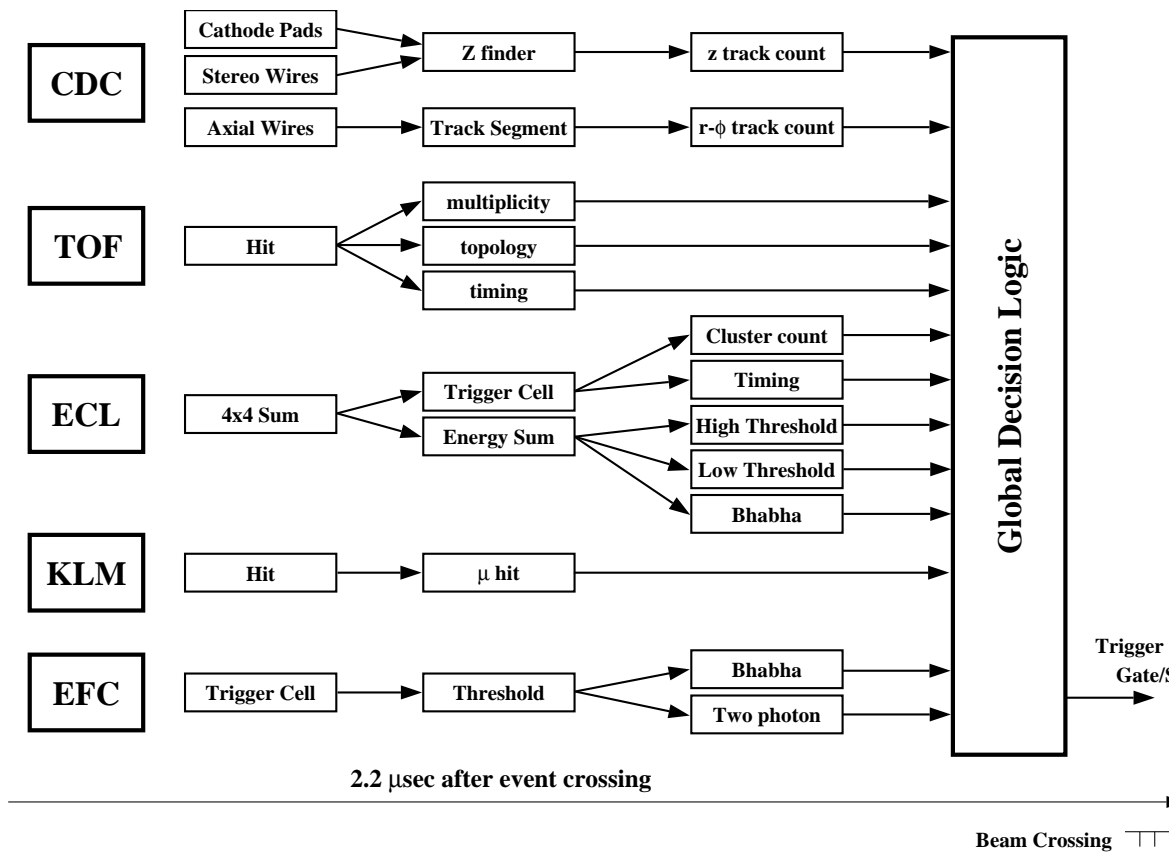
Figure 3.11: Overview of the Level-1 trigger.

3.3.2 The Level-3 trigger

The Level-3 trigger is implemented in software running on a PC farm. It reduces the event rate by about 50% by selecting events with at least one track with z impact parameter less than 5 cm and at least 3 GeV energy deposition in the ECL.

Chapter 4

Reconstruction and selection of $B \to D^{*0}\bar{D}^0 K$ decays
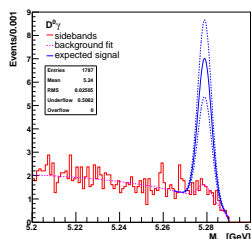
This chapter describes the preliminary studies performed using Monte Carlo simulations. They include the reconstruction procedure and the optimization of the selection criteria.

4.1 Introduction

The study described in this document is a search for the $X(3872) \to D^{*0}\bar{D}^0$ decay mode, followed either by $D^{*0} \to D^0\gamma$ or $D^{*0} \to D^0\pi^0$, in charged and neutral $B \to X(3872)K$ decays. Inclusion of charge conjugate modes is implied throughout the thesis. Furthermore we use the notation $D^{*0}\bar{D}^0$ to indicate both $D^{*0}\bar{D}^0$ and $\bar{D}^{*0}D^0$.

The $X(3872)$ was already observed by Belle in non-resonant $B \to D^0\bar{D}^0\pi^0 K$ decays, using a 414 fb^{-1} data sample. The motivation of the present analysis is to repeat this study with a larger data sample which also includes the $D^{*0} \to D^0\gamma$ mode, and possibly disentangle $X(3872) \to D^0\bar{D}^0\pi^0$ and $X(3872) \to D^{*0}\bar{D}^0$.

The main objectives of the analysis are the measurement of the $X(3872)$ mass and decay width and of the product branching fraction $\mathcal{B}(B \to X(3872)K) \times \mathcal{B}(X(3872) \to D^{*0}\bar{D}^0)$. The measurement of the mass is especially crucial, since it is not yet clear if there are two states, one with a mass around 3872 MeV/c^2 decaying to $J/\psi\pi^+\pi^-$, and another one around 3875 MeV/c^2 decaying to $D^{*0}\bar{D}^0$, or if they are in fact the same state; a precise measurement of the mass could help answer this question. It could also help to distinguish between some of the proposed theoretical models; for example, in the molecular model, one would expect the mass to be slightly below the $D^{*0}\bar{D}^0$ threshold mass, since such a bound state would have a negative binding energy. A measurement of the ratio of branching fractions in neutral and charged B decays is also interesting, since

different models expect different values for this ratio.

B candidates are reconstructed from the following channels (in this graph, whenever a particle appears twice or more, its decay channels are only listed in one instance):

$\Upsilon(4S)$
    $\longrightarrow B^0\bar{B}^0$
        $\longrightarrow X(3872)\, K^0_S$
            $\longrightarrow \pi^+\pi^-$
    $\longrightarrow B^+B^-$
        $\longrightarrow X(3872)\, K^+$
            $\longrightarrow D^{*0}\,\bar{D}^0$
                $\longrightarrow D^0\pi^0$
                    $\longrightarrow \gamma\gamma$
                $\longrightarrow D^0\gamma$
                    $\longrightarrow K^-\pi^+$
                    $\longrightarrow K^-\pi^+\pi^0$
                    $\longrightarrow K^-\pi^+\pi^+\pi^-$
                    $\longrightarrow K^0_S\pi^+\pi^-$
                    $\longrightarrow K^-K^+$
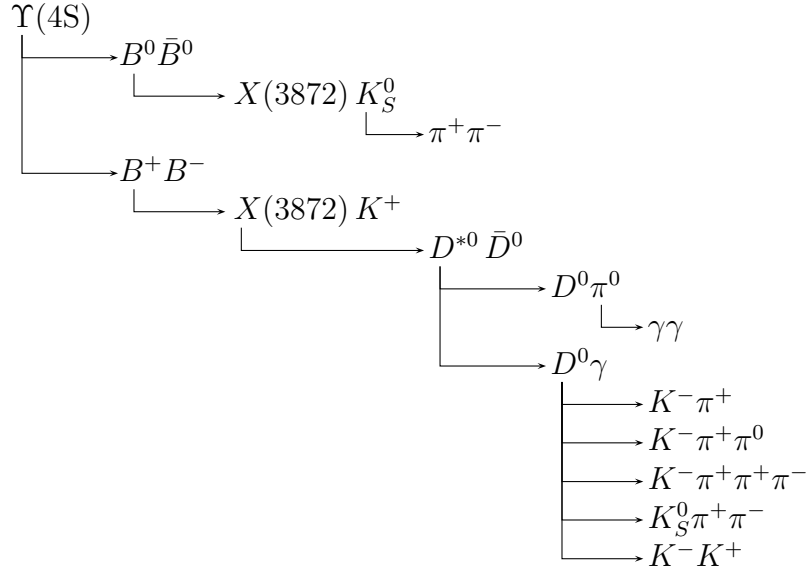
4.1.1   Signal Monte Carlo samples

B decays for the signal channels are studied using Monte Carlo samples. The Belle detector is fully simulated using Monte Carlo software. The simulation is performed in two steps: first, the physical processes are generated using the EVTGEN [58] generator; then the response of the Belle detector is simulated using a GEANT3-based program [59]. Samples are generated for $B^+ \to X(3872)(D^{*0}\bar{D}^0)K^+$ and $B^0 \to X(3872)(D^{*0}\bar{D}^0)K^0_S$ decays. Separate samples are generated for $D^{*0} \to D^0\gamma$ and for $D^{*0} \to D^0\pi^0$; the D^0 mesons decay in the five channels mentioned above. Several sets of samples are generated with different values of the $X(3872)$ mass and width. The D^0 and D^{*0} mesons are generated with nominal masses of $m_{D^0} = 1864.6$ MeV/c^2 and $m_{D^{*0}} = 2006.7$ MeV/c^2. The Belle libraries used to generate the samples are `b20060529_2127`, `b20070402_1209` and `b20070528_1559`. Each sample contains 530,000 events, distributed over experiments 7–49 proportionally to the data available in these experiments.

4.2   Selection criteria

We perform a blind analysis, meaning that the reconstruction procedure and the selection criteria are studied and fixed using Monte Carlo simulations, the real data being used only in the last step of the analysis to obtain the results. Data sidebands can be used to study the background. This is done to prevent the results from being (consciously or unconsciously) biased.

4.2.1   Reconstruction of charged kaons and pions

Charged tracks are required to originate close to the nominal interaction point, so that

$$dr < 2 \text{ cm}, \quad |dz| < 4 \text{ cm}, \tag{4.1}$$

where dr is the radial distance to the interaction point and $|dz|$ is the distance along the beam axis to the interaction point.

Charged kaons are selected from these tracks using a requirement on the likelihood ratio $\mathcal{L}_{K/\pi} = \mathcal{L}_K/(\mathcal{L}_K + \mathcal{L}_\pi) > 0.6$, where $\mathcal{L}_K$ and $\mathcal{L}_\pi$ are the likelihoods for a track to come from a kaon or a pion, respectively, based on the response of the ACC and on measurements from CDC and TOF. This requirement has a kaon identification efficiency of 88% and a pion misidentification rate of 10%. For the cleaner $D^0 \to KK$ and $K\pi$ channels, we require $\mathcal{L}_{K/\pi} > 0.1$, with a kaon identification efficiency of 97% and a pion misidentification rate of 18%. Similarly, charged pions are selected with an efficiency of 98% and a kaon misidentification rate of 12%, by requiring $\mathcal{L}_{K/\pi} < 0.9$. These requirements on the likelihood ratio follow the standard Belle procedure.

4.2.2   Reconstruction of neutral kaons

The K_S^0 candidates are reconstructed from the $K_S^0 \to \pi^+\pi^-$ mode with the requirement $|M_{\pi\pi} - M_{K_S^0}| < 15$ MeV/c^2. Requirements on the K_S^0 vertex displacement from the interaction point and on the difference between vertex and K_S^0 flight directions are applied: the smallest approach of one of the tracks to the interaction point is required to be greater than 0.3 mm; the angle between the momentum vector and the decay vertex vector of the K_S^0 candidate is required to be less than 0.1 rad; the distance between the two daughter tracks at their point of closest approach is required to be less than 1.8 cm; and the decay length of the K_S^0 candidate in the xy plane is required to be greater than 0.8 mm [60]. A mass- and vertex-constrained fit is applied to improve the four-momenta of the K_S^0 candidates: the momentum is fitted to match the nominal mass and to constrain the candidate to originate from the nominal interaction point.

4.2.3   Reconstruction of neutral pions

Photons are detected from ECL energy depositions that can't be matched to a charged track. The π^0 candidates are reconstructed from pairs of photons with energies $E_\gamma > 50$ MeV and with invariant mass in the range $118 < m_{\gamma\gamma} < 150$ MeV/c^2. A mass-constrained fit is applied to obtain the four-momenta of the π^0 candidates.

4.2.4   Reconstruction of photons from $D^{*0} \to D^0 \gamma$

Since the photons from $D^{*0} \to D^0 \gamma$ decays in this analysis have a quite low momentum range (from about 70 to 300 MeV/c, see Figure 4.1), there is a very large background of low-energy photons. This background is partially suppressed by requiring a photon momentum of at least 100 MeV/c in the laboratory frame.

Fake photons can be suppressed through the E_9/E_{25} ratio (ratio of energy in 3×3 over 5×5 calorimeter cell clusters). The distribution of the E_9/E_{25} variable for selected
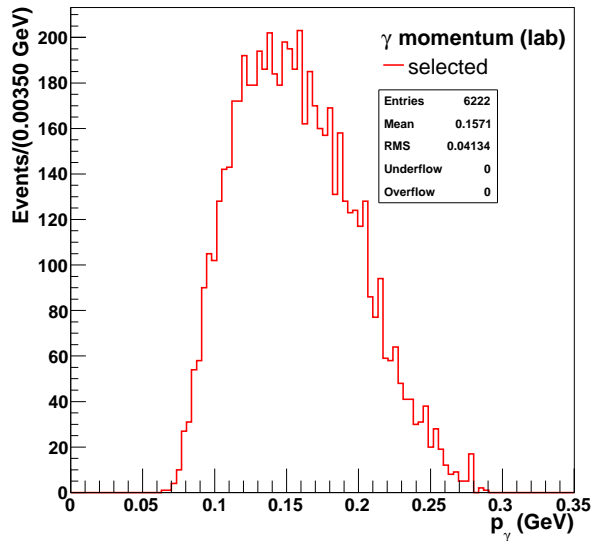
Figure 4.1: Distribution of the photon momentum in the laboratory frame for selected events in signal Monte Carlo.

events in MC signal samples and data sidebands is shown on Figure 4.2. The gap below $E_9/E_{25} = 1$ is due to the energy threshold of the calorimeter cells. It is required that $E_9/E_{25} > 0.8$.

4.2.5 Reconstruction of D^0 mesons

D^0 candidates are reconstructed in the following decay modes: $D^0 \to K^-\pi^+$, $K^-\pi^+\pi^0$, $K^-\pi^+\pi^+\pi^-$, $K_S^0\pi^+\pi^-$ and K^-K^+.

Signal Monte Carlo mass distributions of D^0 mesons are fitted channel by channel with a double Gaussian function. All channels except $K\pi\pi^0$ have similar resolutions (within 5%) and are fitted together; an average resolution of 3.0 ± 0.2 MeV/c^2 is obtained. For the $K\pi\pi^0$ channel the resolution is 7.3 ± 0.5 MeV/c^2. The fit results are shown on Figure 4.3 and the resolutions are summarised in Table 4.1.

Mass- and vertex-constrained fits are applied to improve the four-momenta of the D^0 candidates; the mass is constrained to the value of 1864.6 MeV/c^2. See Appendix A.1 for a study of different kinematical fit strategies. The reduced χ^2 of the vertex fit is required to be less than 25, where the χ^2 is based on the least distance between the track and the vertex.

To reduce the background, at least one of the D^0 or $\bar{D}^0$ meson is required to decay to either $K^-\pi^+$ or $K^+\pi^-$. This requirement reduces the background by a factor 10 while keeping approximately 66% of the signal.

4.2.6 Reconstruction of D^{*0} mesons

D^0 candidates are combined with a photon or a π^0 to obtain D^{*0} candidates. In Figure 4.4, signal Monte Carlo D^{*0} mass distributions are fitted for correctly reconstructed D^0 chil-
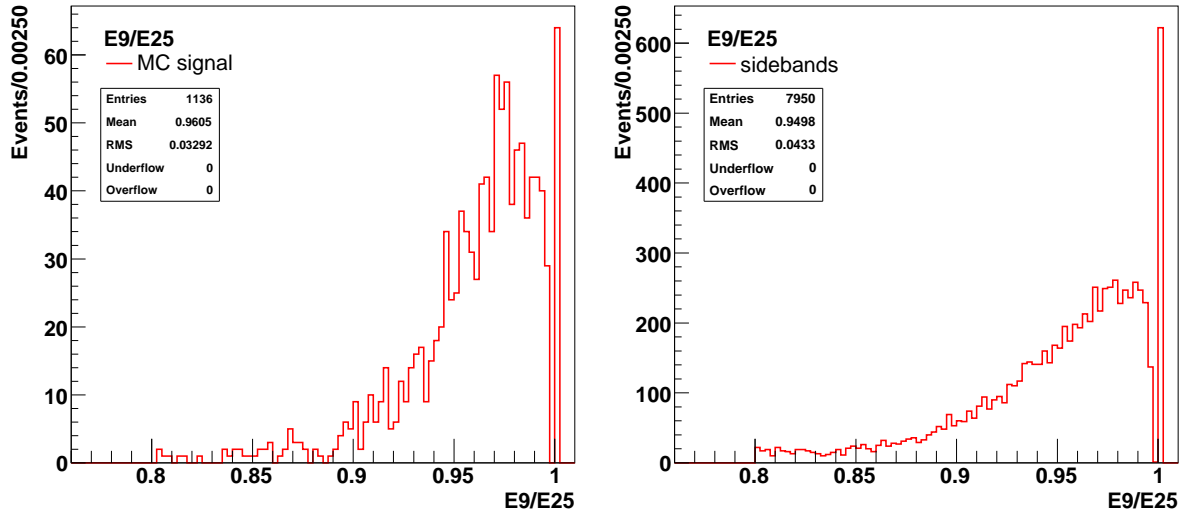
Figure 4.2: Distributions of the photon E_9/E_{25} ratio for selected events in MC signal samples and data sidebands.
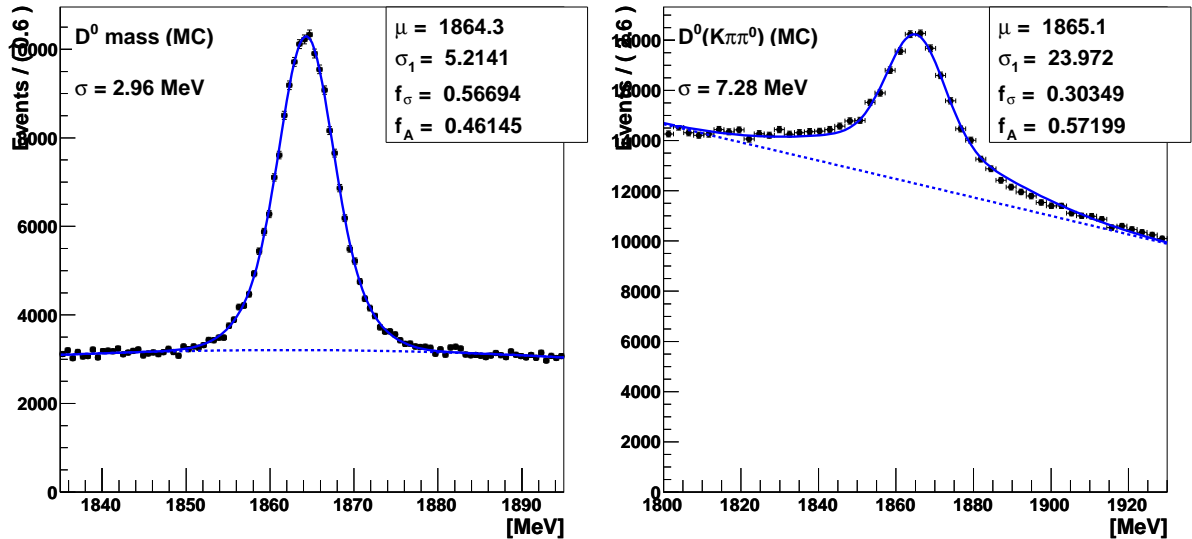
Figure 4.3: Distribution of the reconstructed D^0 mass in signal Monte Carlo events. Left: all D^0 channels except $K\pi\pi^0$; right: $D^0 \to K\pi\pi^0$. The curve is the result of a fit with a double Gaussian function of common mean μ; the resolution σ is the smallest of the two widths, f_σ is the ratio of widths and f_A is the fraction of amplitude in the first Gaussian. The background is described with a second order polynomial.

dren. The obtained resolution is 6.9 ± 0.4 MeV/c^2 for $D^{*0} \to D^0 \gamma$ and 1.75 ± 0.05 MeV/c^2 for $D^{*0} \to D^0 \pi^0$. Table 4.1 gives a summary of D^0 and D^{*0} mass resolutions for Monte Carlo and data. The resolutions on data are estimated by multiplying those obtained on Monte Carlo by a data/MC ratio extracted from control channels, as explained in Appendix A.2. A mass-constrained fit is used to improve the four-momenta of the D^{*0} candidates; the mass is constrained to the value of 2006.7 MeV/c^2.

D^0 and D^{*0} cut selections are described later in Section 4.2.10.
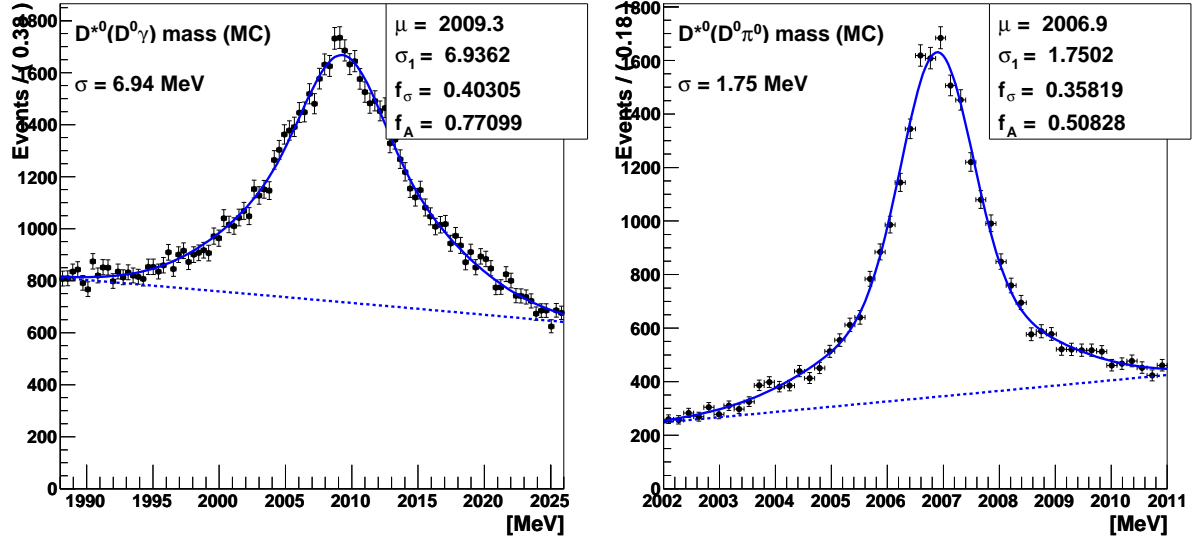
Figure 4.4: Distribution of the reconstructed D^{*0} mass in signal Monte Carlo events. Left: $D^{*0} \to D^0 \gamma$, right: $D^{*0} \to D^0 \pi^0$. The curve is the result of a fit with a double Gaussian function of common mean μ; the resolution σ is the smallest of the two widths, f_σ is the ratio of widths and f_A is the fraction of amplitude in the first Gaussian. The background is described with a second order polynomial.

channel	MC (MeV/c^2)	data (MeV/c^2)	data/MC ratio
$D^0 \to$ not $K\pi\pi^0$	3.0 ± 0.2	3.5 ± 0.2	1.18 ± 0.04
$D^0 \to K\pi\pi^0$	7.3 ± 0.5	8.6 ± 0.6	1.18 ± 0.04
$D^{*0} \to D^0 \gamma$	6.9 ± 0.4	9.2 ± 0.5	1.33 ± 0.15
$D^{*0} \to D^0 \pi^0$	1.75 ± 0.05	2.03 ± 0.06	1.16 ± 0.08

Table 4.1: D^0 and D^{*0} mass resolutions for Monte Carlo and data.

4.2.7   Reconstruction of B mesons

$X(3872)$ candidates are reconstructed from $D^{*0}\bar{D}^0$ pairs with invariant mass $M_{D^*D} <$ 4.0 GeV/c^2. B candidates are reconstructed by combining an $X(3872)$ candidate with a charged or neutral kaon.

Two variables, M_{bc} and ΔE, are useful to distinguish signal events from background. The beam-energy constrained mass

$$M_{\text{bc}} = \sqrt{E_{\text{beam}}^2 - \left(\sum_i \vec{P}_i \right)^2}, \tag{4.2}$$

where $\vec{P}_i$ is the momentum of the ith daughter of the B candidate in the center-of-mass (CM) system, is expected to be close to the nominal B mass for signal events. The difference between the measured CM energy of the B candidate and the CM beam energy

$$\Delta E = \sum_i E_i - E_{\text{beam}}, \tag{4.3}$$

where E_i is the CM energy of the ith daughter of the B candidate, is expected to be close to zero for signal events. M_{bc} is required to be larger than 5.2 MeV/c^2, and ΔE is restricted to the range $|\Delta E| < 25$ MeV.

4.2.8 Best candidate selection

After these selections, there are still several candidates per event. In signal Monte Carlo, the average B candidate multiplicity per event is 2.3 for the $D^{*0} \rightarrow D^0 \gamma$ channel and 2.7 for the $D^{*0} \rightarrow D^0 \pi^0$ channel. The best candidate is chosen by minimizing the quantity

$$\chi^2 = \left(\frac{\Delta M_{D^0}}{\sigma_{M_{D^0}}} \right)^2 + \left(\frac{\Delta M_{\bar{D}^0}}{\sigma_{M_{D^0}}} \right)^2 + \left(\frac{\Delta (M_{D^{*0}} - M_{D^0})}{\sigma_{M_{D^{*0}} - M_{D^0}}} \right)^2 \\ + \left(\frac{\Delta E}{\sigma_{\Delta E}} \right)^2 \left[+ \left(\frac{\Delta M_{\pi^0}}{\sigma_{M_{\pi^0}}} \right)^2 \right], \tag{4.4}$$

where the last term only applies for the $D^{*0} \rightarrow D^0 \pi^0$ channel, and where ΔM_x is the deviation of the measured mass from its nominal value, σ_{M_x} is the resolution on this mass as shown in Table 4.1, $\sigma_{M_{\pi^0}} = 5$ MeV/c^2 and $\sigma_{\Delta E} = 4.5$ MeV for $D^0\gamma$ or 6 MeV for $D^0\pi^0$.

Usually in a Belle analysis, ΔE is used to extract the signal, since it is a powerful variable to distinguish signal from background events. However in this case, ΔE is used in the best candidate selection to suppress the D^0–$\bar{D}^0$ reflection (events where the γ or the π^0 is assigned to the wrong D^0, see Section 5.1.3). In the reflected events, the D^{*0} mass-constrained fit shifts the ΔE distribution by 10 MeV (see Figure 4.5). For the correctly reconstructed signal candidates, the ΔE distribution peaks at zero. Without using ΔE in the selection, the reflection component of the signal would be large (about 40%), and the efficiency about 25% worse.

Table 4.4 shows the obtained best candidate selection efficiency after all selection criteria described in the next section have been applied.

4.2.9 Continuum background rejection

Continuum background consists in $e^+e^- \rightarrow q\bar{q}$ events, where $q = u, d, s, c$. While it is not the main source of background in this analysis, we reject some of it by using Fox-Wolfram
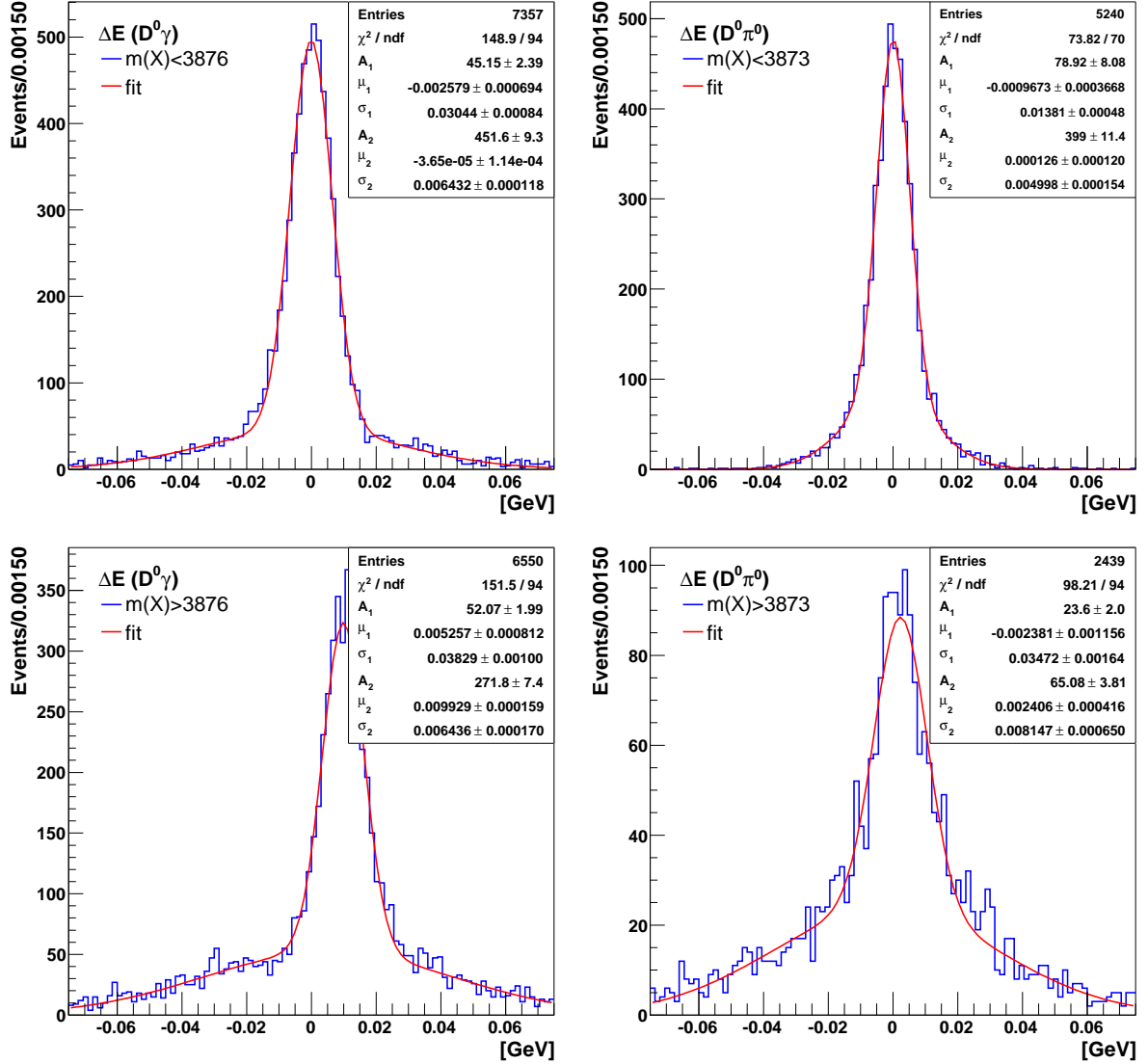
Figure 4.5: Distribution of ΔE for the $X(3872)$ mass region containing mostly correctly reconstructed events (top) and mostly reflected events (bottom). In the bottom plots, the distribution is shifted by 10 MeV for $D^0\gamma$ (left) and by 2.5 MeV for $D^0\pi^0$ (right). Here the best candidate selection is applied without using ΔE. The curves are the results of fits with a double Gaussian function.

moments [61]. These variables are used to distinguish $q\bar{q}$ events from $B\bar{B}$ based on the event shape: in the center-of-mass frame, $q\bar{q}$ events form two back-to-back jets, while $B\bar{B}$ events are more isotropically distributed, as both B mesons are produced almost at rest in the center-of-mass frame. We require the ratio R_2 of the second to zeroth order Fox-Wolfram moments to be less than 0.3, thus keeping most of the signal (Figure 4.6).
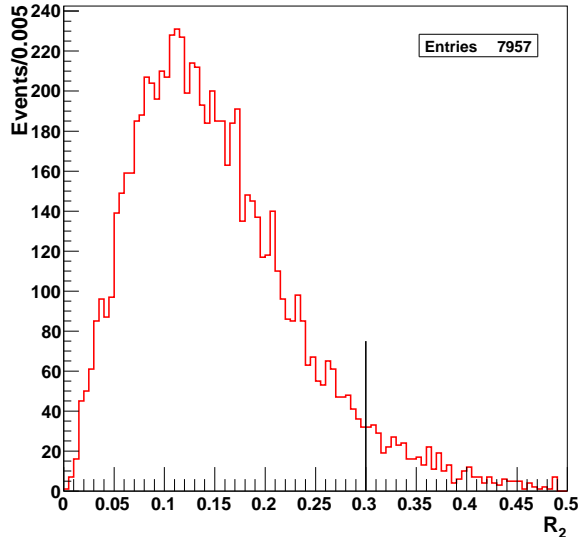
Figure 4.6: Distribution of the ratio of the second to zeroth order Fox-Wolfram moments for selected events in signal Monte Carlo.

4.2.10 Optimisation of D^0, D^{*0} mass cuts and ΔE cut

We determine the values of the D^0, D^{*0} mass cuts and ΔE cut by maximizing the signal significance. The other cuts of the analysis have standard Belle values and don't need to be optimized.

The significance $\frac{S}{\sqrt{S+B}}$ is computed for several combinations of cuts on the D^0, D^{*0} masses and on ΔE. The Monte Carlo is reconstructed using the MC resolutions from Table 4.1, while the data is reconstructed using the data resolutions. For ΔE, the MC resolutions are used for both MC and data. The signal S is obtained from the Monte Carlo assuming all the signal previously seen in the $D^0\bar{D}^0\pi^0$ channel [21] is resonant, so that

$$\begin{aligned}
\mathcal{B}(B^+ \to X(3872)K^+) &=& \mathcal{B}(B^+ \to D^0\bar{D}^0\pi^0 K^+)/\mathcal{B}(D^{*0} \to D^0\pi^0) \\
&=& (1.65 \pm 0.50) \times 10^{-4}.
\end{aligned}$$

Since the data signal region is hidden, the background B is computed in the following way: B_0 is the number of data events in the M_{bc} signal region for $M_{D^*D} > 3890$ MeV/c^2; B_1 (B_2) is the number of events in the M_{bc} sideband for $M_{D^*D} < 3890$ MeV/c^2 ($M_{D^*D} > 3890$ MeV/c^2). The background is estimated by scaling B_0 : $B = B_0\frac{B_1}{B_2}$ (see Figure 4.7).
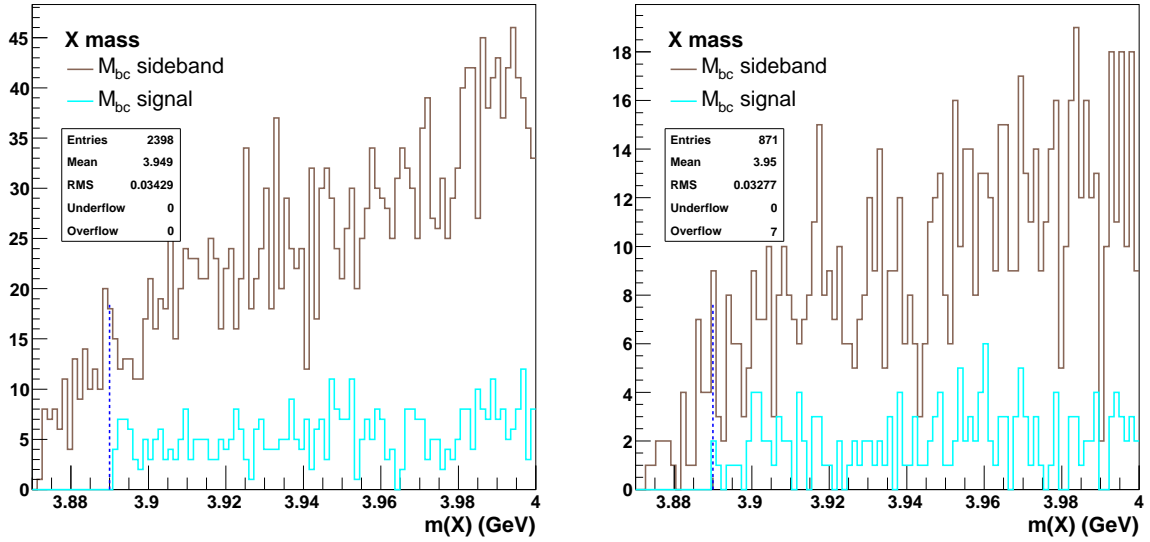
Figure 4.7: Distribution of M_{D^*D} for $M_{\mathrm{bc}} < 5.27$ GeV/c^2 (brown histogram) and for $M_{\mathrm{bc}} > 5.27$ GeV/c^2 (blue histogram) for selected data events in the $D^0\gamma$ channel (left) and in the $D^0\pi^0$ channel (right). The $X(3872)$ signal region is hidden.

This is possible since the M_{D^*D} distribution can be described with a square root function for both the M_{bc} signal and sideband regions.

Table 4.2 and Figure 4.8 show the obtained significance. For both channels, the selected cuts are $\pm 4\sigma$ for the D^0 masses, $\pm 3\sigma$ for the D^{*0} masses and $|\Delta E| < 2\sigma$. These are indicated by arrows on Figure 4.8. Other cut combinations have a similar or slightly better significance, but these are chosen so that the cuts are the same in both channels.

4.2.11 Summary of cut selections

The list of all selection cuts is shown in Table 4.3. The efficiencies and resolutions strongly depend on the parameters of the generated $X(3872)$. Table 4.4 shows the candidate multiplicities, best candidate selection efficiencies and resolutions obtained using the signal Monte Carlo sample generated with a mass of 3872 MeV/c^2 and zero decay width. Figure 4.9 shows the corresponding M_{bc} distributions.

D^0 cut	D^{*0} cut	$|\Delta E|$ cut	B	S	$S/\sqrt{S+B}$
			$D^{*0} \to D^0\gamma$		
3.0σ	3.0σ	1.5σ	17.1 ± 1.0	26.8 ± 0.4	4.04 ± 0.06
3.0σ	3.0σ	2.0σ	21.3 ± 1.2	28.4 ± 0.4	4.03 ± 0.06
3.0σ	3.0σ	2.5σ	23.5 ± 1.2	29.0 ± 0.4	4.00 ± 0.06
3.0σ	3.0σ	3.0σ	27.1 ± 1.3	29.4 ± 0.4	3.91 ± 0.06
3.0σ	3.0σ	4.0σ	31.3 ± 1.4	29.8 ± 0.4	3.81 ± 0.06
3.0σ	3.0σ	5.0σ	36.4 ± 1.5	29.9 ± 0.4	3.67 ± 0.06
4.0σ	2.0σ	1.5σ	18.7 ± 1.1	26.5 ± 0.4	3.94 ± 0.06
4.0σ	2.0σ	2.0σ	23.4 ± 1.3	28.4 ± 0.4	3.95 ± 0.06
4.0σ	2.0σ	2.5σ	25.8 ± 1.3	29.4 ± 0.4	3.96 ± 0.06
4.0σ	2.0σ	3.0σ	29.9 ± 1.4	29.8 ± 0.4	3.86 ± 0.06
4.0σ	2.0σ	4.0σ	36.7 ± 1.5	30.3 ± 0.4	3.70 ± 0.06
4.0σ	2.0σ	5.0σ	42.1 ± 1.7	30.4 ± 0.4	3.57 ± 0.06
4.0σ	3.0σ	1.5σ	23.7 ± 1.2	29.7 ± 0.4	4.06 ± 0.06
4.0σ	**3.0σ**	**2.0σ**	28.4 ± 1.3	31.5 ± 0.4	4.07 ± 0.06
4.0σ	3.0σ	2.5σ	30.7 ± 1.3	32.2 ± 0.4	4.06 ± 0.06
4.0σ	3.0σ	3.0σ	35.3 ± 1.4	32.6 ± 0.4	3.96 ± 0.05
4.0σ	3.0σ	4.0σ	43.3 ± 1.6	33.0 ± 0.4	3.78 ± 0.05
4.0σ	3.0σ	5.0σ	50.0 ± 1.7	33.1 ± 0.4	3.63 ± 0.05
			$D^{*0} \to D^0\pi^0$		
3.0σ	3.0σ	1.5σ	5.1 ± 0.5	20.3 ± 0.4	4.03 ± 0.06
3.0σ	3.0σ	2.0σ	5.6 ± 0.5	21.4 ± 0.4	4.12 ± 0.06
3.0σ	3.0σ	2.5σ	7.5 ± 0.6	21.7 ± 0.4	4.02 ± 0.06
3.0σ	3.0σ	3.0σ	8.3 ± 0.7	21.7 ± 0.3	3.96 ± 0.06
3.0σ	3.0σ	4.0σ	10.3 ± 0.7	22.0 ± 0.3	3.87 ± 0.05
3.0σ	3.0σ	5.0σ	12.2 ± 0.8	22.0 ± 0.3	3.76 ± 0.06
4.0σ	2.0σ	1.5σ	5.8 ± 0.5	22.0 ± 0.4	4.17 ± 0.06
4.0σ	2.0σ	2.0σ	6.7 ± 0.6	23.3 ± 0.4	4.25 ± 0.06
4.0σ	2.0σ	2.5σ	8.8 ± 0.7	23.2 ± 0.4	4.10 ± 0.06
4.0σ	2.0σ	3.0σ	9.2 ± 0.7	23.4 ± 0.4	4.10 ± 0.06
4.0σ	2.0σ	4.0σ	12.4 ± 0.8	23.6 ± 0.4	3.93 ± 0.06
4.0σ	2.0σ	5.0σ	13.6 ± 0.8	23.7 ± 0.4	3.88 ± 0.06
4.0σ	3.0σ	1.5σ	6.2 ± 0.5	22.1 ± 0.4	4.15 ± 0.06
4.0σ	**3.0σ**	**2.0σ**	7.0 ± 0.5	23.1 ± 0.4	4.21 ± 0.06
4.0σ	3.0σ	2.5σ	9.4 ± 0.7	23.4 ± 0.4	4.09 ± 0.06
4.0σ	3.0σ	3.0σ	10.2 ± 0.7	23.5 ± 0.4	4.05 ± 0.06
4.0σ	3.0σ	4.0σ	13.4 ± 0.8	23.6 ± 0.3	3.88 ± 0.05
4.0σ	3.0σ	5.0σ	15.2 ± 0.9	23.7 ± 0.3	3.80 ± 0.06

Table 4.2: Optimisation of D^0, D^{*0} mass cuts and ΔE cut. Top: $D^0\gamma$, bottom: $D^0\pi^0$. Only the relevant part of the table is shown. The optimal values are shown in red; the selected cuts in bold.
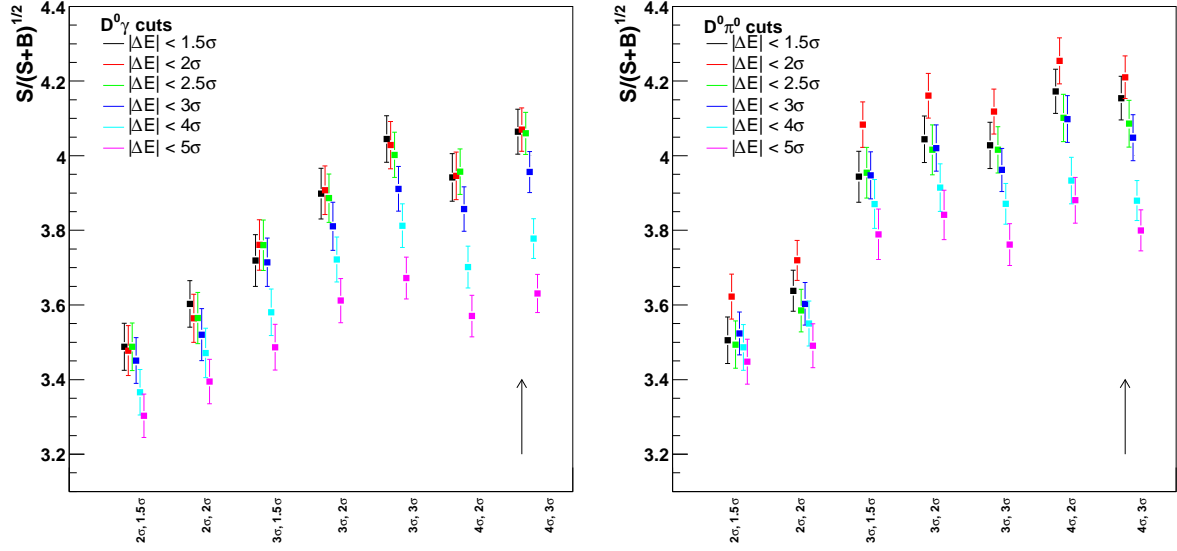
Figure 4.8: Significance as a function of the D^0, D^{*0} mass cuts and ΔE cut in the $D^{*0} \rightarrow D^0\gamma$ channel (left) and in the $D^{*0} \rightarrow D^0\pi^0$ channel (right). Horizontal scale labels correspond to mass cuts, colors to ΔE cuts.

channel	$D^{*0} \rightarrow D^0\gamma$	$D^{*0} \rightarrow D^0\pi^0$
kaon ID	0.6; 0.1 for $KK, K\pi$	
pion ID	0.9	
track origin	d$r < 2$ cm, $\quad$ $\|\mathrm{d}z\| < 4$ cm	
photon momentum	$p > 100$ MeV$/c$	$p > 50$ MeV$/c$
photon quality	$E_9/E_{25} > 0.8$	
K_S^0 mass	± 15 MeV$/c^2$; goodKs [62]	
π^0 mass	± 16 MeV$/c^2$	
D^0 mass	± 14 MeV$/c^2$	
$D^0(K\pi\pi^0)$ mass	± 26 MeV$/c^2$	
D^0 vertex fit χ^2	< 25	
D^{*0} mass	± 27.5 MeV$/c^2$	± 6.0 MeV$/c^2$
$X(3872)$ mass	$M_{D^*D} < 4.0$ GeV$/c^2$	
ΔE range	$\|\Delta E\| < 9$ MeV	$\|\Delta E\| < 12$ MeV
signal box	$M_{\mathrm{bc}} > 5.27$ GeV$/c^2$, $M_{D^*D} < 3.88$ GeV$/c^2$	

Table 4.3: Summary of selection cuts.

channel	$D^{*0} \rightarrow D^0\gamma$	$D^{*0} \rightarrow D^0\pi^0$
candidate multiplicity	2.3	2.7
best cand. selection eff.	78 %	62 %
ΔE resolution	4.5 ± 0.1 MeV	6.1 ± 0.1 MeV
M_{bc} resolution	2.78 ± 0.01 MeV$/c^2$	3.09 ± 0.03 MeV$/c^2$

Table 4.4: Summary of efficiencies, multiplicity and resolutions.
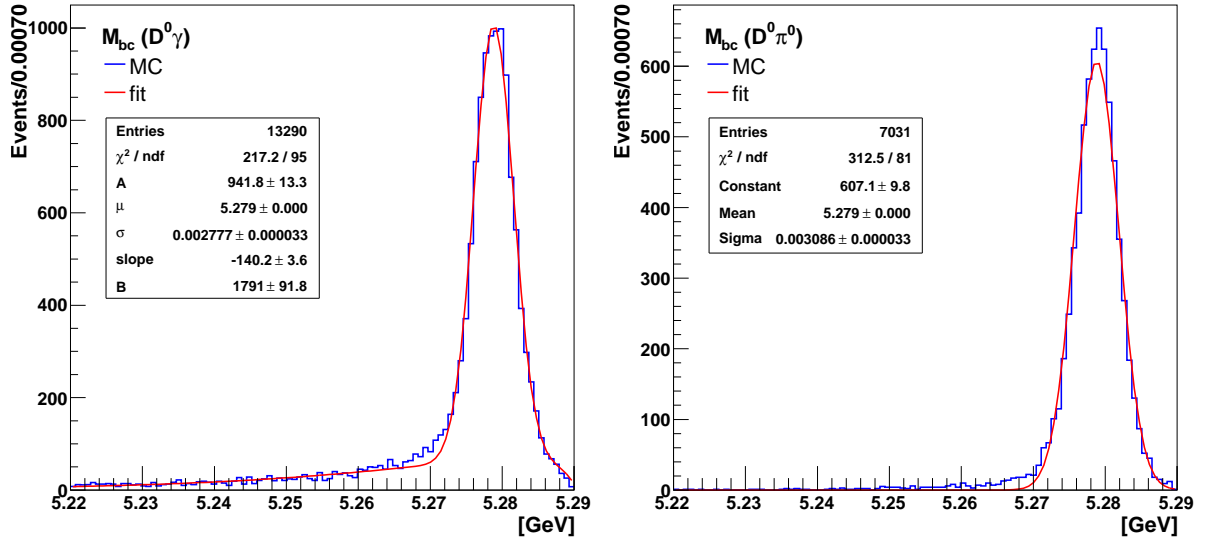
Figure 4.9: Distribution of M_{bc} for candidates in signal Monte Carlo passing the selection. Left: $D^0\gamma$, right: $D^0\pi^0$. The curves are the result of a fit with a single Gaussian function for the signal and an ARGUS function for the background.

Chapter 5

Description of the $D^{*0}\bar{D}^0$ mass distribution
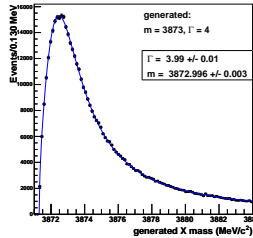
This chapter describes the generated and reconstructed $X(3872)$ mass distributions, the $X(3872)$ mass resolution, the reconstruction efficiencies, the background studies and the construction of the fitting function.

5.1 $X(3872)$ mass signal

In this section, the $X(3872)$ mass signal is examined, starting at generator level. Then the $X(3872)$ mass resolution is studied, which allows the inclusion of the effect of the reconstruction and describe the reconstructed mass distributions, and finally obtain the Monte Carlo efficiencies.

5.1.1 Generated $X(3872)$ mass distributions

In the Monte Carlo generation, it is assumed that the $X(3872)$ has quantum numbers $J^P = 1^+$ and decays to $D^{*0}D^0$ as $1^+ \to 1^- 0^-$, thus its decay can proceed either through an S wave or a D wave (orbital momentum $L = 0$ or 2). EVTGEN uses only the lowest allowed angular momentum, $L = 0$ in this case.

To generate the $X(3872)$ mass distributions, we use a relativistic Breit-Wigner function of the form

$$BW(m) = \frac{\mu m \Gamma(m)}{(m^2 - \mu^2)^2 + \mu^2 \Gamma(m)^2}, \tag{5.1}$$

$$\text{where} \quad \Gamma(m) = \Gamma_0 \left(\frac{\mu}{m}\right) \left(\frac{p(m)}{p(\mu)}\right)^{2L+1},$$

$$p(m) \;\; = \;\; \frac{1}{2m}\sqrt{\left(m^2 - (m_{D^0} + m_{D^{*0}})^2\right)\left(m^2 - (m_{D^0} - m_{D^{*0}})^2\right)},$$

and μ and Γ_0 are the nominal mass and width of the resonance, respectively, $L = 0$ is the relative orbital momentum of its decay products, and $p(m)$ is the momentum of one of the daughters in the rest frame of its parent. The term $m\Gamma(m)$ in the numerator of Eq. (5.1) behaves like a phase-space function, giving a smooth rise near the threshold.

Figure 5.1 shows the generated $X(3872)$ mass distributions for various values of the nominal mass and width, fitted with this relativistic Breit-Wigner function. The $X(3872)$ mass and width are fitted back correctly in each case; Table 5.1 shows the obtained values.
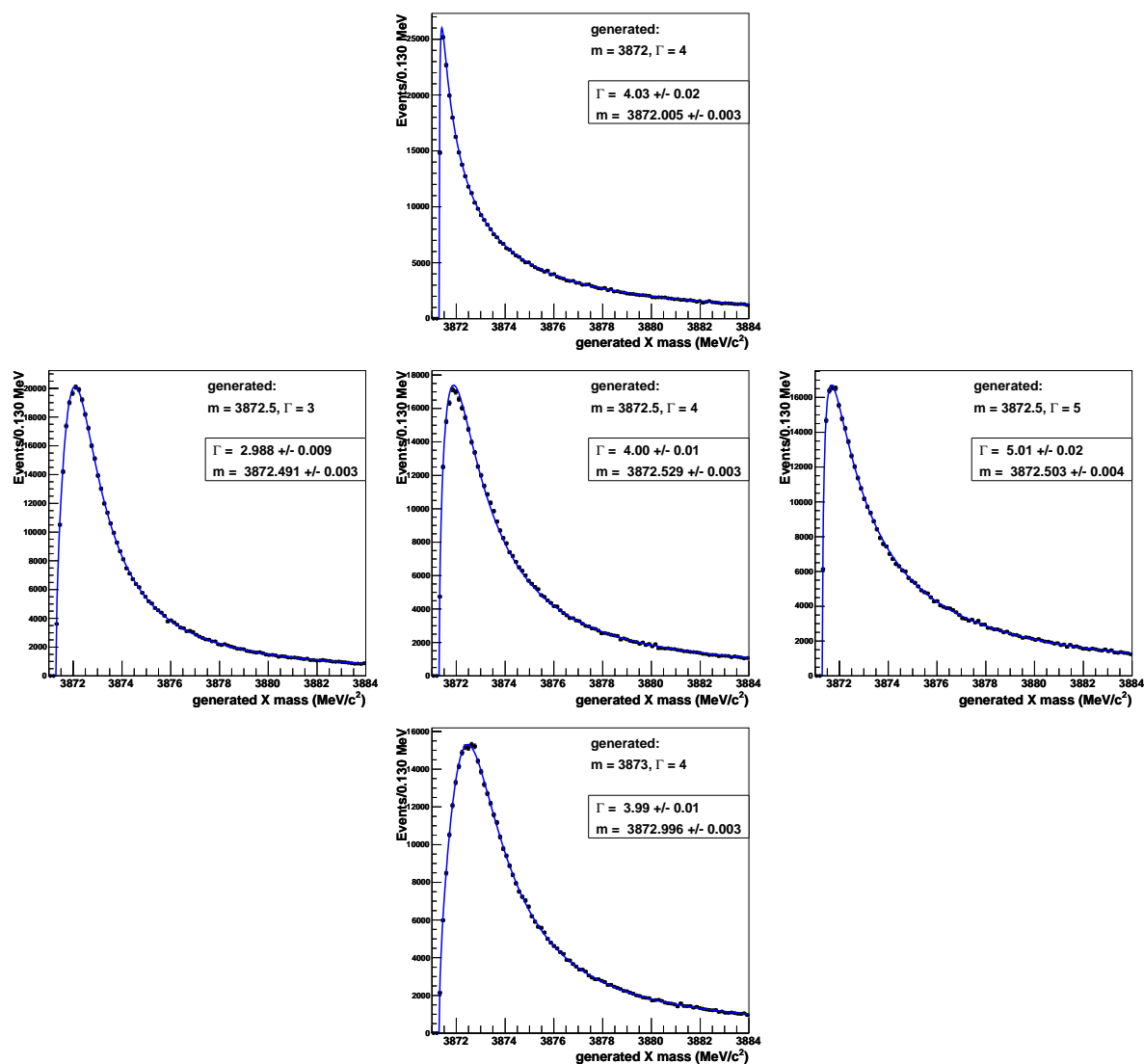

Figure 5.1: Distribution of the generated $X(3872)$ mass from MC samples generated with various masses and widths. The curves are the result of fits with the relativistic Breit-Wigner function described in the text.

generated		fitted	
m (MeV/c^2)	Γ (MeV/c^2)	m (MeV/c^2)	Γ (MeV/c^2)
3872.0	4.0	3872.010 ± 0.003	4.03 ± 0.02
3872.5	4.0	3872.529 ± 0.003	4.00 ± 0.01
3873.0	4.0	3872.996 ± 0.003	3.99 ± 0.01
3872.5	3.0	3872.491 ± 0.003	2.99 ± 0.01
3872.5	5.0	3872.503 ± 0.004	5.01 ± 0.02

Table 5.1: Results of fits to generated $X(3872)$ mass distributions with large statistics.

5.1.2 $X(3872)$ mass resolution

Since the $X(3872)$ mass is very close to the $D^{*0}\bar{D}^0$ threshold, the D^*D mass resolution has a sensitive dependence on the true mass. To determine the $X(3872)$ mass resolution as a function of the generated mass in the whole mass range, a Monte Carlo sample of 200'000 non-resonant $B^+ \rightarrow D^{*0}\bar{D}^0 K^+$ events was generated (half in $D^{*0} \rightarrow D^0\gamma$, half in $D^{*0} \rightarrow D^0\pi^0$). Additionally, the signal Monte Carlo sample generated with mass 3872.7 MeV/c^2 and decay width 4.3 MeV/c^2 is used to better describe the resolution in the signal region $(3871 - 3881 \text{ MeV}/c^2)$.

For several values of the generated $D^{*0}\bar{D}^0$ invariant mass, the resolution $\sigma_X(m_{\text{true}})$ was obtained by fitting the $m(D^*D)_{\text{gen}} - m(D^*D)_{\text{reco}}$ distribution (see Figures 5.2 and 5.3). The result is shown in Figure 5.4 and can be well described with a square root function of the form

$$\sigma_X(m_{\text{true}}) = a\sqrt{m_{\text{true}} - m_0} \tag{5.2}$$

where a and m_0 are free parameters. Fitting both D^{*0} channels together gives $a = 0.172 \pm 0.002$ MeV/c^2 and $m_0 = 3870.9 \pm 0.1$ MeV/c^2, which is consistent with the $D^{*0}D^0$ threshold $(3871.3 \text{ MeV}/c^2)$. Fitting the $D^0\gamma$ and $D^0\pi^0$ channels separately gives a difference in resolution smaller than 1%, which justifies that the same function can be used for both channels.

Appendix A.3 contains a study of the contributions to the $X(3872)$ mass resolution, and an estimation of this resolution in data as compared to Monte Carlo: we expect the $X(3872)$ mass resolution in data to be 1.14 ± 0.05 times worse than in Monte Carlo.
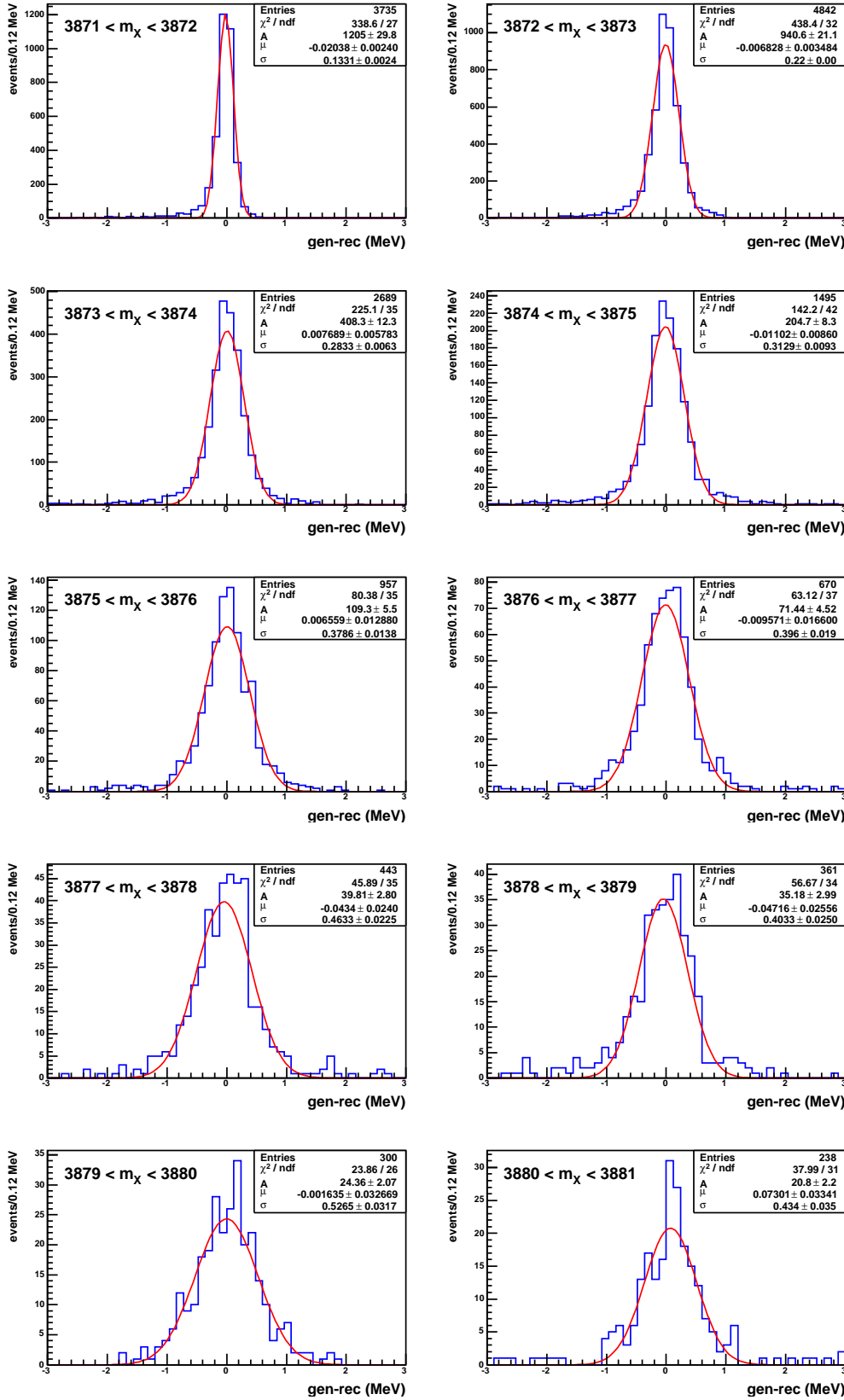
Figure 5.2: Distributions of generated−reconstructed $X(3872)$ masses for several intervals of generated mass in the $D^0\gamma$ channel. The curves are the results of fits with a single Gaussian function.
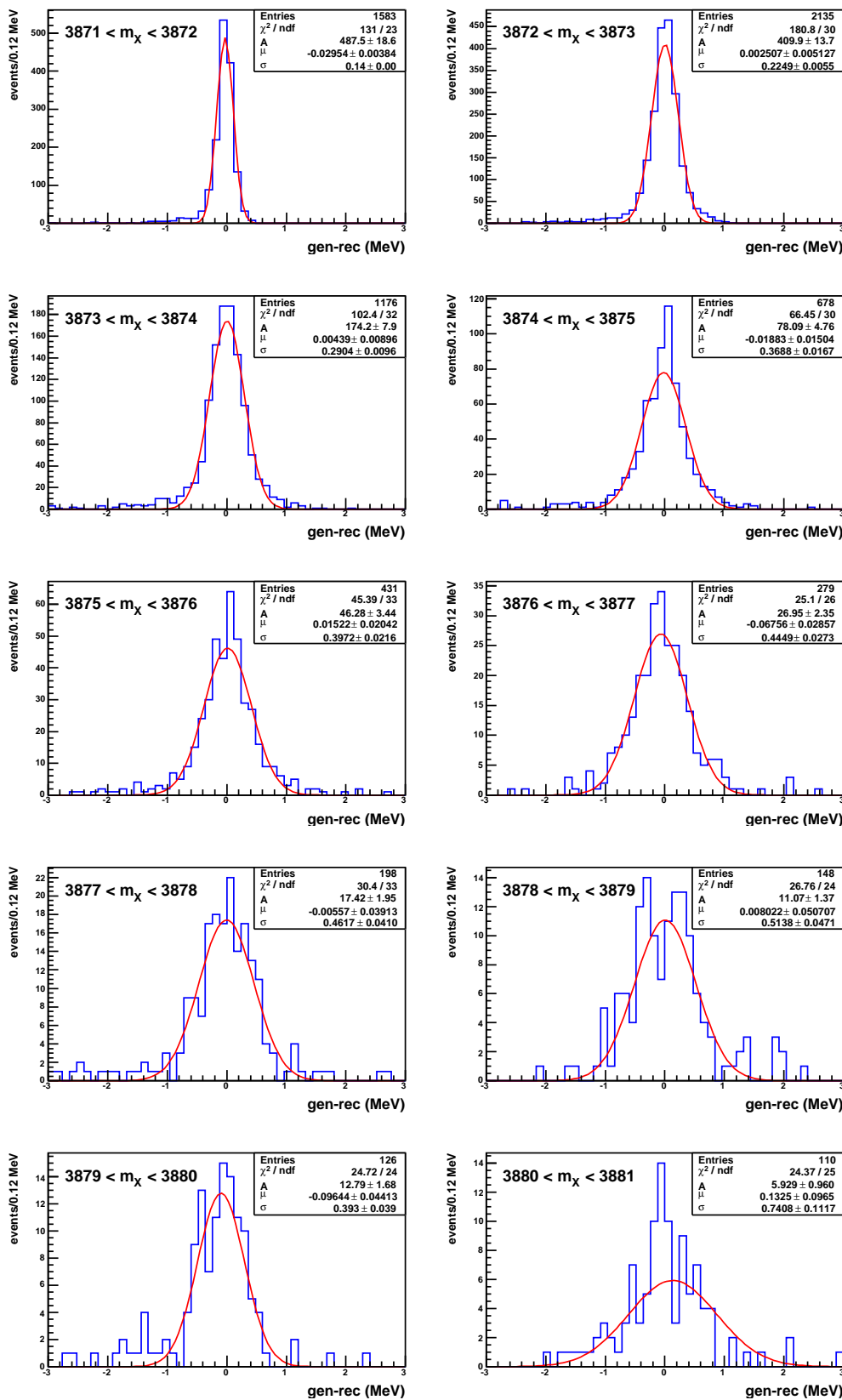
Figure 5.3: Distributions of generated−reconstructed $X(3872)$ masses for several intervals of generated mass in the $D^0\pi^0$ channel. The curves are the results of fits with a single Gaussian function.
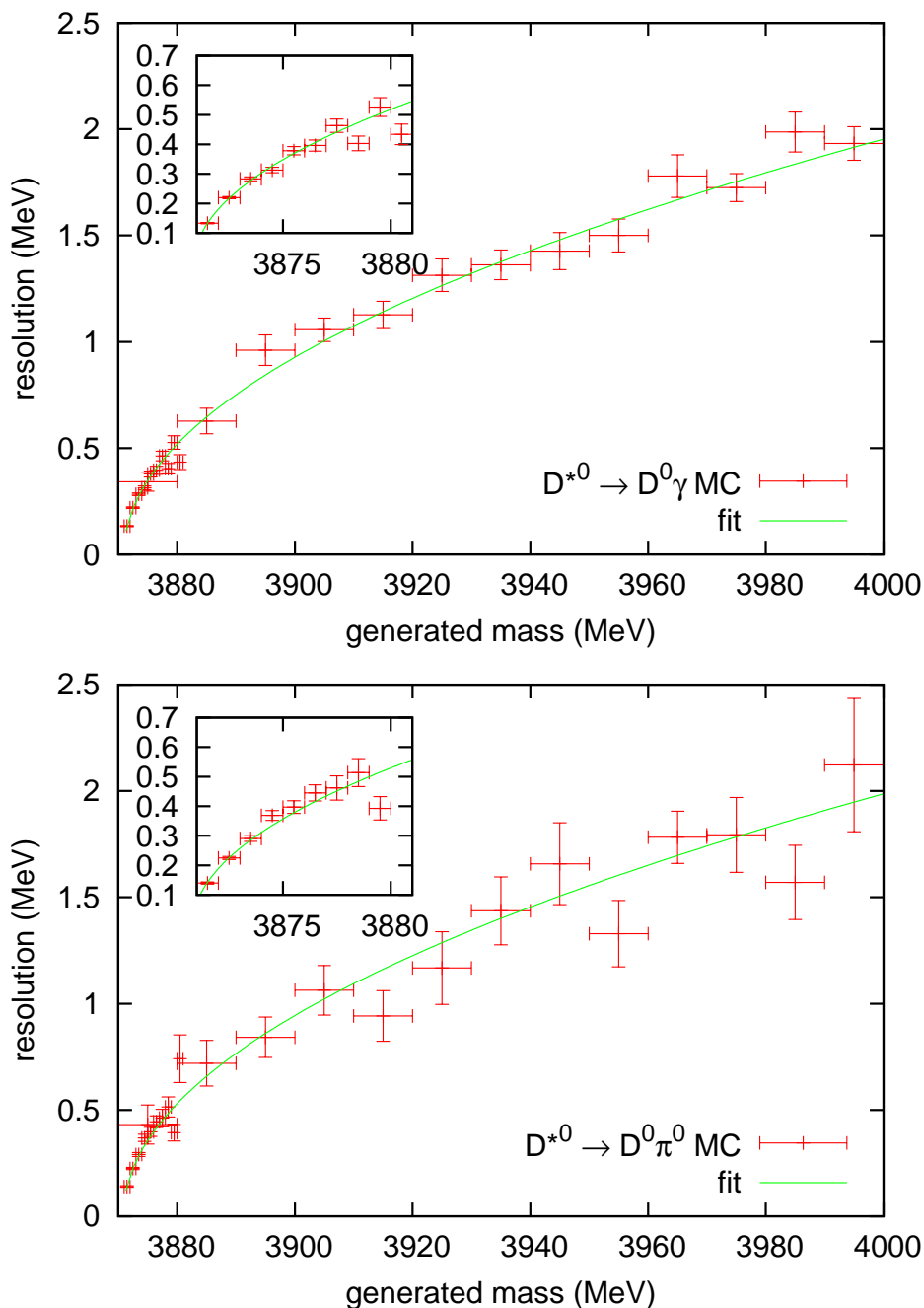
Figure 5.4: $X(3872)$ mass resolution as a function of the generated $X(3872)$ mass in the $D^0\gamma$ channel (top) and the $D^0\pi^0$ channel (bottom). Crosses are Gaussian resolutions for various generated $X(3872)$ masses; the curve is the result of a simultaneous fit with a common square root function.

5.1.3 Reconstructed *X*(3872) mass distributions

To fit the reconstructed $X(3872)$ mass distribution, the relativistic Breit-Wigner $BW(x)$ given by Eq. (5.1) is convolved with a Gaussian resolution function $g(x)$ with a sigma given by Eq. (5.2) obtained in Section 5.1.2. The expression of the resulting probability density function (pdf) is

$$f(m) = \int_{-\infty}^{+\infty} BW(m_{\text{true}})\, g(m - m_{\text{true}}, \, \sigma_X(m_{\text{true}}))\, \mathrm{d}m_{\text{true}}. \qquad (5.3)$$

An example of the resulting pdf is shown in Figure 5.5.
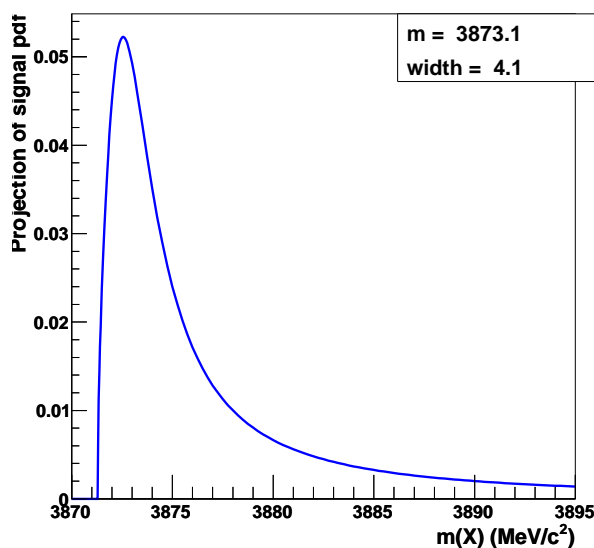
Figure 5.5: Relativistic Breit-Wigner convolved with the Gaussian resolution function. The resonance mass is 3873.1 MeV/c^2 and its width is 4.1 MeV/c^2.

However, to completely describe the reconstructed $X(3872)$ mass distributions, one has to take into account the effect of the D^0 and $\bar{D}^0$ reflections described in the next paragraph.

D^0 and $\bar{D}^0$ reflections

D^0 and $\bar{D}^0$ reflections correspond to wrongly reconstructing

$$X(3872) \rightarrow D^{*0}(D^0\gamma)\bar{D}^0 \quad \text{as} \quad D^0\bar{D}^{*0}(\gamma\bar{D}^0) \quad \text{or}$$
$$X(3872) \rightarrow D^{*0}(D^0\pi^0)\bar{D}^0 \quad \text{as} \quad D^0\bar{D}^{*0}(\pi^0\bar{D}^0).$$

The effect on the $X(3872)$ mass distribution of these reflections is shown in Figure 5.6. Correctly reconstructed candidates are identified using MC truth and the corresponding $X(3872)$ mass distribution is shown as a red histogram. Then the D^0 and $\bar{D}^0$ are swapped and the corresponding $X(3872)$ mass distribution is shown as a blue histogram. This is done for two different sets of $X(3872)$ parameters: in the left plots, the mass is

3872 MeV/c^2 and the decay width is zero; in the right plots, the mass is 3873 MeV/c^2 and the decay width is 3.0 MeV/c^2.

In both channels, the reflected distributions contribute to the signal region and have to be taken into account in the fit as being part of the signal. In the $D^0\gamma$ channel, the centre of the reflected distribution doesn't depend on the $X(3872)$ decay width; only its width becomes larger as the decay width of the resonance increases. In the $D^0\pi^0$ channel, for a large $X(3872)$ decay width, the effect of the reflections becomes small: $D^{*0}(D^0\pi^0)\bar{D}^0$ is undistinguishable from $D^0\bar{D}^0\pi^0$. Thus if the $X(3872)$ width is large, the reflection can be ignored in the signal function for the $D^0\pi^0$ channel.
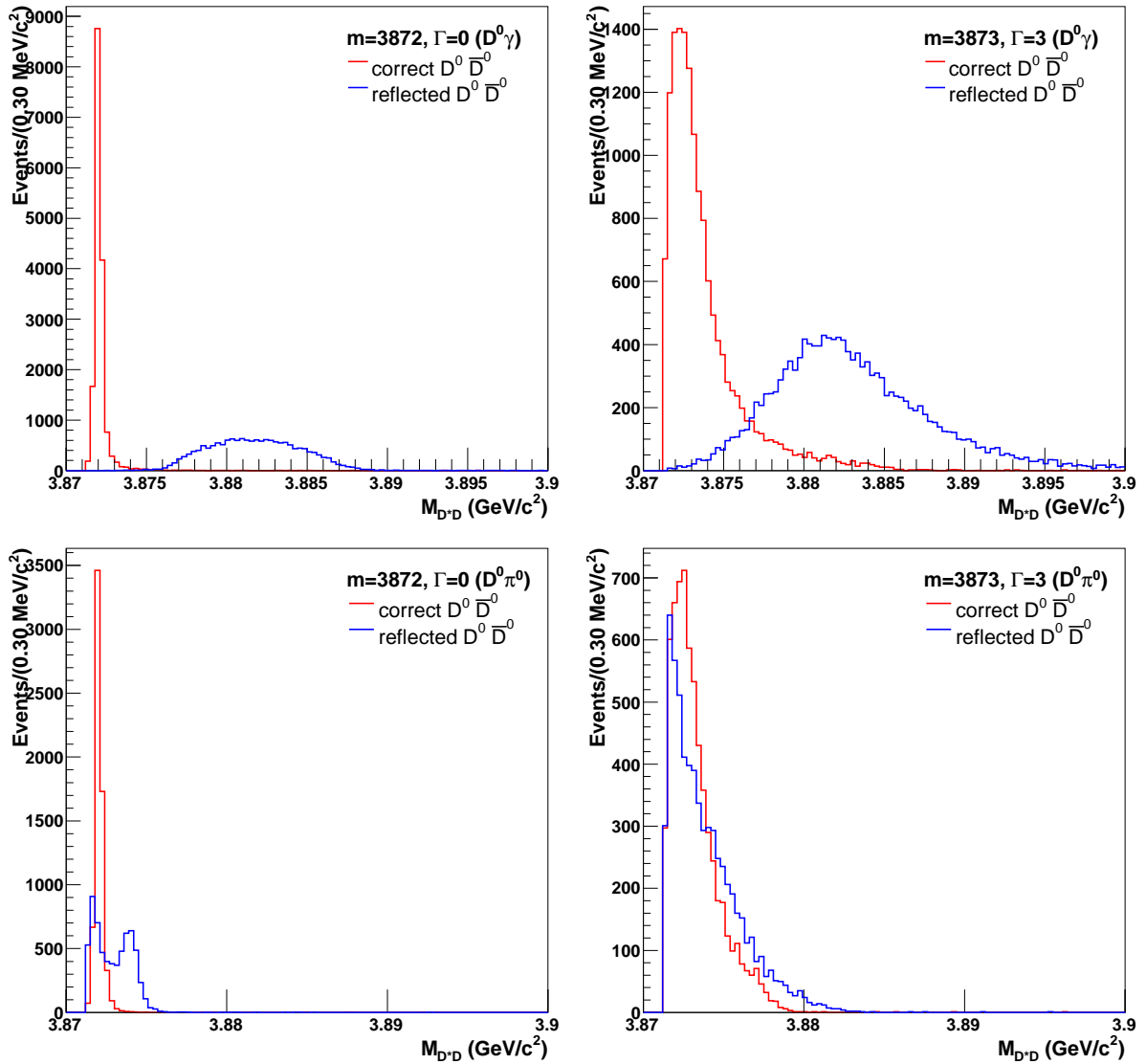
Figure 5.6: Distribution of M_{D^*D} for correctly reconstructed MC signal events (red histograms) and for the same, but reflected events (blue histograms), in the $D^0\gamma$ (top) and $D^0\pi^0$ channel (bottom).

5.1.4   Monte Carlo efficiencies

To obtain the reconstruction efficiency, a two-dimensional unbinned extended maximum likelihood fit to M_{bc} and M_{D^*D} is performed on five different signal Monte Carlo samples (see Figures 5.7 to 5.11). The M_{bc} distribution is described with a single Gaussian function. The M_{D^*D} signal is described with the convolved relativistic Breit-Wigner function of Eq. (5.3). The contribution from the D^0–$\bar{D}^0$ reflections is added as a histogram pdf; the fraction f_{sig} of signal in the Breit-Wigner peak is fixed to 0.78 in the $D^{*0} \to D^0\gamma$ channel and to 0.65 in the $D^{*0} \to D^0\pi^0$ channel; $1 - f_{\mathrm{sig}}$ is the fraction of signal in the reflection.

Figure 5.7: Distribution of M_{bc} for $M_{D^*D} < 3.88$ GeV/c^2 (left) and of M_{D^*D} for $M_{\mathrm{bc}} > 5.27$ GeV/c^2 (right); the top row is for $D^{*0} \to D^0\gamma$ and the bottom row for $D^{*0} \to D^0\pi^0$. The points are selected events using the signal MC sample generated with a mass of 3872.0 MeV/c^2 and a width of 4.0 MeV/c^2; the solid curve is the result of a fit using the pdf described in the text, and the dashed curve is the contribution from D^0–$\bar{D}^0$ reflections.

Figure 5.8: Distribution of M_{bc} for $M_{D^*D} < 3.88$ GeV/c^2 (left) and of M_{D^*D} for $M_{\mathrm{bc}} > 5.27$ GeV/c^2 (right); the top row is for $D^{*0} \to D^0\gamma$ and the bottom row for $D^{*0} \to D^0\pi^0$. The points are selected events using the signal MC sample generated with a mass of 3872.5 MeV/c^2 and a width of 4.0 MeV/c^2; the solid curve is the result of a fit using the pdf described in the text, and the dashed curve is the contribution from D^0–$\bar{D}^0$ reflections.

Table 5.2 gives the $X(3872)$ mass and width and the total efficiencies obtained for each sample. The total efficiency in each D^{*0} channel is

$$\begin{aligned}
\epsilon^\gamma_{\mathrm{tot}} &= \epsilon\beta^2 \mathcal{B}(D^{*0} \to D^0\gamma) \quad \text{and} \\
\epsilon^{\pi^0}_{\mathrm{tot}} &= \epsilon\beta^2 \mathcal{B}(D^{*0} \to D^0\pi^0),
\end{aligned} \tag{5.4}$$

where ϵ is the reconstruction efficiency and

$$\begin{aligned}
\beta &= \mathcal{B}(D^0 \to (K\pi, K\pi\pi^0, K\pi\pi\pi, K^0_S\pi\pi, KK)) \\
&= \frac{\Gamma_{K\pi}}{\Gamma_{\mathrm{tot}}}\left(1 + \frac{\Gamma_{K\pi\pi^0}}{\Gamma_{K\pi}}\right) + \frac{\Gamma_{K\pi\pi\pi}}{\Gamma_{\mathrm{tot}}} + \frac{\Gamma_{K^0_S\pi\pi}}{\Gamma_{\mathrm{tot}}} + \frac{\Gamma_{KK}}{\Gamma_{\mathrm{tot}}} = 0.2927 \pm 0.0071 \quad [4].
\end{aligned}$$
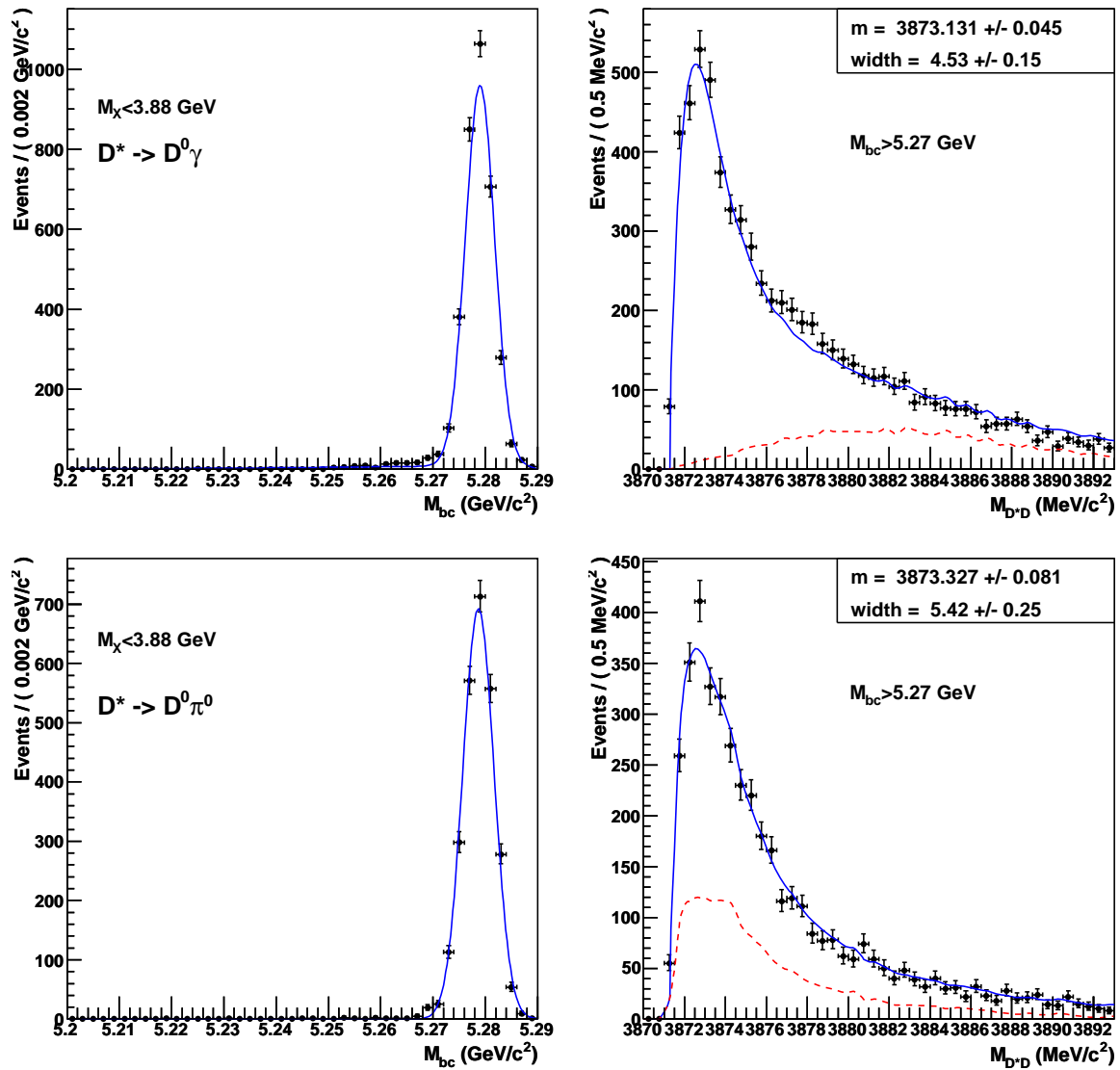
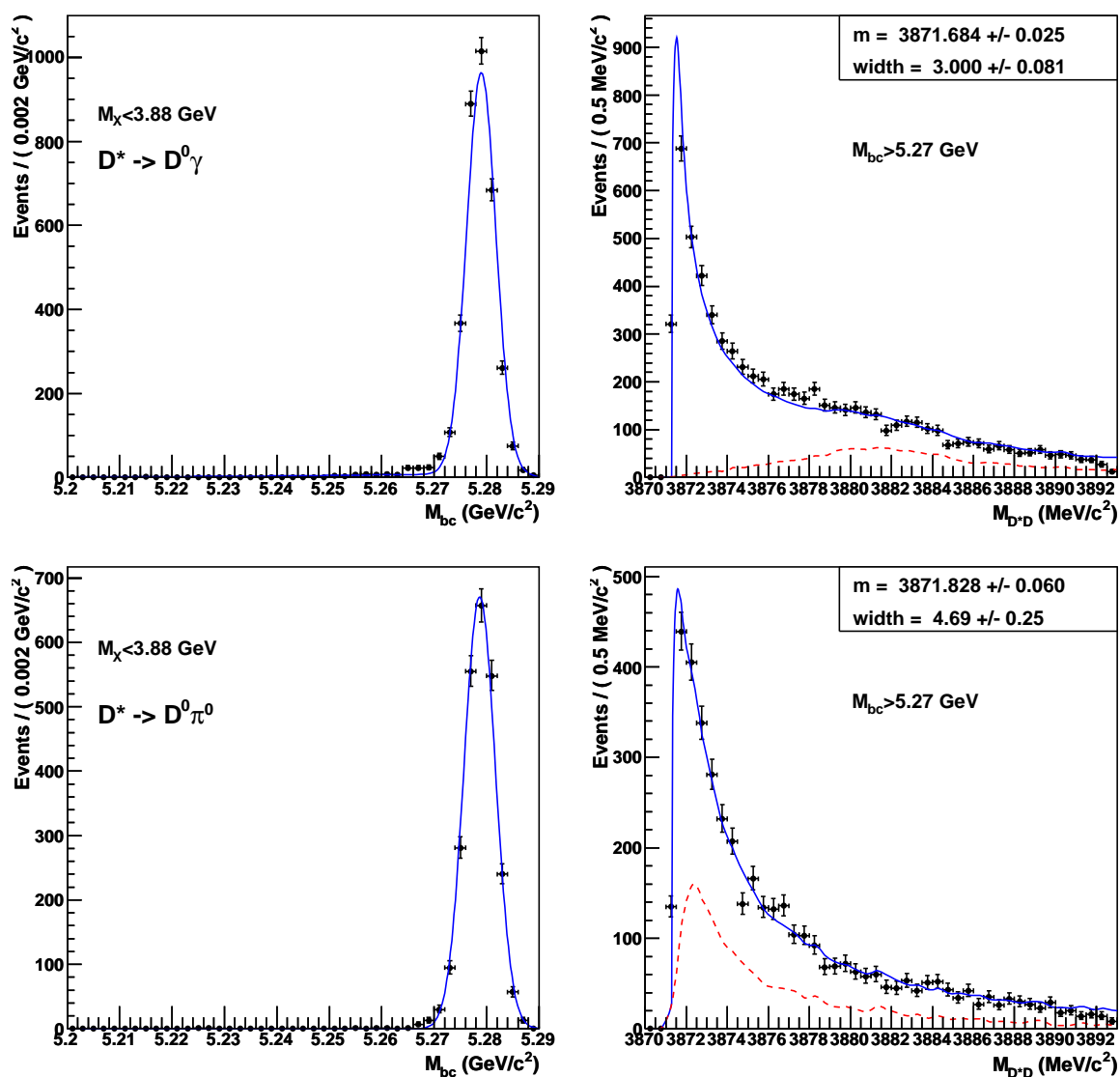Figure 5.9: Distribution of M_{bc} for $M_{D^*D} < 3.88$ GeV/c^2 (left) and of M_{D^*D} for $M_{\mathrm{bc}} > 5.27$ GeV/c^2 (right); the top row is for $D^{*0} \to D^0\gamma$ and the bottom row for $D^{*0} \to D^0\pi^0$. The points are selected events using the signal MC sample generated with a mass of 3873.0 MeV/c^2 and a width of 4.0 MeV/c^2; the solid curve is the result of a fit using the pdf described in the text, and the dashed curve is the contribution from D^0–$\bar{D}^0$ reflections.
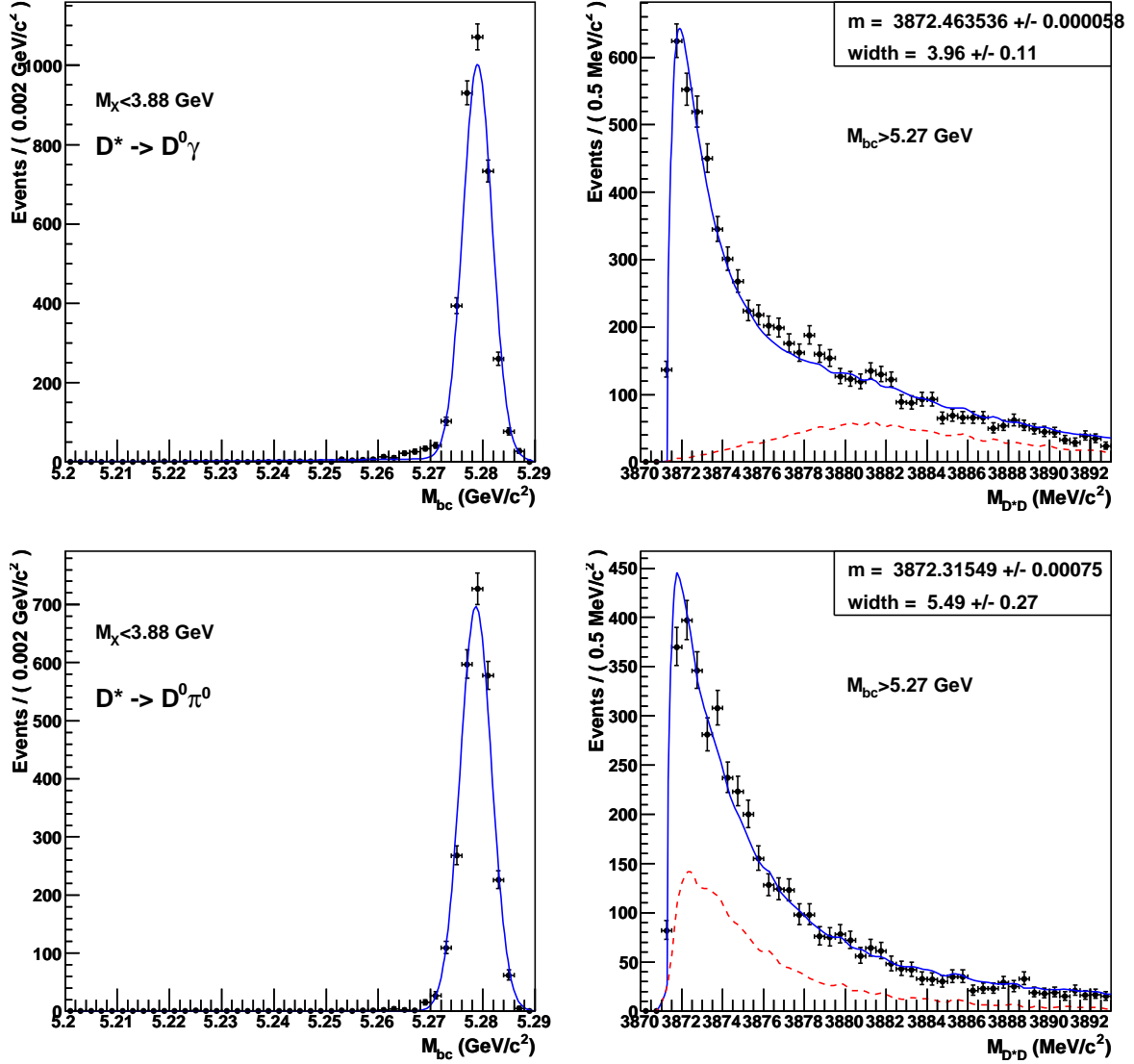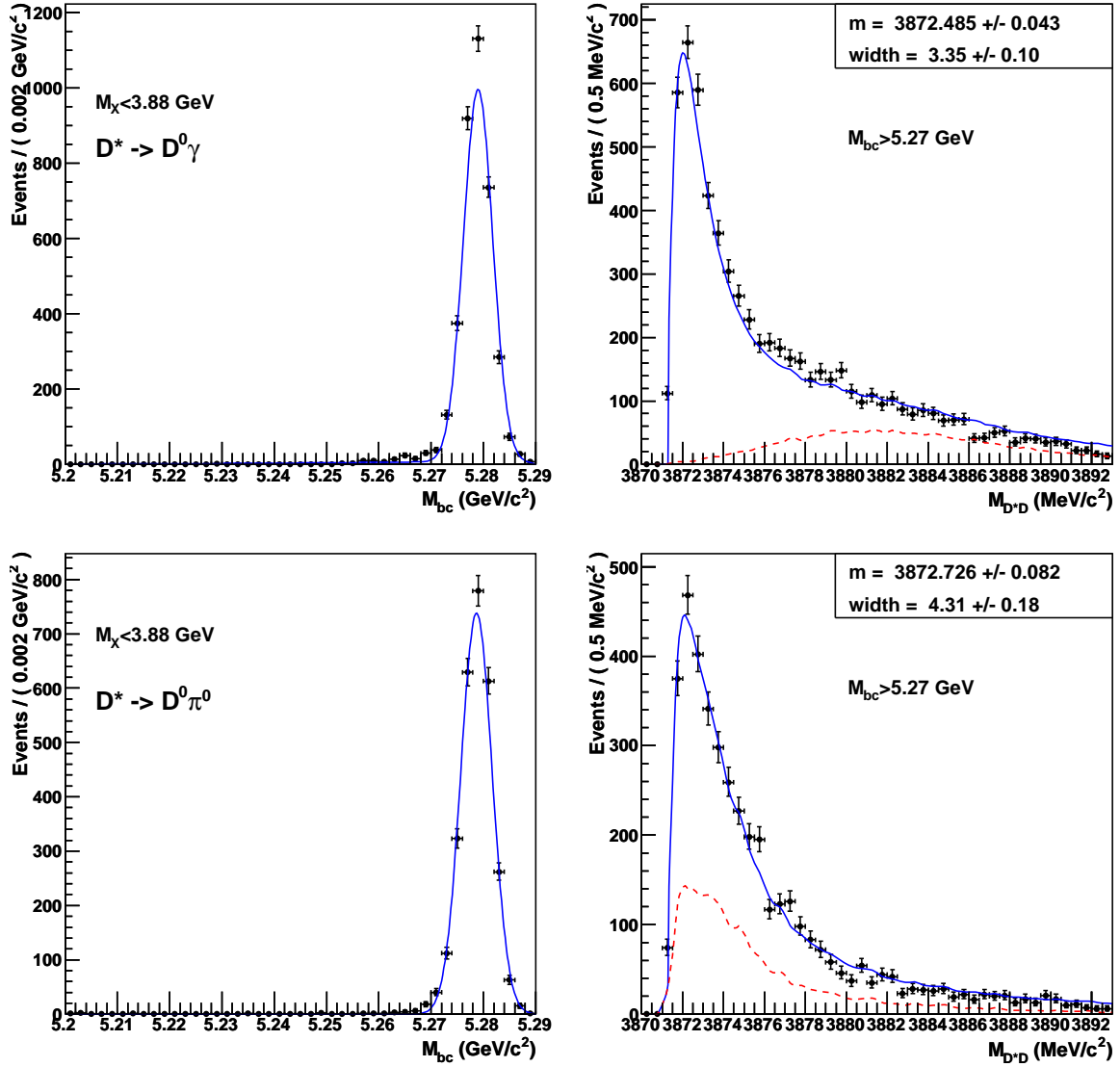
Figure 5.10: Distribution of M_{bc} for $M_{D^*D} < 3.88$ GeV/c^2 (left) and of M_{D^*D} for $M_{\mathrm{bc}} > 5.27$ GeV/c^2 (right); the top row is for $D^{*0} \to D^0\gamma$ and the bottom row for $D^{*0} \to D^0\pi^0$. The points are selected events using the signal MC sample generated with a mass of 3872.5 MeV/c^2 and a width of 3.0 MeV/c^2; the solid curve is the result of a fit using the pdf described in the text, and the dashed curve is the contribution from D^0–$\bar{D}^0$ reflections.

Figure 5.11: Distribution of $M_{\rm bc}$ for $M_{D^*D} < 3.88$ GeV/c^2 (left) and of M_{D^*D} for $M_{\rm bc} > 5.27$ GeV/c^2 (right); the top row is for $D^{*0} \to D^0\gamma$ and the bottom row for $D^{*0} \to D^0\pi^0$. The points are selected events using the signal MC sample generated with a mass of 3872.5 MeV/c^2 and a width of 5.0 MeV/c^2; the solid curve is the result of a fit using the pdf described in the text, and the dashed curve is the contribution from D^0–$\bar{D}^0$ reflections.
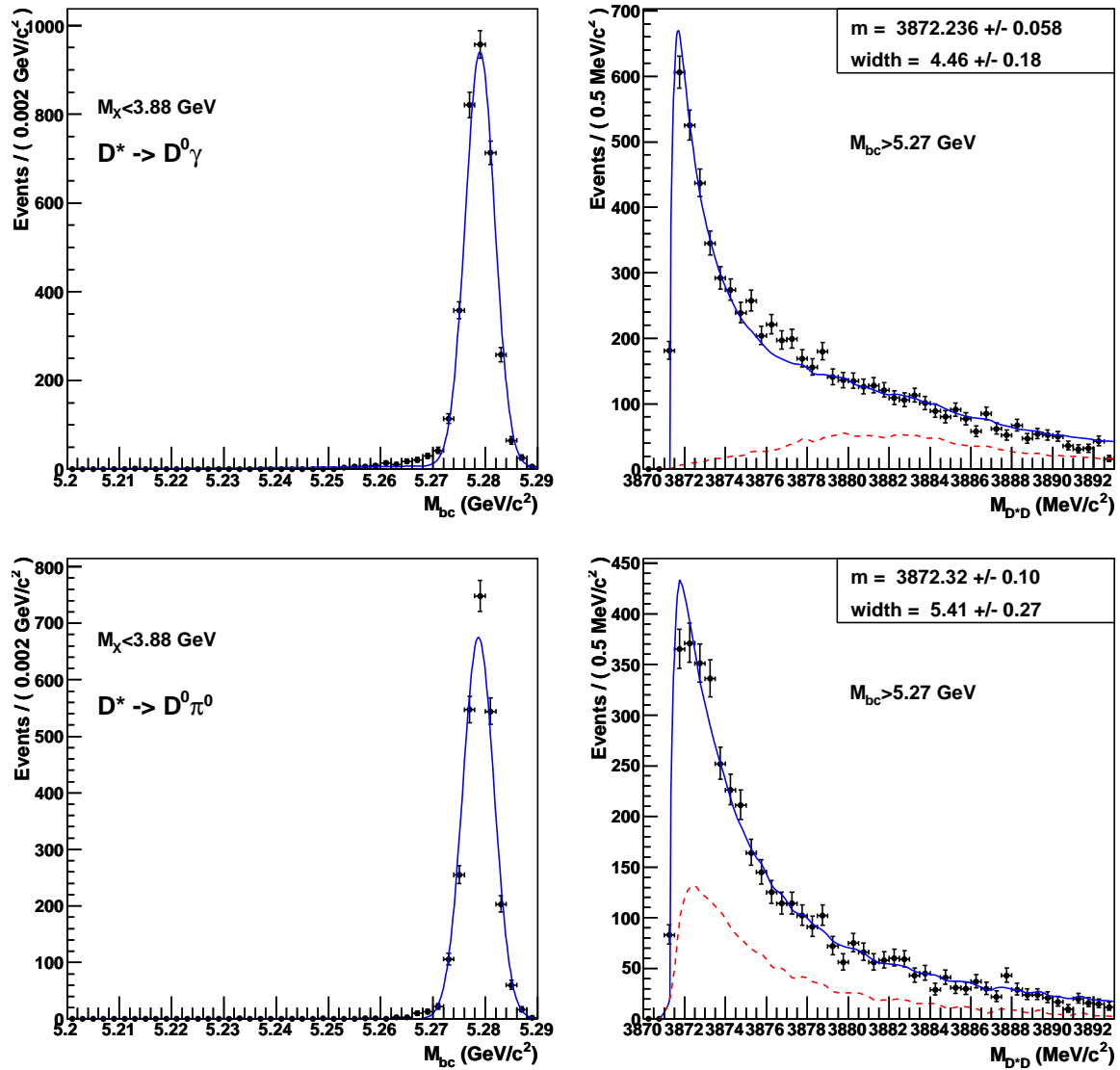
The obtained total efficiencies are fairly independent of the generated mass and width of the $X(3872)$. In Appendix A.4, we check that the Monte Carlo efficiency doesn't depend on the D^{*0} helicity distribution in $X(3872) \rightarrow D^{*0}(D^0\pi^0)\bar{D}^0$ decays.

In some cases, especially when the generated mass is close to the threshold and the generated width is large, the fitted mass and width are biased. This will be taken into account later in the systematic uncertainties (see Section 6.3.1).

B channel	generated		fitted		$\epsilon_{\rm tot}$
	m (MeV/c^2)	Γ (MeV/c^2)	m (MeV/c^2)	Γ (MeV/c^2)	(10^{-4})
			$D^{*0} \rightarrow D^0\gamma$		
$B^+ \rightarrow XK^+$	3872.0	4.0	3871.68 ± 0.03	3.00 ± 0.08	3.86 ± 0.05
$B^+ \rightarrow XK^+$	3872.5	4.0	3872.46 ± 0.05	3.96 ± 0.11	3.93 ± 0.05
$B^+ \rightarrow XK^+$	3873.0	4.0	3873.13 ± 0.05	4.53 ± 0.15	3.88 ± 0.05
$B^+ \rightarrow XK^+$	3872.5	3.0	3872.48 ± 0.04	3.35 ± 0.10	3.75 ± 0.05
$B^+ \rightarrow XK^+$	3872.5	5.0	3872.24 ± 0.06	4.46 ± 0.18	3.84 ± 0.05
$B^0 \rightarrow XK_S^0$	3872.5	4.0	3872.59 ± 0.05	4.55 ± 0.20	1.82 ± 0.03
			$D^{*0} \rightarrow D^0\pi^0$		
$B^+ \rightarrow XK^+$	3872.0	4.0	3871.83 ± 0.06	4.69 ± 0.25	4.16 ± 0.06
$B^+ \rightarrow XK^+$	3872.5	4.0	3872.32 ± 0.08	5.49 ± 0.20	4.24 ± 0.06
$B^+ \rightarrow XK^+$	3873.0	4.0	3873.33 ± 0.08	5.42 ± 0.25	4.22 ± 0.06
$B^+ \rightarrow XK^+$	3872.5	3.0	3872.73 ± 0.08	4.31 ± 0.18	4.14 ± 0.06
$B^+ \rightarrow XK^+$	3872.5	5.0	3872.32 ± 0.10	5.41 ± 0.27	4.19 ± 0.06
$B^0 \rightarrow XK_S^0$	3872.5	4.0	3872.83 ± 0.12	5.68 ± 0.20	2.00 ± 0.04

Table 5.2: Reconstructed $X(3872)$ mass and width, and total Monte Carlo efficiencies.

5.2   Background study

In this section we study various sources of backgrounds: we first look at the crossfeed between the $D^{*0} \rightarrow D^0\gamma$ and $D^{*0} \rightarrow D^0\pi^0$ channels; then we study the non-resonant $B \rightarrow D^{*0}\bar{D}^0K$ background; we look at a possible contribution from another XYZ state lying in our M_{D^*D} mass range, the $Y(3940)$; and finally we check our background contributions using generic Monte Carlo samples.

5.2.1   Crossfeed between $D^0\gamma$ and $D^0\pi^0$ channels

We check, in each D^{*0} channel, the crossfeed from the other D^{*0} channel. In Figure 5.12, the $D^0\pi^0$ signal Monte Carlo sample is reconstructed using the $D^0\gamma$ reconstruction (left). The crossfeed is scaled by a factor $\frac{\mathcal{B}(D^{*0} \rightarrow D^0\pi^0)}{\mathcal{B}(D^{*0} \rightarrow D^0\gamma)} = 1.62$ to be compared with the $D^0\gamma$ signal. The signal is not affected by this crossfeed. The crossfeed in $D^0\pi^0$ from $D^0\gamma$ is
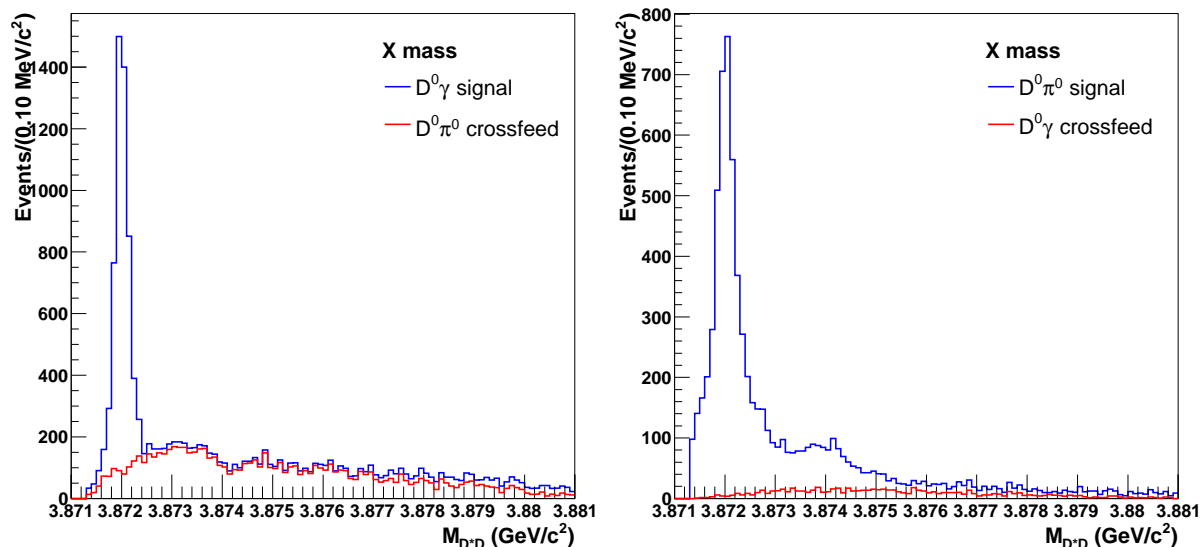
Figure 5.12: Left: distribution of M_{D^*D} for the crossfeed in $D^0\gamma$ from $D^0\pi^0$ (red), and sum of this crossfeed and selected events in $D^0\gamma$ signal MC (blue). Right: distribution of M_{D^*D} for the crossfeed in $D^0\pi^0$ from $D^0\gamma$ (red), and sum of this crossfeed and selected events in $D^0\pi^0$ signal MC (blue). The signal MC samples are generated with a mass of 3872 MeV/c^2 and zero width.

negligible (right plot); however, since the signal MC samples used here are generated with zero width, the contribution from reflections is clearly visible in the $D^0\pi^0$ channel.

5.2.2 Non-resonant $B \to D^{*0}\bar{D}^0K$ background

The background from non-resonant $B \to D^{*0}\bar{D}^0K$ was checked by reconstructing Monte Carlo samples of $B^+ \to D^{*0}(D^0\gamma)\bar{D}^0K^+$ and $B^+ \to D^{*0}(D^0\pi^0)\bar{D}^0K^+$ decays using the standard reconstruction procedure.

Figure 5.13 shows the resulting M_{bc} and M_{D^*D} distributions. This background peaks in the M_{bc} distribution, which is fitted using a double Gaussian for the peak and an ARGUS function for the background; the $X(3872)$ mass distribution is fitted using a square root function.

5.2.3 Contribution from $Y(3940)$

Both the $X(3940)$ and the $Y(3940)$ have nominal masses lying within our M_{D^*D} range, thus they could contribute to the background. Assuming that they are different states, we expect a contribution from the $Y(3940)$ rather than from the $X(3940)$, since it is the $Y(3940)$ that was observed in B decays.

We generate MC samples of $B^+ \to Y(3940)K^+$ in both D^{*0} modes and reconstruct them with the standard procedure (Figure 5.14). The $Y(3940)$ is generated with a mass of 3943 MeV/c^2 and a width of 87 MeV/c^2 (Belle values; BaBar finds somewhat different values, which will be taken into account in the systematic uncertainties, see Section 6.3.1).
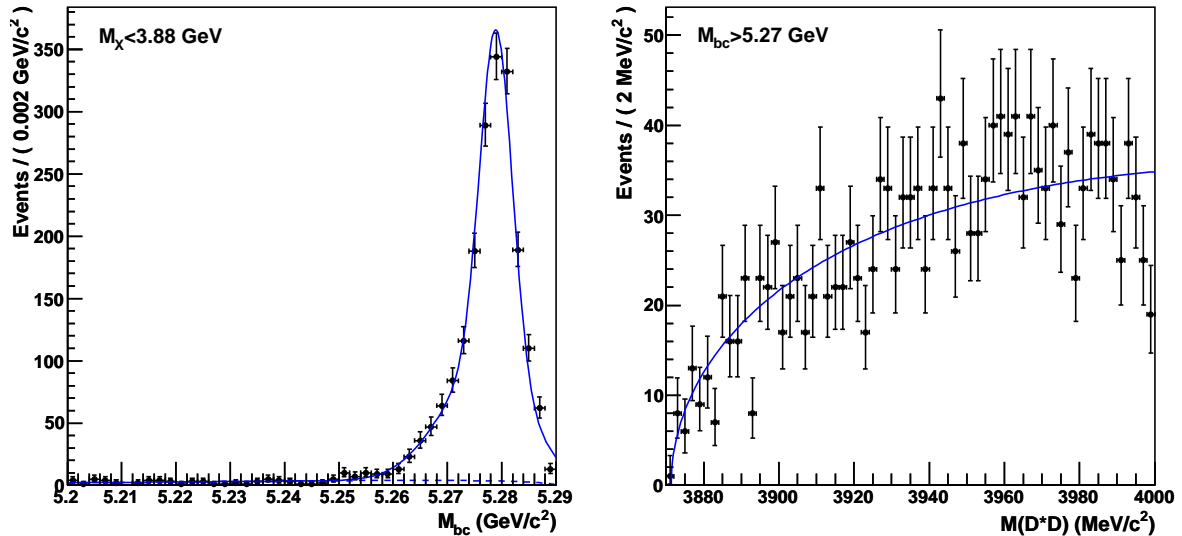
Figure 5.13: Distribution of M_{bc} for $M_{D^*D} < 3.88$ GeV/c^2 (left) and of M_{D^*D} for $M_{\text{bc}} > 5.27$ GeV/c^2 (right) for selected candidates in a MC sample of non-resonant $B^+ \to D^{*0}\bar{D}^0 K^+$ events. The curve is the result of a fit using the function described in the text.

As for the $X(3872)$, we perform a fit where the M_{bc} distribution is described with a single Gaussian function for the signal and an ARGUS function for the background, and the M_{D^*D} distribution is described with the convolved relativistic Breit-Wigner function for the signal and a square root function for the background. We obtain the following $Y(3940)$ total Monte Carlo efficiencies: $\epsilon_{\text{tot}}^{\gamma} = (3.87 \pm 0.12) \times 10^{-4}$ and $\epsilon_{\text{tot}}^{\pi^0} = (3.65 \pm 0.14) \times 10^{-4}$.

5.2.4   Generic Monte Carlo

Generic Monte Carlo is used to study the background. There are two generic MC samples, one containing $\Upsilon(4S) \to B^+B^-$ decays and another one containing $\Upsilon(4S) \to B^0\bar{B}^0$ decays, where the B^0 and $\bar{B}^0$ undergo coherent mixing. The charged sample contains a number of events equivalent to 1185 fb^{-1}, and the mixed sample is equivalent to 1103 fb^{-1}. These samples contain almost all physical processes known to occur at the $\Upsilon(4S)$ resonance, including $B \to D^{*0}\bar{D}^0 K$, thus they can be used to study the background.

To this effect, the two samples are reconstructed in both D^{*0} channels. The result is shown in Figure 5.15. We perform a simultaneous fit of both D^{*0} modes, using the probability density function described in Section 5.3.1. The mass and width of the $X(3872)$ are fixed to 3872.4 MeV/c^2 and 3.9 MeV/c^2, respectively. We obtain a total of 18.2 ± 9.2 $X(3872)$ signal events, with a statistical significance of 1.6σ. Since the generic Monte Carlo doesn't contain any $X(3872)$ decays, we consider this signal a statistical fluctuation. We don't observe any signal from the $Y(3940)$, but we obtain a significant contribution from the $B \to D^{*0}\bar{D}^0 K$ background, as expected.
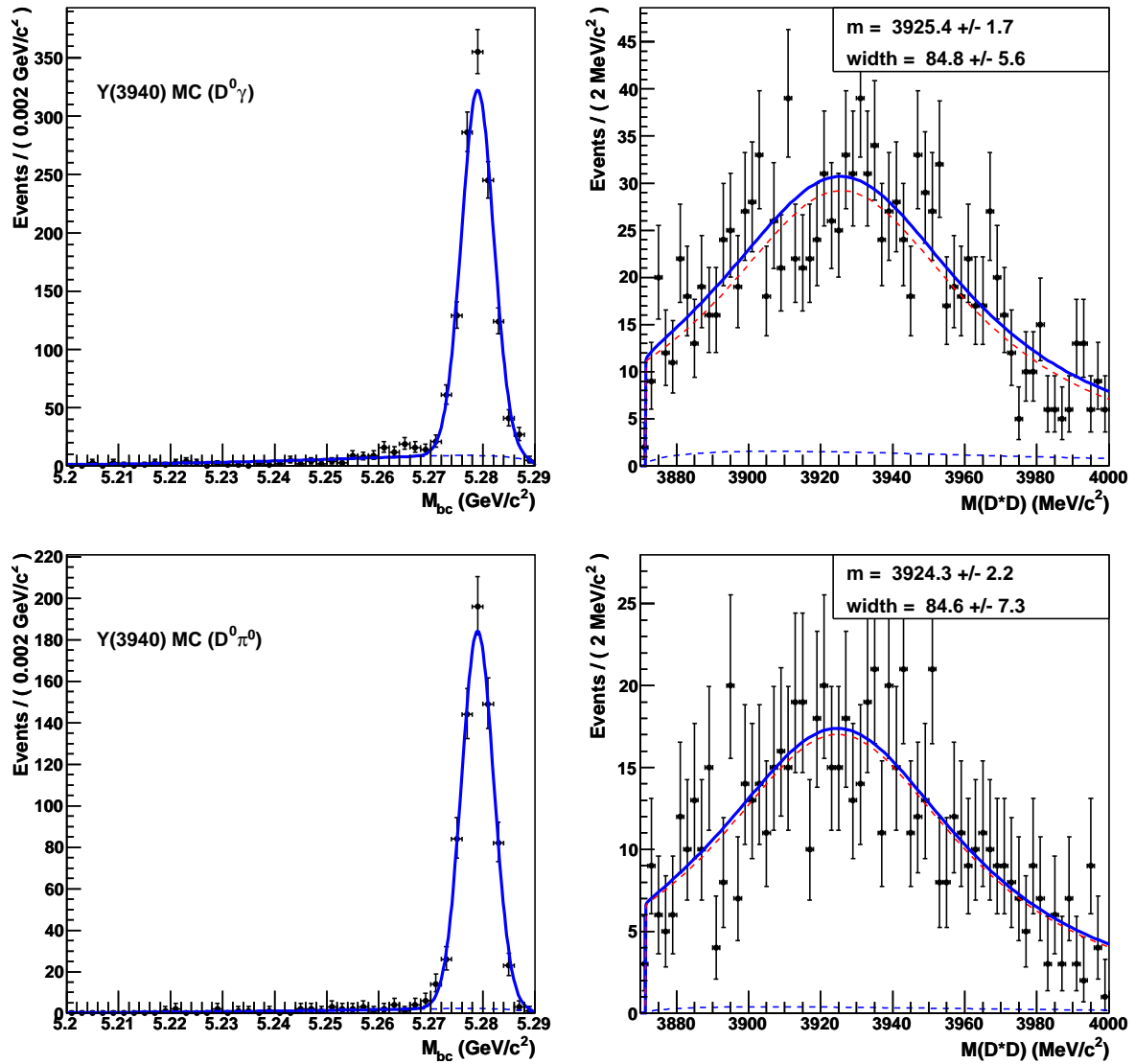
Figure 5.14: Distribution of M_{bc} for $M_{D^*D} < 3.88$ GeV/c^2 (left) and of M_{D^*D} for $M_{\mathrm{bc}} > 5.27$ GeV/c^2 (right); the top row is for $D^{*0} \to D^0\gamma$ and the bottom row for $D^{*0} \to D^0\pi^0$. The points are selected events using the $B^+ \to Y(3940)K^+$ MC samples; the solid curve is the result of a fit using the pdf described in the text.
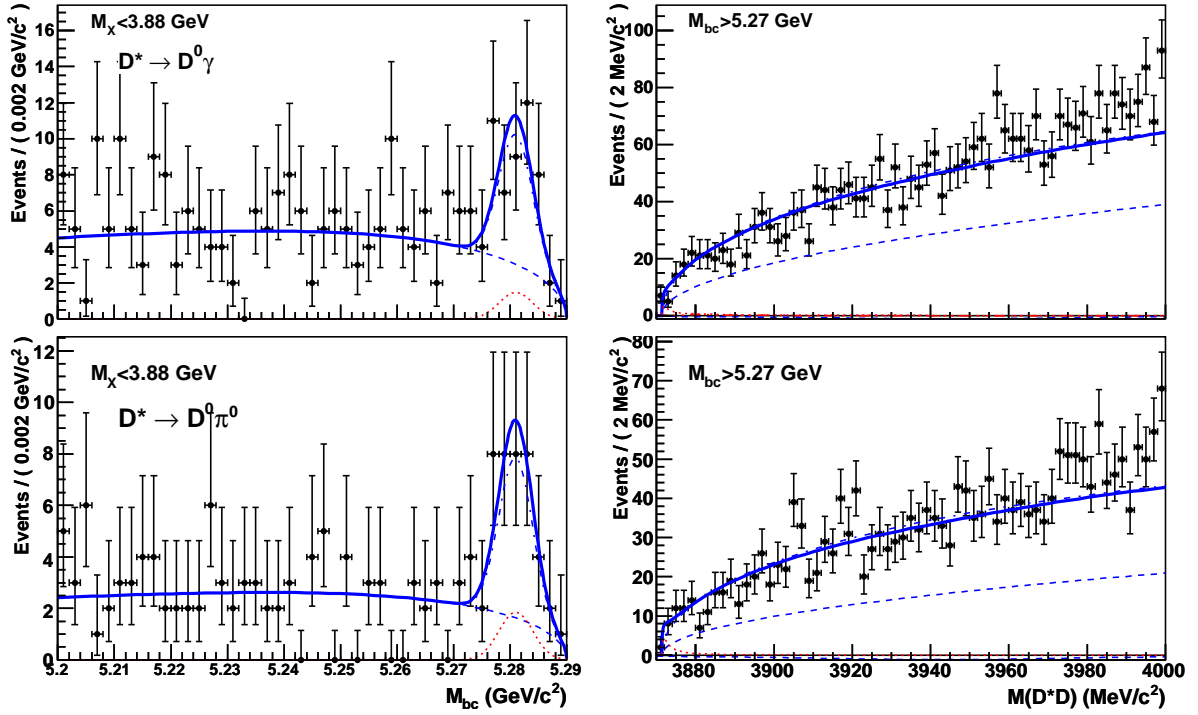
Figure 5.15: Distribution of M_{bc} for $M_{D^*D} < 3.88$ GeV/c^2 (left) and of M_{D^*D} for $M_{\mathrm{bc}} > 5.27$ GeV/c^2 (right); the top row is for $D^{*0} \to D^0\gamma$ and the bottom row for $D^{*0} \to D^0\pi^0$. The points with error bars are selected events using the generic MC samples, the dotted curve is the signal, the dashed curve is the background, the dash-dotted curve is the sum of the background and the $B \to D^*DK$ component, and the solid curve is the total fitting function.

5.3 Fitting function and toy Monte Carlo checks

This section describes the components of the probability density function that will be used to fit the data, and the toy Monte Carlo checks performed to validate this function.

5.3.1 Fitting function

The data are fitted using a two-dimensional pdf in $M_{\rm bc}$ and M_{D^*D} (Figure 5.16). The $M_{\rm bc}$ distribution is described with an ARGUS function [63] for the background and a single Gaussian function for the signal. The mean of this Gaussian is constrained at $5.281\,{\rm GeV}/c^2$ and its width at $3.0\,{\rm MeV}/c^2$. The $X(3872)$ mass distribution is described with the relativistic Breit-Wigner function given in Eq. (5.1) convolved with the Gaussian resolution (see Section 5.1.3) for the signal and a square root function for the background.

In the $D^{*0} \to D^0\gamma$ channel, the signal also contains a contribution from the D^0–$\bar{D}^0$ reflections (see Figure 5.6). The fraction of signal events in the peak and in the reflection shape is fixed from Monte Carlo: 78% of the signal is in the peak. We don't include any contribution from the reflections in the $D^{*0} \to D^0\pi^0$ channel, because in this case the shape of the reflection depends strongly on the $X(3872)$ mass and width, which is not the case in the $D^{*0} \to D^0\gamma$ channel, where the shape is nearly constant. This omission will be taken into account later as a systematic uncertainty (see Section 6.3.1).

The fit also includes a non-resonant $B \to D^*DK$ background component, described with a single Gaussian function in $M_{\rm bc}$ and a square root function in M_{D^*D}, and a $Y(3940)$ component, described with a relativistic Breit-Wigner function. The $Y(3940)$ mass is fixed to $3943\,{\rm MeV}/c^2$ and its decay width to $87\,{\rm MeV}/c^2$, using the values from Ref. [25].

5.3.2 Toy Monte Carlo tests

This pdf is tested using a statistical method involving toy Monte Carlo samples to identify possible biases and correct for them if needed, or estimate the corresponding systematic errors. Toy Monte Carlo tests consist in generating a large number of Monte Carlo samples according to the pdf and fit them with this pdf. The distributions of fit parameter errors, residuals (computed as fitted − generated) and pulls (defined as $\frac{{\rm fitted}-{\rm gen}}{{\rm error}}$) are then studied to identify possible biases. The fitted parameter values are expected to be consistent, within errors, with the generated values. In particular, the pull is expected to have a standard normal distribution.

We study the behavior of four variables: the $X(3872)$ mass, width and yield, and the $Y(3940)$ yield. We generate and fit 1000 samples, each containing 4100 events, which is roughly the size of the available data. The $X(3872)$ mass is generated at $3872.6\,{\rm MeV}/c^2$, its width at $4\,{\rm MeV}/c^2$, and the number of $X(3872)$ and $Y(3940)$ events are generated according to Poisson distributions centered at 50 and 15 events, respectively.

Figure 5.17 shows the distributions of residuals, errors and pulls for these four variables. In the case of the width, the asymmetric errors (returned by MINOS) are used to compute the pull, as they are quite different from each other. In the other cases only the symmetric error is used. The pull distributions are fitted with a single Gaussian function. They are consistent within errors with standard normal distributions, except for the
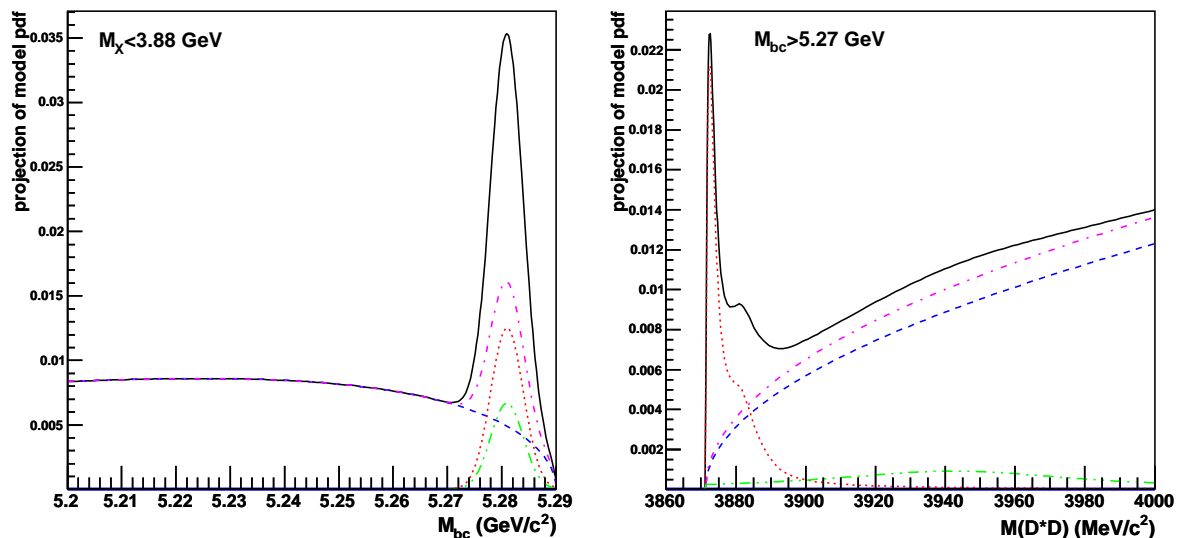
Figure 5.16: Projections of the fitting pdf in M_{bc} for $M_{D^*D} < 3.88$ GeV/c^2 (left) and in M_{D^*D} for $M_{\mathrm{bc}} > 5.27$ GeV/c^2 (right). The red dotted curve is the signal, the blue dashed curve is the background, the purple dash-dotted curve is the sum of the background and the $B \to D^*DK$ component, the green dot-dot-dashed curve is the contribution from the $Y(3940)$, and the black solid curve is the total fitting function. The $X(3872)$ mass is set to 3872.5 MeV/c^2 and its width to 4.0 MeV/c^2.

$X(3872)$ width and yield and the $Y(3940)$ yield. Biases are included in the systematic uncertainties (see Table 6.3).
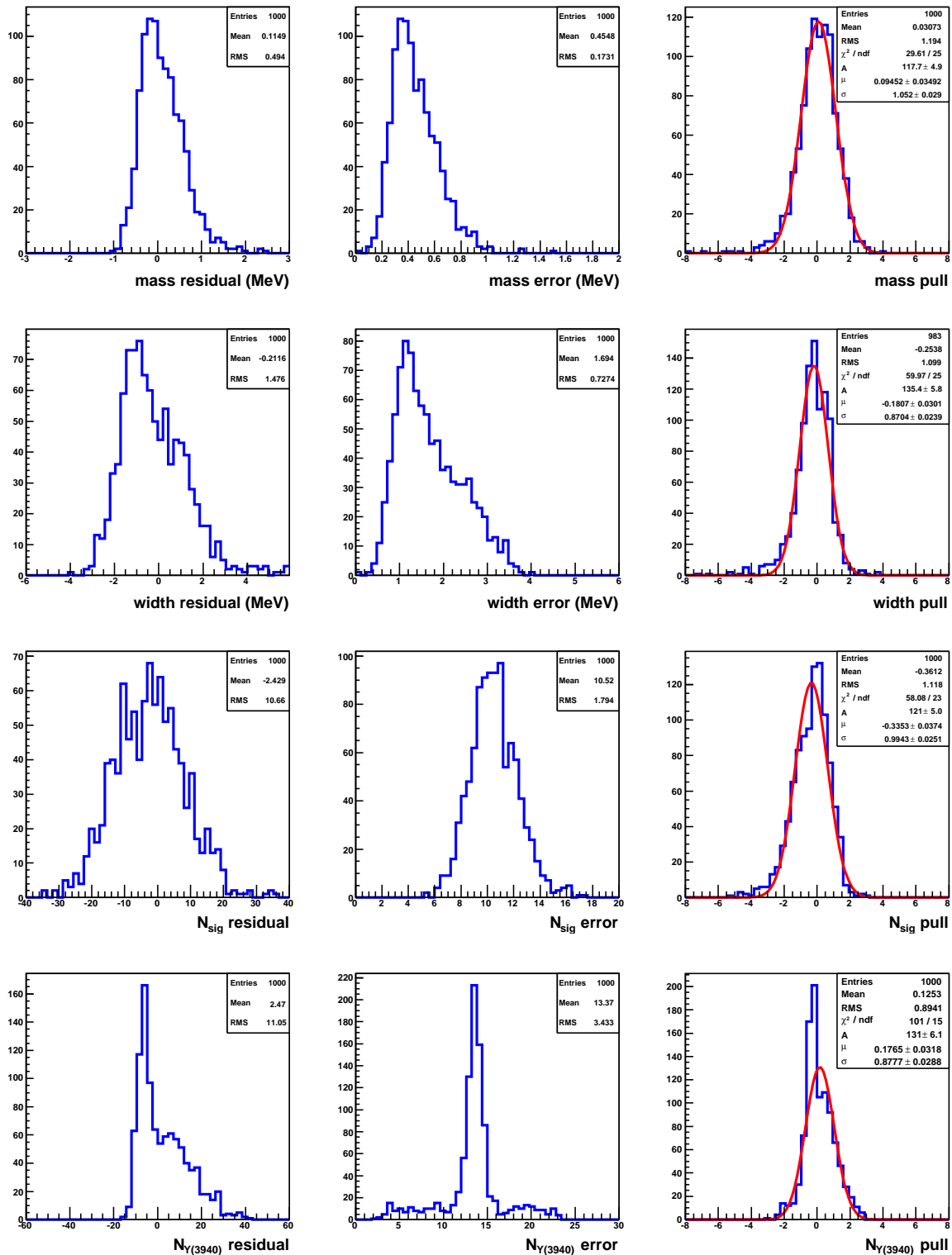
Figure 5.17: Toy MC tests: distributions of residuals (left), errors (middle), and pulls fitted with a single Gaussian function (right), for the four variables mentioned in the text.

Chapter 6

Extraction of $X(3872)$ signal
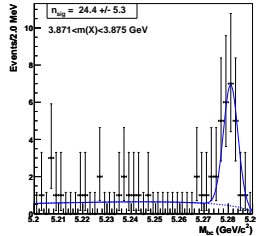
In this chapter, we look at the reconstructed Belle data and fit them in several ways. We then check our results and estimate the systematic uncertainties.

6.1   Fits to data

This section shows the signal obtained in the data, and various fits performed to extract the signal. Figure 6.1 (left) shows the distribution of $M_{\rm bc}$ and M_{D^*D} for selected events in the data, for both D^{*0} channels. In each bin, the surface of the square is proportional to the number of events in that bin. The blue rectangle at the bottom right shows the signal region. Figure 6.1 (right) shows the $X(3872)$ mass distribution for the $M_{\rm bc}$ signal ($M_{\rm bc} > 5.27$ GeV/c^2) and sideband ($M_{\rm bc} < 5.27$ GeV/c^2) regions, where the sideband region is scaled to the signal region.

We perform several fits to extract the signal:

- first, we fit each D^{*0} channel separately, for the sum of charged and neutral B channels;

- then both D^{*0} channels are fitted simultaneously, with the ratio of the yields in the $D^0\gamma$ over $D^0\pi^0$ channels left free;

- this last fit is repeated, but fixing the $D^0\gamma/D^0\pi^0$ yield ratio using MC;

- finally each B channel is fitted separately.

All these different fits are expected to give consistent results. The final results are obtained from the simultaneous fit with fixed $D^0\gamma/D^0\pi^0$ yield ratio, which is the most complete fit.

Figure 6.1: Left: distribution of M_{bc} and M_{D^*D} for selected events in the data. In each bin, the square area is proportional to the number of events in that bin. The blue rectangle at the bottom right shows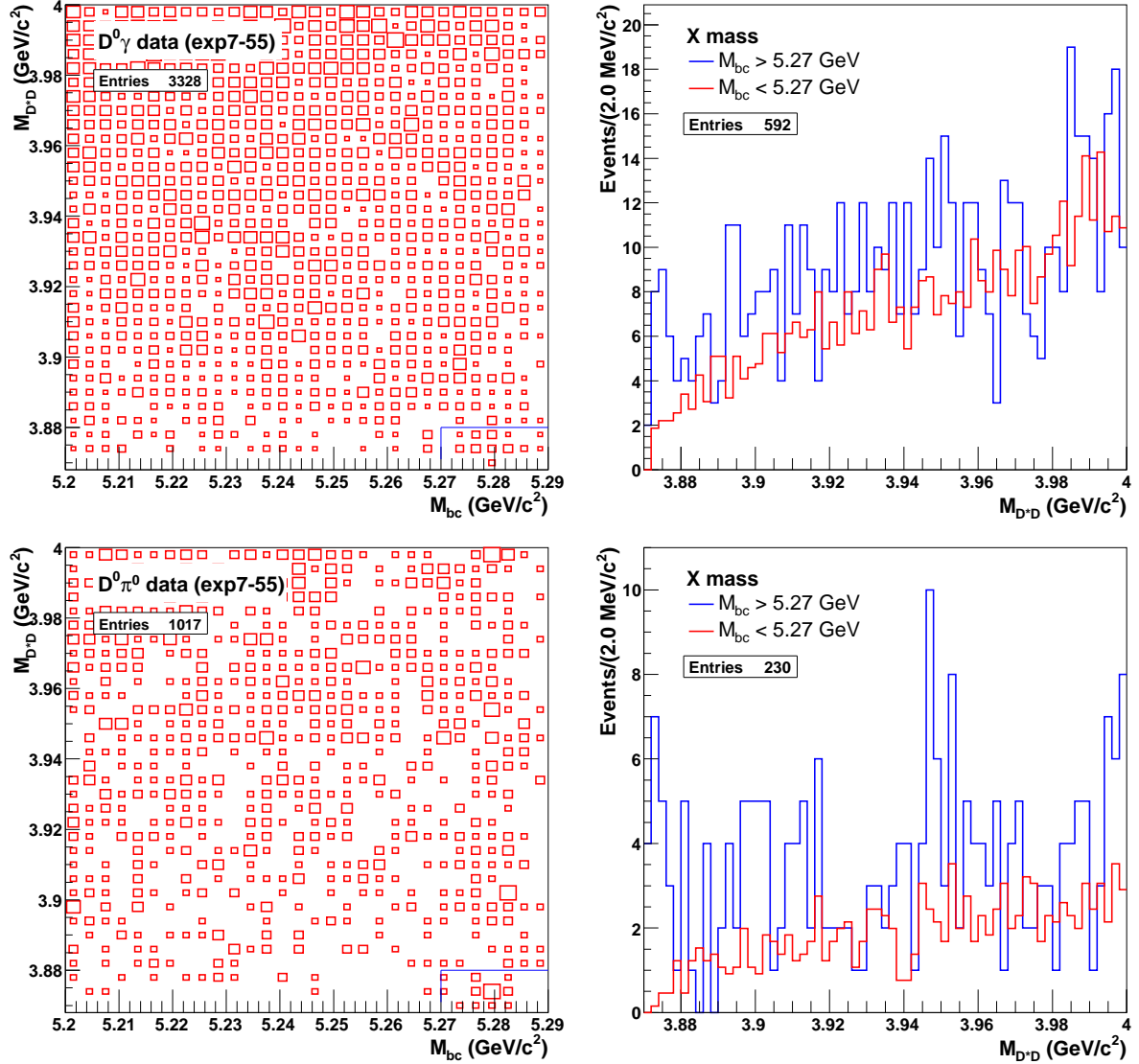 the signal region. Right: distribution of M_{D^*D} for the M_{bc} signal (blue histograms) and scaled M_{bc} sideband regions (red histograms). Top: $D^0\gamma$ channel, bottom: $D^0\pi^0$ channel.

6.1.1 Individual fits

An unbinned extended maximum likelihood fit is performed separately for each D^{*0} mode. The likelihood is defined as

$$\mathcal{L} = e^{-\sum_j S_j} \prod_i \left(\sum_j S_j P^i_j \right), \tag{6.1}$$

where i runs over all selected B meson candidates, j runs over the event categories (signals and backgrounds), S_j is the number of events in each category and P^i_j is the corresponding pdf evaluated for event i.

The $X(3872)$ yield, mass and decay width are free parameters of the fit, as well as the $Y(3940)$ yield and the number of background and non-resonant $B \to D^* D K$ events. Both $B^+ \to X(3872)K^+$ and $B^0 \to X(3872)K^0_S$ modes are included. Figures 6.2 and 6.3 and Table 6.1 show the fit results. In the figures, the error bars of the data points are asymmetric; they correspond to the 68% confidence intervals for Poisson statistics, or more precisely, to the classical central intervals as described in Table 1 of Ref. [64].

6.1.2 Simultaneous fit with free $D^0\gamma/D^0\pi^0$ yield ratio

The next step is to perform a simultaneous fit of both D^{*0} modes where the $X(3872)$ mass and width are constrained to have the same values in both modes, but the ratio of the yields in the $D^0\gamma$ over $D^0\pi^0$ channels is left free. Figure 6.4 and Table 6.1 show the fit results. The results for the mass, width and yields are very consistent with the values from the individual fits. We obtain a yield ratio of $N_{D^0\gamma}/N_{D^0\pi^0} = 1.16^{+0.53}_{-0.37}$, which is consistent with the value of 0.92 we expect from Monte Carlo.

6.1.3 Simultaneous fit with fixed $D^0\gamma/D^0\pi^0$ yield ratio

Next, a simultaneous unbinned extended maximum likelihood fit of both D^{*0} modes is performed. Both $B^+ \to X(3872)K^+$ and $B^0 \to X(3872)K^0_S$ modes are included. The ratio of the signal yields of the two modes is fixed to $N_{D^0\gamma}/N_{D^0\pi^0} = \epsilon^\gamma_{\text{tot}}/\epsilon^{\pi^0}_{\text{tot}} = 0.92$, using the Monte Carlo total efficiencies shown in Table 5.2, for the samples generated with a mass of 3872.5 MeV/c^2 and a width of 4.0 MeV/c^2. The ratios of $Y(3940)$ yields and $B \to D^{*0}\bar{D}^0 K$ backgrounds are also fixed from Monte Carlo, to the values of 1.06 and 1.16, respectively.

Figure 6.5 and Table 6.1 show the results of the fit. The simultaneous fit of both D^{*0} modes is in good agreement with the individual fits. We find a total signal of $N_{\text{sig}} = 50.1^{+14.8}_{-11.1}$ events with a mass of $3872.4^{+0.6}_{-0.4}$ MeV/c^2, and a width of $3.9^{+2.8}_{-1.4}$ MeV/c^2. The statistical significance of the signal is 7.9σ.

We compute the significance using $-2\ln(\mathcal{L}_0/\mathcal{L}_{\text{max}})$, where $\mathcal{L}_0$ and $\mathcal{L}_{\text{max}}$ are the maximized likelihoods with the signal yield fixed at zero and left free, respectively. This quantity should be distributed as $\chi^2(n_{\text{dof}})$, where $n_{\text{dof}} = 3$ is the difference in free parameters between the two fits.

Figure 6.6 shows the sum of both D^{*0} modes with the results of the fit, and Figure 6.7 shows the negative log-likelihood profiles for this fit, plotted as a function of the $X(3872)$ mass and width parameters.
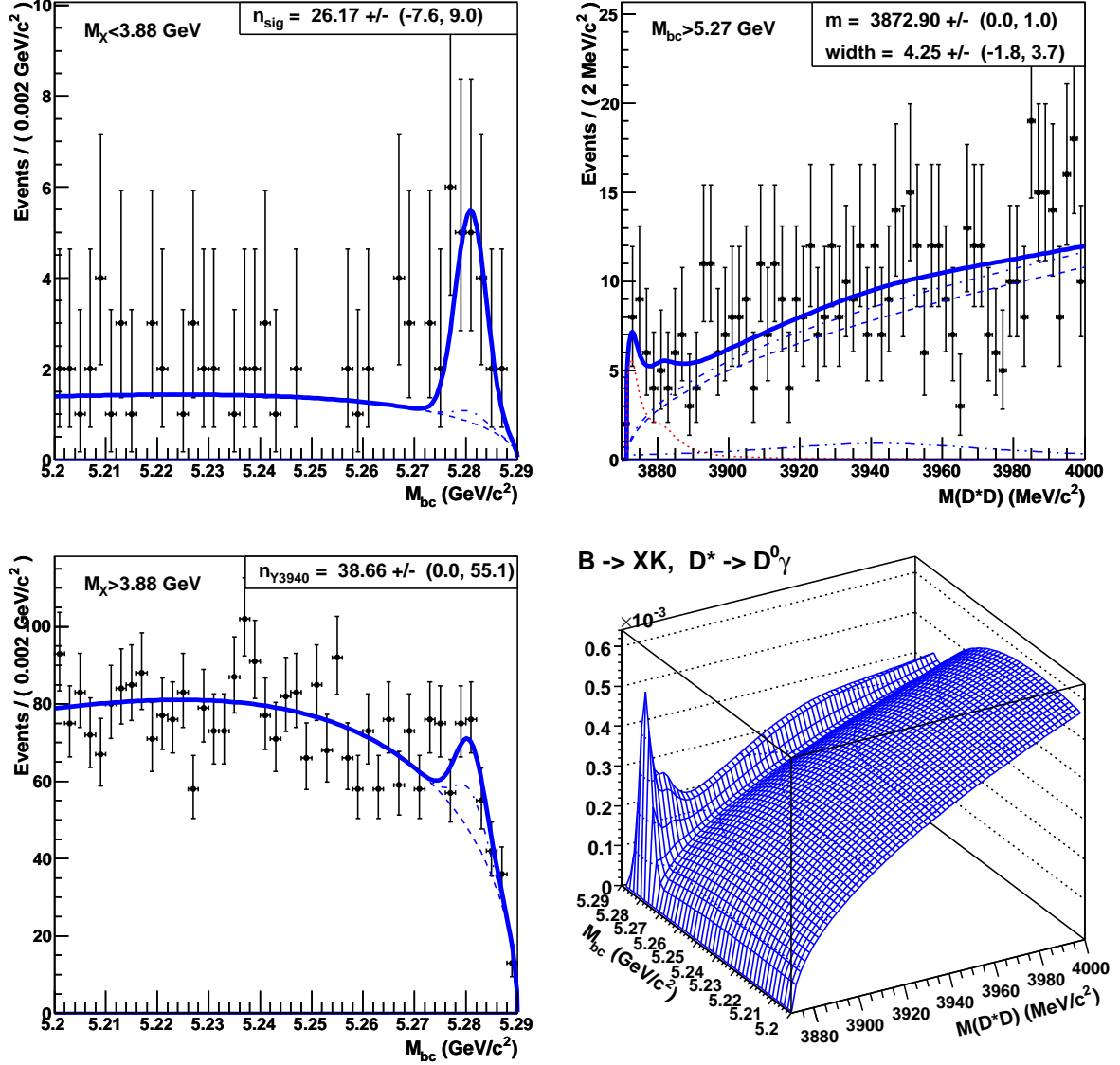
Figure 6.2: Selected events in the $D^0\gamma$ channel. Top left: distribution of $M_{\rm bc}$ for $M_{D^*D} <$ 3.88 GeV/c^2; top right: distribution of M_{D^*D} for $M_{\rm bc} > 5.27$ GeV/c^2; bottom left: distribution of $M_{\rm bc}$ for $M_{D^*D} > 3.88$ GeV/c^2. The points with error bars are data, the dotted curve is the signal, the dashed curve is the background, the dash-dotted curve is the sum of the background and the $B \to D^*DK$ component, the dot-dot-dashed curve is the contribution from the $Y(3940)$, and the solid curve is the total fitting function. Bottom right: three-dimensional view of the fitted pdf (not normalised to data).
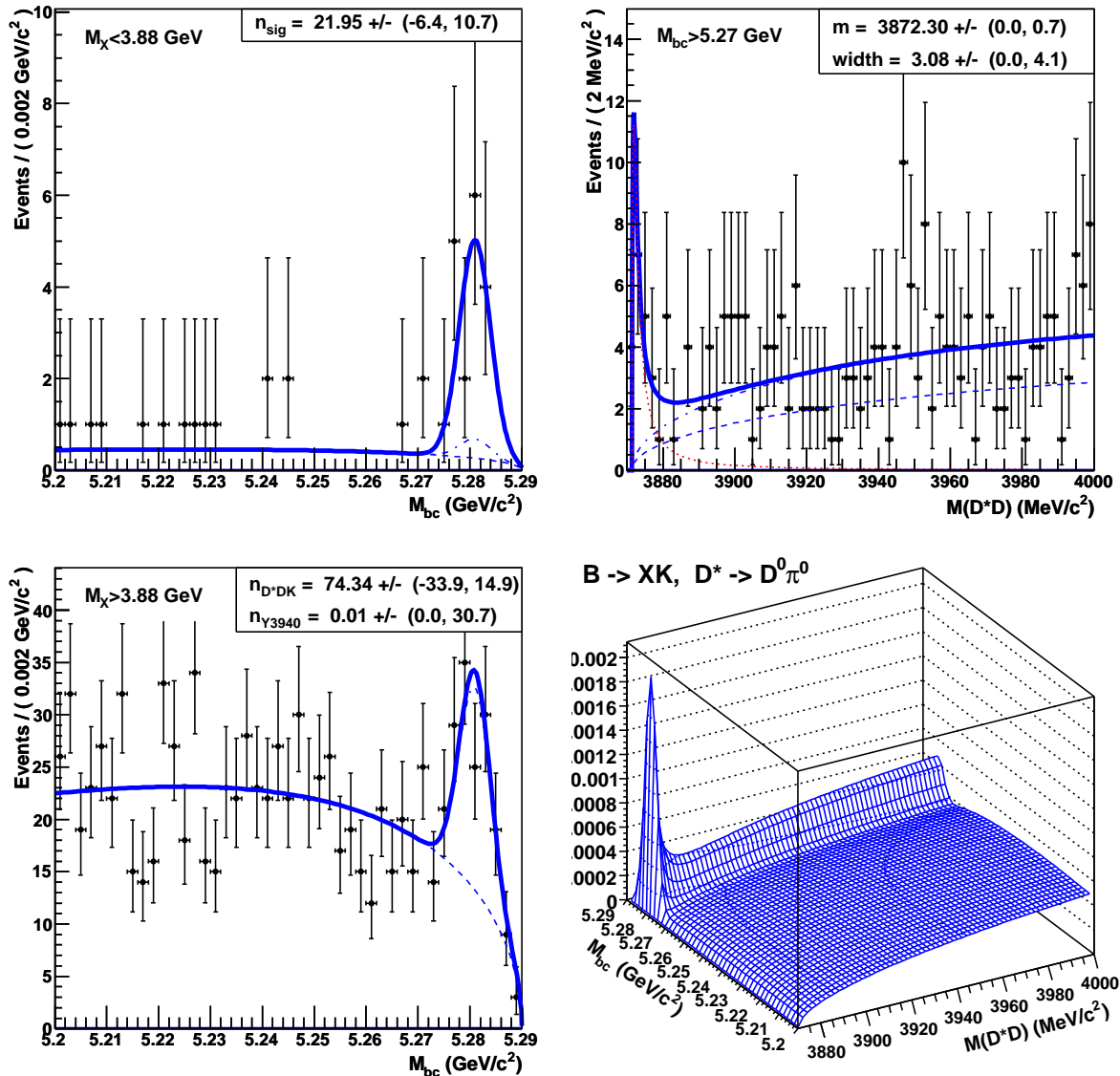
Figure 6.3: Selected events in the $D^0\pi^0$ channel. Top left: distribution of M_{bc} for $M_{D^*D} < 3.88$ GeV/c^2; top right: distribution of M_{D^*D} for $M_{\text{bc}} > 5.27$ GeV/c^2; bottom left: distribution of M_{bc} for $M_{D^*D} > 3.88$ GeV/c^2. The points with error bars are data, the dotted curve is the signal, the dashed curve is the background, the dash-dotted curve is the sum of the background and the $B \to D^*DK$ component, the dot-dot-dashed curve is the contribution from the $Y(3940)$, and the solid curve is the total fitting function. Bottom right: three-dimensional view of the fitted pdf (not normalised to data).
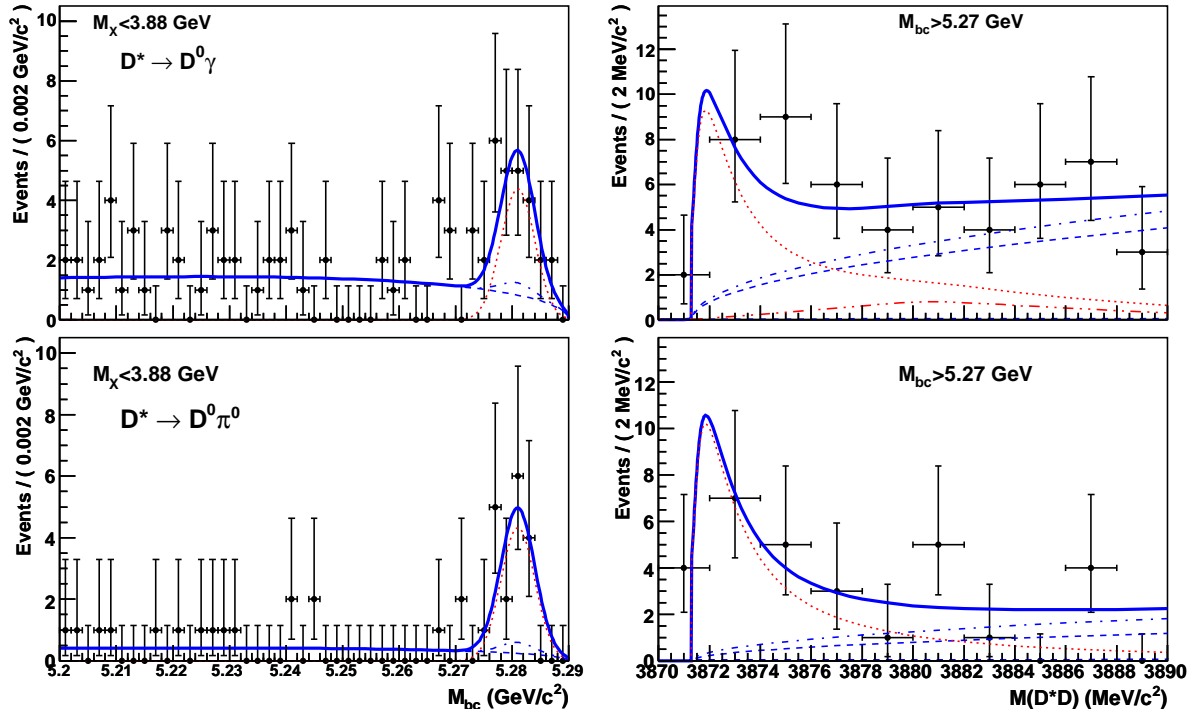
Figure 6.4: Distribution of M_{bc} for $M_{D^*D} < 3.88$ GeV/c^2 (left) and of M_{D^*D} for $M_{\mathrm{bc}} > 5.27$ GeV/c^2 (right); the top row is for $D^{*0} \to D^0\gamma$ and the bottom row for $D^{*0} \to D^0\pi^0$. The points with error bars are data, the dotted curve is the signal, the dashed curve is the background, the dash-dotted curve is the sum of the background and the $B \to D^*DK$ component, the dot-dot-dashed curve is the contribution from D^0–$\bar{D}^0$ reflections, and the solid curve is the total fitting function. The $D^0\gamma/D^0\pi^0$ yield ratio is left free.
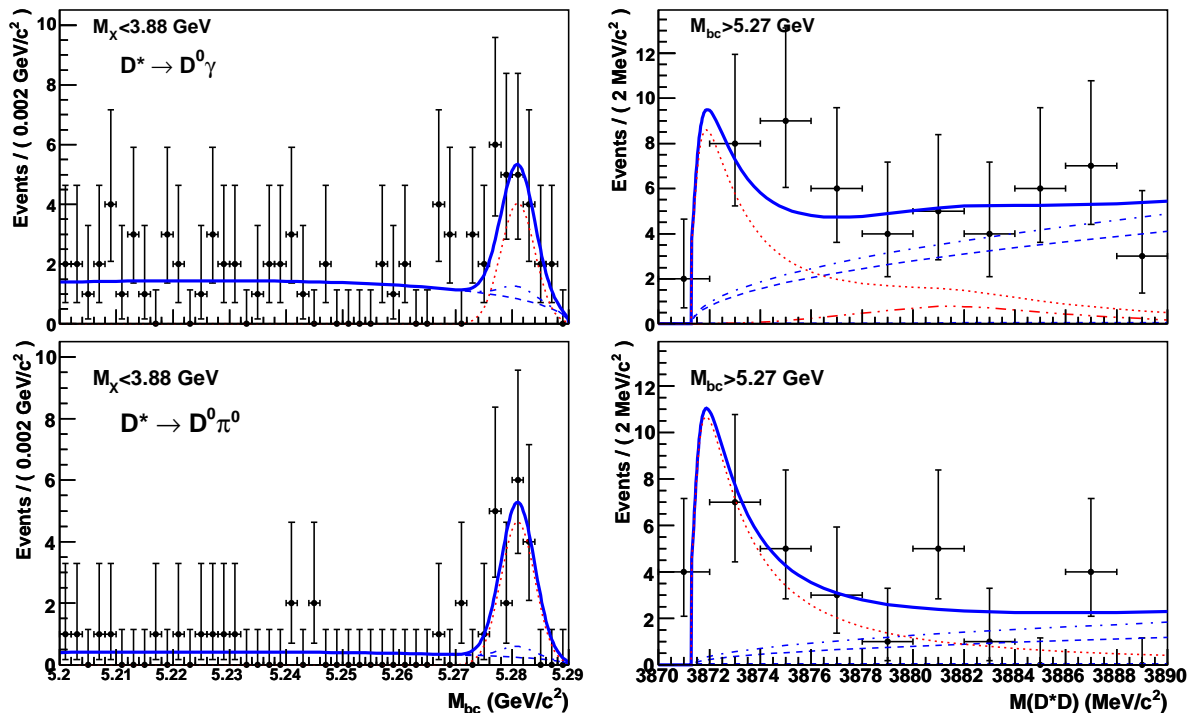
Figure 6.5: Distribution of M_{bc} for $M_{D^*D} < 3.88$ GeV/c^2 (left) and of M_{D^*D} for $M_{\mathrm{bc}} > 5.27$ GeV/c^2 (right); the top row is for $D^{*0} \to D^0\gamma$ and the bottom row for $D^{*0} \to D^0\pi^0$. The points with error bars are data, the dotted curve is the signal, the dashed curve is the background, the dash-dotted curve is the sum of the background and the $B \to D^*DK$ component, the dot-dot-dashed curve is the contribution from D^0–$\bar{D}^0$ reflections, and the solid curve is the total fitting function. The $D^0\gamma/D^0\pi^0$ yield ratio is fixed from MC.
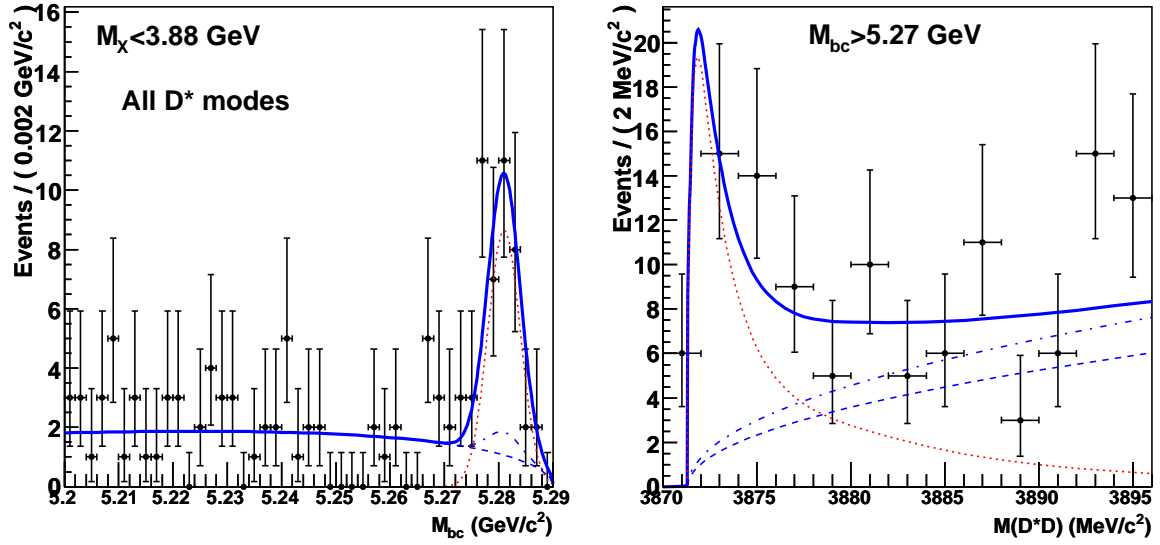
Figure 6.6: Distribution of $M_{\rm bc}$ for $M_{D^*D} < 3.88$ GeV/c^2 (left) and of M_{D^*D} for $M_{\rm bc} > 5.27$ GeV/c^2 (right), for the sum of both D^{*0} modes. The points with error bars are data, the dotted curve is the signal, the dashed curve is the background, the dash-dotted curve is the sum of the background and the $B \to D^*DK$ component and the solid curve is the total fitting function.
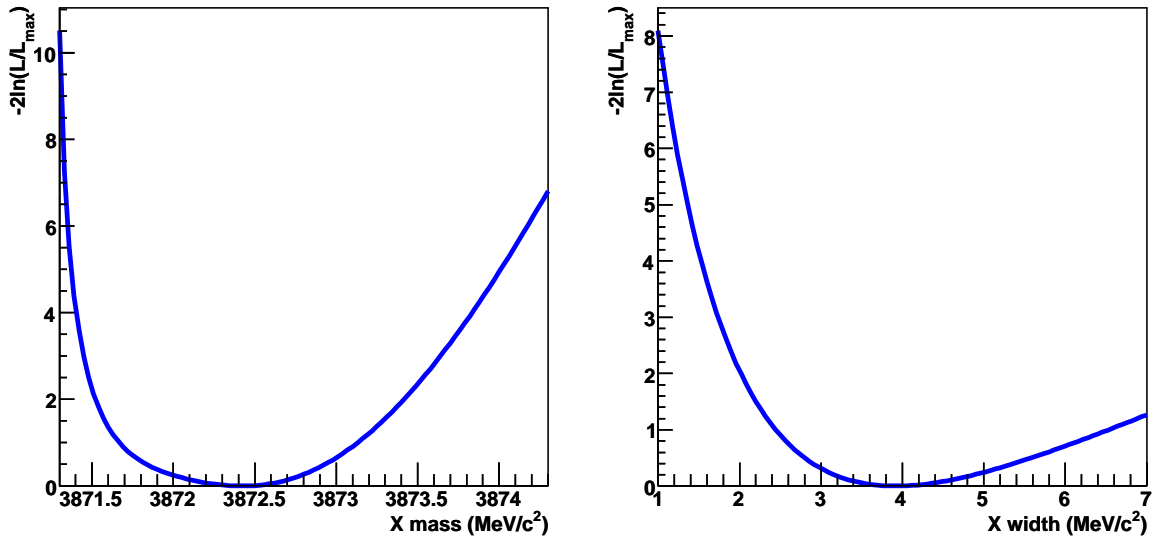
Figure 6.7: $-2\ln(\mathcal{L}/\mathcal{L}_{\rm max})$ as a function of the $X(3872)$ mass (left) and width (right).

sample	m (MeV/c^2)	Γ (MeV/c^2)	yield	significance
$D^{*0} \to D^0\gamma$	3872.9 ± 1.0	$4.2\,^{+3.7}_{-1.8}$	$26.2\,^{+9.0}_{-7.6}$	4.4σ
$D^{*0} \to D^0\pi^0$	3872.3 ± 0.7	$3.1\,^{+4.1}_{-1.5}$	$22.0\,^{+10.7}_{-6.4}$	6.8σ
all (free $D^0\gamma/D^0\pi^0$ ratio)	$3872.4\,^{+0.6}_{-0.4}$	$3.9\,^{+2.7}_{-1.4}$	$50.6\,^{+14.2}_{-11.0}$	7.9σ
all (fixed $D^0\gamma/D^0\pi^0$ ratio)	$3872.4\,^{+0.6}_{-0.4}$	$3.9\,^{+2.8}_{-1.4}$	$50.1\,^{+14.8}_{-11.1}$	7.9σ
$B^+ \to XK^+$	fixed	fixed	$41.3\,^{+9.1}_{-8.1}$	7.6σ
$B^0 \to XK^0_S$	fixed	fixed	$8.4\,^{+4.5}_{-3.6}$	2.8σ

Table 6.1: Summary of 2D fit results.
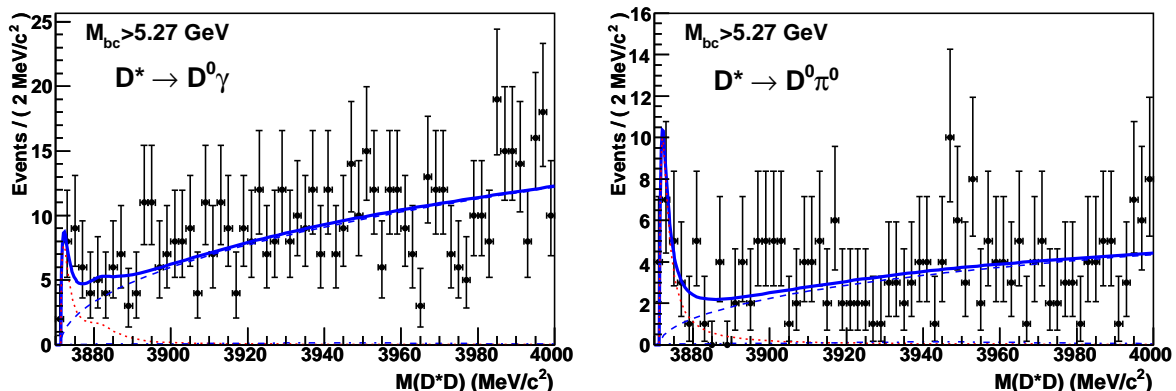
Figure 6.8: Distribution of M_{D^*D} for $M_{\mathrm{bc}} > 5.27$ GeV/c^2, for selected events in the $D^{*0} \to D^0\gamma$ (left) and $D^{*0} \to D^0\pi^0$ channel (right). The points with error bars are data, the dotted curve is the signal, the dashed curve is the sum of the background and the $B \to D^*DK$ component, the dash-dotted curve is the contribution from the $Y(3940)$, and the solid curve is the total fitting function.

Upper limit on the $Y(3940)$ yield

We don't observe any significant contribution from the $Y(3940)$; the simultaneous fit gives $7 \pm 21 \pm 4$ $Y(3940)$ events in total (Figure 6.8). We set an upper limit at 90% confidence level (CL) on the yield N_{lim} by integrating the likelihood of the fit to 90% according to

$$\int_0^{N_{\mathrm{lim}}} \mathcal{L}(N)\mathrm{d}N = 0.9 \int_0^1 \mathcal{L}(N)\mathrm{d}N$$

(see Figure 6.9). We find an upper limit of 40 events at 90% CL.

6.1.4   Fits to charged and neutral B modes

Next we fit the $B^+ \to X(3872)K^+$ and $B^0 \to X(3872)K^0_S$ modes separately. We fix the $X(3872)$ mass and width to the values obtained with the simultaneous fit in Section 6.1.3,
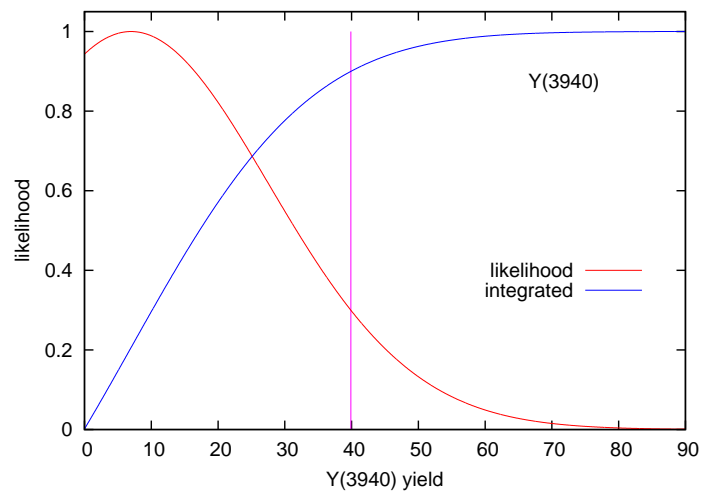
Figure 6.9: Upper limit on the $Y(3940)$ yield. The red curve is the likelihood of the fit as a function of the $Y(3940)$ yield, and the blue curve is the normalised integrated likelihood. The vertical line shows the position of the upper limit at 90% CL.

since in the neutral B mode the statistics are not sufficient to allow the fit of these parameters. Figures 6.10 and 6.11 and Table 6.1 contain the results of these fits.
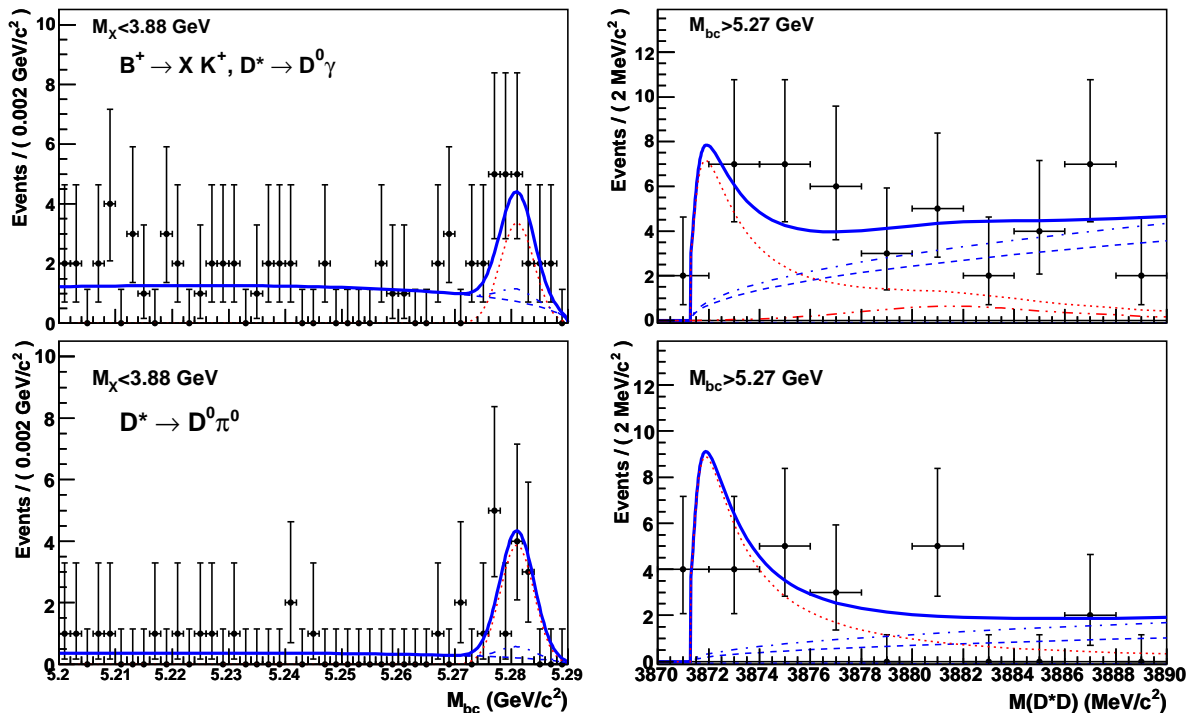
Figure 6.10: Distribution of $M_{\rm bc}$ for $M_{D^*D} < 3.88$ GeV/c^2 (left) and of M_{D^*D} for $M_{\rm bc} > 5.27$ GeV/c^2 (right); the top row is for $D^{*0} \to D^0\gamma$ and the bottom row for $D^{*0} \to D^0\pi^0$. The points with error bars are selected events in the $B^+ \to X(3872)K^+$ channel, the dotted curve is the signal, the dashed curve is the background, the dash-dotted curve is the sum of the background and the $B \to D^*DK$ component, the dot-dot-dashed curve is the contribution from D^0–$\bar{D}^0$ reflections, and the solid curve is the total fitting function.
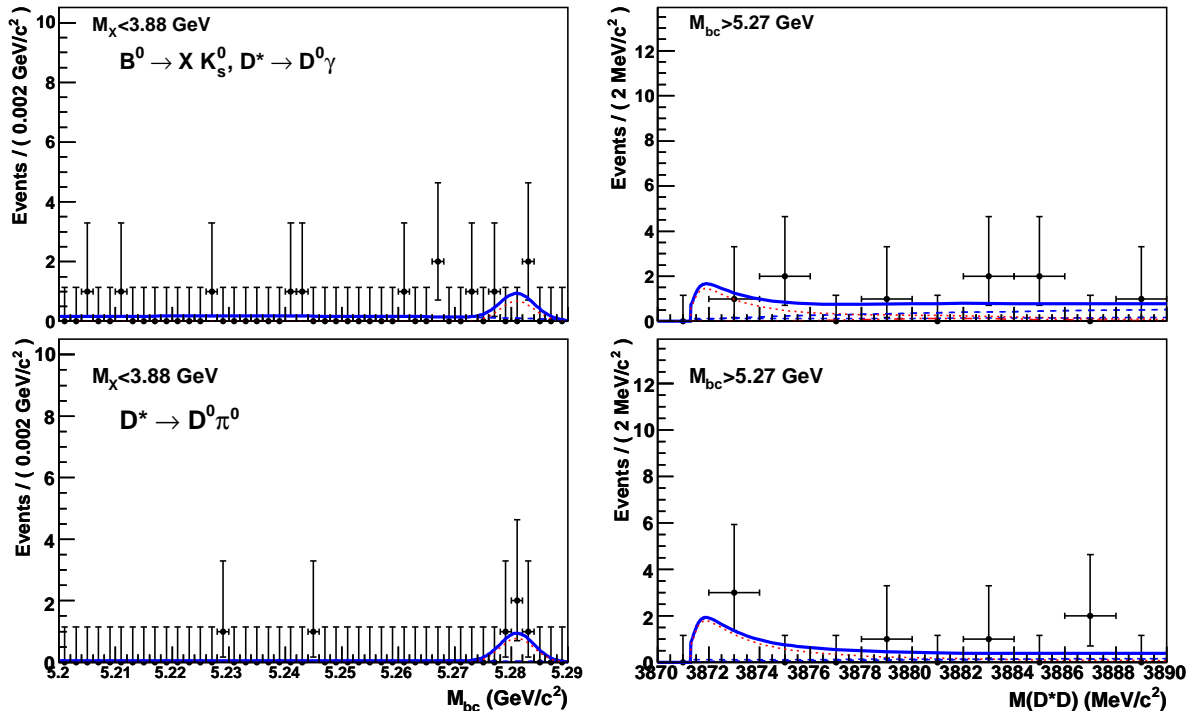
Figure 6.11: Distribution of M_{bc} for $M_{D^*D} < 3.88$ GeV/c^2 (left) and of M_{D^*D} for $M_{\mathrm{bc}} > 5.27$ GeV/c^2 (right); the top row is for $D^{*0} \to D^0\gamma$ and the bottom row for $D^{*0} \to D^0\pi^0$. The points with error bars are selected events in the $B^0 \to X(3872)K_S^0$ channel, the dotted curve is the signal, the dashed curve is the background, the dash-dotted curve is the sum of the background and the $B \to D^*DK$ component, the dot-dot-dashed curve is the contribution from D^0–$\bar{D}^0$ reflections, and the solid curve is the total fitting function.

6.2 Checks

In this section we perform several checks to validate our results. First we look at the D^{*0} sidebands to make sure that they don't contain any significant signal. Then we compare our results with the previous ones published by Belle in the $B \to D^0 \bar{D}^0 \pi^0 K$ channel and check for consistency. Finally, we perform another fit to the data, using the Flatté distribution instead of the Breit-Wigner function to describe the signal.

6.2.1 D^{*0} sidebands

$D^{*0} \to D^0 \gamma$ sidebands

We use the $D^{*0} \to D^0 \gamma$ sidebands to check our results. We consider two sidebands, on each side of the nominal D^{*0} mass. The lower sideband corresponds to the $D^0 \gamma$ invariant mass range 1951 ± 27.5 MeV/c^2, and the upper one to the range 2063 ± 27.5 MeV/c^2. No signal from $X(3872)$ is expected in the upper sideband, as this mass region is below the $X(3872)$ mass threshold. The lower sideband could contain non-resonant $X(3872) \to D^0 \bar{D}^0 \gamma$ signal, hence using $D^{*0} \to D^0 \gamma$ sidebands could in principle help to distinguish between resonant or non-resonant signal. Signal in one of the sidebands could also be due to some other state decaying to $D^0 \bar{D}^0 \gamma$, or to some bias in the reconstruction procedure.

Candidates in the lower and upper sidebands are reconstructed using the standard procedure, except that in the D^{*0} mass-constrained fit, the mass is constrained to the center of the mass range. The same mass window cut of ± 27.5 MeV/c^2 is applied around the constrained mass, and for the best candidate selection the term $\frac{\Delta(M_{D^{*0}} - M_{D^0})}{\sigma_{M_{D^{*0}} - M_{D^0}}}$ of Eq. (4.4) is also computed around the constrained mass.

Figures 6.12 and 6.13 show the results of two-dimensional fits to M_{bc} and M_{D^*D} in the D^{*0} lower and upper sidebands, respectively. The mass and width of the $X(3872)$ are fixed to 3872.4 MeV/c^2 and 3.9 MeV/c^2, respectively. No significant signal is observed in any of the sidebands: the fits give 0 ± 2 events for the lower sideband, and 5.0 ± 4.6 events for the upper sideband, with a statistical significance of 0.8σ.

$D^{*0} \to D^0 \pi^0$ sideband

We also look at the $D^{*0} \to D^0 \pi^0$ sideband. In this case, only the upper sideband is accessible, since the $D^0 \pi^0$ threshold at 1999.6 MeV/c^2 is just 7 MeV/c^2 below the nominal D^{*0} mass. The upper sideband corresponds to the $D^0 \pi^0$ invariant mass range 2032 ± 6 MeV/c^2.

Figure 6.14 shows the result of a two-dimensional fit to M_{bc} and M_{D^*D} in the $D^{*0} \to D^0 \pi^0$ sideband. The mass and width of the $X(3872)$ are fixed to 3872.4 MeV/c^2 and 3.9 MeV/c^2, respectively. The fit gives 9.2 ± 4.7 events with a statistical significance of 2.8σ; these events could be non-resonant $X(3872) \to D^0 \bar{D}^0 \pi0$ decays.
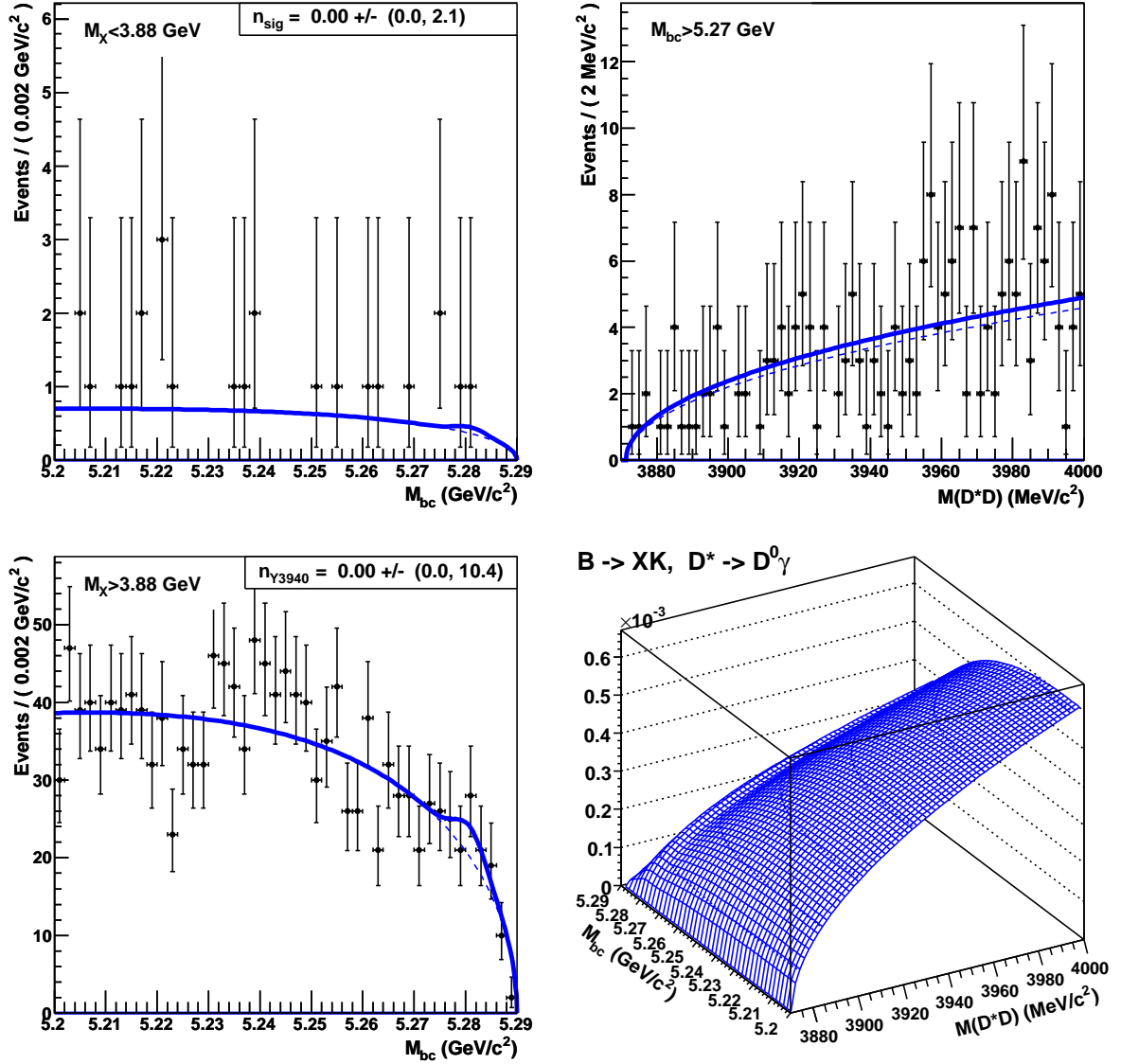
Figure 6.12: Selected events in the lower $D^{*0} \to D^0\gamma$ sideband. Top left: distribution of $M_{\rm bc}$ for $M_{D^*D} < 3.88$ GeV$/c^2$; top right: distribution of M_{D^*D} for $M_{\rm bc} > 5.27$ GeV$/c^2$; bottom left: distribution of $M_{\rm bc}$ for $M_{D^*D} > 3.88$ GeV$/c^2$. The points with error bars are data, the solid curve is the total fitting function, and the dashed curve is the background.

Figure 6.13: Selected events in the upper $D^{*0} \to D^0\gamma$ sideband. Top left: distribution of M_{bc} for $M_{D^*D} < 3.88$ GeV/c^2; top right: distribution of M_{D^*D} for $M_{\mathrm{bc}} > 5.27$ GeV/c^2; bottom left: distribution of M_{bc} for $M_{D^*D} > 3.88$ GeV/c^2. The points with error bars are data, the solid curve is the total fitting function, and the dashed curve is the background.
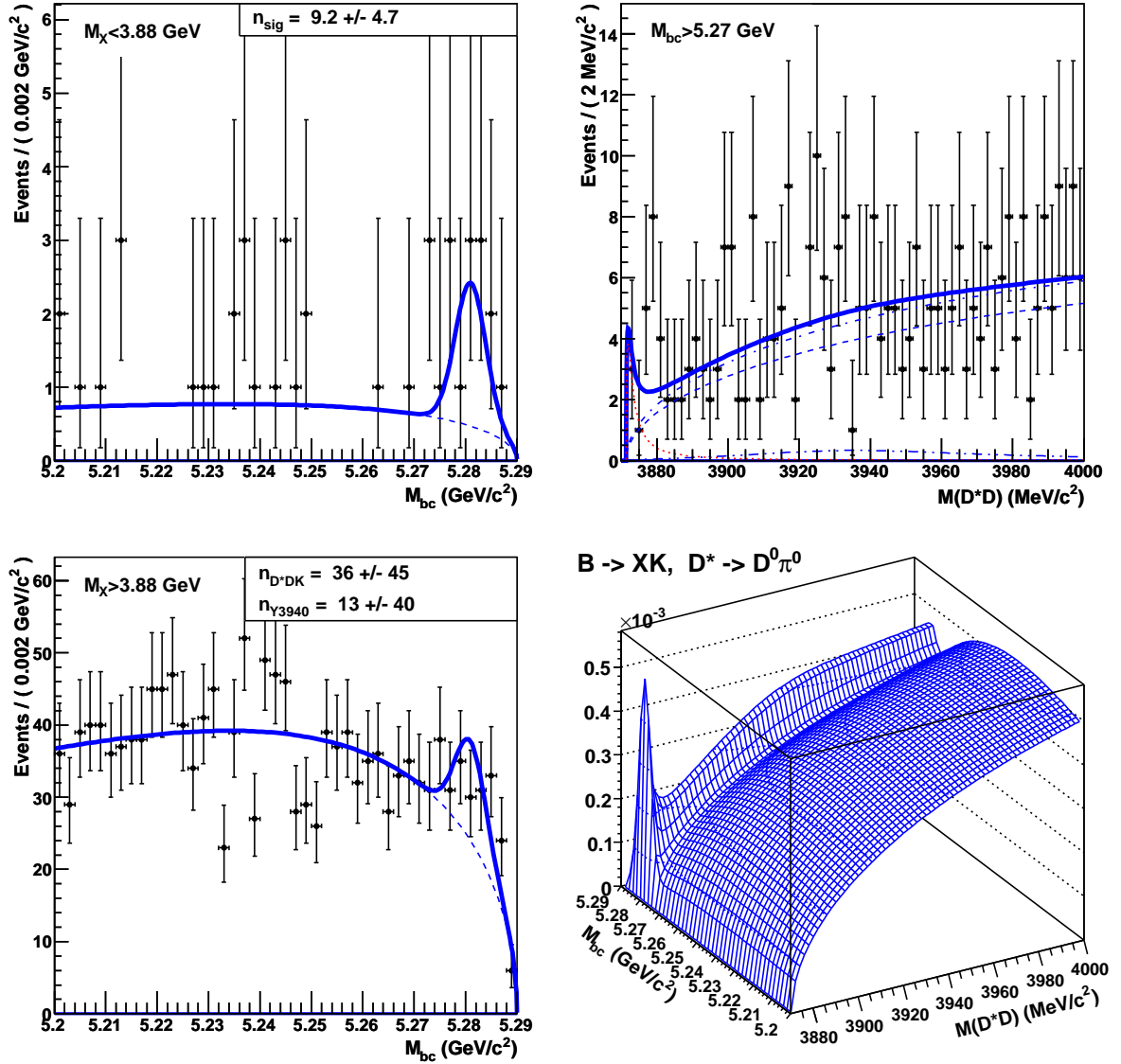
Figure 6.14: Selected events in the $D^{*0} \to D^0\pi^0$ sideband. Top left: distribution of $M_{\rm bc}$ for $M_{D^*D} < 3.88$ GeV$/c^2$; top right: distribution of M_{D^*D} for $M_{\rm bc} > 5.27$ GeV$/c^2$; bottom left: distribution of $M_{\rm bc}$ for $M_{D^*D} > 3.88$ GeV$/c^2$. The points with error bars are data, the dotted curve is the signal, the dashed curve is the background, the dash-dotted curve is the sum of the background and the $B \to D^*DK$ component, the dot-dot-dashed curve is the contribution from the $Y(3940)$, and the solid curve is the total fitting function.

6.2.2   Comparison with the previous Belle result

Next we compare our results with the ones previously obtained by Belle in the $B \to D^0 \bar{D}^0 \pi^0 K$ channel [65]. In this analysis, the signal was described with a single Gaussian function; the $X(3872)$ mass was fitted to 3875.2 ± 0.7 MeV/c^2, which is 1.8σ greater than our result, and a Gaussian width of 2.42 ± 0.55 MeV/c^2 was obtained. The equivalent Breit-Wigner width is 5.7 ± 1.3 MeV/c^2 (using $\Gamma_{\text{BW}} = 2.355 \, \Gamma_{\text{Gauss}}$), which is compatible with our result. Figure 6.15 shows the result of a fit where the mass and width are fixed to these values. The obtained signal yield is $48.5^{+10.1}_{-9.2}$ events, which is very consistent with our result. The statistical significance is 7.0σ.
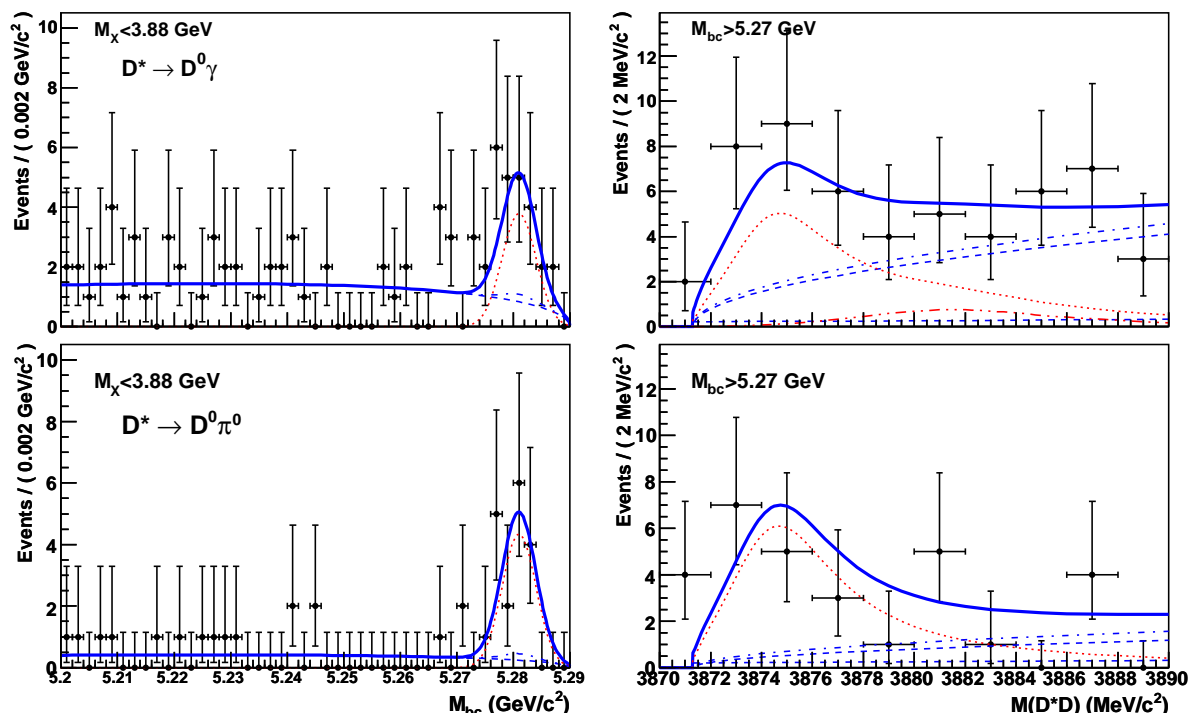
Figure 6.15: Distribution of M_{bc} for $M_{D^*D} < 3.88$ GeV/c^2 (left) and of M_{D^*D} for $M_{\text{bc}} > 5.27$ GeV/c^2 (right); the top row is for $D^{*0} \to D^0\gamma$ and the bottom row for $D^{*0} \to D^0\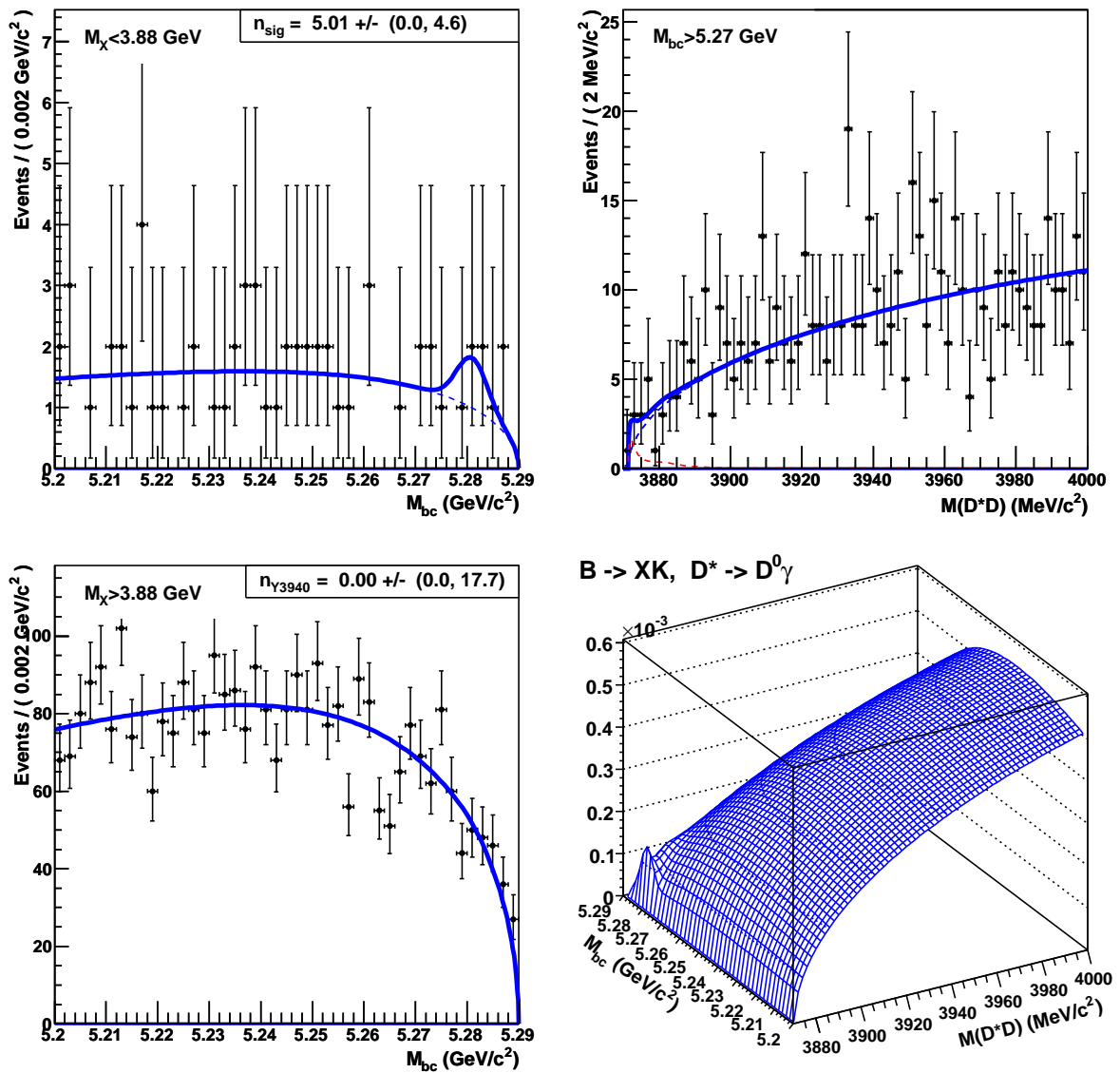pi^0$. The points with error bars are data, the dotted curve is the signal, the dashed curve is the sum of the background and the $B \to D^*DK$ component, the dash-dotted curve is the contribution from the $Y(3940)$, and the solid curve is the total fitting function. Here the $X(3872)$ mass is fixed to 3875.2 MeV/c^2 and the width to 5.7 MeV/c^2.

6.2.3   Fit with Flatté distribution

We perform an alternative fit to the data, using a Flatté distribution instead of the Breit-Wigner function. This distribution is described in details in Ref. [52]. The authors of this paper attempt to reconcile the near-threshold enhancement in the $D^0\bar{D}^0\pi^0$ final state observed by Belle at a mass of approximately 3875 MeV/c^2 [21] with the $X(3872)$ observed in the $J/\psi \, \pi^+\pi^-$ mode [17]. They assume that the nominal $X(3872)$ mass is below the

$D^{*0}\bar{D}^0$ threshold; thus only the high-mass tail of the mass distribution contributes to the $X(3872) \to D^{*0}\bar{D}^0$ decay. They perform a Flatté analysis of the Belle data in the $D^0\bar{D}^0\pi^0$ mode and obtain a peak in the $D^{*0}\bar{D}^0$ mass distribution at 2 ± 3 MeV/c^2 above the $D^{*0}\bar{D}^0$ threshold, with a distinctive non-Breit-Wigner shape.

Description of Flatté parametrization

This section describes the implementation of the Flatté parametrization used to fit the signal. The pdf is taken from Eq. (19) of Ref. [52]:

$$f(E) = \frac{gk_1}{|D(E)|^2} \tag{6.2}$$

with

$$D(E) = \begin{cases} E - E_f - \frac{1}{2}g\kappa + \frac{i}{2}\left(gk_1 + \Gamma(E)\right), & 0 < E < \delta \\ E - E_f + \frac{i}{2}\left(g(k_1 + k_2) + \Gamma(E)\right), & E > \delta \end{cases}$$

and

$$\delta = m_{D^+} + m_{D^{*-}} - m_{D^{*0}} - m_{\bar{D}^0},$$

$$k_1 = \sqrt{2\mu_1 E}, \quad k_2 = \sqrt{2\mu_2(E - \delta)}, \quad \kappa = \sqrt{2\mu_2(\delta - E)},$$

where μ_1 and μ_2 are the reduced masses in the $D^{*0}\bar{D}^0$ and D^+D^{*-} channels, respectively, and the energy E is defined relative to the $D^{*0}\bar{D}^0$ threshold, so that $E = M - m_{D^0} - m_{D^{*0}}$; g and E_f are free parameters.

The width $\Gamma(E)$ has contributions from the $\rho J/\psi$ and $\omega J/\psi$ channels, so that

$$\Gamma(E) = \Gamma_{\pi\pi J/\psi}(E) + \Gamma_{\pi\pi\pi^0 J/\psi}(E), \tag{6.3}$$

$$\Gamma_{\pi\pi J/\psi}(E) = f_\rho \int_{2m_\pi}^{M - m_{J/\psi}} \frac{\mathrm{d}m}{2\pi} \frac{q(m)\Gamma_\rho}{(m - m_\rho)^2 + \Gamma_\rho^2/4}, \tag{6.4}$$

$$\Gamma_{\pi\pi\pi^0 J/\psi}(E) = f_\omega \int_{3m_\pi}^{M - m_{J/\psi}} \frac{\mathrm{d}m}{2\pi} \frac{q(m)\Gamma_\omega}{(m - m_\omega)^2 + \Gamma_\omega^2/4}, \tag{6.5}$$

$$q(m) = \frac{\sqrt{(M^2 - (m + m_{J/\psi})^2)(M^2 - (m - m_{J/\psi})^2)}}{2M},$$

where $M = E + m_{D^0} + m_{D^{*0}}$ and $m_\rho, \Gamma_\rho, m_\omega, \Gamma_\omega$ are the nominal masses and widths of the $\rho(770)$ and $\omega(782)$ particles, respectively. f_ρ is a free parameter; f_ω is proportional to f_ρ. The two integrals in Eq. (6.4) and (6.5) were computed numerically. Figure 6.16 shows the shape of these integrals. $\Gamma_{\pi\pi J/\psi}(E)$ (left) is very smooth and can be described with a second order polynomial. $\Gamma_{\pi\pi\pi^0 J/\psi}(E)$ (right) is approximated using a look-up table with linear interpolation. The relative error of these approximations is less than 10^{-4}.

As a check, the pdf is shown on Figure 6.17 with the Flatté parameters obtained by the authors of Ref. [52] for their best fit of Belle data: $g = 0.3, E_f = -11$ MeV, $f_\rho = 0.007$. The shape is as expected. The slight difference which occurs mainly in the tail could be due to different nominal masses of the D and D^* mesons. The drop at around $E = 8$ MeV is due to the $D^{*+}D^-$ threshold.

In this distribution, the $X(3872)$ mass and width are not parameters. Figure 6.18 shows the effect of the three parameters g, E_f and f_ρ on the shape: g and E_f affect the
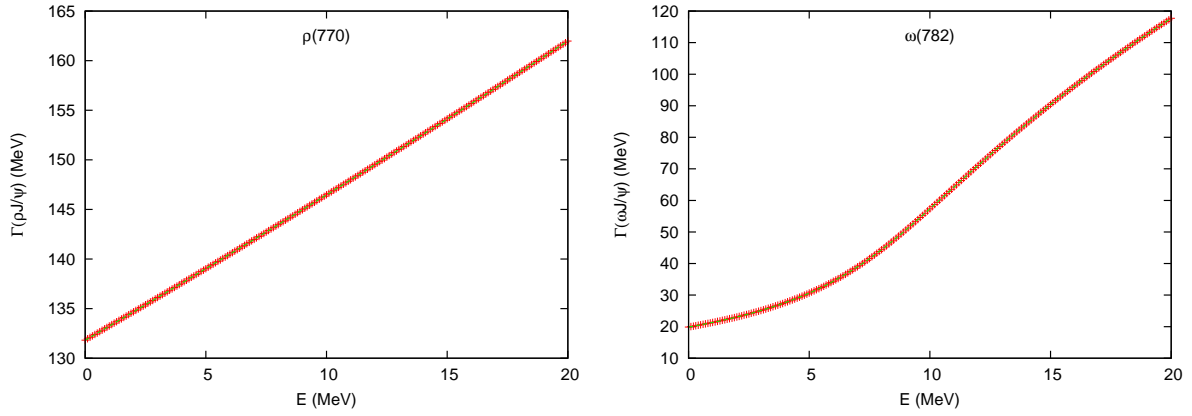
Figure 6.16: Left: $\Gamma_{\pi\pi J/\psi}(E)$, right: $\Gamma_{\pi\pi\pi^0 J/\psi}(E)$. The red crosses are the results of a numerical computation, and the curves are the approximations described in the text.
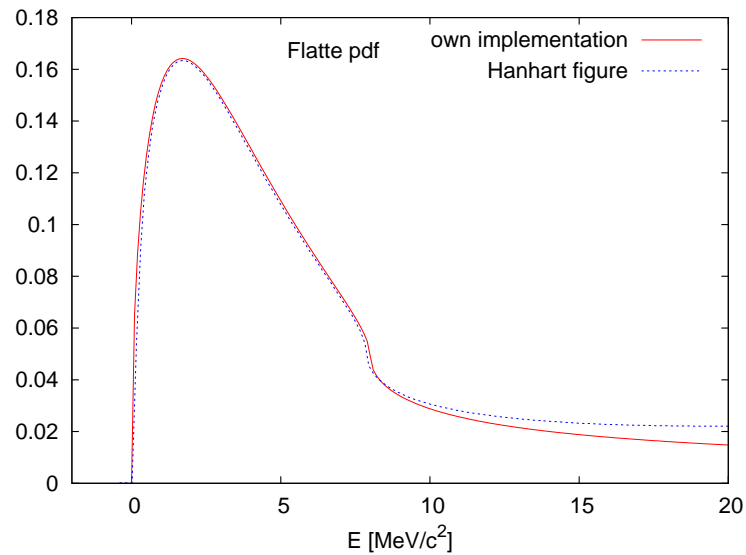
Figure 6.17: Flatté distribution. Solid red: own implementation; dotted blue: shape taken from Ref. [52] for comparison.
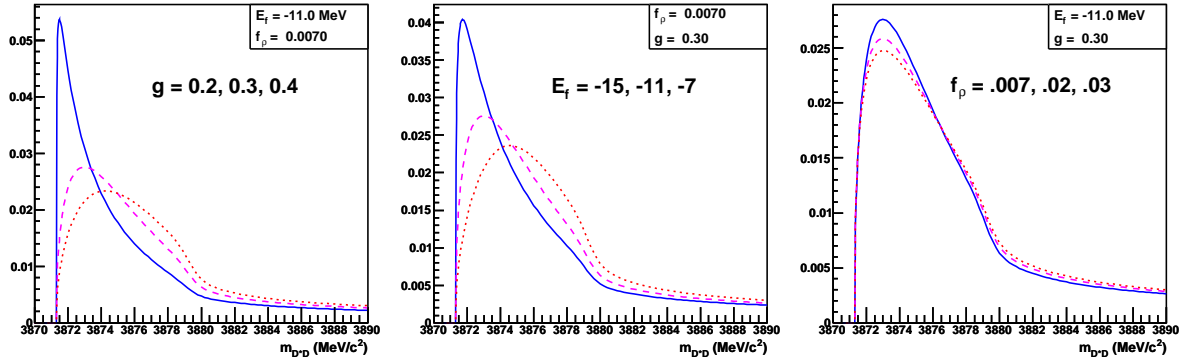
Figure 6.18: Effect of varying the Flatté parameters g (left), E_f (center) and f_ρ (right). The distribution is shown for three different values of each parameter. In each plot, the solid blue line corresponds to the first quoted value of the parameter, the dashed purple line to the second and the dotted red line to the third value.

peak position and width; their effects are correlated. f_ρ affects the peak/tail ratio and is strongly correlated to the numbers of signal and background events. Because of these correlations, it is not possible to fit all three parameters without additional information (for example from the $J/\psi\,\pi^+\pi^-$ channel). Thus in the following, only E_f is left free, while we fix $g = 0.3$ and $f_\rho = 0.007$ using the best fit to Belle data from Ref. [52].

To describe the M_{D^*D} signal, the Flatté distribution is convolved with the Gaussian resolution function, as described in Eq. (5.3) for the relativistic Breit-Wigner pdf.

Toy Monte Carlo tests for Flatté distribution

The fitting procedure with a Flatté distribution was also tested using toy Monte Carlo samples. 1280 samples with 1100 events each were generated and fitted. The Flatté parameter E_f is free ($-20 < E_f < 0$), while $g = 0.3$ and $f_\rho = 0.007$ are fixed. Two other variables are the $X(3872)$ yield and the $Y(3940)$ yield.

Figure 6.19 shows the distribution of residuals, errors, pulls, and the linearity tests (comparison of generated and fitted values) for these three parameters. The tests are successful, except for the E_f pull distribution, which is slightly narrower than a standard normal distribution. For the linearity tests, we fit the fitted values as a function of the generated ones using a first-order polynomial, and the results are consistent with the identity function.

Simultaneous fit with Flatté distribution

In Figure 6.20, the data candidates are fitted with the Flatté distribution, simultaneously in the $D^0\gamma$ and $D^0\pi^0$ channels, with fixed $D^0\gamma/D^0\pi^0$ yield ratio. The Flatté parameter E_f is free, while $g = 0.3$ and $f_\rho = 0.007$ are fixed.

The fitted yield is 63.5 ± 12.0 events with a significance of 8.8σ. We obtain $E_f = -14.9 \pm 2.0$ MeV, which is close to the value -11 MeV found in Ref. [52].

Table 6.2 gives a comparison of Breit-Wigner and Flatté fit results, including χ^2 values. These values are computed over 2925 bins, separately for each D^{*0} channel. Since the
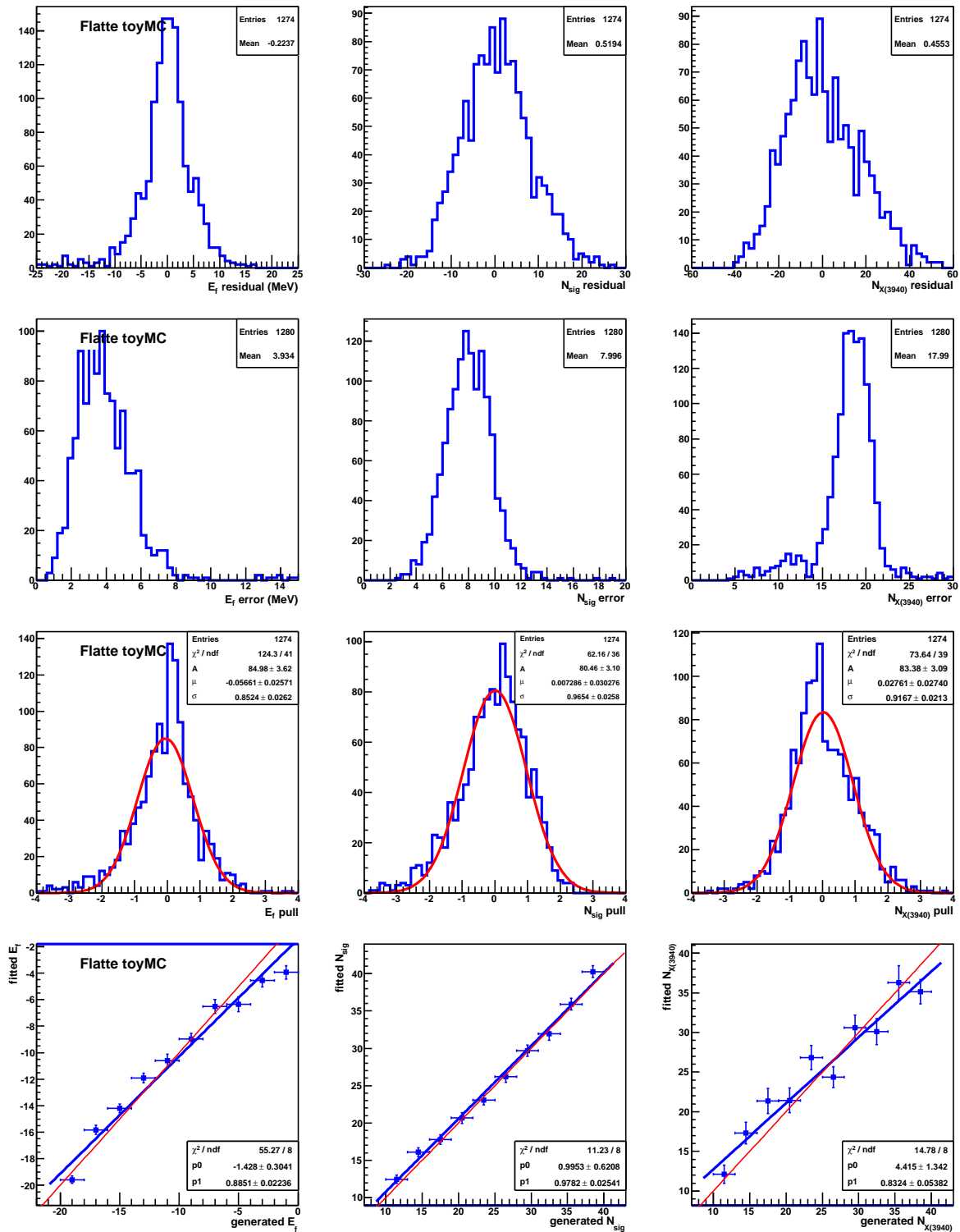
Figure 6.19: Toy MC tests: distributions of residuals (first row), errors (second row), pulls fitted with a single Gaussian function (third row), and linearity checks (bottom row) for the variables E_f, $X(3872)$ yield and $Y(3940)$ yield, using the Flatté distribution to describe the $X(3872)$ signal.
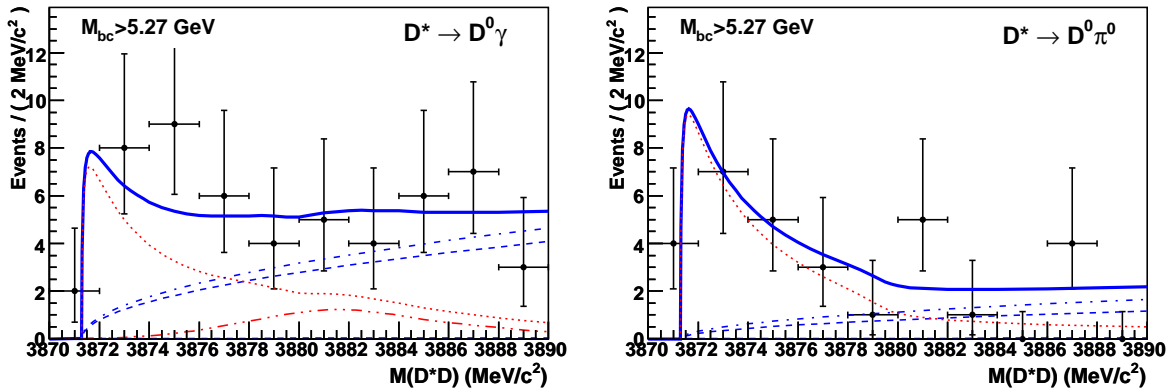
Figure 6.20: Distribution of M_{D^*D} for $M_{\mathrm{bc}} > 5.27$ GeV/c^2, for $D^{*0} \rightarrow D^0\gamma$ (left) and $D^{*0} \rightarrow D^0\pi^0$ (right). The points with error bars are data, the dotted red curve is the Flatté distribution, the dashed curve is the background, the dash-dotted curve is the sum of the background and the $B \rightarrow D^*DK$ component, the dot-dot-dashed curve is the contribution from D^0–$\bar{D}^0$ reflections, and the solid curve is the total fitting function.

shape	yield		signif.	χ^2	
	full region	signal region		$D^0\gamma$	$D^0\pi^0$
Breit-Wigner	$50.1\,^{+14.8}_{-11.1}$	32.1 ± 7.2	7.9σ	1644.8	847.7
Flatté	63.5 ± 12.0	32.8 ± 6.2	8.8σ	1644.3	847.9

Table 6.2: Comparison of Breit-Wigner and Flatté fit results. The signal region corresponds to $M_{D^*D} < 3880$ MeV/c^2.

fits are log-likelihood fits, these χ^2 values are not optimized. The yield obtained from the fit with the Flatté distribution is larger than the one obtained from the Breit-Wigner fit, because the Flatté distribution has a long much longer tail. Computing the yield in the signal region ($M_{D^*D} < 3.88$ GeV/c^2) in both cases gives consistent results. The significance and χ^2 of the two fit methods are very similar; from these values it is not possible to determine which function fits the data best.

6.3   Systematic uncertainties

6.3.1   Systematic uncertainties on $X(3872)$ mass, width and yield

The systematic uncertainties for the $X(3872)$ mass, width and signal yield are estimated by varying some of the parameters in the simultaneous fit with fixed yield ratio. We consider the following variations:

- Fixing the contribution from the $Y(3940)$ to its lower limit (zero events) or to its upper limit (40 events).

- Fixing the $Y(3940)$ mass and width to the values measured by BaBar ($3914.6\,{}^{+3.8}_{-3.4}\pm$ 1.9 MeV/c^2 and $34\,{}^{+12}_{-8}\pm 5$ MeV/c^2 [26]) instead of Belle.

- Amplifying the resolution function by a factor 0.8 or 1.2, to account for a possibly worse $X(3872)$ mass resolution in data than in Monte Carlo. This variation covers the data/MC resolution ratio of 1.14 ± 0.04 obtained in Section A.3.3.

- Using the $D^0\gamma$ reflection shape from the Monte Carlo sample generated with a mass of 3872.0 MeV/c^2 (Figure 5.7) or from the sample generated with a mass of 3873.0 MeV/c^2 (Figure 5.9).

- Fixing the fraction of events in the $D^0\gamma$ peak/reflection to the values of $f_{\mathrm{sig}} = 0.75$ or 0.81 instead of 0.78 ($\pm 3\sigma$ variation).

- Fluctuating the total efficiency fraction $\epsilon^\gamma_{\mathrm{tot}}/\epsilon^{\pi^0}_{\mathrm{tot}}$ within statistical uncertainties.

- Using an inverted ARGUS function instead of the square root function to describe the M_{D^*D} background. The inverted ARGUS function is defined as

$$
f(M) = \exp\left(c\left(1 - \left(\frac{M}{m_0}\right)^2\right)\right)\sqrt{\left(\frac{M}{m_0}\right)^2 - 1},
$$

where m_0 is the $D^{*0}\bar{D}^0$ threshold mass and c is a free slope parameter.

Additional uncertainties are due to the bias from the toy Monte Carlo checks of the fitting pdf (Figure 5.17). We obtain biases of -0.05 MeV/c^2 for the $X(3872)$ mass, $+0.36$ MeV/c^2 for its width, and $+3.7$ events for the $X(3872)$ yield.

We also consider systematic uncertainties due to the fact that we don't include a contribution from D^0-$\bar{D}^0$ reflections in the $D^{*0} \to D^0\pi^0$ channel in our fit of the data. To estimate this uncertainty, we perform a simultaneous fit of both D^{*0} modes in the signal Monte Carlo, where the reflections are included in the $D^{*0} \to D^0\gamma$ channel, but not in the $D^{*0} \to D^0\pi^0$ channel, just like it is done for the data. Figure 6.21 shows the result of this fit. We obtain a bias of -0.30 MeV/c^2 on the $X(3872)$ mass and of -1.0 MeV/c^2 on its width, which we add as systematic uncertainties.

The largest systematic uncertainty on the $X(3872)$ mass is due to the uncertainties on the D^0 and D^{*0} nominal masses [4]. This uncertainty is ± 0.25 MeV/c^2. The uncertainties on the $X(3872)$ mass, width and yield are summarised in Table 6.3.

6.3.2 Systematic uncertainties on branching fraction

The systematic uncertainties for the product branching fraction $\mathcal{B}(B \to X(3872)K to D^{*0}\bar{D}^0 K)$ are estimated from the following sources:

- Limited Monte Carlo statistics to assess the total efficiency.

- Number of $B\bar{B}$ events: $N_{B\bar{B}} = (656.725 \pm 8.940) \times 10^6$.

- D^0 branching fractions: $\beta = 0.2927 \pm 0.0071$ (2.4%).
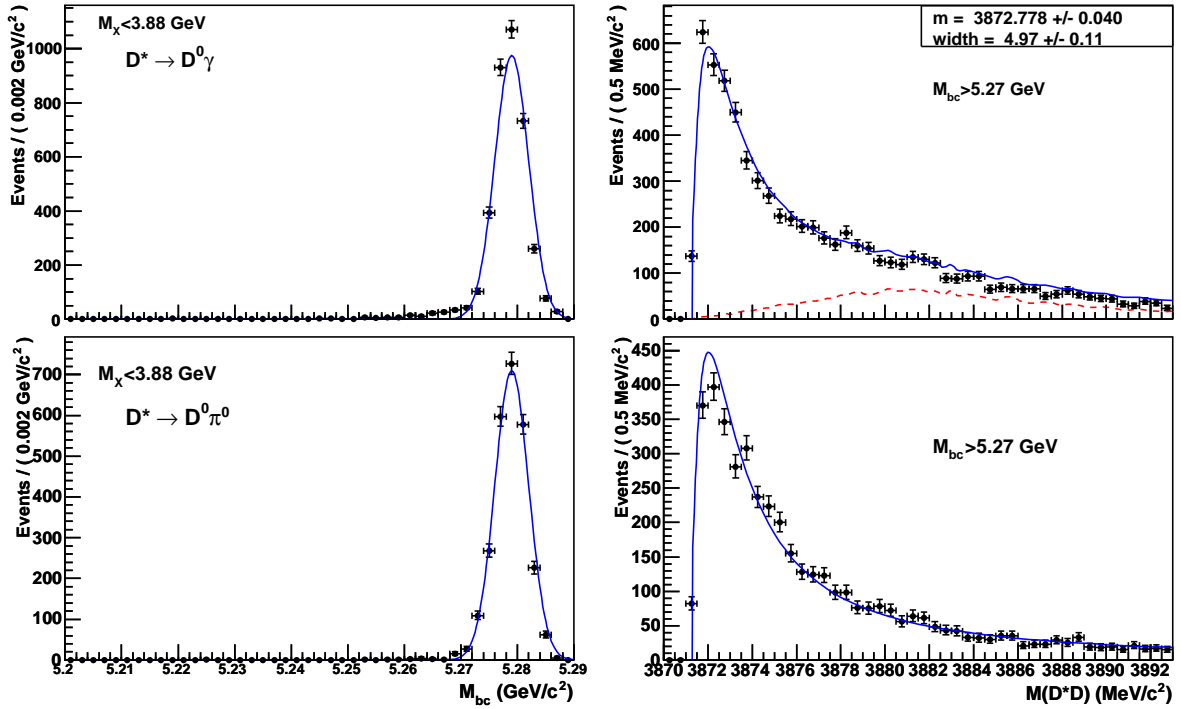
Figure 6.21: Distribution of M_{bc} for $M_{D^*D} < 3.88$ GeV/c^2 (left) and of M_{D^*D} for $M_{bc} > 5.27$ GeV/c^2 (right); the top row is for $D^{*0} \rightarrow D^0\gamma$ and the bottom row for $D^{*0} \rightarrow D^0\pi^0$. The points are selected events using the signal MC sample generated with a mass of 3872.5 MeV/c^2 and a width of 4.0 MeV/c^2; the solid curve is the result of a simultaneous fit including a contribution from D^0–$\bar{D}^0$ reflections only in the $D^0\gamma$ channel (dashed curve). The other signal MC samples give very similar bias.

Source	mass (Mev/c^2)	width (MeV/c^2)	yield
contribution from $Y(3940)$	$+0.01$ -0.00	$+0.08$ -0.07	$+0.76$ -0.60
$Y(3940)$ parameters	$+0.01$	-0.32	-2.13
data/MC resolution	$+0.02$ -0.04	$+0.09$ -0.09	$+0.18$ -0.00
shape of $D^0\gamma$ reflections	$+0.00$ -0.00	$+0.02$ -0.00	$+0.10$ -0.00
peak/reflections fraction	$+0.01$ -0.02	$+0.11$ -0.10	$+0.20$ -0.12
γ/π^0 efficiency ratio	$+0.00$ -0.01	$+0.00$ -0.00	$+0.14$ -0.10
shape of M_{D^*D} background	0.00	-0.14	-1.10
toy MC bias	-0.05	$+0.36$	$+3.7$
signal MC bias	-0.30	-1.00	-
D^0, D^{*0} masses	±0.41	-	-
quadratic sum	$+0.41$ -0.51	$+0.40$ -1.07	$+3.79$ -2.48

Table 6.3: Sources of systematic uncertainties from simultaneous 2D fit: absolute variations for mass, width and yield.

- Track finding efficiencies. This uncertainty was estimated by comparing the yield ratio $r^\eta = N(\eta \to \pi^+\pi^-\pi^0)/N(\eta \to \gamma\gamma)$ in MC and data [66]. They obtain a tracking efficiency ratio between data and MC of

$$\epsilon_{\text{data}}/\epsilon_{\text{MC}} \simeq \sqrt{r^\eta_{\text{data}}/r^\eta_{\text{MC}}} = 0.993 \pm 0.018,$$

 so that the uncertainty on the tracking efficiency is assumed to be 1% per track.

- Kaon and pion identification efficiency. This systematic uncertainty was estimated by studying the decay $D^{*+} \to D^0\pi^+$ followed by $D^0 \to K^-\pi^+$ in data and generic MC [67].

- γ or π^0 detection efficiency. The ratio of π^0 reconstruction efficiency between data and MC is estimated using two methods: first studying the ratio $N(\eta \to 3\pi^0)/N(\eta \to \gamma\gamma)$, second studying $N(\eta \to 3\pi^0)/N(\eta \to \pi^+\pi^-\pi^0)$ [68]. Combining both methods and for a photon energy $E_\gamma > 50$ MeV, they obtain an efficiency ratio of $0.924 \pm 0.009 \pm 0.011$, thus we estimate the systematic uncertainty on the π^0 detection efficiency to be 7.6%. The systematic uncertainty on the photon detection efficiency is estimated from the uncertainty on the π^0 detection efficiency quoted above.

- K^0_S reconstruction efficiency. This systematic uncertainty was estimated by comparing the ratio of the number of $D^+ \to K^0_S\pi^+$ and $D^+ \to K^-\pi^+\pi^+$ events in data and MC [69].

- Systematic uncertainty on the $X(3872)$ yield, discussed in Section 6.3.1. The largest of the positive or negative uncertainty shown in Table 6.3 is used.

These uncertainties are listed in Table 6.4.

Source	uncertainty (%)		reference
	$D^0\gamma$	$D^0\pi^0$	
MC statistics	1.3	1.5	
$N_{B\bar{B}}$	1.4	1.4	
D^0 branching fractions	2.4	2.4	
tracking	5.0	5.0	[66]
particle identification	4.0	4.0	[67]
γ reconstruction	7.0		
π^0 reconstruction		7.6	[68]
K_S^0 reconstruction	4.5	4.5	[69]
fitted yield	7.6	7.6	
total (quadrature)	13.3	13.7	

Table 6.4: Sources of systematic uncertainties for the branching fraction.

6.4   Final results

6.4.1   Final results on the $X(3872)$ mass and width

The analysis presented in this document was performed with nominal D^0 and D^{*0} meson masses of $m_{D^0} = 1864.6$ MeV/c^2 and $m_{D^{*0}} = 2006.7$ MeV/c^2, so that the value of the $D^{*0}\bar{D}^0$ threshold mass is 3871.3 MeV/c^2 (PDG'06 values [70]). From the simultaneous fit with fixed $D^0\gamma/D^0\pi^0$ yield ratio, we obtain an $X(3872)$ mass of $3872.4\,^{+0.6}_{-0.4}$ MeV/c^2 and a width of $3.9\,^{+2.8}_{-1.4}$ MeV/c^2.

This measurement translates to a mass difference between the $X(3872)$ mass and the $D^{*0}\bar{D}^0$ threshold mass of

$$\delta M = M_X - m_{D^{*0}} - m_{D^0} = 1.1\,^{+0.6}_{-0.4}\,^{+0.1}_{-0.3} \text{ MeV}/c^2. \tag{6.6}$$

The values of the nominal D^0 and D^{*0} meson masses were recently updated to $m_{D^0} = 1864.84 \pm 0.17$ MeV/c^2 and $m_{D^{*0}} = 2006.97 \pm 0.19$ MeV/c^2; their mass difference is $\Delta(m_{D^{*0}} - m_{D^0}) = 142.12 \pm 0.07$ MeV/c^2, giving a value of the $D^{*0}\bar{D}^0$ threshold mass of $2m_{D^0} + \Delta(m_{D^{*0}} - m_{D^0}) = 3871.80 \pm 0.41$ MeV/c^2 (PDG'08 values [4]). We assume that our measurement of δM is still valid with these updated values; to check this assumption, we plot the relativistic Breit-Wigner function of Eq. (5.1) for the PDG'06 and PDG'08 values in Figure 6.22, and find the maximal relative difference between the two curves to be approximately 4×10^{-7}.
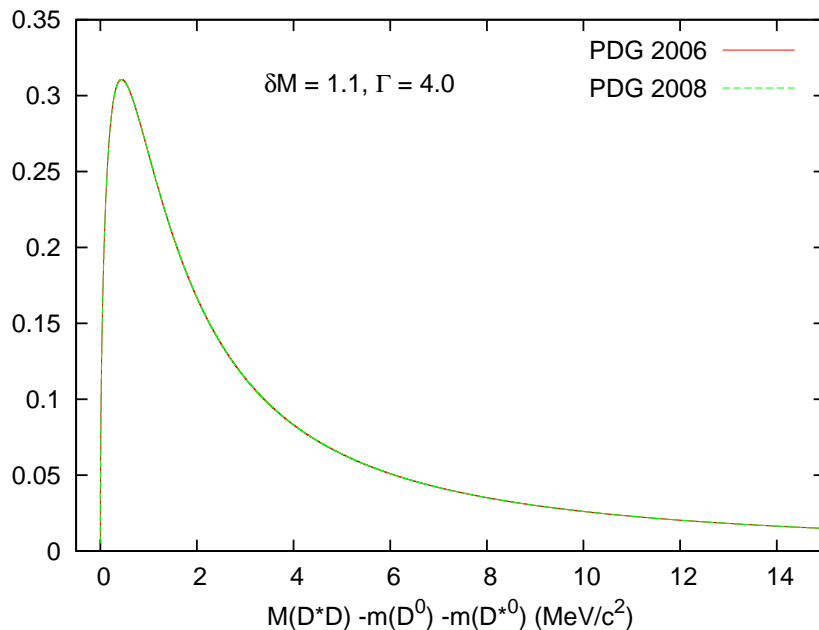
Figure 6.22: Relativistic Breit-Wigner as a function of $M_{D^*D} - m_{D^{*0}} - m_{D^0}$ for the PDG'06 (solid red) and PDG'08 (dashed green) values of the nominal D^0 and D^{*0} masses. The two curves are indistinguishable. The other Breit-Wigner parameters δM and Γ have been fixed to the observed values.

For the PDG'08 values, and taking into account the systematic uncertainties, we obtain a mass of

$$3872.9\,^{+0.6}_{-0.4}\,^{+0.4}_{-0.5}\ \mathrm{MeV}/c^2$$

and a width of

$$3.9\,^{+2.8}_{-1.4}\,^{+0.4}_{-1.1}\ \mathrm{MeV}/c^2.$$

The signal has a statistical significance of 7.9σ.

6.4.2   Branching fractions

Using the $X(3872)$ yield obtained from the simultaneous fit with fixed $D^0\gamma/D^0\pi^0$ yield ratio (Section 6.1.3), we compute the product branching fraction averaged over charged and neutral B mesons

$$
\begin{aligned}
\mathcal{B}(B \to X(3872)K) \times \mathcal{B}(X(3872) \to D^{*0}\bar{D}^0) &= \frac{N_{\mathrm{sig}}}{\epsilon_{\mathrm{tot}}\, N_{B\bar{B}}} \qquad\qquad (6.7)\\
&= (0.80 \pm 0.20 \pm 0.11) \times 10^{-4},
\end{aligned}
$$

where $\mathcal{B}(X(3872) \to D^{*0}\bar{D}^0)$ stands for $\mathcal{B}(X(3872) \to D^{*0}\bar{D}^0) + \mathcal{B}(X(3872) \to \bar{D}^{*0}D^0)$ and $N_{B\bar{B}} = 656.7 \times 10^6$; ϵ_{tot} is the Monte Carlo total efficiency:

$$\epsilon_{\mathrm{tot}} = \epsilon_{K^+}^{\gamma} + \epsilon_{K^+}^{\pi^0} + f_{K_S^0}\,\mathcal{B}(K_S^0 \to \pi^+\pi^-)(\epsilon_{K_S^0}^{\gamma} + \epsilon_{K_S^0}^{\pi^0}), \qquad\qquad (6.8)$$

where $\mathcal{B}(K_S^0 \to \pi^+\pi^-) = 0.692$ and $f_{K_S^0} = 0.5$, since we assume the $B^0 \to X(3872)K^0$ transition rate to be equal to twice the $B^0 \to X(3872)K_S^0$ rate.

Within large uncertainties, the obtained product branching fraction is consistent with the previous ones from Belle in the $D^0\bar{D}^0\pi^0$ channel [21],

$$\mathcal{B}(B \to X(3872)K) \times \mathcal{B}(X(3872) \to D^0\bar{D}^0\pi^0) = (1.22 \pm 0.31 \,^{+0.23}_{-0.30}) \times 10^{-4},$$

and from BaBar [22],

$$\mathcal{B}(B \to X(3872)K) \times \mathcal{B}(X(3872) \to D^0\bar{D}^0\pi^0) = (1.22 \pm 0.31 \,^{+0.23}_{-0.30}) \times 10^{-4}.$$

The product branching fraction in the $J/\psi\pi^+\pi^-$ channel [36],

$$\mathcal{B}(B^+ \to X(3872)K^+) \times \mathcal{B}(X(3872) \to J/\psi\pi^+\pi^-) = (8.10 \pm 0.92 \pm 0.66) \times 10^{-6},$$

shows that the $D^{*0}\bar{D}^0$ mode is dominant.

We use the yields obtained from the fits to charged and neutral B modes in Section 6.1.4 to compute the corresponding product branching fractions:

$$
\begin{aligned}
\mathcal{B}(B^0 \to X(3872)K^0) \times \mathcal{B}(X(3872) \to D^{*0}\bar{D}^0) &= (0.97 \pm 0.46) \times 10^{-4}, \\
\mathcal{B}(B^+ \to X(3872)K^+) \times \mathcal{B}(X(3872) \to D^{*0}\bar{D}^0) &= (0.77 \pm 0.16) \times 10^{-4}.
\end{aligned}
$$

Then we evaluate the ratio of neutral to charged branching fractions. In this ratio, some systematic uncertainties cancel out; the remaining uncertainties are MC statistics, particle identification and tracking for the K^+, and K_S^0 reconstruction efficiency. These add up to a 5% uncertainty and the ratio is

$$\frac{\mathcal{B}(B^0 \to X(3872)K^0)}{\mathcal{B}(B^+ \to X(3872)K^+)} = 1.26 \pm 0.65 \pm 0.06, \tag{6.9}$$

consistent with unity within a large statistical uncertainty.

6.4.3   Upper limit on the $Y(3940)$ branching fraction

The upper limit on the $Y(3940)$ yield obtained in Section 6.1.3 is used to give an upper limit on the $\mathcal{B}(B \to Y(3940)K \to D^{*0}\bar{D}^0K)$ product branching fraction. Using the Monte Carlo efficiencies obtained in Section 5.2.3, we find an upper limit of

$$\mathcal{B}(B \to Y(3940)K) \times \mathcal{B}(Y(3940) \to D^{*0}\bar{D}^0) < 0.67 \times 10^{-4} \tag{6.10}$$

at 90% CL. By averaging the branching fractions in Refs [25] and [26], we have $\mathcal{B}(B \to Y(3940)K) \times \mathcal{B}(Y(3940) \to \omega J/\psi) = (0.51 \pm 0.11) \times 10^{-4}$; combining this with the upper limit (6.10) we get

$$\frac{\mathcal{B}(Y(3940) \to \omega J/\psi)}{\mathcal{B}(Y(3940) \to D^{*0}\bar{D}^0)} > 0.71$$

at 90% CL, while in Ref. [24] we find the 90% CL limits $\mathcal{B}(X(3940) \to \omega J/\psi) < 0.26$ and $\mathcal{B}(X(3940) \to D^{*0}\bar{D}^0) > 0.45$, thus

$$\frac{\mathcal{B}(X(3940) \to \omega J/\psi)}{\mathcal{B}(X(3940) \to D^{*0}\bar{D}^0)} < 0.58$$

with more than 90% CL, which suggests that the $X(3940)$ and the $Y(3940)$ are different states.

Conclusion

We have studied the $B \to X(3872)K \to D^{*0}\bar{D}^0 K$ decay in both the $D^{*0} \to D^0\gamma$ and $D^{*0} \to D^0\pi^0$ sub-modes, using data collected by the Belle detector at the KEKB collider in Tsukuba, Japan. This study is challenging, because the signal is expected to peak just above the DD^* threshold, and the $X(3872)$ width is comparable with the DD^* mass resolution. However, using mass-constrained fits for the D^0 and D^{*0}, we obtain an extremely good resolution, of the order of 200 keV in the signal region.

We find a near-threshold enhancement in the $D^{*0}\bar{D}^0$ invariant mass spectrum at $3872.9 \, ^{+0.6}_{-0.4} \, ^{+0.4}_{-0.5}$ MeV/c^2, with a width of $3.9 \, ^{+2.8}_{-1.4} \, ^{+0.4}_{-1.1}$ MeV/c^2, and a total signal of $50.1 \, ^{+14.8}_{-11.1}$ events. The mass difference between the $X(3872)$ mass and the $D^{*0}\bar{D}^0$ threshold mass is

$$\delta M = M_X - m_{D^{*0}} - m_{D^0} = 1.1 \, ^{+0.6}_{-0.4} \, ^{+0.1}_{-0.3} \text{ MeV}/c^2.$$

The statistical significance of this enhancement is 7.9σ. We obtain a product branching fraction

$$\mathcal{B}(B \to X(3872)K) \times \mathcal{B}(X(3872) \to D^{*0}\bar{D}^0) = (0.80 \pm 0.20 \pm 0.11) \times 10^{-4}$$

and a ratio of neutral to charged branching fractions

$$\frac{\mathcal{B}(B^0 \to X(3872)K^0)}{\mathcal{B}(B^+ \to X(3872)K^+)} = 1.26 \pm 0.65 \pm 0.06,$$

consistent with unity and with previous measurements by the Belle and BaBar collaborations. It would be interesting to measure the mass difference between the $X(3872)$ states produced in B^+ and B^0 decays, but especially in the B^0 decay mode there are not enough statistics to do this.

The results presented in this thesis are consistent with the ones previously published by Belle in Ref. [21] for $D^0\bar{D}^0\pi^0$ decays. We used a three times larger data sample and included the $D^{*0} \to D^0\gamma$ mode; only 30% of the data sample is in common. We also used a more sophisticated fitting procedure including a mass-dependent resolution function and a two-dimensional unbinned fit with two different shapes, the relativistic Breit-Wigner function and the Flatté distribution. The obtained branching fraction and width are compatible with the previous values, and the mass is 1.8σ lower.

The observed $D^{*0}\bar{D}^0$ mass and width are consistent with the current world-average values for the $X(3872)$ [4]; the mass is 2.3σ lower than the value obtained by BaBar [22]. Our significance is about 1.6 times larger than theirs. This can be explained partly by the fact that we used a 50% larger data sample, but the main reason is that BaBar performed a one-dimensional binned fit to M_{D^*D}, while we performed a two-dimensional unbinned fit to M_{D^*D} and M_{bc}.

The alternative fitting method using the Flatté distribution gives results similar to the ones obtained with a traditional Breit-Wigner function.

This study doesn't give an explanation on the nature of the $X(3872)$; we cannot determine if the $X(3872)$ mass is above the $D^{*0}D^0$ threshold (corresponding to the relativistic Breit-Wigner fit) or below (fit with the Flatté distribution). More statistics are needed to solve this problem.

We don't observe any significant contribution from the $Y(3940)$ state and we set an upper limit on the $\mathcal{B}(B \to Y(3940)K) \times \mathcal{B}(Y(3940) \to D^{*0}\bar{D}^0)$ branching fraction which suggests that the $X(3940)$ and the $Y(3940)$ are different states.

Prospects

The $X(3872)$ has been studied during five years by four experiments. Nevertheless, it is still a mysterious state; in particular, the ambiguity in quantum numbers $J^{PC} = 1^{++}$ or 2^{-+} remains. More experimental data is needed to understand this state; two new experiments will be able to provide large data samples.

The Super B factory is currently in preparation at KEK. For this new generation experiment, the KEK collider and the Belle detector will be upgraded to reach a luminosity 50 times larger than the current peak luminosity. To achieve this, all subdetectors will be optimized, and a new pixel sensor will be installed around the interaction point. Super B is expected to collect a sample of 50 billion $B\bar{B}$ pairs, while the Belle experiment has collected 900 million $B\bar{B}$ pairs.

The LHCb experiment at CERN (see Section B.1) is expected to start data taking in 2009. Thanks to the large luminosity of the LHC accelerator, it could quickly collect the world largest $X(3872)$ samples, both from prompt and from B decays. Using a sample from B decays, LHCb could perform an improved angular analysis and distinguish 1^{++} and 2^{-+}. LHCb also has good prospects for the confirmation of other current XYZ states, and for the search of new states in the bottomium sector with large statistics.

Appendix A

Additional Monte Carlo studies
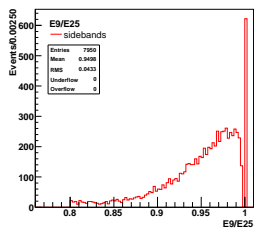
In this appendix we present several Monte Carlo studies, such as the choice of a strategy for kinematical fits, the comparison of the $D^{(*)0}$ mass resolutions with those in data, and $X(3872)$ mass resolution checks.

A.1   Kinematical fits

In this section, different kinematical fit strategies for the D^0 and D^{*0} are compared by checking the improvement of the resolutions on the $X(3872)$ mass, ΔE and M_{bc}. Four different strategies are studied:

- no kinematical fits,

- vertex-constrained fits for D^0,

- mass- and vertex-constrained fits for D^0,

- mass- and vertex-constrained fits for both D^0 and D^{*0}.

Histograms are shown only for events where the B was correctly reconstructed (Figure A.1). When mass-constrained fits are not used, the $X(3872)$ mass difference

$$M_X = M_{D^*D} - M_{\bar{D}^0} - M_{D^{*0}} + m_{D^0} + m_{D^{*0}}$$

is shown, replacing the reconstructed D^0 and D^{*0} masses by their nominal values, and ΔE is corrected by the nominal $X(3872)$ mass. The M_{bc} distributions are fitted with a single Gaussian function, while the $X(3872)$ mass and the ΔE distributions are fitted with a double Gaussian function; A_2/A is the ratio of wide/total Gaussian amplitudes in the $X(3872)$ mass distribution, and w_2/w_1 is the ratio of wide/narrow Gaussian widths in the $X(3872)$ mass distribution.
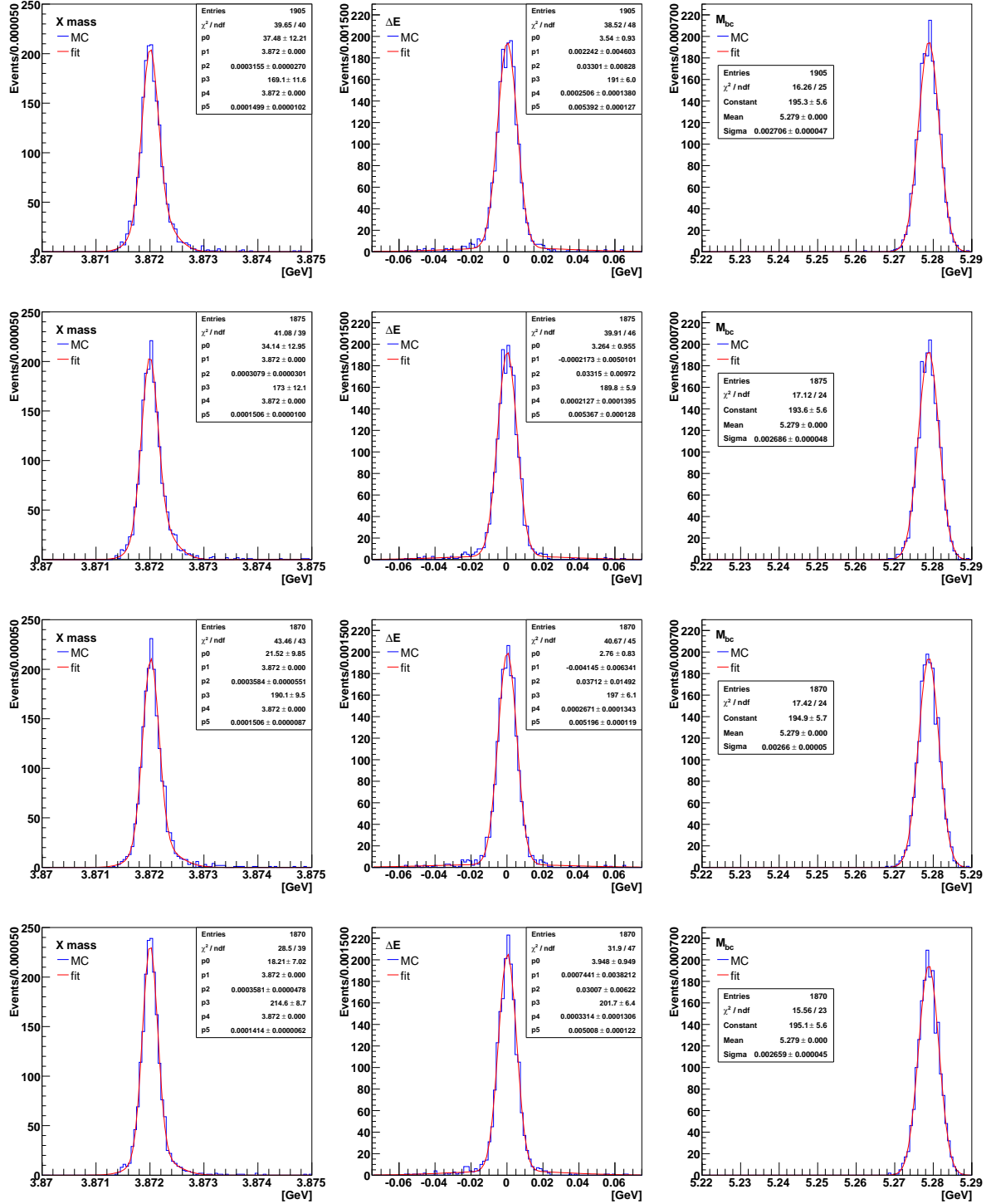
Figure A.1: $X(3872)$ mass, ΔE and M_{bc} distributions for various kinematical fit strategies. First row: no kinematical fits; second row: vertex-constrained fits for D^0; third row: mass- and vertex-constrained fits for D^0; fourth row: mass- and vertex-constrained fits for both D^0 and D^{*0}.

The results of this study are shown in Table A.1, where the narrow widths are quoted as resolutions. The $X(3872)$ mass resolution is the same in all cases: using the $X(3872)$ mass difference has the same effect as using mass- and vertex-constrained fits. The best strategy is to use mass- and vertex-constrained fits for both D^0 and D^{*0}, since it gives the best ΔE resolution and suppresses the tails in the $X(3872)$ mass distribution.

Fits	$X(3872)$ width (MeV/c^2)	ΔE width (MeV)	A_2/A	w_2/w_1
No kinematical fits	0.150 ± 0.010	5.39 ± 0.12	18%	2.13
Vertex-constrained fits	0.151 ± 0.010	5.37 ± 0.13	16%	2.07
Mass- and vertex-const. fits for D^0	0.151 ± 0.009	5.20 ± 0.12	10%	2.40
Mass- and vertex-const. fits for $D^{(*)0}$	0.143 ± 0.006	5.01 ± 0.12	8%	2.57

Table A.1: Summary of kinematical fit results.

A.2 Estimation of mass resolutions in data

In this section we estimate the D^0 and D^{*0} mass resolutions on data, as they could be different than on Monte Carlo. To achieve this we use control samples of fully-reconstructed $B^+ \to D^{*0}(D^0\gamma)h^+$ events available for both Monte Carlo and data. We estimate the ratio of data/MC resolutions using the control samples and scale the resolutions obtained from signal Monte Carlo samples to obtain the resolutions on data.

A.2.1 D^0 mass resolution in data

A control sample of fully-reconstructed $B^+ \to D^{*0}(D^0\gamma)h^+$ decays is used to estimate the D^0 mass resolutions in data. The D^0 resolution is fitted on the control sample for Monte Carlo and data using the following cuts: $M_{\rm bc} > 5.27$ GeV/c^2, $|\Delta E| < 30$ MeV, and $p(D^0) < 1.4$ GeV/c to have the same momentum range as in the $B \to X(3872)(D^{*0}\bar{D}^0)K$ signal Monte Carlo.

The ratio R of data/MC resolutions is computed by fitting the D^0 mass distribution with a double Gaussian function with the same shape in Monte-Carlo and data: the fraction f_A of events in the first Gaussian and the ratio of widths $f_\sigma = \sigma_2/\sigma_1$ are constrained to be the same in both fits. The σ shown on the plots is the smallest of the two widths. The background is described with a linear function.

In Figure A.2, the D^0 mass distribution is fitted in the $D^0 \to K\pi$ (top) and in the $D^0 \to K\pi\pi^0$ sub-modes (bottom). The corresponding data/MC resolution ratio is $R = 1.18 \pm 0.04$ in both cases. The D^0 resolutions obtained from the $B \to X(3872)(D^{*0}\bar{D}^0)K$ signal Monte Carlo are then multiplied by this factor 1.18 to obtain the D^0 resolutions in data mentioned in Table 4.1.

The width obtained from the control sample are slightly larger than those from the signal Monte Carlo; this can be explained by the fact that vertex-constrained fits were used in the signal Monte Carlo, but not in the control sample.
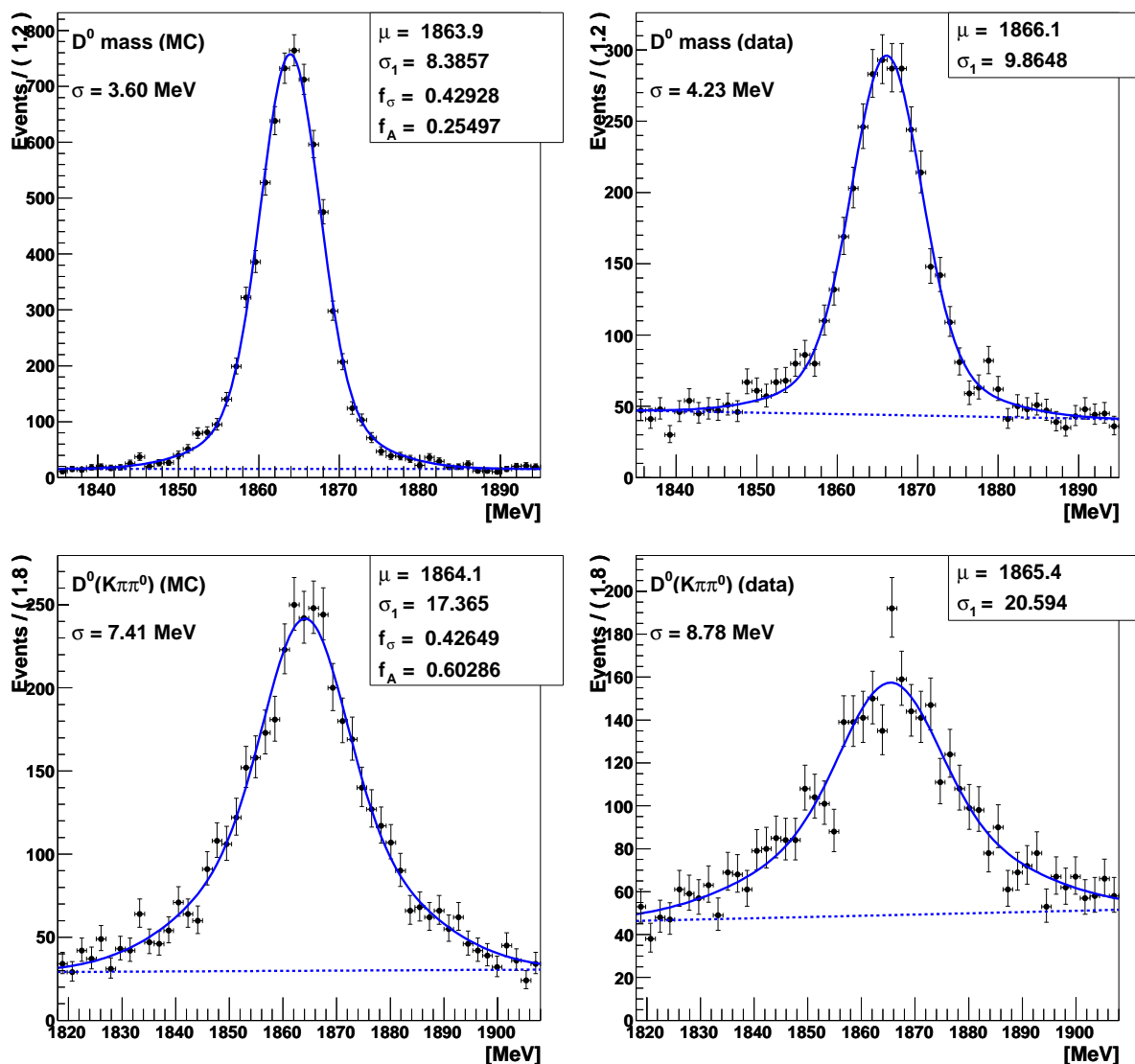
Figure A.2: Distributions of the D^0 mass for control sample MC (left) and control sample data (right), in the $D^0 \to K\pi$ channel (top) and in the $D^0 \to K\pi\pi^0$ channel (bottom). The solid curve is the result of a fit with the function described in the text; the dashed curve is the linear function used to describe the background.

A.2.2 D^{*0} mass resolution in data

Control samples of fully-reconstructed $B^+ \rightarrow D^{*0}(D^0\gamma)h^+$ and $B^+ \rightarrow D^{*0}(D^0\pi^0)h^+$ decays are used to estimate the D^{*0} resolutions in data, applying the following cuts: $M_{bc} > 5.27$ GeV/c^2, $|\Delta E| < 30$ MeV, $\Delta M(D^0) < 12$ MeV/c^2, and $p(D^{*0}) < 1.6$ GeV/c to have the same momentum range as in the $B \rightarrow X(3872)(D^{*0}\bar{D}^0)K$ signal Monte Carlo.

In Figure A.3, the D^{*0} mass distributions are fitted for the $D^0 \rightarrow K\pi$ sub-mode only. Again, the Monte Carlo and data distributions are fitted with the same shape, as described in Section A.2.1. In the $D^{*0} \rightarrow D^0\gamma$ channel, the corresponding data/MC ratio is $R = 1.33 \pm 0.15$, thus the $D^{*0}(D^0\gamma)$ resolution in data for $B \rightarrow X(3872)(D^{*0}\bar{D}^0)K$ decays is 9.2 ± 0.5 MeV/c^2. In the $D^{*0} \rightarrow D^0\pi^0$ channel, the ratio is $R = 1.16 \pm 0.08$, thus the $D^{*0}(D^0\pi^0)$ resolution in data for $B \rightarrow X(3872)(D^{*0}\bar{D}^0)K$ decays is 2.03 ± 0.06 MeV/c^2.

A.3 $X(3872)$ mass resolution checks

Since the photon momentum is small (see Figure 4.1), it is possible that the data are not well described by the Monte Carlo. Thus the role of the photon in the $X(3872)$ mass resolution has to be studied. The D^0 mesons have the usual momentum range, so they should be well described by the Monte Carlo.

We study the contributions of the photon and the D^0 mesons to the $X(3872)$ mass resolution using a fast Monte Carlo sample. This sample consists in the generated four-momenta of the $D^0, \bar{D}^0$ and γ obtained from a signal Monte Carlo sample where the $X(3872)$ is generated with a zero width and a mass of 3872 MeV/c^2. We can then imitate the effect of the reconstruction by randomly smearing the generated four-momenta according to the resolutions on Monte Carlo shown in the next section, and study the effect on the $X(3872)$ mass distribution.

A.3.1 Resolutions on Monte Carlo

Table A.2 shows the Monte Carlo resolutions for momenta and directions and for the masses. These resolutions are computed by looking at the difference between generated and reconstructed values (Figure A.4).

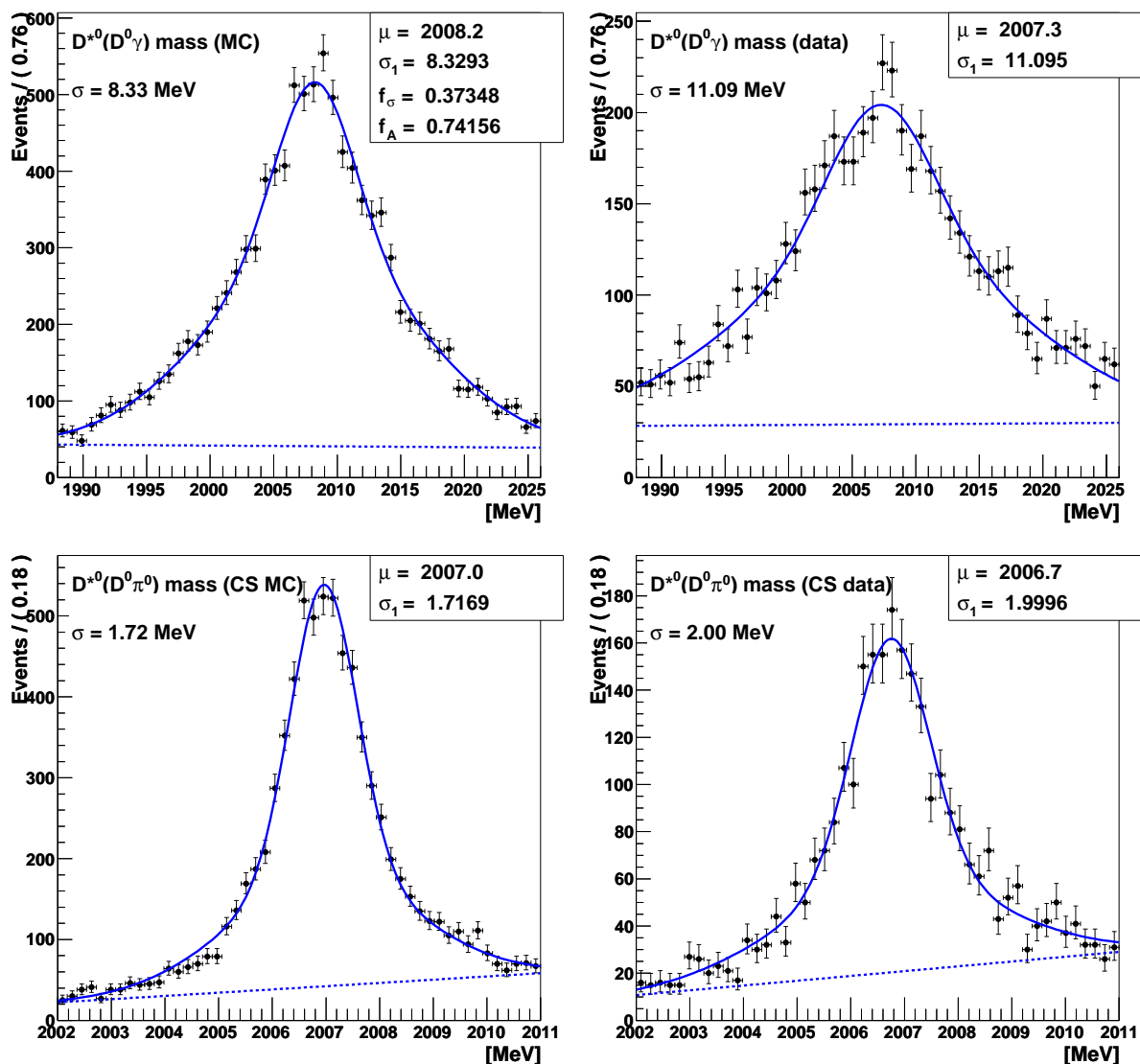| Quantity	Resolution
D^0 momentum	$\sigma_p/p = 0.45\%$
γ energy	$\sigma_E/E = 2.5\%$
D^0 mass	$\sigma_m = 3$ MeV/c^2
D^0 direction	$\sigma_\theta = 7$ mrad
γ direction	$\sigma_\theta = 10$ mrad
π^0 direction	$\sigma_\theta = 60$ mrad

Table A.2: Monte Carlo resolutions.

Figure A.3: Distributions of the D^{*0} mass for control sample MC (left) and control sample data (right), in the $D^{*0} \to D^0\gamma$ channel (top) and in the $D^{*0} \to D^0\pi^0$ channel (bottom). The solid curve is the result of a fit with the function described in the text; the dashed curve is the linear function used to describe the background.
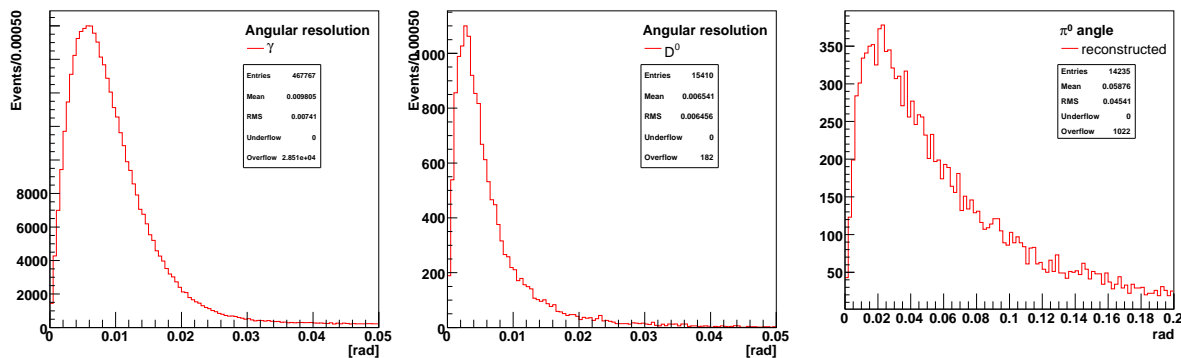
Figure A.4: Distribution of the angle between the generated and reconstructed momenta of the γ, D^0 and π^0 for correctly reconstructed events in signal Monte Carlo.

A.3.2 Contributions to the $X(3872)$ mass resolution

We look for the main contributions to the $X(3872)$ mass resolution, using only generated quantities, except:

1. reconstructed γ momenta

2. reconstructed γ directions

3. reconstructed D^0 momenta

4. reconstructed D^0 directions

5. all reconstructed momenta and directions for comparison

and look at the $X(3872)$ mass difference resolution, without using any kinematical fits (see Figure A.5). The Gaussian widths of the first four cases are added in quadrature and compared to the resolution in Table A.3. The largest contribution to the resolution comes from the D^0 directions.

reconstructed	resolution (MeV$/c^2$)
γ momenta	0.058 ± 0.001
γ directions	0.048 ± 0.001
D^0 momenta	0.085 ± 0.001
D^0 directions	0.124 ± 0.001
sum for γ	0.075 ± 0.001
sum for D^0	0.150 ± 0.001
all (standard reconstruction)	0.145 ± 0.001

Table A.3: Contributions to the $X(3872)$ mass resolution.

The conclusion of this toy Monte Carlo study is that the largest contribution to the resolution comes from the D^0 direction errors, while the photon momenta and direction errors contribute much less.

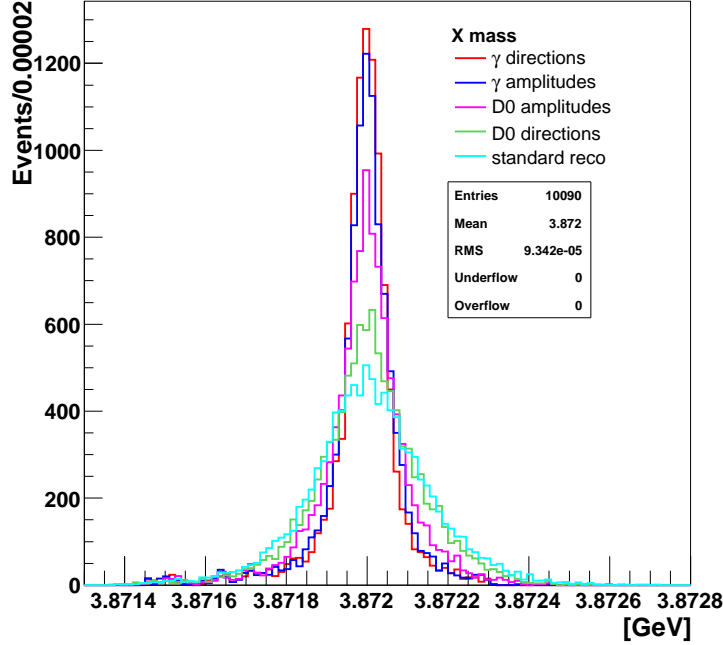Figure A.5: Distributions of M_{D^*D} obtained by smearing γ or D^0 momentum amplitudes or directions as described in the text.

A.3.3 Estimation of the $X(3872)$ mass resolution in data

Other fast Monte Carlo samples are used to estimate the expected errors in data for γ and π^0 and determine the effect of those errors on the $X(3872)$ mass resolution.

This study is based on four different fast Monte Carlo samples:

- $B^+ \to D^{*0}(D^0\gamma)h^+$ for errors on γ;

- $B^+ \to D^{*0}(D^0\pi^0)h^+$ for errors on π^0;

- $B^+ \to X(D^{*0}\bar{D}^0)K^+$ with $D^{*0} \to D^0\gamma$ and

- $B^+ \to X(D^{*0}\bar{D}^0)K^+$ with $D^{*0} \to D^0\pi^0$ to estimate the effect of those errors on the $X(3872)$ mass resolution.

The ratios R of D^0 and D^{*0} mass resolutions in data and MC are shown in Table 4.1. We now estimate the ratio of the $X(3872)$ mass resolution in data and MC, using the fast Monte Carlo samples mentioned above. (In this section, "D^{*0} mass" actually means $D^{*0} - D^0$ mass difference.)

The fast Monte Carlo samples contain the generated four-momenta of the daughters of the D^{*0}. The momentum directions and amplitudes of the daughters are smeared using the resolutions from Table A.2 to imitate the D^{*0} mass resolution obtained in signal Monte Carlo. Then an additional smearing is applied to imitate the D^{*0} mass resolution obtained in data: the D^0 momenta are smeared by multiplying their resolution by the factor from Table 4.1, and the momenta of the γ or π^0 are smeared using a factor chosen to reproduce the ratio R.

To this effect, both $D^0\gamma$ and $D^0\pi^0$ fast Monte Carlo D^{*0} mass distributions are fitted with a double Gaussian function of the same shape: the ratios of amplitudes and widths are the same in both fits. The D^{*0} momentum range is restricted to $p(D^*) < 1.6$ GeV/c to have the same range as in the signal channels.

Smearing of γ errors

The fast MC sample used here is based on fully-reconstructed $B^+ \to D^{*0}(D^0\gamma)h^+$ decays. In Figure A.6, the D^{*0} mass distribution is fitted and the corresponding ratio is $R = 1.33 \pm 0.13$, as in the contol sample. To achieve this ratio, the D^0 momenta are smeared by multiplying the resolution with the factor 1.18 from Table 4.1, and the additional factor needed to smear the γ momenta is 1.36.

Figure A.6: Distribution of the D^{*0} mass in the $D^{*0} \to D^0\gamma$ channel obtained with a fast MC. Left: smearing to Monte Carlo resolution, right: smearing to data resolution.

The effect on the $X(3872)$ mass resolution is shown on Figure A.7. On the $B^+ \to X(D^{*0}\bar{D}^0)K^+$ fast MC sample, the D^0 errors are smeared with the factor 1.18, and the γ errors with the factor 1.36 obtained above. The resulting $X(3872)$ mass resolution is 1.14 ± 0.05 times worse than on Monte Carlo.

Smearing of π^0 errors

The fast MC sample used here is based on fully-reconstructed $B^+ \to D^{*0}(D^0\pi^0)h^+$. decays. In Figure A.8, the D^{*0} mass is fitted and the corresponding ratio is $R = 1.16 \pm 0.05$, as in the contol sample. To achieve this ratio, the D^0 momenta are smeared by multiplying the resolution with the factor 1.18 from Table 4.1, and the additional factor needed to smear the π^0 momenta is 1.18.
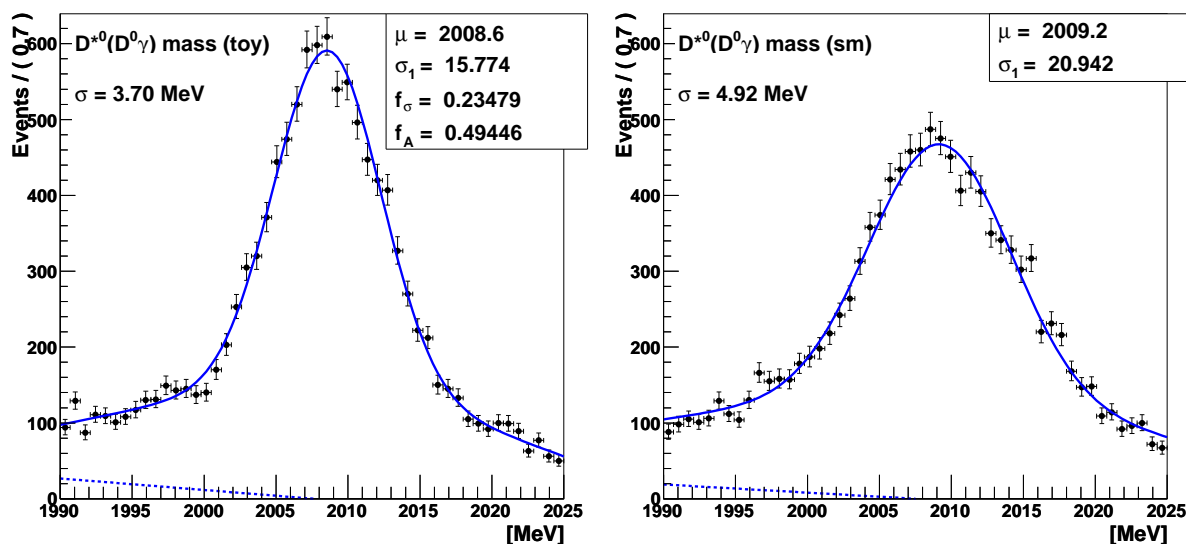
The effect on the $X(3872)$ mass resolution is shown on Figure A.9. On the $B^+ \to X(D^{*0}\bar{D}^0)K^+$ fast MC sample, the D^0 errors are smeared with the factor 1.18, and the
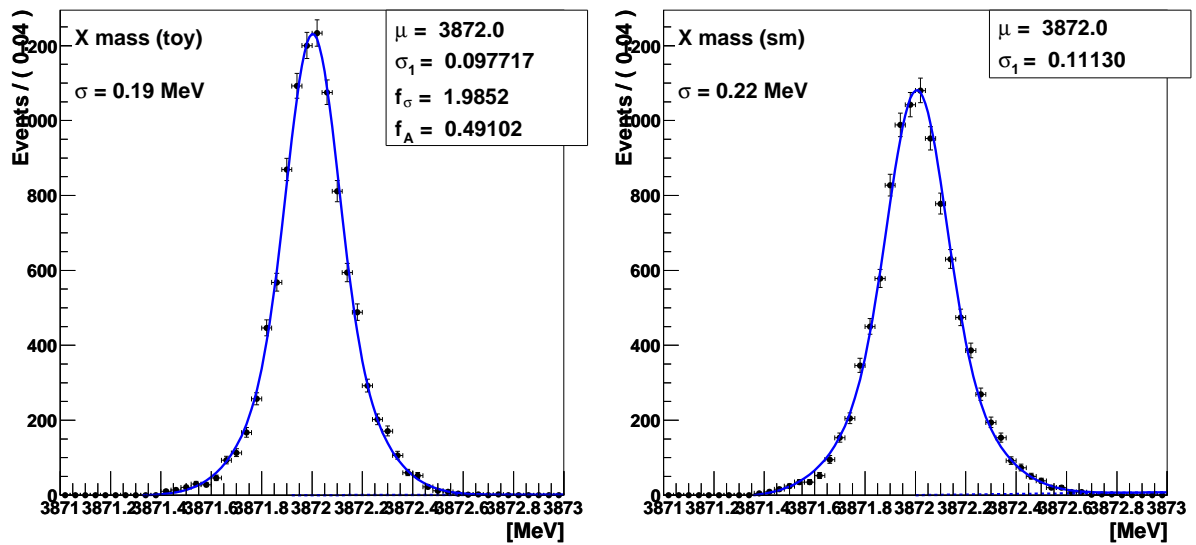
Figure A.7: Distribution of the $X(3872)$ mass in the $D^{*0} \to D^0\gamma$ channel obtained with a fast MC. Left: smearing to Monte Carlo resolution, right: smearing to data resolution.
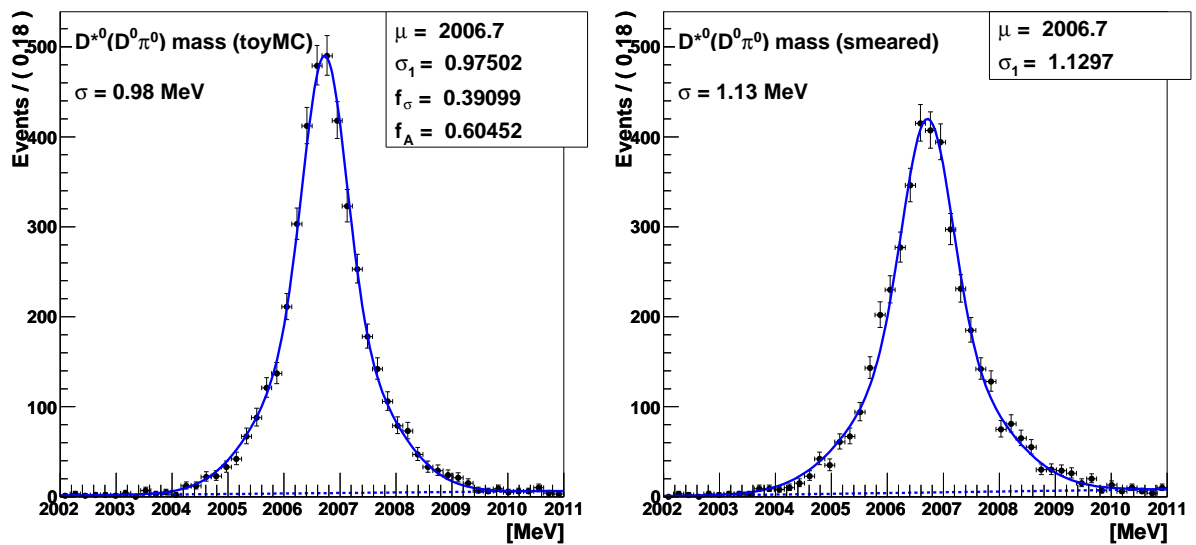
Figure A.8: Distribution of the D^{*0} mass in the $D^{*0} \to D^0\pi^0$ channel obtained with a fast MC. Left: smearing to Monte Carlo resolution, right: smearing to data resolution.

π^0 errors with the 1.18 factor obtained above. The resulting $X(3872)$ mass resolution is 1.14 ± 0.04 times worse than on Monte Carlo.
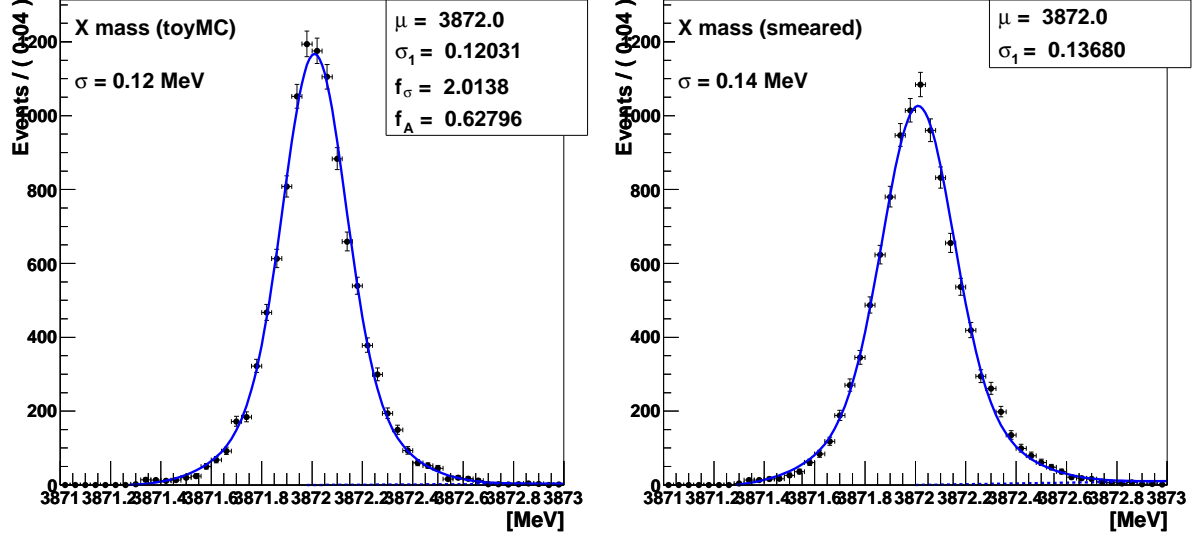
Figure A.9: Distribution of the $X(3872)$ mass in the $D^0\pi^0$ channel obtained with a fast MC. Left: smearing to Monte Carlo resolution, right: smearing to data resolution.

A.4   Helicity distributions

In order to check the influence of the D^{*0} helicity distribution in $X(3872) \to D^{*0}(D^0\pi^0)\bar{D}^0$ decays on the MC efficiency, samples are generated with the distribution of $\cos\theta$ as $\cos^2$ and $\sin^2$, where θ is the angle between the π^0 momentum in the D^{*0} rest frame and the D^{*0} momentum in the $X(3872)$ rest frame. Figure A.10 shows the generated D^{*0} helicity distributions.

In both cases, the generated $X(3872)$ mass is fitted back correctly (see Figure A.11), and a consistent efficiency is obtained (see Table A.4). Thus the helicity distribution does not contribute to the systematic uncertainties.

mass (MeV)	width (MeV)	helicity	$\epsilon_{\text{tot}}^{\pi^0}$ (10^{-4})
3872.7	4.3	$\cos^2$	4.10 ± 0.06
3872.7	4.3	$\sin^2$	4.07 ± 0.07

Table A.4: MC efficiencies for $\cos^2$ and $\sin^2$ D^{*0} helicity distributions.
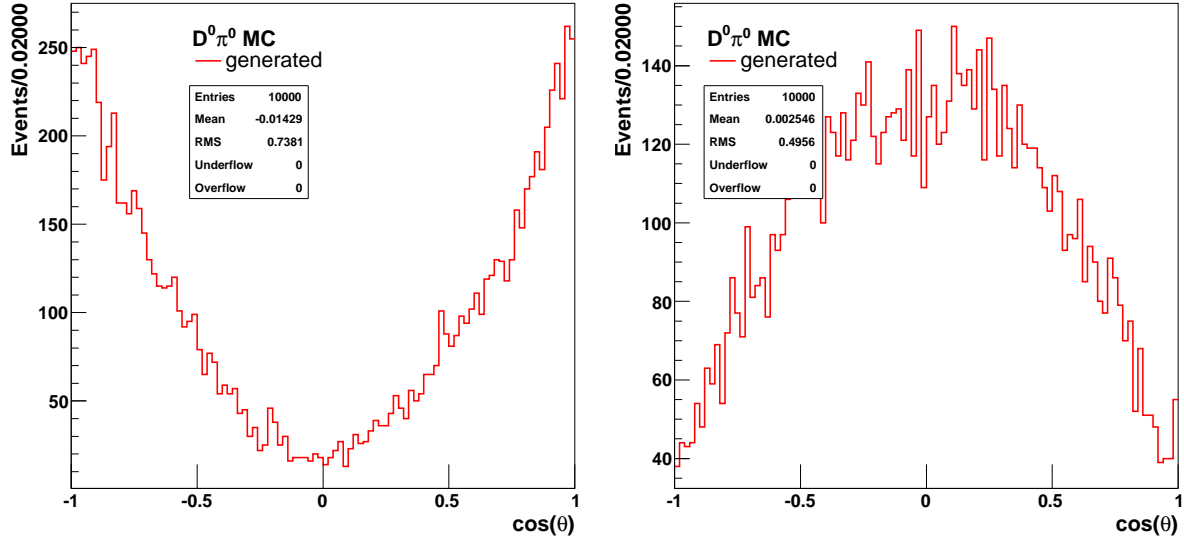
Figure A.10: Generated distributions of $\cos\theta$ in Monte Carlo samples generated as $\cos^2$ (left) and $\sin^2$ (right).
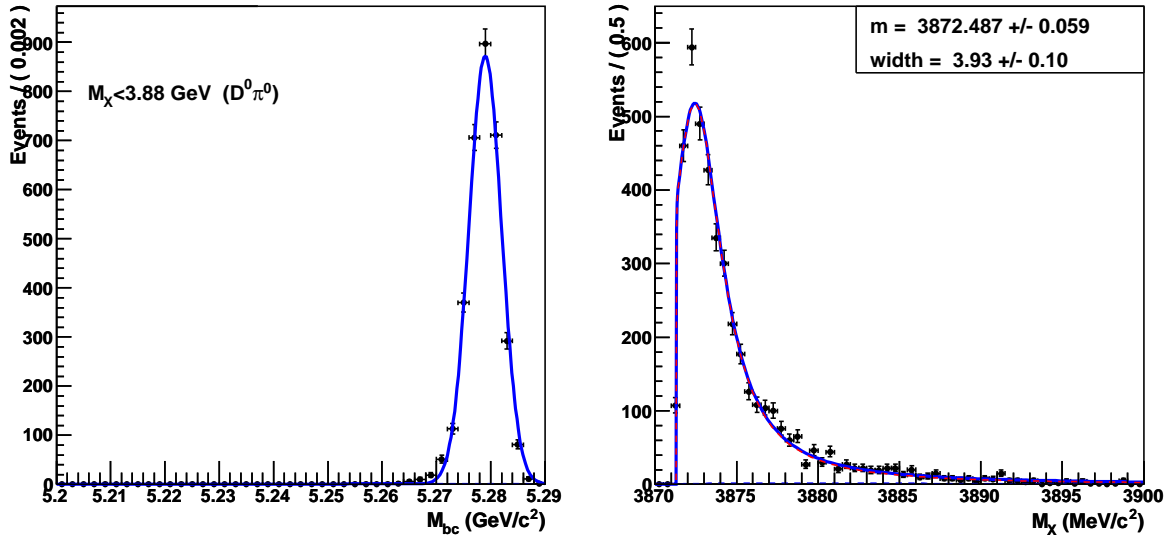
Figure A.11: Distribution of M_{bc} for $M_{D^*D} < 3.88\ \mathrm{GeV}/c^2$ (left) and of M_{D^*D} for $M_{\mathrm{bc}} > 5.27\ \mathrm{GeV}/c^2$ (right). The points are selected events using the signal MC sample generated with a mass of 3872.7 MeV/c^2, a width of 4.3 MeV/c^2, and $\sin^2$ helicity distribution; the solid curve is the result of a fit using the pdf described in Section 5.1.4.

Appendix B

Contribution to the development of the High-Level Trigger software of the LHCb experiment

This chapter concerns the topic of the first 18 months of my thesis, when I contributed to software development for the High-Level Trigger of the LHCb experiment.

B.1   Introduction

B.1.1   The LHCb experiment

LHCb [71] is a next-generation experiment dedicated to precision measurements of CP violation and rare decays of b hadrons. It will take advantage of the huge $b\bar{b}$ production rate at CERN's Large Hadron Collider (LHC), which will deliver proton-proton collisions at a center-of-mass energy of $\sqrt{s} = 14$ TeV. The LHC is expected to start in 2009.

The luminosity at the LHCb interaction point will be 2×10^{32} cm^{-2}s^{-1}, corresponding to an expected production of 10^5 $b\bar{b}$ pairs per second. These b and $\bar{b}$ quarks will fragment into all types of b hadrons, giving LHCb the additional opportunity to perform measurements with heavier B mesons (B_s^0 and B_c^+) and b baryons, which the $\Upsilon(4S)$ machines don't offer.

Since the b decay products that LHCb is designed to study will be flying close to the beam axis, LHCb is a single-arm forward spectrometer (Figure B.1). In the following, the LHCb subdetectors which are mentioned in this chapter (as their information is used in the first stages of the trigger) are briefly described.

Vertex Locator (VeLo). The VeLo is a silicon strip detector designed for precise measurement of charged particle tracks near the interaction point. It is located outside
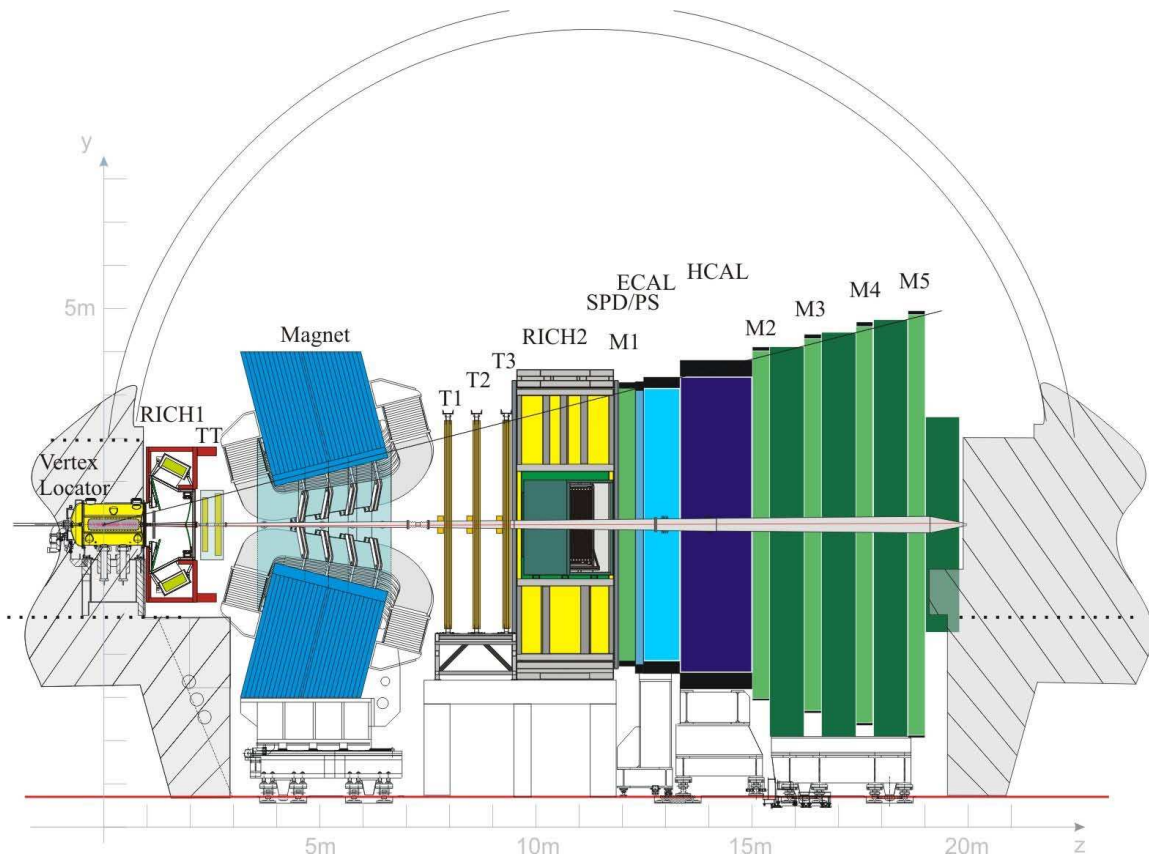
Figure B.1: The LHCb detector.

of the magnetic field to simplify the track reconstruction. It is one meter long and contains 21 stations spread along the beam direction. Each station, perpendicular to the beam axis (z axis), measures the radial (r) and polar (ϕ) coordinates of the charged particles flying through.

Trigger Tracker (TT). The TT is placed just in front of the magnet and consists of four silicon strip detector planes. It is used to measure momenta of charged tracks.

Magnet. LHCb has a classic warm dipole magnet providing an integrated magnetic field of $\int B\mathrm{d}l = 4$ Tm with a 1.1 T maximal field intensity. The field is oriented in the vertical direction and bends tracks in the horizontal plane xz.

Hadronic Calorimeter (HCAL). The HCAL is used to detect hadrons and measure their position and energy. It is made of iron and scintillating tiles parallel to the beam. The scintillation light passes through wavelength shifting fibers and is amplified by multi-anode photomultipliers.

Muon chambers (M1 – M5). Muons and neutrinos are the only particles capable of passing through the calorimeters. There are five muon stations made out of multiple wire proportional chambers. The first station is used to measure the transverse

momentum of tracks, which is an input for the trigger, and the four other stations are used for reconstructing muon tracks.

B.1.2   The LHCb Trigger system

The role of the trigger is to reduce the very high event rate delivered by the LHC (40 MHz) to a rate that can be saved to storage for later offline analysis (a few kHz). This reduction has to preserve the physically interesting events and reject background events. To achieve this, the LHCb Trigger [72] consisted in three main parts:

- The *Level 0 Trigger* (L0) reduces the LHCb beam crossing rate of 40 MHz to 1 MHz, by selecting high E_T or high p_T particles. It has access to calorimeter and muon chamber data. The L0 is implemented in custom electronics.

- The *Level 1 Trigger* (L1) uses the data from the Vertex Locator and the Trigger tracker to reduce the rate to 40 kHz. It also has access to information from the L0. The L1 is implemented in software.

- The *High Level Trigger* (HLT) has access to all data. It confirms the L1 decision with better resolution and selects interesting events in specific final states. The HLT is implemented in software.

In September 2005, the LHCb Trigger software underwent a major redesign in response to a decision to read out the full detector at 1 MHz (previously 40 kHz) [73]. In this new scheme L1 has already access to all data. Thus the distinction between L1 and HLT was no longer relevant, and L1 was merged into HLT, while L0 remained unchanged.

B.1.3   The L0 Confirmation strategy

In the 1 MHz readout scheme, the HLT consists in subtrigger alleys for muons, hadrons, photons and electrons. Each alley starts by confirming the L0 object that triggered it. This L0 confirmation didn't exist before the 1 MHz readout scheme.

The L0 confirmation in the hadronic trigger is motivated by the fact that about 50% of L0 calorimeter clusters can't be associated to a single, high-energy track [74]. This corresponds to cases where combinations of low-energy tracks, neutrons and K_L reach the same calorimeter cell and add up enough energy to trigger L0. Another reason is the bad energy resolution of HCAL clusters. The gain of the confirmation step is to reduce the number of trigger objects and thus the systematics.

This chapter describes the `HltHadAlleyMatchCalo` tool that performs the L0 confirmation in the HLT hadronic alley. It presents the results shown at the Trigger and Reconstruction meeting in March and May 2006 [75, 76] in an updated and more detailed way.

The code of the tool has been taken from N. Tuning's `MatchVeloL0Tool` [77], which was written in 2003. It had the aim of using the L0 information in order to improve the L1 trigger, which is historically referred to as Super-L1. Although this project is no longer part of the trigger, the hadronic part of the matching can now be used for the L0 confirmation.

The following sections are taken from the LHCb note [78]. As of January 2009, the concept of L0 confirmation is still in use in the hadronic alley of the HLT; there are two possible ways to confirm the L0 candidate, either using the VeLo or using the T stations. The default implementation is using the VeLo, as described in the following; it seems to be slightly faster than the second option for the same performance in terms of efficiency and retention.

B.2   Matching strategy

The energy deposition at the calorimeter can be used to estimate the amount of bending induced by the magnetic field on the track. By correcting the calorimeter position for this magnetic kick, one can estimate the slope of the track before the magnet, and compare it to the actual slope of the VeLo track. The difference is used to compute a χ^2 criterion which is used for selecting tracks. Figure B.2 shows an overview of this matching principle.
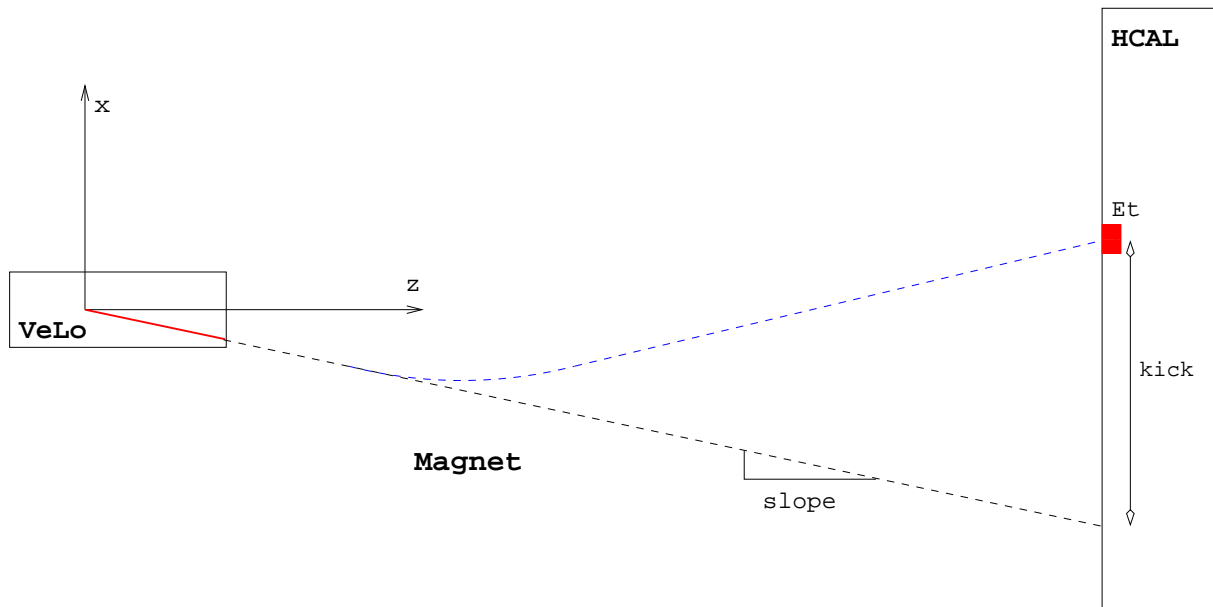
Figure B.2: Schematic drawing of the matching strategy (not to scale).

The L0 confirmation is done in two steps: 2D and 3D matching. The first step uses VeLo 2D tracks reconstructed by the `PatVeloRTracking` algorithm. These tracks have r-ϕ coordinates deduced from the 8 VeLo r-reading sectors, so that ϕ only takes 8 possible values (see Figure B.11 on page 123). The second step uses VeLo 3D tracks reconstructed by the `PatVeloSpaceTracking` algorithm. These tracks have a cartesian geometry.

Both confirmation functions take one track and try to match it with all the L0CaloCandidates that triggered L0 ($E_{\mathrm{T}} > 3.5$ GeV). Only the smallest χ^2 is returned. As there is a charge ambiguity, the matching is tried with negative and positive charge, so that each track is actually matched twice to each `L0CaloCandidate`. The charge that is assigned to a track by the tool is not used in the further reconstruction steps; in addition, the tool has no polarity information.

The following sections give a detailed description of these two confirmation steps.

B.3 Matching 2D tracks

The 2D confirmation uses VeLo tracks in r–ϕ coordinates, so that the calorimeter coordinates have to be translated to r–ϕ geometry.

Given a VeLo 2D track with slope $t_r = \frac{\mathrm{d}r}{\mathrm{d}z}$ and azimuthal angle ϕ, and a `L0Calo-Candidate` with position x, y, z and transverse energy E_T, the χ^2 is computed in the following way for charge $q = \pm 1$:

$$
\begin{aligned}
\chi^2 &= \chi_r^2 + \chi_\phi^2 \\
\chi_r^2 &= \left(\left.\frac{\Delta r}{\Delta z}\right|_{\mathrm{L0}} - t_r \right)^2 \frac{1}{\sigma_r^2} \\
\chi_\phi^2 &= \frac{(\phi_{\mathrm{L0}} - \phi_{\mathrm{VeLo}})^2}{\sigma_\phi^2} \\
\left.\frac{\Delta r}{\Delta z}\right|_{\mathrm{L0}} &= \frac{\sqrt{(x - q x_{\mathrm{kick}})^2 + y^2}}{z} \\
\phi_{\mathrm{L0}} &= \arctan\left(\frac{y}{x - q x_{\mathrm{kick}}} \right)
\end{aligned}
\tag{B.1}
$$

The kick correction uses a first-order approximation in $\frac{1}{E}$

$$
\begin{aligned}
x_{\mathrm{kick}} &= C_{\mathrm{kick}} \frac{z - z_o}{E} \\
E &= \sqrt{\frac{x^2 + y^2 + z^2}{x^2 + y^2}} E_\mathrm{T}
\end{aligned}
\tag{B.2}
$$

where $C_{\mathrm{kick}} = 1.263\,\mathrm{GeV}$ and $z_0 = 5.25$ m is taken as the center of the magnetic field, using field 043. The errors σ_r and σ_ϕ take into account the uncertainty on the calorimeter coordinates and energy, and the uncertainty on the ϕ value of the track. The uncertainty on the track slope measurement is small compared to the L0 measurement uncertainty and is therefore neglected.

$$
\begin{aligned}
\sigma_r^2 &= \left(\sigma\left(\frac{\Delta x}{\Delta z}\right)^2 \left(\frac{\Delta x}{\Delta z}\right)^2 + \sigma\left(\frac{\Delta y}{\Delta z}\right)^2 \left(\frac{\Delta y}{\Delta z}\right)^2 \right) \left.\frac{\Delta r}{\Delta z}\right|_{\mathrm{L0}}^{-2} \\
\sigma_\phi^2 &= \left(\sigma\left(\frac{\Delta x}{\Delta z}\right)^2 \left(\frac{\Delta y}{\Delta z}\right)^2 + \sigma\left(\frac{\Delta y}{\Delta z}\right)^2 \left(\frac{\Delta x}{\Delta z}\right)^2 \right) \left.\frac{\Delta r}{\Delta z}\right|_{\mathrm{L0}}^{-2} \\
&\quad + \left(\frac{2\pi}{8\sqrt{12}}\right)^2 \\
\sigma\left(\frac{\Delta x}{\Delta z}\right) &= \frac{1}{z} \sqrt{\sigma_x^2 + \sigma_{\mathrm{kick}}^2} \\
\sigma\left(\frac{\Delta y}{\Delta z}\right) &= \frac{1}{z} \sigma_y \\
\sigma_x &= \sigma_y = \frac{4s}{\sqrt{12}}
\end{aligned}
$$

$$\sigma_{\text{kick}} = x_{\text{kick}} \frac{\sigma_E}{E}$$
$$\frac{\sigma_E}{E} = 60\% \oplus \frac{70\%}{\sqrt{E}} \qquad (B.3)$$

s is the half-size of the corresponding cell, given by the `L0CaloCandidate::posTol()` function. There is a factor 4 because in L0 the cells are read out in clusters of $2 \cdot 2$ cells. The energy error parameters[1] are found by fitting

$$\frac{(E_{\text{MC}} - E_{\text{Calo}})^2}{E_{\text{MC}}^2} \quad \text{vs} \quad \frac{1}{E_{\text{MC}}}$$

with a straight line (see Figure B.4, right plot).

B.3.1 Tests with extrapolators

The code has been tested using information from the Monte Carlo truth. VeLo tracks are updated with the missing momentum information and extrapolated to the Calorimeter, taking into account the magnetic bending. The position of the extrapolated track is compared to the position of the cluster, showing that the matching resolution is dominated by the size of the Calorimeter clusters.

These tests where run using a stand-alone Gaudi application on 3000 $B_d \rightarrow \pi^+\pi^-$ events, matching each track to `L0CaloCandidates` with $E_{\text{T}} > 2.0$ GeV. Only correct matches are kept; a match is considered to be correct if the the VeLo track and the `L0CaloCandidate` are linked to the same MCParticle.

First the track is linked with its MCParticle and the state is updated with the q/p from the MCParticle. Then the track is extrapolated iteratively for 100 z values between the original position and the z of the matched `L0CaloCandidate`. The `TrackParabolic-Extrapolator` tool is used for the extrapolation[2]. 2D tracks have to be converted to cartesian geometry before extrapolation.

The position where the extrapolated track reaches the HCAL can be compared to the position of the matched `L0CaloCandidate`, giving the matching resolution. The geometrical distance between the extrapolated track and the hit should be correlated to the χ^2 value (small distances for small χ^2). This can be used for testing the validity of the matching procedure.

Another test criterium is to compute a χ^2_{MC} in the same way as the tool does, but using the extrapolated track to compute the x_{kick}:

$$x_{\text{kick}} = |x_{\text{ex}} - z_{\text{ex}} t_x| \qquad (B.4)$$

where 'ex' refers to the extrapolated track and t_x is the slope of the original track (see Figure B.2 on page 112). χ^2_{MC} should be correlated to χ^2.

---

[1]The σ_E parameterization shown in equation B.3 was taken from the original code by N. Tuning. It is actually quite different from the one found in the Calorimeter technical design report; however it seems to work better for the matching. This requires further investigation, as σ_E is an important value for the χ^2 calculation.

[2]attempts were made to use the `TrackMasterExtrapolator`, but this tool caused DaVinci to crash for some events.
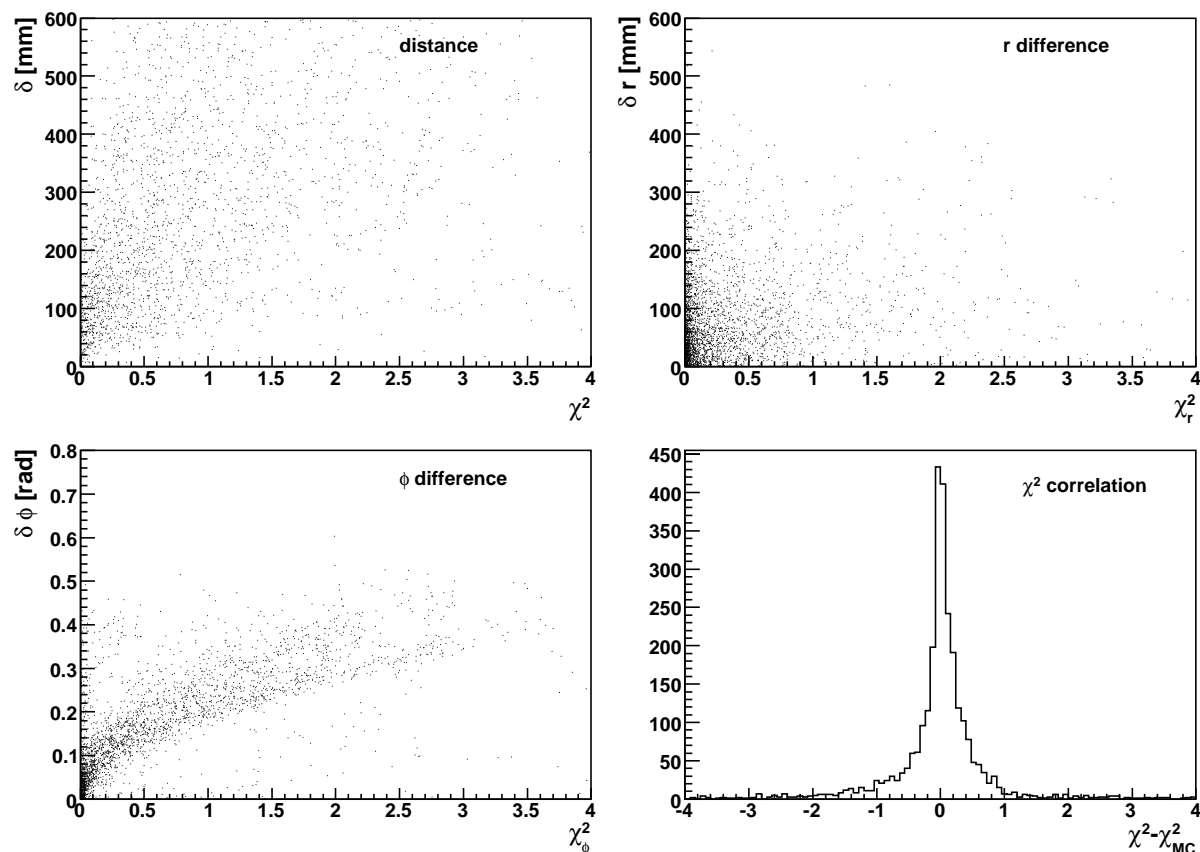
Figure B.3: Tests for 2D matching. Top left: distance between extrapolated track and Calo hit vs χ^2; top right: r-projection of the distance vs χ^2_r; bottom left: ϕ-projection vs χ^2_ϕ; bottom right: χ^2 correlation.

Figure B.3 shows the test results for 2D matching. The resolution is rather bad, some good matches (small χ^2) having a distance of 40 cm or more. This clearly comes from the difference in ϕ, which shows a good correlation with χ^2 but can be as large as 23 degrees. The difference in r shows no correlation with χ^2, due to the imprecision of the x_{kick} correction. χ^2_{MC} is well correlated to χ^2.

B.3.2   Kick correction

The effect of the magnetic field is approximated by an instant kick of the momentum vector at the center of the magnet (see [79], section 6.2.3). The center of the magnet is defined by a plane at $z = z_0$ where the integrated field equals half the total value. The kick correction is only applied in the x-direction.

The track extrapolation allows one to compute the C_{kick} constant, using the x_{kick} value from equation B.4. For L0CaloCandidates with $E_{\text{T}} > 3.5\,\text{GeV}$, this gives a mean value of $C_{\text{kick}} = 1.240\,\text{GeV}$, and the mean value of the correction is 29 cm, which is much more than the matching resolution.

Figure B.4 shows x_{kick} computed from equation B.4 as a function of $\frac{z-z_o}{E}$. A linear fit gives $C_{\text{kick}} = 1.130\,\text{GeV}$.

A more precise kick correction has been studied, using a second-order approximation

in x and in y. Figure B.4 shows that the parabolic version of the x kick correction isn't very different from the linear one, all the more at high energies, while introducing an additional parameter.

The kick correction in the y direction doesn't significantly improve the matching resolution, as its mean amplitude only is 6 mm. Thus it was decided to only apply a linear correction in the x direction, using just one parameter.
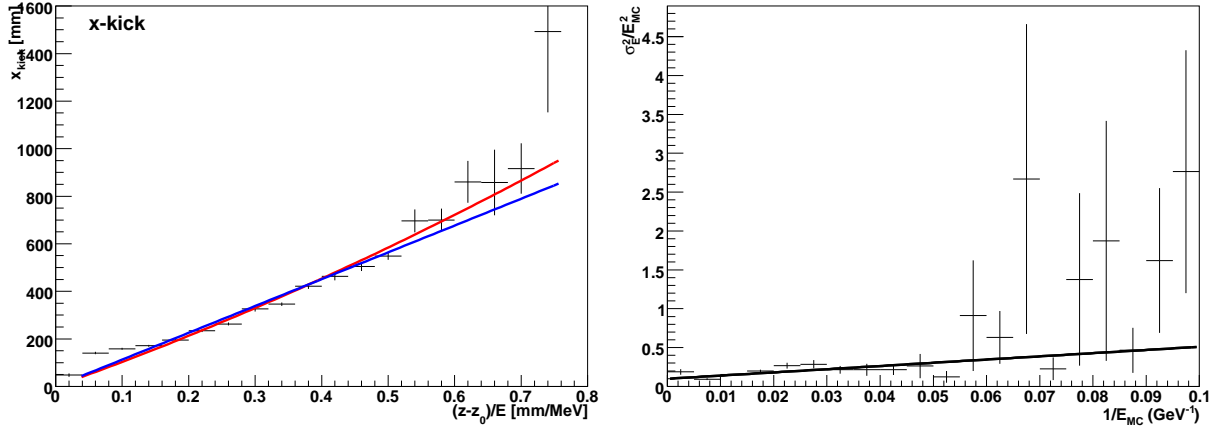

Figure B.4: left: kick corrections in the x direction, with linear and parabolic fit; right: energy error and linear fit

B.3.3 χ^2 distributions

Figure B.5 shows the χ^2 distributions. Beyond $\chi^2 \sim 4$ the contribution from correct matches becomes negligible.

B.4   Matching 3D tracks

Given a VeLo 3D track with slopes $t_x = \frac{dx}{dz}$ and $t_y = \frac{dy}{dz}$, and a `L0CaloCandidate` with position x, y, z and transverse energy E_T, the χ^2 is computed in the following way for charge $q = \pm 1$:

$$
\begin{aligned}
\chi^2 &= \chi_x^2 + \chi_y^2 \\
\chi_x^2 &= \left(\frac{x - q x_{\text{kick}}}{z} - t_x \right)^2 \frac{1}{\sigma_x^2} \\
\chi_y^2 &= \left(\frac{y}{z} - t_y \right)^2 \frac{1}{\sigma_y^2}
\end{aligned}
\tag{B.5}
$$

The kick correction is the same as in the 2D matching. The errors σ_x and σ_y take into account the uncertainty on the calorimeter hit position and energy. Again, s is the half-size of the corresponding calorimeter cell.

$$
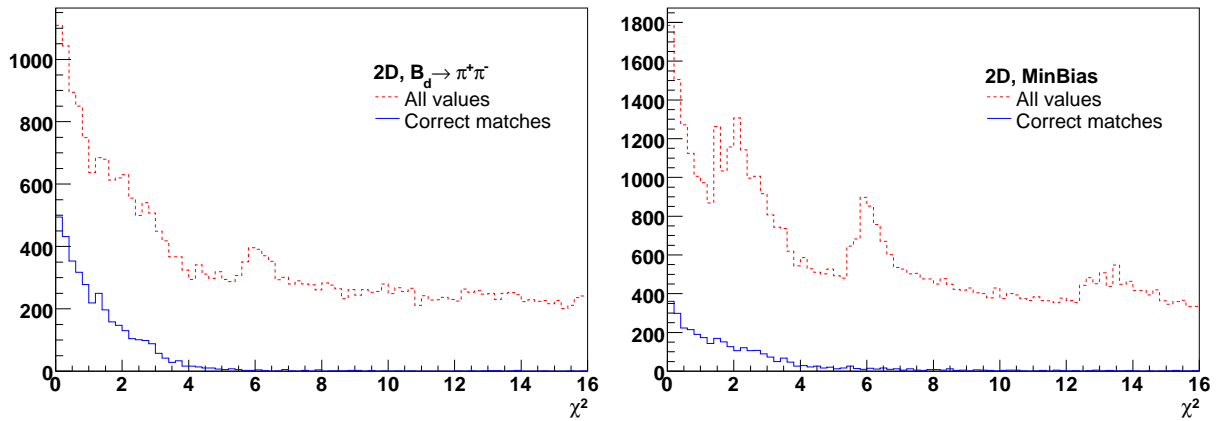\sigma_x = \frac{1}{z} \sqrt{e_x^2 + e_{\text{kick}}^2}
$$

Figure B.5: 2D χ^2 distributions for $B_d \rightarrow \pi^+\pi^-$ and minimum bias. In dotted red, all matches; in solid blue, only correct matches.

$$
\begin{aligned}
e_x &= \frac{4s}{\sqrt{12}} \\
e_{\text{kick}} &= x_{\text{kick}} \frac{\sigma_E}{E} \\
\sigma_y &= \frac{1}{z} \frac{4s}{\sqrt{12}}
\end{aligned}
$$

B.4.1 Tests with extrapolators

The same tests as for the 2D confirmation where performed. Figure B.6 shows the results for 3D matching. The difference in x shows no correlation with χ^2_x, due to the imprecision of the x_{kick} correction. The y difference has a very good correlation to χ^2_y with the expected parabolic shape. The lower parabola, in red, corresponds to matches in the inner HCAL region[3], with $13 \cdot 13 \, \text{cm}^2$ cells, and the upper parabola, in blue, corresponds to the outer region, with $26 \cdot 26 \, \text{cm}^2$ cells. In both cases, the maximal y difference corresponds to the cell size. Both the calorimeter cell size and the kick correction contribute to the matching resolution. χ^2_{MC} is very well correlated to χ^2.

B.4.2 χ^2 distributions

Figure B.7 shows the χ^2 distributions. Beyond $\chi^2 \sim 8$ the contribution from correct matches becomes negligible.

B.5 Tool interface

All the L0 confirmation tools of the HLT share the same interface `IHltMatchTrackCalo`.

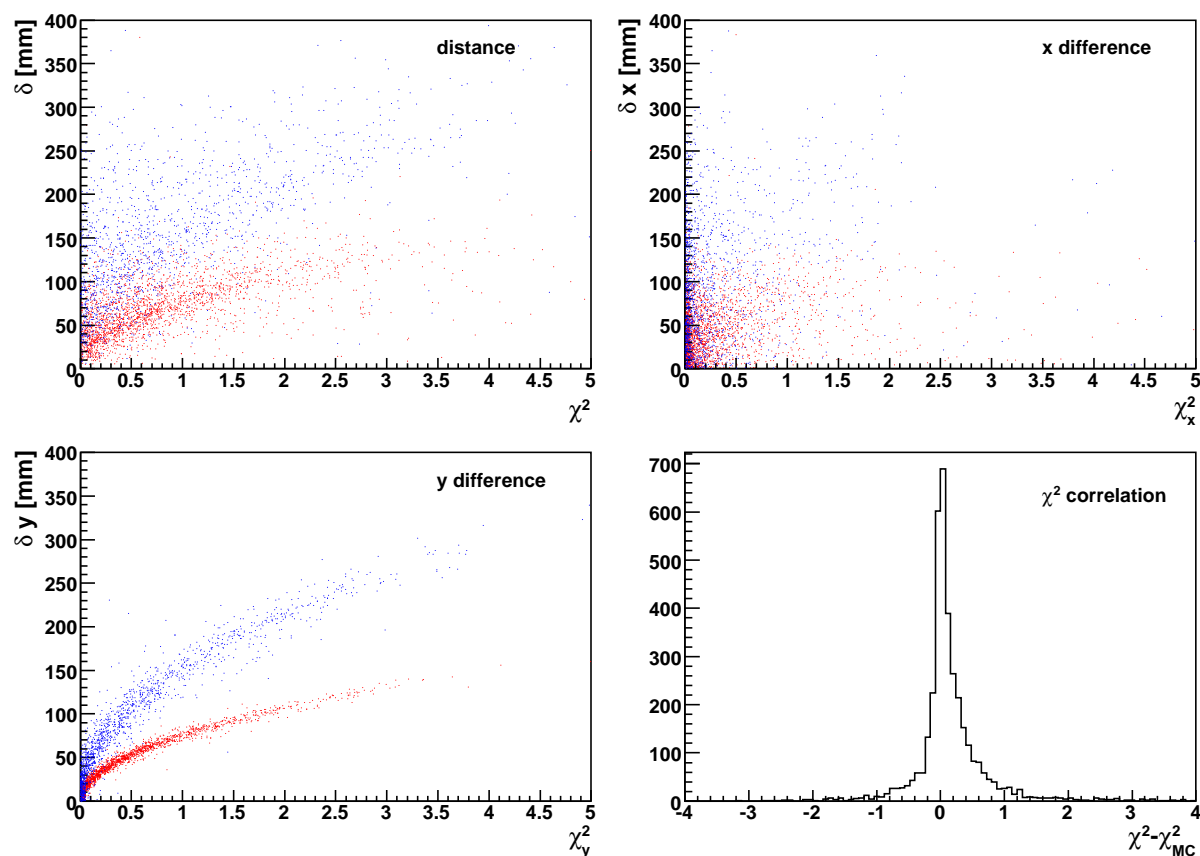[3]*inner region* means $|x| < 2000$ mm and $|y| < 2000$ mm

Figure B.6: Tests for 3D matching. Top left: distance between extrapolated track and Calo hit as a function of χ^2; top right: x-projection of the distance vs χ^2_x; bottom left: y-projection vs χ^2_y; red is for the HCAL inner region and blue for the outer region. Bottom right: χ^2 correlation.

B.5.1   Tool functions

This is how to access the tool:

```
#include "HltInterfaces/IHltMatchTrackCalo.h"
IHltMatchTrackCalo* m_matchL0Hadron =
    tool<IHltMatchTrackCalo>("HltHadAlleyMatchCalo");
```

There is a function to tell the tool which L0CaloCandidates to use, requiring candidates with $E_T > $ etCut. The function returns the number of candidates found.

```
double etCut = 3.5*GeV;
int nCandidates;
nCandidates = m_matchL0Hadron->getCandidates(etCut);
```

The confirmation functions take a track and return the best χ^2:

```
Track track;
double chi2;
chi2 = m_matchL0Hadron->confirmation2D(track);
chi2 = m_matchL0Hadron->confirmation3D(track);
```
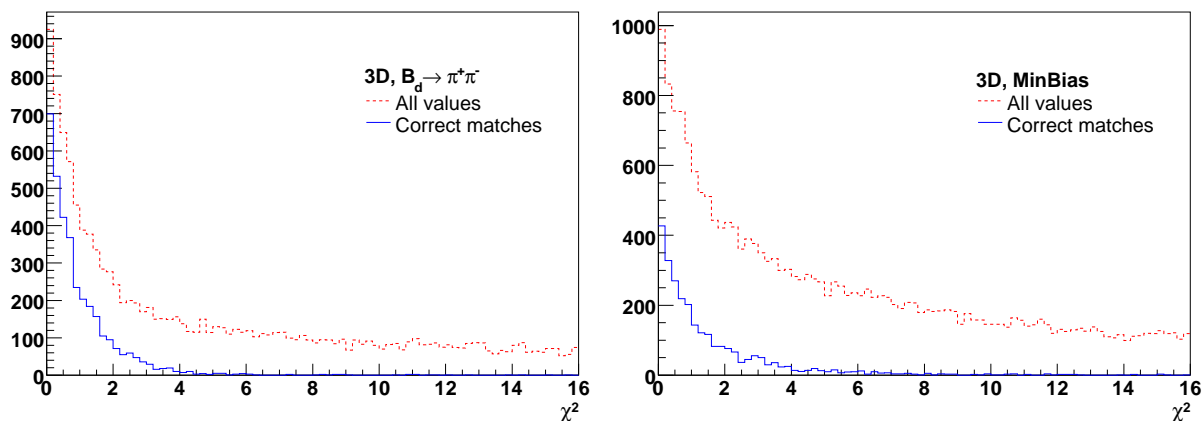
Figure B.7: 3D χ^2 distributions for $B_d \rightarrow \pi^+\pi^-$ and minimum bias. In dotted red, all matches; in solid blue, only correct matches.

There is a function that returns a vector of pairs $(\chi^2,$ `L0CaloCandidate`$)$ for all matches with $\chi^2 <$ `chi2Cut{2D,3D}` :

```
std::vector< std::pair<double, L0CaloCandidate*> >
    matchedPairs = m_matchL0Hadron->matchedCandidates();
```

This function should be used after 2D or 3D confirmation to see which `L0CaloCandidates` have been matched with the track, since sometimes there is more than one, and the right one is not necessarily the one with the smallest χ^2.

B.5.2   Tool options

The following properties can be modified in an option file:

`ptkickConstant = 1.263*GeV` constant for kick correction

`ptkickZ0 = 5250.0*mm` z_0 for kick correction

`caloCandidatesName = "Trig/L0/FullCalo"` location of `L0CaloCandidates` in the Transient Event Store

`chi2Cut2D = 7.0`

`chi2Cut3D = 7.0` χ^2 limits for the return values of the `matchedCandidates()` function

B.6   Performance

The analysis described in the next paragraphs is performed by a stand-alone Gaudi application running on 3212 $B_d \rightarrow \pi^+\pi^-$ events, 1376 $B_s \rightarrow D_s K$ events and 6000 minimum bias events (of which 4179 are L0-hadron triggered). All events are in RTTC format with a luminosity of $2 \cdot 10^{32}\,\mathrm{cm}^{-2}\mathrm{s}^{-1}$. The signal events are offline selected events. 3D efficiencies are computed after the 2D confirmation, which is used as a filter, with a loose χ^2 cut at 7.0.

B.6.1   Offline selection efficiency and retention
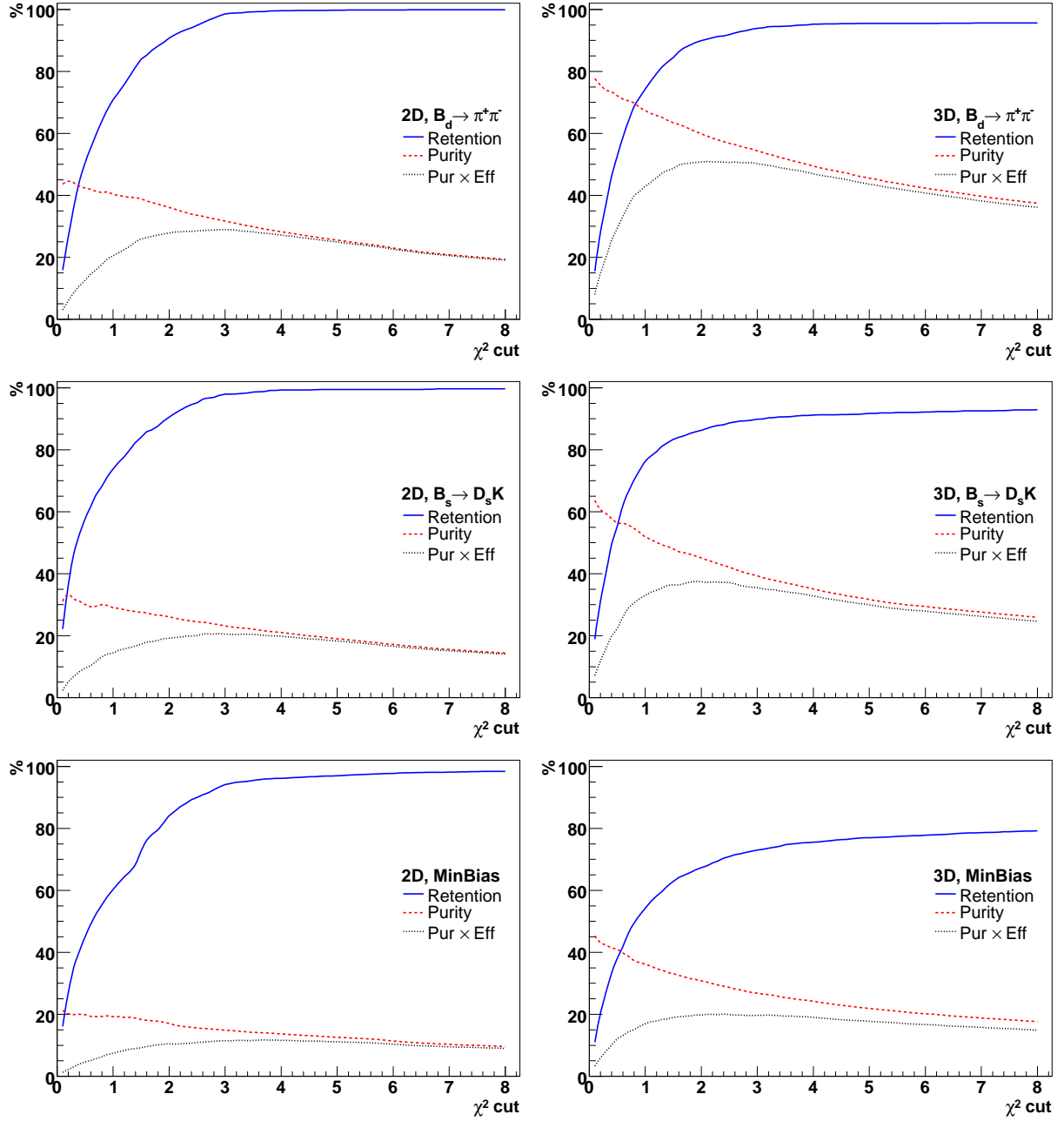
Figure B.8: Signal and minimum bias retention and purity as a function of the χ^2 cut.

Figure B.8 shows the signal and minimum bias retention and purity. An event is rejected if there is no track that passes the χ^2 cut; the purity is defined as the fraction of correct matches normalized to all matches. It should be noticed that these results are very similar to those obtained by N. Tuning [77].

Figure B.9 shows the average number of tracks per event, after 2D and 3D matching. For minimum bias events, there are in average 70.7 forward tracks per event before 2D matching. Cutting at $\chi^2 < 7$, there are 7.2 tracks left after 2D confirmation, and 3.4 after

Figure B.9: Average number of tracks/event as a function of the χ^2 cut.

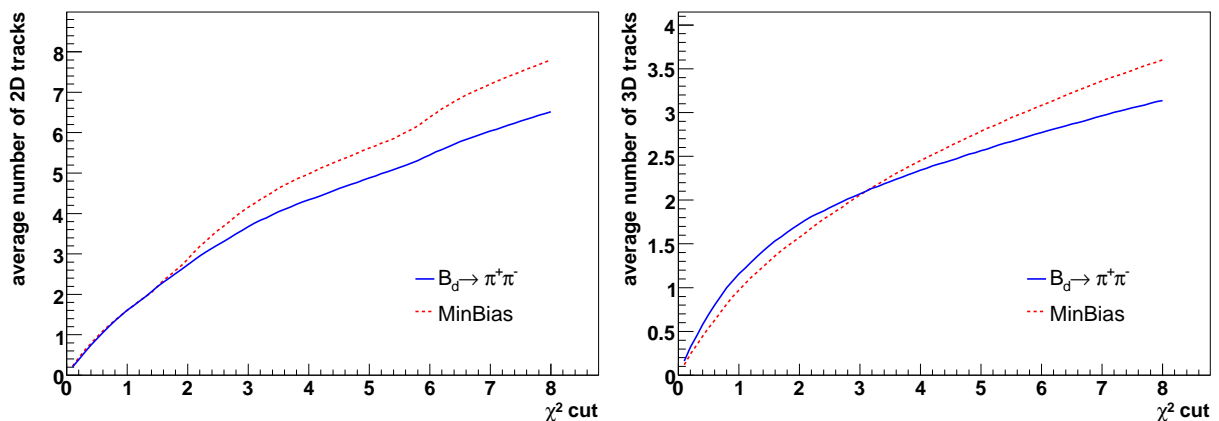3D confirmation. Thus the total L0 confirmation track retention rate is 4.8% (including VeLo space tracking efficiency and acceptance cut, see paragraph B.6.3). This rate can be further improved by applying an impact parameter cut, as is discussed in the next paragraph. Table B.1 shows a summary of the efficiencies for both cuts set to 7.0.

Channel	Retention		Tracks		Events
	2D	3D	2D	3D	
$B_d \to \pi^+\pi^-$	99.9%	95.7%	6.0	3.0	3212
$B_s \to D_s K$	99.7%	92.6%	7.8	4.0	1376
MinBias	98.2%	78.9%	7.2	3.4	6000

Table B.1: Summary of 2D and 3D efficiencies, with both χ^2 cuts set to 7.0.

B.6.2   Impact parameter cut

It is possible to further reduce the number of tracks by applying an impact parameter (IP) cut before the 2D confirmation. A negative IP is assigned to tracks coming from a secondary vertex which is behind the primary vertex; thus 50% of background tracks have a negative IP, while this is rare for signal tracks (but possible, due to the IP resolution or vertexing errors, or because the B decays away from the beam-line; in the determination of the sign of the IP it is assumed that the B travels exactly along the beam-line). Cutting out these negative IP tracks reduces the $B_d \to \pi^+\pi^-$ selection efficiency by 3%, but reduces the number of tracks per minimum bias event to 3.7 instead of 7.2 (see Figure B.10; only the 2D confirmation efficiencies are considered). These 3% signal events would be lost anyway further down the alley because of timing constraints.

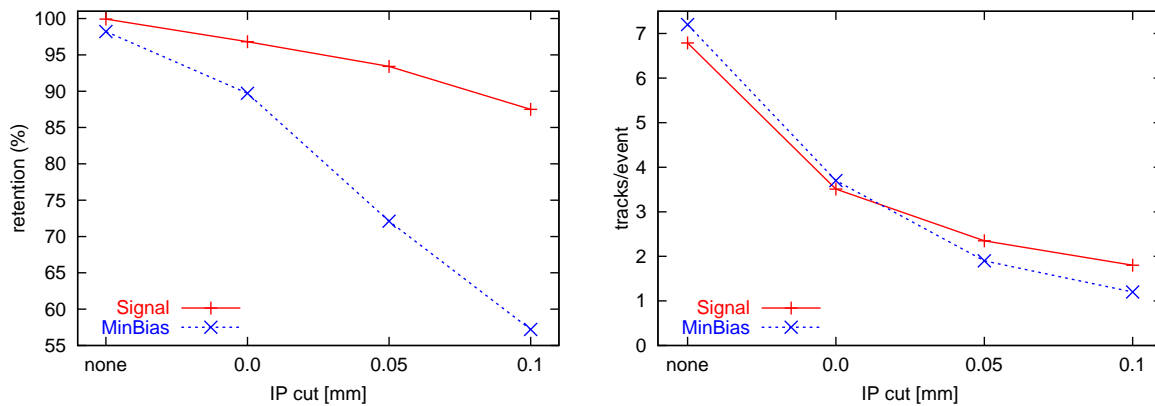Applying a tighter IP cut (IP > 0.05 or 0.1 mm) saves even more tracks but also degrades the signal retention rate.

Figure B.10: 2D confirmation event and track retention rates for various impact parameter cuts.

B.6.3   Acceptance cut

The VeLo has an acceptance of $\theta < 390$ mrad for all ϕ, in order to cover the LHCb acceptance $(0.25^2 + 0.3^2 \approx 0.39^2)$. This means that a fraction of the 3D reconstructed tracks will be outside the LHCb acceptance (see Figure B.11). Although these tracks might be useful for vertices, isolation etc., they should not be used for HCAL matching.

For minimum bias, without applying the 2D confirmation, the fraction of 3D input tracks that are outside the acceptance is about 10%. Applying the 2D confirmation, this fraction goes down to 4%, while only 0.23% of the correct 3D matches come from tracks outside the acceptance. Thus the 2D confirmation gets rid of most out-of-acceptance tracks. Still, it is reasonable to apply the acceptance cut:

$$
\begin{aligned}
t_x = \tan(\theta_x) &< \tan(0.3) \\
t_y = \tan(\theta_y) &< \tan(0.25)
\end{aligned}
$$

where t_x and t_y are the track slopes.

B.7   Role of the Tool in the HLT Hadronic Alley

The HLT hadronic alley [74] consists of four boxes, each box being a sequencer of algorithms. The L0 confirmation is the second box; it is preceded by the *entry point*, which takes the decision to enter the alley, and followed by the *pre-trigger* (old Level-1) and the *trigger* (old HLT-generic).

This section shows how the matching tool can be used in the L0 confirmation box, and takes a first look at timing.

In addition to the VeLo-Calo matching described in this note, the L0 confirmation could be completed by also matching with TT, but this is still under study.
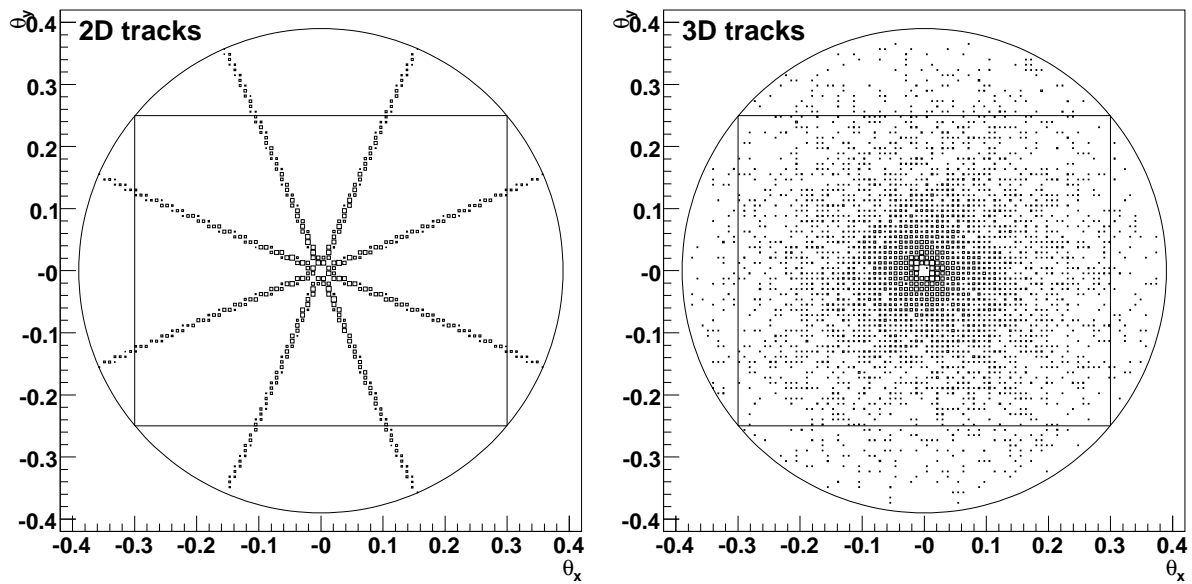
Figure B.11: Polar angle distributions of 2D and 3D input tracks. The circle shows the VeLo acceptance, while the rectangle represents the LHCb acceptance.

B.7.1 Algorithmic sequence

Two algorithms call the tool to perform the L0 confirmation, as illustrated in Figure B.12. Their basic task is to select the tracks based on a χ^2 criterion. Selected tracks are flagged, and can also be copied to a separate location in the `PatDataStore`. The procedures of these algorithms are very similar :

- retrieve the 2D or 3D tracks from the `PatDataStore`
- tell the tool to use the `L0CaloCandidates` that triggered L0
- filter backward 2D tracks
- apply the impact parameter cut for 2D tracks
- apply the acceptance cut for 3D tracks
- for each track, get the smallest χ^2 from the tool
- if the track passes the χ^2-cut, set a flag and clone the track in another path in the `PatDataStore` for further reconstruction
- filter the events, rejecting events where no track passes the χ^2-cut
- write a `HltSummaryBox` including the event filter decision, the number of selected tracks and the smallest χ^2.

Since both algorithms are very similar, and in order to avoid code duplication as much as possible, the 3D algorithm inherits the common functions from the 2D algorithm. This also allows for an easier maintenance. Note that this is not done in the tool, as there is very little duplication in the tool code.
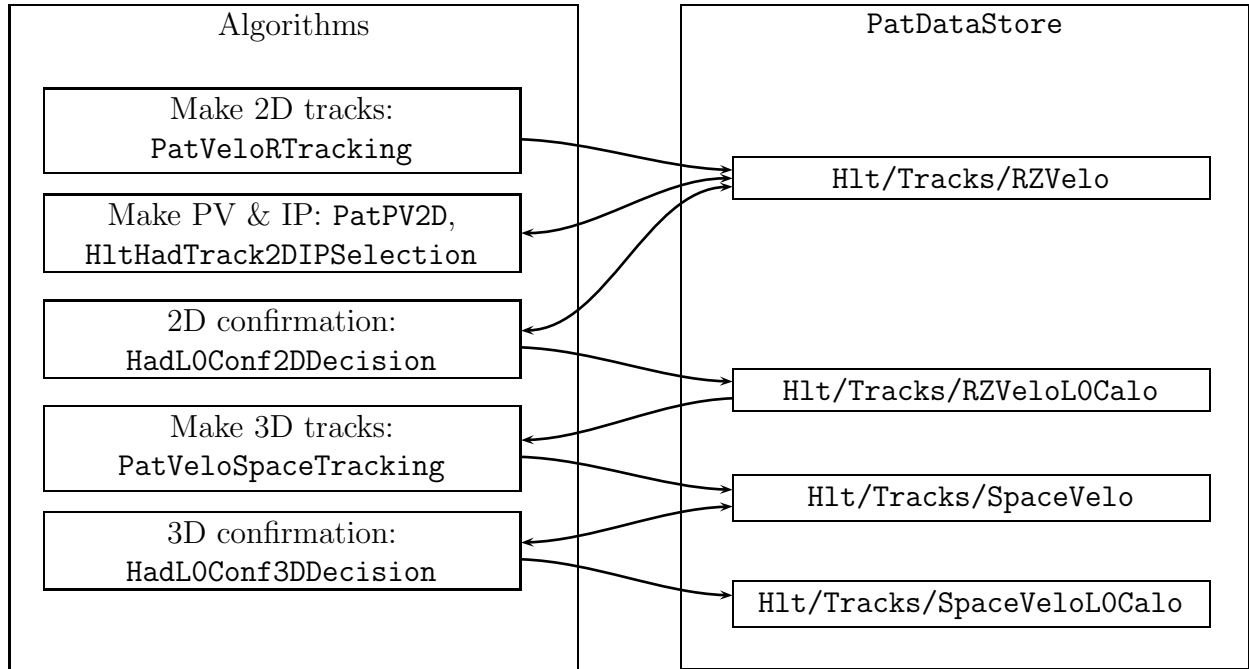
Figure B.12: Design of the L0 Confirmation box

B.7.2   Algorithm options

Both algorithms have the same set of options:

chi2Cut χ^2 cut for track selection. This doesn't have to be the same value as in the tool options.

L0EtCut = 3500.*MeV   minimal E_{T} of the L0CaloCandidates that should be used for matching

CopyTracks = true   if set to false, do not copy the selected tracks to OutputTracksName, just flag them

InputTracksName   location of input tracks in the PatDataStore

OutputTracksName   location of output tracks in the PatDataStore

HltSummaryLocation   location of the HLT summary in the TES

UseIPCut = true   if set to false, do not apply the impact parameter cut (only for 2D confirmation). The cut value has to be set using the IPMin property of the HltHadTrack2DIPSelection algorithm.

B.7.3   Timing

Table B.2 shows the timing for the L0 Confirmation box, running 10'000 minimum bias events on a machine that is about 0.98 times faster than a 2.8 GHz Xeon. The timing has been performed using the standard SequencerTimerTool.

     More than half the time is spent for the tracking, while the confirmation algorithms only take about 10% of the time each.

Algorithm	ms/event	%
HltHadL0Confirmation	4.580	100 %
PatInitEvent	0.276	6.0 %
CreateRawEvent	0.140	3.0 %
PatVeloDecodeRaw	0.412	9.0 %
PatVeloRTracking	1.344	29.3 %
PatPV2D	0.203	4.4 %
HltHadTrack2DIPSelection	0.167	3.6 %
HadL0Conf2DDecision	0.526	11.5 %
HltHadVeloSpacePartial	1.659	24.9 %
HadL0Conf3DDecision	0.477	7.1 %

Table B.2: L0 Confirmation box timing. Time spent in each algorithm, in milliseconds per event or as a fraction of the total time spent in the box.

B.8 Conclusion

The L0 confirmation code for VeLo to HCAL is available in the form of a tool and two algorithms. The code compiles and runs with RTTC data, which is a major step towards DC06. Hence the migration to DC06 should only imply minor changes, and an easy transition can be expected.

Code, documentation, presentations and other material concerning the subject of this note are available on a dedicated web page [80].

The resolution of the matching could be greatly improved by applying the *s-curve correction* on the calorimeter clusters [81], which improves the position of the L0Calo-Candidate. This correction method is still under investigation.

The selection efficiencies and track retention rates that have been studied show that the L0 confirmation is a very powerful way of selecting tracks in the hadronic alley.

Bibliography

[1] N. Zwahlen, T. Aushev et al. (Belle Collaboration), *Study of the B $\to$ X(3872)($D^{*0}\bar{D}^0$)K decay*, hep-ex/0810.0358v2 (2008).

[2] N. Zwahlen, T. Aushev, *Study of B $\to$ X(3872)($D^{*0}\bar{D}^0$)K*, Belle Note 1006 (2008).

[3] W. N. Cottingham, D. A. Greenwood, *An Introduction to the Standard Model of Particle Physics*, Cambridge University Press (1998).

[4] C. Amsler et al. (Particle Data Group), *Review of particle physics*, Phys. Lett. B **667**, 1 (2008).

[5] J. Sexton, A. Vaccarino, D. Weingarten, *Numerical evidence for the observation of a scalar glueball*, Phys. Rev. Lett. **75**, 4563 (1995).

[6] N. Isgur, R. Kokoski, J. Paton, *Gluonic excitations of mesons: Why they are missing and where to find them*, Phys. Rev. Lett. **54**, 869 (1985).

[7] D. R. Thompson et al. (E852 Collaboration), *Evidence for exotic meson production in the reaction $\pi^- p \to \eta\pi^- p$ at* 18 GeV/c, Phys. Rev. Lett. **79**, 1630 (1997).

[8] G. S. Adams et al. (E852 Collaboration), *Observation of a new $J^{PC} = 1^{-+}$ exotic state in the reaction $\pi^- p \to \pi^+\pi^-\pi^- p$ at* 18 GeV/c, Phys. Rev. Lett. **81**, 5760 (1998).

[9] A. Zhang, T. Huang, T. G. Steele, *Diquark and light four-quark states*, Phys. Rev. D **76**, 036004 (2007).

[10] B. Aubert et al. (BaBar Collaboration), *Observation of a narrow meson state decaying to $D_s^+\pi^0$ at a mass of* 2.32 GeV/c^2, Phys. Rev. Lett **90**, 242001 (2003).

[11] D. Besson et al. (CLEO Collaboration), *Observation of a narrow resonance of mass* 2.46 GeV/c^2 *decaying to $D_s^{*+}\pi^0$ and confirmation of the $D_{sJ}^*(2317)$ state*, Phys. Rev. D **68**, 032002 (2003).

[12] J. Hicks, *An experimental review of the Θ^+ pentaquark*, J. Phys. Conf. Ser. **9**, 183 (2005).

[13] G. C. Branco, L. Lavoura, J. P. Silva, *CP Violation*, Oxford University Press (1999).

[14] S. L. Olsen, *What's new with the XYZ mesons?*, hep-ex/0801.1153v3 (2008).

[15] E. S. Swanson, *New heavy mesons*, hep-ph/0601110v3 (2006).

[16] G. V. Pakhlova, *Exotic $c\bar{c}$ spectroscopy*, hep-ex/0810.4114 (2008).

[17] S.-K. Choi et al. (Belle Collaboration), *Observation of a narrow charmoniumlike state in exclusive $B^{\pm} \to K^{\pm}\pi^+\pi^- J/\psi$ decays*, Phys. Rev. Lett. **91**, 262001 (2003).

[18] B. Aubert et al. (BaBar Collaboration), *Study of the $B^- \to J/\psi\, K^-\pi^+\pi^-$ decay and measurement of the $B^- \to X(3872)K^-$ branching fraction*, Phys. Rev. D **71**, 071103 (2005).

[19] D. Acosta et al. (CDF Collaboration), *Observation of the narrow state $X(3872) \to J/\psi\,\pi^+\pi^-$ in $\bar{p}p$ collisions at $\sqrt{s} = 1.96\ TeV$*, Phys. Rev. Lett. **93**, 072001 (2004).

[20] V.M. Abazov et al. (DØ Collaboration), *Observation and properties of the $X(3872)$ decaying to $J/\psi\,\pi^+\pi^-$ in $p\bar{p}$ collisions at $\sqrt{s} = 1.96\ TeV$*, Phys. Rev. Lett. **93**, 162002 (2004).

[21] G. Gokhroo et al. (Belle Collaboration), *Observation of a near-threshold $D^0\bar{D}^0\pi^0$ enhancement in $B \to D^0\bar{D}^0\pi^0 K$ decays*, Phys. Rev. Lett. **97**, 162002 (2006).

[22] B. Aubert et al. (BaBar Collaboration), *Study of resonances in exclusive B decays to $\bar{D}^{(*)}D^{(*)}K$*, Phys. Rev. D **77**, 011102 (2008).

[23] S. Uehara et al. (Belle Collaboration), *Observation of a χ'_{c2} candidate in $\gamma\gamma \to D\bar{D}$ production at Belle*, Phys. Rev. Lett. **96**, 082003 (2005).

[24] P. Pakhlov et al. (Belle Collaboration), *Observation of a charmoniumlike state produced in association with a J/ψ in e^+e^- annihilation at $\sqrt{s} \approx 10.6\ GeV$*, Phys. Rev. Lett. **98**, 082001 (2007).

[25] S.-K. Choi, S. L. Olsen et al. (Belle Collaboration), *Observation of a near-threshold $\omega J/\psi$ mass enhancement in exclusive $B \to K\omega J/\psi$ decays*, Phys. Rev. Lett. **94**, 182002 (2005).

[26] B. Aubert et al. (BaBar Collaboration), *Observation of $Y(3940) \to J/\psi\,\omega$ in $B \to J/\psi\,\omega K$ at BaBar*, Phys. Rev. Lett. **101**, 082001 (2008).

[27] P. Pakhlov et al. (Belle Collaboration), *Production of new charmoniumlike states in $e^+e^- \to J/\psi D^{(*)}\bar{D}^{(*)}$ at $\sqrt{s} \approx 10.6\ GeV$*, Phys. Rev. Lett. **100**, 202001 (2008).

[28] C. Z. Yuan et al. (Belle Collaboration), *Measurement of the $e^+e^- \to \pi^+\pi^- J/\psi$ cross section via initial-state radiation at Belle*, Phys. Rev. Lett. **99**, 182004 (2007).

[29] B. Aubert et al. (BaBar Collaboration), *Observation of a broad structure in the $\pi^+\pi^- J/\psi$ mass spectrum around 4.26 GeV/c^2*, Phys. Rev. Lett. **95**, 142001 (2005).

[30] T. E. Coan et al. (CLEO Collaboration), *Charmonium Decays of $Y(4260)$, $\psi(4160)$, and $\psi(4040)$*, Phys. Rev. Lett. **96**, 162003 (2006).

[31] B. Aubert et al. (BaBar Collaboration), *Evidence of a broad structure at an invariant mass of 4.32 GeV/c^2 in the reaction $e^+e^- \to \pi^+\pi^-\psi(2S)$ measured at BaBar*, Phys. Rev. Lett. **98**, 212001 (2007).

[32] X. L. Wang et al. (Belle Collaboration), *Observation of two resonant structures in $e^+e^- \to \pi^+\pi^-\psi(2S)$ via initial-state radiation at Belle*, Phys. Rev. Lett. **99**, 142002 (2007).

[33] R. Mizuk, R. Chistov et al. (Belle Collaboration), *Observation of two resonance-like structures in the $\pi^+\chi_{c1}$ mass distribution in exclusive $\bar{B}^0 \to K^-\pi^+\chi_{c1}$ decays*, hep-ex/0806.4098v2 (2008).

[34] S.-K. Choi, S. L. Olsen et al. (Belle Collaboration), *Observation of a resonancelike structure in the $\pi^{\pm}\psi'$ mass distribution in exclusive $B \to K\pi^{\pm}\psi'$ decays*, Phys. Rev. Lett. **100**, 142001 (2008).

[35] The CDF Collaboration, *Mass Measurement of the $X(3872)$ State*, CDF Note 9454 (2008).

[36] K. Trabelsi et al. (Belle Collaboration), *Study of $X(3872)$ in B meson decays*, hep-ex/0809.1224v1 (2008).

[37] B. Aubert et al. (BaBar Collaboration), *Study of $B \to X(3872)K$, with $X(3872) \to J/\psi\,\pi^+\pi^-$*, Phys. Rev. D **77**, 111101 (2008).

[38] K. Abe et al. (Belle Collaboration), *Evidence for $X(3872) \to \gamma J/\psi$ and the sub-threshold decay $X(3872) \to \omega J/\psi$*, hep-ex/0505037 (2005).

[39] B. Aubert et al. (BaBar Collaboration), *Evidence for $X(3872) \to \psi(2S)\gamma$ in $B^{\pm} \to X(3872)K^{\pm}$ decays, and a study of $B \to c\bar{c}\gamma K$*, hep-ex/0809.0042v1 (2008).

[40] K. Abe et al. (Belle Collaboration), *Experimental constraints on the possible J^{PC} quantum numbers of the $X(3872)$*, hep-ex/0505038 (2005).

[41] D. Abulancia et al. (CDF Collaboration), *Measurement of the dipion mass spectrum in $X(3872) \to J/\psi\pi^+\pi^-$ decays*, Phys. Rev. Lett. **96**, 102002 (2006).

[42] D. Abulancia et al. (CDF Collaboration), *Analysis of the quantum numbers J^{PC} of the $X(3872)$ particle*, Phys. Rev. Lett. **98**, 132002 (2007).

[43] C. Cawlfield et al. (CLEO Collaboration), *Precision determination of the D^0 mass*, Phys. Rev. Lett. **98**, 092002 (2007).

[44] T. Barnes, S. Godfrey, *Charmonium options for the X(3872)*, Phys. Rev. D **69**, 054008 (2004).

[45] S. Godfrey, N. Isgur, *Mesons in a relativized quark model with chromodynamics*, Phys. Rev. D **32**, 189 (1985).

[46] N. A. Törnqvist, *Isospin breaking of the narrow charmonium state of Belle at 3872 MeV as a deuson*, Phys. Lett. B **590**, 209 (2004).

[47] N. A. Törnqvist, *From the deuteron to deusons, an analysis of deuteron-like meson-meson bound states*, Z. Phys. C **61**, 525 (1994).

[48] E. Braaten, M. Lu, *The effects of charged charm mesons on the line shapes of the X(3872)*, Phys. Rev. D **77**, 014029 (2008).

[49] L. Maiani et al., *Diquark-antidiquark states with hidden or open charm and the nature of X(3872)*, Phys. Rev. D **71**, 014028 (2005).

[50] L. Maiani et al., *Indications of a four-quark structure for the X(3872) and X(3876) particles from recent Belle and BaBar data*, Phys. Rev. Lett. **99**, 182003 (2007).

[51] B. A. Li, *Is X(3872) a possible candidate as a hybrid meson?*, Phys. Lett. B **605**, 306 (2005).

[52] C. Hanhart et al., *Reconciling the X(3872) with the near-threshold enhancement in the $D^0\bar{D}^{*0}$ final state*, Phys. Rev. D **76**, 034007 (2007).

[53] E. Kou, O. Pene, *Suppressed decay into open charm for the Y(4260) being an hybrid*, Phys. Lett. B **631**, 164 (2005).

[54] X. Liu, Y.-R. Liu and W.-Z. Deng, *Dynamics study of $Z^+(4430)$ and X(3872) in molecular picture*, hep-ph/0802.3157v3 (2008).

[55] A. G. Mokhtar, *Searches for exotic X,Y, and Z- states with BaBar*, hep-ex/0810.1073 (2008).

[56] S. Kurokawa, E. Kikutani, *Overview of the KEKB accelerators*, Nucl. Instr. and Meth. A **499**, 1 (2003).

[57] A. Abashian et al. (Belle Collaboration), *The Belle detector*, Nucl. Instr. and Meth. A **479**, 117–232 (2002).

[58] D. J. Lange, *The EvtGen particle decay simulation package*, Nucl. Instr. and Meth. A **462**, 152–155 (2001).

[59] R. Brun et al., *GEANT 3.21*, CERN Report DD/EE/84-1 (1984).

[60] F. Fang, *Study of $K_S^0 \to \pi^+\pi^-$ selection*, Ph.D. thesis, University of Hawaii (2003).

[61] G. C. Fox, S. Wolfram, *Observables for the analysis of event shapes in e^+e^- annihilation and other processes*, Nucl. Rev. Lett **41**, 1581 (1978).

[62] F. Fang, *Study of $K_S^0 \to \pi^+\pi^-$ selection*, Belle Note 323 (2000).

[63] H. Albrecht et al. (ARGUS Collaboration), *Reconstruction of B mesons*, Phys. Lett. B **185**, 218 (1987).

[64] R. D. Cousins, *Why isn't every physicist a Bayesian?*, Am. J. Phys. **63**, 398 (1995).

[65] G. Gokhroo, G. Majumder, S. Banerjee, *Observation of a near-threshold enhancement in the $D^0\bar{D}^0\pi^0$ invariant mass in $B \to D^0\bar{D}^0\pi^0 K$*, Belle Note 781 (2006).

[66] Belle tracking group, *Charged Particle Tracking in Belle*, Belle Note 327 (2000).

[67] S. Nishida, *Study of kaon and pion identification using inclusive D^* sample*, Belle Note 779, see also `http://belle.kek.jp/group/pid_joint/` (2005).

[68] S. W. Lin, P. Chang and H. C. Huang, *Update of π^0 systematics using inclusive η (*78 fb^{-1}*)*, Belle Note 645 (2003).

[69] S. W. Lin, P. Chang, *Br. of hh with 449 million $B\bar{B}$ pairs*, Belle Note 901 (2006).

[70] W.-M. Yao et al. (Particle Data Group), *Review of particle physics*, J. Phys. G **33** (2006).

[71] *LHCb Technical Proposal, LHCb Re-optimixation TDR, see also LHCb web site*, `http://lhcb.cern.ch/`.

[72] R. Antunes Nobrega et al. (LHCb Collaboration), *Trigger Technical Design Report*, CERN/LHCC 2003-31 (2003).

[73] T. Schietinger, *High-Level Trigger Strategy at 1 MHz*, LHCb Collaboration meeting, CERN (30th November 2005).

[74] J. Hernando, *HLT Alleys Implementation*, 26th LHCb Software Week, CERN (27th April 2006).

[75] N. Zwahlen, *HLT VeLo track – L0 Hadron Confirmation Tool*, LHCb Trigger and Reconstruction Meeting, CERN (27th March 2006).

[76] N. Zwahlen, *Status of L0 Confirmation (hadrons and Velo)*, LHCb Trigger and Reconstruction Meeting, CERN (22nd May 2006).

[77] N. Tuning, *Matching VELO tracks to L0 objects for L1* (LHCb note 2003-039, 2003).

[78] N. Zwahlen, *HLT Hadronic L0 Confirmation*, LHCb note 2006-040, LPHE note 2006-014 (2006).

[79] J. van Tilburg, *Track simulation and reconstruction in LHCb*, Ph.D. thesis, CERN thesis 2005-040 (2005).

[80] `http://lphe.epfl.ch/~nzwahlen/work/lhcb/l0confirmation/`.

[81] M. John, *L0 Confirmation (hadrons and T)*, LHCb Trigger and Reconstruction Meeting, CERN (22nd May 2006).

Nicolas Zwahlen

Avenue du Tir-Fédéral 79
1022 Chavannes-près-Renens
Switzerland

E-mail: `nicolas.zwahlen@epfl.ch`

Date of birth	November 17, 1979
Nationality	Swiss
Marital status	single

Education and degrees

since 2006	Member of the Belle collaboration
June 2006	CERN European School of High-Energy Physics in Aronsborg, Sweden
2005 – 2006	Member of the LHCb collaboration
2005 – 2009	Ph.D. studies in High-Energy Physics at LPHE, EPFL
2004	Master thesis in Physics at EPFL
1999 – 2004	Physics studies at UNIL and EPFL

Publications

- N. Zwahlen et al. (Belle Collaboration), *Study of the $B \to X(3872)(D^{*0}\bar{D}^0)K$ decay*, hep-ex/0810.0358v2 (2008).

- N. Zwahlen et al., *A purely geometric distance to the binary star Atlas, member of the Pleiades*, Astronomy and Astrophysics 425, L45-L48 (2004).